The Evolution and Decay of Sunspots

A High-Resolution Study of Flows and Magnetic Fields in and around Sunspots

Dissertation
zur Erlangung des akademischen Grades
doctor rerum naturalium
(Dr. rer. nat.)
in der Wissenschaftsdisziplin Astronomie und Astrophysik

eingereicht an der
Mathematisch-Naturwissenschaftlichen Fakultät
der Universität Potsdam

Meetu Verma

April 3, 2013

Leibniz-Institut für Astrophysik Potsdam
An der Sternwarte 16
14482 Potsdam

Universität Potsdam, Campus Golm
Institut für Physik und Astronomie (Haus 28)
Karl-Liebknecht-Strasse 24/25
14476 Potsdam-Golm

Table of Contents

Abstract . . . 1

1 Introduction 4

1.1 Flows on the Solar Surface . . . 4

1.1.1 Granulation . . . 4

1.1.2 Mesogranulation . . . 5

1.1.3 Supergranulation . . . 5

1.1.4 Flows in and around Sunspots . . . 7

1.1.5 Evershed Flow . . . 7

1.1.6 Moat Flow and Moving Magnetic Features . . . 10

1.1.7 Shear Flows in and around Active Regions . . . 12

1.2 Methods to Mesasure Flows . . . 13

1.3 Applications of Cross-Correlation Techniques . . . 14

1.3.1 Sea Surface Velocity . . . 14

1.3.2 Cloud Motion Wind . . . 15

1.3.3 Particle Image Velocimetry . . . 16

2 Local Correlation Tracking 17

2.1 Observations . . . 18

2.1.1 High-Cadence Sequence . . . 18

2.1.2 Long-Duration Sequence . . . 19

2.1.3 High-Spatial Resolution Sequence . . . 19

2.2 Implementation of the LCT Algorithm . . . 20

2.2.1 Preprocessing of the G-band Images . . . 20

2.2.2 Aligning the Images within a Time-Series . . . 20

2.2.3 LCT Algorithm . . . 21

2.2.4 LCT Data Products . . . 22

2.2.5 Timing Issues Related to the Image Capture . . . 24

2.3 Results . . . 25

2.3.1 Statistical Properties of Flow Maps and Time Cadence Selection . . . 25

2.3.2 Determining the Duration of the Time Averages . . . 26

2.3.3 Selection of the Sampling Window . . . 27

2.3.4 Numerical Errors in Calculating Flow Maps . . . 29

2.3.5 Long-Lived Features in Flow Maps . . . 29

2.3.6 Frequency Distributions for Different Solar Features . . . 31

2.3.7 Flow Maps for Different Spatial Resolution . . . 32

2.4 Conclusions . . . 34

3 Evaluating Local Correlation Tracking Using CO5BOLD Simulations of Solar Granulation 36

3.1 CO5BOLD Simulation of Granulation . . . 37

3.2 Local Correlation Tracking . . . 38

3.3 Results . . . 38

3.3.1 Persistent Flows and the Duration of Time Averages . . . 38

3.3.2 Convergence Properties of the Mean Flow Speeds . . . 40

3.3.3 Morphology of Flow Maps and Frequency Distributions of Flow Speeds . . . 43

3.3.4 Dynamics of Horizontal Proper Motions . . . 46
3.3.5 Comparison with Plasma Velocities . . . 46
3.4 Conclusions . . . **49**

4 Flow Fields in the Final Stages of Sunspot Decay **51**
4.1 Observations . . . **52**
4.1.1 SDO/HMI Full-Disk Images . . . 52
4.1.2 Hinode G-band and Ca II H Images . . . 54
4.1.3 Hα Echelle Spectra . . . 54
4.1.4 Hinode Spectro-Polarimeter . . . 55
4.2 Results . . . **55**
4.2.1 Photospheric Evolution . . . 55
4.2.2 Chromospheric Evolution . . . 58
4.2.3 Horizontal Proper Motions . . . 59
4.2.4 Line-of-sight Velocities . . . 61
4.2.5 Magnetic Fields . . . 62
4.3 Conclusions . . . **65**

5 The Decay of a Satellite Sunspot and the Role of Magnetic Flux Removal in Flaring **66**
5.1 Observations . . . **67**
5.2 Results . . . **68**
5.2.1 Morphology . . . 68
5.2.2 Decay Rates . . . 70
5.2.3 Flow Fields in Photosphere and Chromosphere . . . 71
5.2.4 Decorrelation Times . . . 73
5.2.5 Homologous M2.0 Flare . . . 77
5.3 Conclusions . . . **77**

6 Statistical Properties of the Dynamical Environment around Pores **79**
6.1 Observations . . . **81**
6.2 Selection of Pores . . . **82**
6.3 Results . . . **83**
6.3.1 Parameters Describing Morphology of Pores and Associated Flow Fields . . . 83
6.3.2 Illustrative Examples of the Data Analysis . . . 83
6.3.3 Area vs. Perimeter . . . 84
6.3.4 Frequency Distributions . . . 85
6.4 Conclusions . . . **87**

7 Conclusions **89**
Bibliography . . . **94**
Acknowledgments . . . **108**
Appendix A – Abstracts . . . **109**
Appendix B – List of Acronyms . . . **111**

Abstract

The interaction of plasma motions and magnetic fields is an important mechanism, which drives solar activity in all its facets visible on the solar surface. For example, photospheric flows are responsible for the advection of magnetic flux, the redistribution of flux during the decay of sunspots, and the buildup of magnetic shear in flaring active regions. Systematic studies based on data from the Japanese *Hinode* mission provide the means to gather the statistical properties of such flow fields, thus, enhancing our understanding of the dynamic Sun. The objective of this work was to develop methods to accurately measure photospheric horizontal flow fields and to lay the foundation for a statistical analysis of motions associated with solar features. This facilitates comparative studies of solar features such as G-band bright points, magnetic knots, pores, and sunspots at various stages of evolution and in distinct magnetic environments. For this, we adapted *Local Correlation Tracking* (LCT) to measure horizontal flow fields based on G-band images obtained with the *Solar Optical Telescope* (SOT) on board *Hinode*. In total, about 200 time-series with a duration between 1–16 h and a cadence between 15–90 s were analyzed. We optimized and validated the LCT input parameters, hence, ensuring a robust, reliable, uniform, and accurate processing of a huge data volume (about one terabyte). The LCT algorithm produces best results for G-band images having a cadence of 60–90 s. If the cadence is high, the velocity of slowly moving features will not be reliably detected. If the cadence is low, the scene on the Sun will have evolved too much to bear any resemblance with the earlier situation. Consequently, in both instances horizontal proper motions are underestimated. The most reliable and yet detailed flow maps are produced using a Gaussian kernel with a size of 2560 km $\times$ 2560 km and a full-width-at-half-maximum of 1200 km (corresponding to the size of a typical granule) as sampling window. Smoothing can be applied in later stages of the data analysis to improve the signal-to-noise ratio or to focus on more global properties of the flow field.

Radiation hydrodynamics simulations of solar granulation (e.g., CO^{5}BOLD) provide access to both the wavelength-integrated, emergent continuum intensity and the three-dimensional velocity field at various heights in the solar atmosphere. Thus, applying LCT to continuum images yields horizontal proper motions, which are then compared to the velocity field of the simulated (non-magnetic) granulation. We evaluate the performance of our LCT algorithm, establish it as a quantitative tool for measuring horizontal proper motions, and clearly work out the limitations of LCT or similar techniques designed to track optical flows. Horizontal flow maps and frequency distributions of the flow speed were computed for a variety of LCT input parameters including the spatial resolution, the width of the sampling window, the time cadence of successive images, and the averaging time used to determine persistent flow properties. Smoothed velocity fields at three atmospheric layers ($\log\tau = -1$, 0, and $+1$) served as a point of reference for the LCT results. LCT recovers many of the granulation properties, e.g., the shape of the flow speed distributions, the relationship between mean flow speed and averaging time, and with significant smoothing of the simulated velocity field also morphological features of the flow and divergence maps. However, the horizontal proper motions are grossly underestimated by as much as a factor of three. The LCT flows match best the flows deeper in the atmosphere at $\log\tau = +1$. Despite the limitations of optical flow techniques, they are a valuable tool in describing horizontal proper motions on the Sun, as long as the results are not taken at face-value but with a proper understanding of the input parameter space and the limitations inherent to the algorithm. Once the the LCT algorithm was thoroughly validated, the input parameters were carefully selected, and the flow field database was established, we performed case studies followed by a statistical study of flow fields in the vicinity of pores.

Generation and dissipation of magnetic fields are fundamental physical processes on the Sun. In comparison to flux emergence and the initial stages of sunspot formation, the demise of sunspots still lacks a comprehensive description. The evolution of sunspots is most commonly discussed in terms of their intensity and magnetic field. In our attempt to complete the picture for sunspots towards the end of their existence, we present a case study with additional information regarding the three-dimensional flow field. To accomplish this, we used a subset of multi-wavelengths observations obtained with the *Hinode* mission, the *Solar Dynamics Observatory* (SDO), and the *Vacuum Tower Telescope* (VTT) at *Observatorio del Teide*, Tenerife, Spain during the time period from 2010 November 18–23. Horizontal proper motions were derived from G-band and Ca II H images, whereas line-of-sight velocities were extracted from VTT Echelle Hα λ656.28 nm spectra and Fe I λ630.25 nm spectral data of the *Hinode/Spectro-*

Polarimeter, which also provided three-dimensional magnetic field information. The *Helioseismic and Magnetic Imager* on board SDO provided continuum images and line-of-sight magnetograms as context for the high-resolution observations for the entire disk passage of the active region. Using the extensive dataset from ground-based observations and complementing it with observation by space-borne telescopes, we performed a quantitative study of photospheric and chromospheric flow fields in and around decaying sunspots in active region NOAA 11126. In one of the trailing sunspots of the active region, we observed moat flow and moving magnetic features (MMFs), even after its penumbra had decayed. We also noticed a superpenumbral structure around this spot. MMFs follow well-defined, radial paths from the spot all the way to the border of a supergranular cell surrounding the spot. In contrast, flux emergence near the other sunspot prevented it from establishing such well ordered flow patterns, which could even be observed around a tiny pore with a diameter of just 2 Mm. After the disappearance of the sunspots/pores, a coherent patch of abnormal granulation remained at their location, which was characterized by more uniform horizontal proper motions, low divergence values, and diminished photospheric Doppler velocities. This region, thus, differs significantly from granulation and other areas covered by G-band bright points. We concluded that this peculiar flow pattern is a signature of sunspot decay and the dispersal of magnetic flux.

What exactly initiates a flare? Newly emerging magnetic flux is known to trigger flares. However, the role of submerging magnetic flux in prompting flares is more ambiguous, not the least because of the scarcity of observations. In the second case study, we concentrated on flow fields around a decaying satellite sunspot located in the flare-prolific active region NOAA 10930. We followed the evolution of the satellite spot over 16 hours with observations in *Hinode* G-band and Ca II H images. We computed horizontal proper motions using LCT. Shear flows occurred along a light-bridge between two umbral cores in the center of the satellite sunspot, i.e., in close proximity to the magnetic neutral line. These shear flows continue as long as penumbral filaments exist in proximity to the central umbral cores. Areal decay rates computed using linear regression are in good agreement with other studies. Using the concept of autocorrelation, we aggregated decorrelation times into two-dimensional maps. Typical lifetimes of solar features measured from intensity maps are: granulation 3–5 min, G-band bright points 25–35 min, and magnetic features (penumbrae, umbrae, and pores) 200–235 min. Long-lived intensity features are not related to long-lived flow features. The long-lived flow features are found in the northern part of the sunspot, where horizontal flow kernels with velocity values up to 1 km s^{-1} are located. We conclude that the decay of the satellite sunspot led to a substantial restructuring of the magnetic field topology. This in turn is responsible for a homologous M2.0 flare, which shares many characteristics with an X6.5 flare on the previous day. Thus, flux removal has to be considered as an important ingredient in triggering flares.

Solar pores are penumbra-lacking magnetic features, which are the link between small magnetic features and sunspots. They offer an ideal opportunity to study the interaction of umbra-like vertical magnetic fields with the surrounding convective plasma. The aim of this part of the work is to scrutinize the statistical properties of horizontal proper motions in and around pores. The seeing-free and uniform data of *Hinode* provided an opportunity to compare flow fields in the vicinity of pores in different environments and at various stages of their evolution. Horizontal flow fields were computed by applying LCT to *Hinode* G-band images observed from 2006–2008. In total, 357 one-hour sequences containing 2863 pores were selected. Statistical parameters including information about morphology, horizontal flows, evolutionary stage, and complexity of the surrounding magnetic field were collected.

The LCT algorithm developed in this work was successful in estimating horizontal proper motions for the different scenes on the solar surface. After the statistical study of flow fields in the vicinity of pores, a future task will be to perform a similar study of flows surrounding sunspots (moat flow) to fully exploit the already established database of flow fields of *Hinode* G-band images. Since the launch of SDO a wealth of new data became available. Following the evolution of flow fields in the vicinity of active regions during their disk passage and the possibility to identify localized changes in flow fields will furnish a global picture regarding the coupling between plasma flows and magnetic fields from the photosphere and chromosphere, throughout the transition region, and finally to the corona. Global maps of horizontal proper motions might become a decisive ingredient for space weather forecast and prediction tools because they uniquely uncover where persistent flows contribute to the buildup of magnetic shear.

This doctoral thesis is based on the following articles published and presented during the doctoral studies. In principle, this is a cumulative thesis, and the cross-references between thesis chapters and refereed journal articles are provide in the list below. However, the published articles were modified to provide a consistent layout for the entire thesis. The only exception is Chapt. 6, which introduces preliminary results of a statistical investigation of flow fields in and around pores. The whole study will be published in a forthcoming journal article. The light-blue links refer to bibliographic entries in the *Smithsonian Astrophysical Observatory/NASA Astrophysics Data System*. Abstracts of additional articles and poster presentations, which were not directly included in the thesis, are provided in Appendix A for reference.

Beauregard, L., Verma, M., Denker, C.: 2012, Horizontal Flows Concurrent with an X2.2 Flare in the Active Region NOAA 11158. *Astron. Nachr./AN* **333**, 125–130, 2012AN....333..125B [two figures were used in Chapt. 7, Laurent Beauregard adapted the LCT algorithm to SDO images].

Denker, C., Verma, M.: 2010, Velocity Fields in and around Sunspots at the Highest Resolution. In: Choudhary, D.P., Strassmeier, K.G. (eds.) *Physics of Sun and Star Spots, Proc. IAU Symp.* **273**, 204–211, 2011IAUS..273..204D [one figure was used in Chapt. 1].

Verma, M., Denker, C.: 2011, Horizontal Flow Fields Observed in Hinode G-Band Images. I. Methods. *Astron. Astrophys.* **529**, A153, 2011A&A...529A.153V [see Chapt. 2].

Verma, M., Denker, C.: 2012, Horizontal Flow Fields Observed in Hinode G-Band Images. III. The Decay of a Satellite Sunspot and the Role of Magnetic Flux Submergence in Flaring. *Astron. Astrophys.* **545**, A92, 2012A&A...545A..92V [see Chapt. 5].

Verma, M., Denker, C.: 2012, Statistical Characteristics of Horizontal Proper Motions in the Vicinity of Pores. In: A.G. Kosovichev, E.M. de Gouveia Dal Pino, and Y.Yan (eds.) *Solar and Astrophysical Dynamos and Magnetic Activity, Proc. IAU Symp.* **294**, in press, 2012arXiv1210.5145V [see Chapt. 6].

Verma, M., Balthasar, H., Deng, N., Liu, C., Shimizu, T., Wang, H., Denker, C.: 2012, Horizontal Flow Fields Observed in Hinode G-Band Images. II. Flow Fields in the Final Stages of Sunspot Decay, *Astron. Astrophys.* **538**, A109, 2012A&A...538A.109V [see Chapt. 4, Dr. Horst Balthasar performed the Stokes inversions of the *Hinode* spectropolarimetric data].

Verma, M., Steffen, M., Denker, C.: 2013, Evaluating Local Correlation Tracking Using CO^{5}BOLD Simulations of Solar Granulation. *Astron. Astrophys.*, submitted [see Chapt. 3, Dr. Matthias Steffen provided the simulations of solar granulation].

Chapter 1

Introduction

The influence of this eminent body (Sun),
on the globe we inhabit,
is so great, and so widely diffused,
that it becomes almost a duty for us
to study the operations
which are carried on upon the solar surface.

Herschel (1801)

1.1 Flows on the Solar Surface

Understanding the ever changing Sun is a challenge in modern astrophysics and has direct consequences for mankind of which space weather effects and influences on Earth's climate are the most prominent ones. High-resolution observations and statistical studies of complex photospheric plasma flows are needed to advance our knowledge concerning the generation and dissipation of magnetic fields on the solar surface. The photospheric flows can be divided in two broad categories: flows in the quiet and active Sun. The introduction follows this classification scheme by first discussing motions related to granulation and at larger scales meso- and supergranulation. This is followed by a brief review of the flow fields related to the active Sun starting with the Evershed flow, continuing with the moat flow connecting sunspots to the surrounding supergranulation, and finally shear flows as encountered in complex, flaring active regions. These flows can be measured using spectroscopic techniques for line-of-sight (LOS) flows and optical flow methods for horizontal proper motions. This technical section constitutes the middle part of the introduction. Applications beyond solar physics are presented towards the end of the introdction showing the strength of local correlation tracking (LCT) as a universal technique.

1.1.1 Granulation

Convection is the main process of transferring energy from the radiative zone to the solar surface. On solar surface, we see the manifestation of convection in various forms of granulation with distinct spatial scales and different lifetimes (granulation, mesogranulation, and supergranulation).

Herschel (1801) was among the first to observe the granular structure on the solar surface. The term granule was coined by Dawes (1864). However, it took about 90 years to obtain first clear photographs of granules (Janssen, 1896). Unsöld (1930) was the first one to associate granulation and convection. Various studies have verified its convective origin (e.g., Richardson and Schwarzschild, 1950; Stuart and Rush, 1954; Leighton, Noyes, and Simon, 1962). Namba and Diemel (1969) found that the mean diameter of solar granule is about 850 km. However, in various studies two kinds of granular cells were found: dissolving granules with an average size of 1000 km and fragmenting granules with a diameter larger than 1000 km (Hirzberger *et al.*, 1997; Ploner *et al.*, 1998; Berrilli *et al.*, 2002). Bahng and Schwarzschild (1961) computed from good quality photographs average lifetimes of 8.6 min using correlation methods. They defined the lifetime as twice the time interval before the correlation drops to half. This has not changed much over time. In recent studies, the lifetime of solar granulation ranges between 5–10 min,

and the associated horizontal velocities range from 0.5 to 1.5 km s^{-1}. Brandt *et al.* (1988) found a mean horizontal velocity of 0.67 km s^{-1} with a maximum of 1.2 km s^{-1} from granulation images of *Swedish Solar Telescope* (SST). Title *et al.* (1989) used the data from the *Solar Optical Universal Polarimeter* (SOUP) instrument on *Space Lab* to derive the statistical properties of granulations. They concluded that the root-mean-square value of the horizontal flow speed depends on the type of structure and size of the LCT sampling window. In the quiet Sun, the values fall in the range between 0.4–1.4 km s^{-1} and for regions with interspersed magnetic fields are between 0.3–0.75 km s^{-1} when the sampling window size decreases from 4″ to 1″. In granules, upflows are observed near the centers and downflows occur along the dark intergranular lanes. However, some studies indicated that large granules have a different flow pattern, where the maximum upflow velocity is near to the intergranular downflow lanes (e.g., Krieg *et al.*, 2000; Hirzberger, 2002). Before having access to images from space, a reliable measurement of of the granular intensity contrast was a big challenge. The contrast values varied over a broad range in the literature from 8–18% (see e.g., Sánchez Cuberes *et al.*, 2000). Advances in numerical simulations provided an opportunity to connect theory to observations. As expected the contrast values from high-resolution simulations (e.g., Stein and Nordlund, 2000; Vögler *et al.*, 2005; Freytag *et al.*, 2012) are much higher. To carefully compare simulated granulation with observations, one needs to take into account modulation transfer function of the telescope (e.g., Danilovic *et al.*, 2008; Wedemeyer-Böhm and Rouppe van der Voort, 2009). There are many articles where the morphological properties of granules have been summarized (e.g., Leighton, 1963; Title *et al.*, 1989; Hirzberger, 2002) and many articles reviewed the observational and theoretical aspect of granulation (e.g., Spruit, Nordlund, and Title, 1990; Rast, 2003; Nordlund, Stein, and Asplund, 2009).

1.1.2 Mesogranulation

November *et al.* (1981) reported the presence of mesogranulation in time-averaged Doppler images. Alternatively, mesogranulation is more clearly observed in the divergence maps of horizontal flows computed using cross-correlation (e.g., November and Simon, 1988; November, 1989; Muller *et al.*, 1992; Roudier *et al.*, 1998; Shine, Simon, and Hurlburt, 2000). The spatial scale of mesogranulation is about 5–10 Mm, and mesogranules live for 30 min to 6 h. From the three-hour time sequence of images from Pic du Midi observatory, Muller *et al.* (1992) found mesogranular structures with lifetime of ≈3 h, and the structures were advected towards the boundaries of supergranules with velocities of about 0.3–0.4 km s^{-1}. Shine, Simon, and Hurlburt (2000) analyzed a 45.5-hour time-series of continuum images from the *Michelson Doppler Imager* (MDI) on board the *Solar and Heliospheric Observatory* (SoHO) and found that the mesogranulation lives for 4–6 h and possesses an advection speed of 0.5–1.0 km s^{-1}. Simon, Title, and Weiss (1991) explored the relation between exploding granules and mesogranulation by numerical modelling. They concluded that the mesogranluar flows can be produced by a certain distribution of exploding granules. However, the velocity pattern produced by modeled exploding granules drops rapidly, opposite to mesogranulation which lives for hours. However, the existence of mesogranulation is questioned in many studies (e.g., Chou *et al.*, 1992), where the power spectra of Doppler velocities do not show the signature of mesogranulation. Nevertheless, Ginet and Simon (1992) presented in their kinematic modelling evidence that the observed power spectra will be different in the absence of structures with mesogranular size. This was again refuted by others (e.g., Straus, Deubner, and Fleck, 1992; Hathaway *et al.*, 2000) who reproduced the spectra without incorporating motions of mesogranular scale in their models. Using cross-correlation techniques, Roudier *et al.* (1999) concluded that mesogranulation could be a by-product of systematic errors of cross-correlation methods. However, the work of Shine, Simon, and Hurlburt (2000) and Domínguez Cerdeña (2003) confirmed the existence of mesogranulation using SoHO and SST data.

1.1.3 Supergranulation

The first indirect account of supergranulation was given by Hart (1954, 1956), where the author, while measuring the mean rotation speed of the Sun, found velocity fluctuations with a horizontal scale-length of 26 Mm. However, it was only after the work of Leighton, Noyes, and Simon (1962) that supergranules were recognized as convective features on the solar surface. Simon and Leighton (1964) described su-

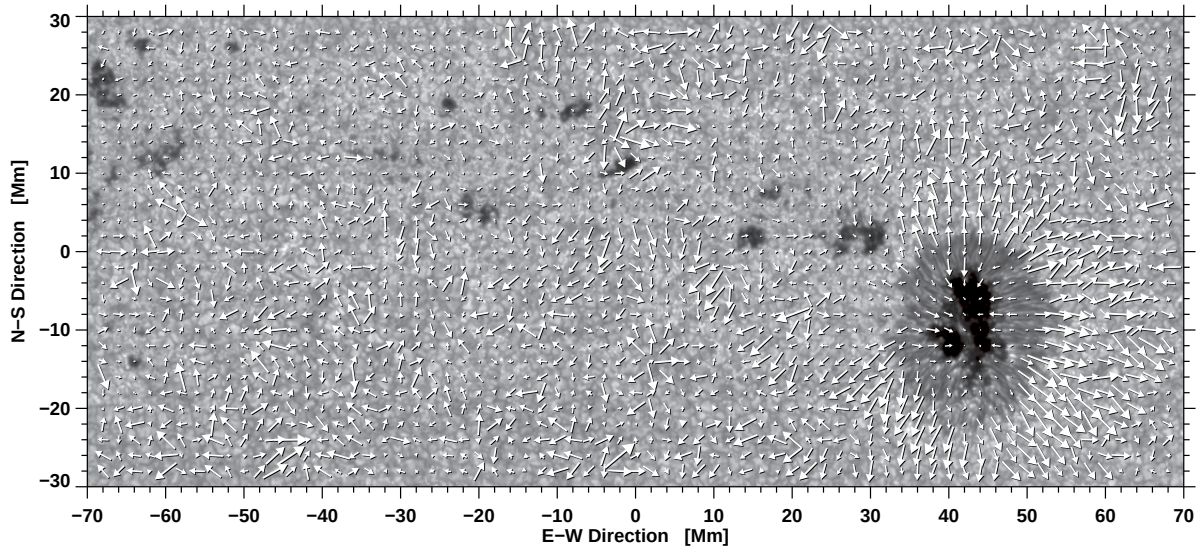

Figure 1.1: *Hinode* G-band image of active region NOAA 10921 observed near disk center on 2006 November 3. The arrows indicate magnitude and direction of horizontal proper motions (Figure 1 in Denker and Verma, 2011).

pergranular flows as a cellular pattern with diverging centers and flows terminating at boundaries marked by strong photospheric magnetic fields and the chromospheric network. The spatial scale of supergranulation was deduced from various methods starting from measuring the position of the maximum spectral power (e.g., Hathaway *et al.*, 2000), using LCT to identifying the horizontal divergence (e.g., De Rosa, Duvall, and Toomre, 2000; DeRosa and Toomre, 2004), or using local helioseismology (Del Moro *et al.*, 2004). The range of supergranule sizes measured using various methods lies between 12–30 Mm. In an early work, Worden and Simon (1976) computed a lifetime of 36 h for supergranulation. Hirzberger *et al.* (2008) used SoHO/MDI data to determine the lifetime of supergranular, which lies between 1.6±0.7 or 1.8±0.9 days, which in turn depends on the various methods employed by the authors. The horizontal velocity associated with supergranulation as originally estimated by Hart (1954) is about 0.17 km s^{-1}. The most recent value computed by Hathaway *et al.* (2002) is around 0.36 km s^{-1}.

Rieutord and Rincon (2010) reviewed the observational and theoretical aspects of supergranulation including numerical models. They summarized that there are two main theories explaining the origin of supergranulation. One describes its origin as pure convective in nature (e.g., Simon and Leighton, 1964), whereas the other explained it as the collective interaction of small-scale structures (granules), which may lead to a large-scale instability resulting in supergranular flows (e.g., Cloutman, 1979; Rieutord *et al.*, 2000). Till now none of the numerical simulations (e.g., Rieutord *et al.*, 2002; Ustyugov, 2009) are able to retrieve all the observed properties of supergranulations and a comprehensive statistical description of solar surface magnetohydrodynamic (MHD) turbulence might be needed first. Finally, Rieutord and Rincon (2010) suggests a concerted effort in observational, theoretical, and numerical aspects of the research before attempting to solve the supergranulation puzzle.

- ☐ What is the origin of supergranulation? Is it the largest instantiation of a convective cell or the combined action of small-scale features?
- ☐ Does mesogranulation really exist or it is just an artifact of methods used to estimate horizontal proper motions?
- ☐ How do global flow fields, e.g., in the vicinity of active regions alter the distinct characteristics of convective motions?
- ☐ There is a wide range of measured values for the velocities of granular proper motions. However, it is still an open question on what parameters the measurement of granular velocities depends. How does the LCT sampling window size and shape effect the results?

1.1.4 Flows in and around Sunspots

Sunspots as the name suggest are the dark spots observed on the solar surface. Since their original discovery by Galileo Galilei, sunspots are still an intriguing aspect of solar physics (Bray and Loughhead, 1964). A regular sunspot has a dark core (umbra) with less dark filamentary structure (penumbra) encircling it. Active regions typically with a bipolar magnetic structure harbor sunspots. Magnetic flux tubes (Ω loops) penetrate the solar surface and appear as active regions. The sunspots are only the visible intersection of the flux tube with the solar surface, whereas the sub-surface structure is only coarsely accessible with methods of local helioseismology (e.g., Zhao, Kosovichev, and Duvall, 2001). The magnetic topology above an active region can nowadays be observed in ultra-violet (UV) and extrem ultra-violet (EUV) images in intricate detail but magnetic field information is still limited to the photosphere and to some extend to the chromosphere. In a bipolar active region follower spots (with respect to the solar rotation) rarely form stable spots. They often only last for hours to a few days, whereas the leader spots can exist for several months. An extensive overview of sunspots has been given by Solanki (2003). A detailed discussion of the magnetic structure of sunspots was provided by Borrero and Ichimoto (2011).

Figure 1.1 show a *Hinode* G-band image of the active region NOAA 10921 observed near disk center on 2006 November 3. The active region consisted of a leading regular sunspot with many pores (umbral cores without penumbra) in the diffuse follower part. The leading sunspot was of negative polarity and the following magnetic features (far left in Fig. 1.1) were of positive polarity. The difference between follower and leader spots is not yet understood (Martínez Pillet, 2002). Active region evolution has been a prime subject of solar physics for many decades. Some of the questions about the physics of sunspots raised in the review of Moore and Rabin (1985) are still valid even after three decades. The generation of a filamentary penumbra, the on-set of the Evershed flow, and the change of the magnetic field topology take place in less than 20–30 minutes (see e.g., Leka and Skumanich, 1998; Yang *et al.*, 2004), which makes penumbra formation and decay a challenging observational task and explains why many processes of non-linear convection involved in sunspot formation are still elusive.

High-resolution observations have provided the opportunity to closely examine sunspots fine structures. These fine structures consist of umbral dots, light-bridges, and penumbral filaments and grains. Umbral dots appear as the bright dots in the dark umbral core (e.g., Tritschler and Schmidt, 1997; Sobotka and Hanslmeier, 2005). Umbral dots are supposed to be related to the convection in the umbra (e.g., Schüssler and Vögler, 2006; Ortiz, Bellot Rubio, and Rouppe van der Voort, 2010). Apart from umbral dots another manifestation of convection in the umbra is related to the light-bridges (e.g., Sobotka *et al.*, 1995; Rimmele, 1997), which appear as elongated structures dividing umbrae in two or more parts (see leading spot in Fig. 1.1). Penumbral fine structures are highly dynamic. In penumbrae, the Evershed flow represents a radial outflow of gas. This radial flow is mostly aligned with more horizontally placed magnetic flux tubes in dark penumbral filaments. Penumbral grains move predominantly inwards in the inner penumbra and outwards in the outer penumbra (Denker, 1998; Sobotka, Brandt, and Simon, 1999). This diverging line in a sunspot penumbra is clearly visible in the leading sunspot of Fig. 1.1. The interpretation, however, is far from simple. Inward moving penumbral grains are related to initially horizontal flux tubes, which become more vertical with time, so that their intersection with the solar surface (bright penumbral grains) appears to move inward. In the outer penumbra, penumbral grains travel outwards and at the periphery of the penumbra, individual granules squeeze through the penumbral filaments. These contrast variations are picked up by the LCT algorithm and are interpreted as horizontal proper motions. However, the correspondence with real plasma motions still needs to be established.

1.1.5 Evershed Flow

The photospheric outflow of plasma in sunspot penumbrae was discovered by Evershed (1909) at the Kodaikanal Observatory, hence the name Evershed flow. A brief history of the observatory is provided in the box on page 9. Based on his observations of shifted absorption lines in the penumbra of sunspots (see Fig. 1.2), he concluded that the motion must be horizontal to the solar surface. The speed of Evershed flow varies between 1–3 km s^{-1} and is confined to thin radial channels with almost horizontal magnetic field (e.g., Rimmele, 1995). Since its detection, the Evershed flow has been the center of many studies, which reveal the complexity of flows in sunspot penumbrae (e.g., Schröter, 1967; Rimmele, 1995;

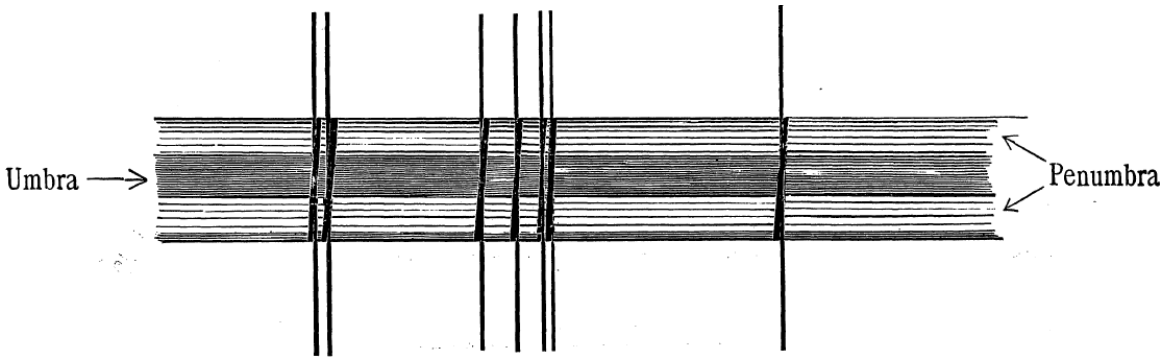

Figure 1.2: A line sketch by John Evershed showing the shift of an absorption line in the penumbra of a sunspot (Figure 3 in Hasan *et al.*, 2010b).

Scharmer *et al.*, 2002). The three-dimensional geometry of Evershed flow channels becomes evident as upflows in the penumbral grains of the inner penumbra, then turning horizontal in the mid-penumbra, and finally returning below solar surface as downflows at or slightly beyond the outer penumbral boundary. (e.g., Rimmele, 1995; Stanchfield, Thomas, and Lites, 1997; Westendorp Plaza *et al.*, 1997; Tritschler *et al.*, 2004; Rimmele and Marino, 2006). The Evershed flow appears reversed in higher atmospheric layers and radial inflows are observed in chromospheric lines (Maltby, 1975). In Fig. 1.4, a simple sunspot is shown at various atmospheric layers reaching from the photosphere (Fe I λ543.45 nm) to the lower and upper chromosphere (Na D_1 λ589.59 nm, Hα λ656.28 nm, and Ca II λ854.21 nm). The associated LOS velocties are depicted in Fig. 1.5 illustrating the rich detail of flows in and around sunspots.

The two main theoretical models explaining different aspects of the Evershed flow are the siphon flow model (Meyer and Schmidt, 1968; Thomas, 1988; Montesinos and Thomas, 1997) and the moving flux tube model (Schlichenmaier, Jahn, and Schmidt, 1998b,a). In the Montesinos and Thomas (1997) siphon flow model, the Evershed flow resembles the flow in a siphon, where liquid is driven by the atmospheric pressure difference. In the case of the solar atmosphere, the siphon flow establishes itself along a magnetic flux tube with footpoints of different magnetic field strength, which lead to a (magnetic) pressure difference initiating the Evershed flow. This model was able to reproduce the observations of Westendorp Plaza *et al.* (1997), where Evershed mass flux and some of the magnetic field lines submerged to deeper atmospheric layers at the outer boundary of the sunspot. This offered an explanation for the puzzle of where this submerged Evershed flux will eventually go. Once the Evershed flux tubes are submerged, they are anchored to furnish the radial inward force to maintain the equilibrium. If the force is relaxed, it will make the footpoints to move radially outward. Montesinos and Thomas (1997) related this radial outward motion of footpoints to the moving magnetic features (MMFs) streaming radially outward from sunspots. However, their model only explained the case of a steady Evershed flow, which is in reality dynamic, so that questions about the stability of flux tubes are raised.

The moving flux tube model is explained in Schlichenmaier, Jahn, and Schmidt (1998a,b): A flux tube initially embedded in the sunspot along the magnetopause becomes buoyant because of radiative heat exchange between the tube and the adjacent quiet Sun, hence it starts rising through the subphotospheric penumbra. The tube stops to rise above the photosphere. During its rise the tube's footpoint moves inwards just like penumbral grains. As the tube rises, the magnetic field strength of the tube decreases more rapidly than the background magnetic field strength. The tube stops to rise, once the stratification is convectively stable and the tube's surplus heat is lost by radiation. Extra gas pressure builds up within the tube because the total pressure (gas + magnetic) reaches an equilibrium between the tube and its surroundings. The resulting pressure gradient drives an outflow, which is accelerated in the tube. Schlichenmaier (2002) presented an updated version of the Schlichenmaier, Jahn, and Schmidt (1998b) moving flux tube model, where he explored the time dependent nature of a thin magnetic flux tube embedded in the penumbra. The model was able to explain the penumbral grains as hot upflows, also their inward and outward migration in the inner and outer penumbra, respectively. It also reproduced the Evershed flow in similar ways as shown in the Montesinos and Thomas (1997) siphon model. However, to gain more insight, Schlichenmaier (2002) emphasized that self-consistent three-dimensional simulations of magnetoconvection are needed to join theory and observations.

Figure 1.3: Tunnel telescope at the Kodaikanal Observatory. The tower contains a coelostat and a spectrograph, which is located in a 60-meter-long tunnel. The sunlight is directed by a flat mirror into the tunnel, which can be seen here as a grass-covered hill on the left with two cylindrical pipes used for the ventilation of the tunnel.

Kodaikanal Observatory. The earliest scientific contributions to solar physics in India date back to the solar eclipse observation by Norman Pogson in 1868 (Hasan *et al.*, 2010b). Because of the efforts of English astronomers during 1879–1893, a proposal for an observatory in the highlands of Southern India was put forward, which led to the foundation of Kodaikanal Observatory in 1895. The observations at Kodaikanal Observatory started in 1901 using a spectrograph, i.e., a 28-cm polar siderostat with a 15-cm lens and a concave grating. In 1904, a Calcium-K spectroheliograph designed according to the specification of George Ellery Hale arrived in Kodaikanal. It consisted of a Foucault siderostat with a 46-cm aperture plane mirror and a 30-cm triple achromatic lens with focal length of 6 m. John Evershed worked on this spectroheliograph and made it fully functional soon after his arrival at the observatory in 1907. He carried out systematic studies of sunspot spectra using two high-dispersion spectrographs. In 1909, Evershed observed radially outward moving plasma in sunspots (Evershed, 1909), which we now know as the Evershed effect. Apart from sunspot spectra, Evershed also studied the dynamics and rich fine structure of prominences. Even after Evershed's departure, the Kodaikanal Observatory thrived with many interesting solar observations, such as the observation of Royd's flare in 1926 (Royds, 1926) and the discovery of the infrared triplet of oxygen lines in 1935 (Royds, 1935). International collaborations were maintained with the Greenwich, Cambridge, Meudon, and the Mt. Wilson Observatories. After India achieved independence in 1947, the Kodaikanal Observatory actively pursued new technologies. A solar tunnel telescope was commissioned in 1960, which served many solar physicists in India. Since 1960, many studies were carried out related to various aspects of solar physics: oscillations in the solar atmosphere (e.g., Bhatnagar and Tanaka, 1972), solar magnetic fields (e.g., Bhattacharyya, 1970), studies of Ca II K line spectra (e.g., Bappu and Sivaraman, 1971), and dependence of supergranular size on the solar cycle (Singh and Bappu, 1981) are just few examples of the exhaustive work carried out at the Kodaikanal Observatory. The current facilities at the Kodaikanal Observatory include the tunnel telescope (Fig. 1.3) with a Littrow-type spectrograph and a twin-telescope taking images of the Sun in Ca II K and white-light (Singh and Ravindra, 2012).

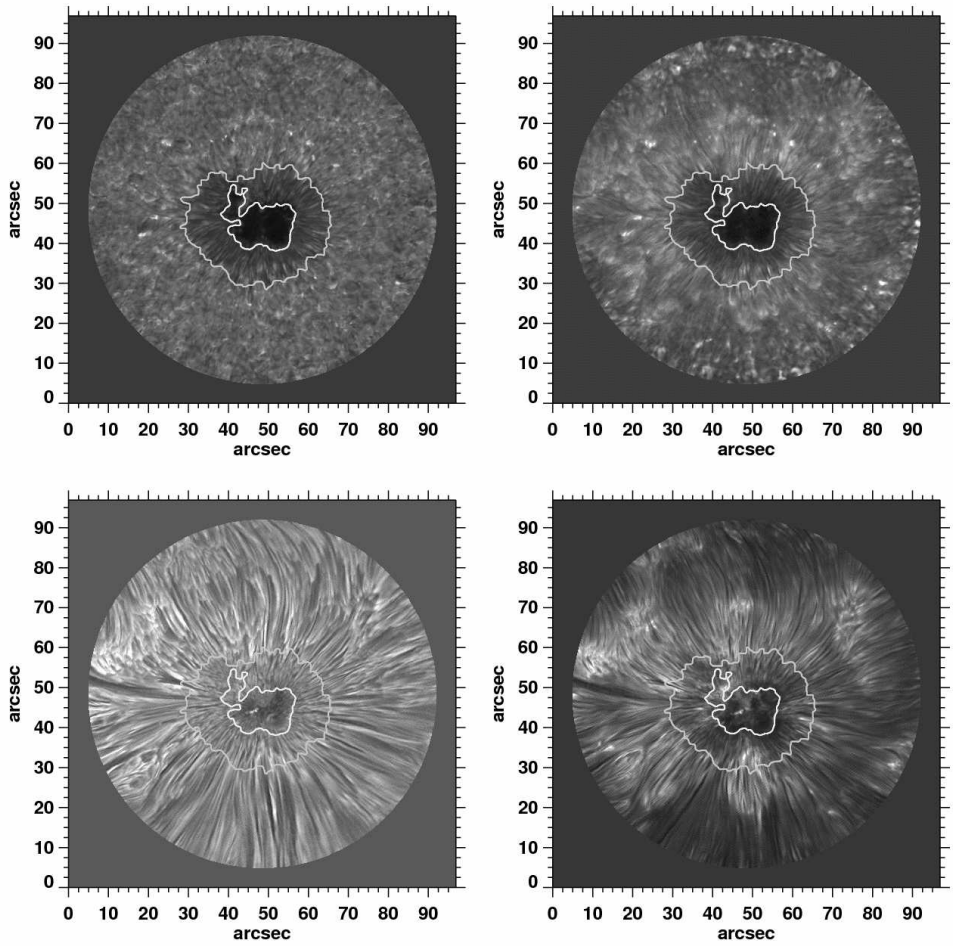

Figure 1.4: Speckle reconstructed (Wöger, von der Lühe, and Reardon, 2008) line-core images of active region NOAA 11203 on 2011 May 4 covering the spectral lines Fe I λ543.45 nm, Na D_1 λ589.59 nm, Hα λ656.28 nm, and Ca II λ854.21 nm. The data are courtesy of Dr. Alexandra Tritschler and were obtained with IBIS operated at the *Dunn Solar Telescope* (DST) *National Solar Observatory* (NSO), New Mexico.

Recent developments in numerical simulations, including MHD and radiative transfer calculations (Heinemann *et al.*, 2007; Rempel, 2011), are able to provide more insight regarding the Evershed flow in a sunspot's penumbra. Rempel (2011) suggested two components of penumbral flows (deep and shallow), where the former corresponds to the moat flow and the later is related to the Evershed flow. Rempel and Schlichenmaier (2011) summarized the knowledge and development achieved so far in sunspot modelling including formation, decay, and its fine structures.

1.1.6 Moat Flow and Moving Magnetic Features

An annular structure of horizontal flows starting from the penumbra reaching the nearest supergranular boundary surrounding sunspots was first detected by Sheeley (1972) while studying Doppler spectroheliograms. This flow pattern envelops the sunspot like a moat surrounding a fortified medieval town, hence its name moat flow. Initially, the moat flow was detected with spectroscopic Doppler measurements of sunspots near the solar limb, because near the limb the horizontal component of the flow velocity is more easily quantified, and because there it is more parallel to the LOS. Later, the detection of the moat flow near solar disk center became possible once LCT techniques were introduced (November and Simon, 1988). Sheeley (1972) found that the speed of this outflow is about 0.5–1.0 km s^{-1}. Harvey and Harvey (1973) related the moat flows to decaying sunspots. They also pointed out that fine structure in the moat, i.e., MMFs play a major role in the flux dispersal during the decay of sunspots. MMFs are small concentrations of flux moving outward from the sunspots, and they migrate to the nearest supergranular boundary. Meyer *et al.* (1974) also connected the moat flow with the slow phase of sunspot decay. Brickhouse and Labonte (1988) concluded based on the study of 44 sunspots that moat flows are not

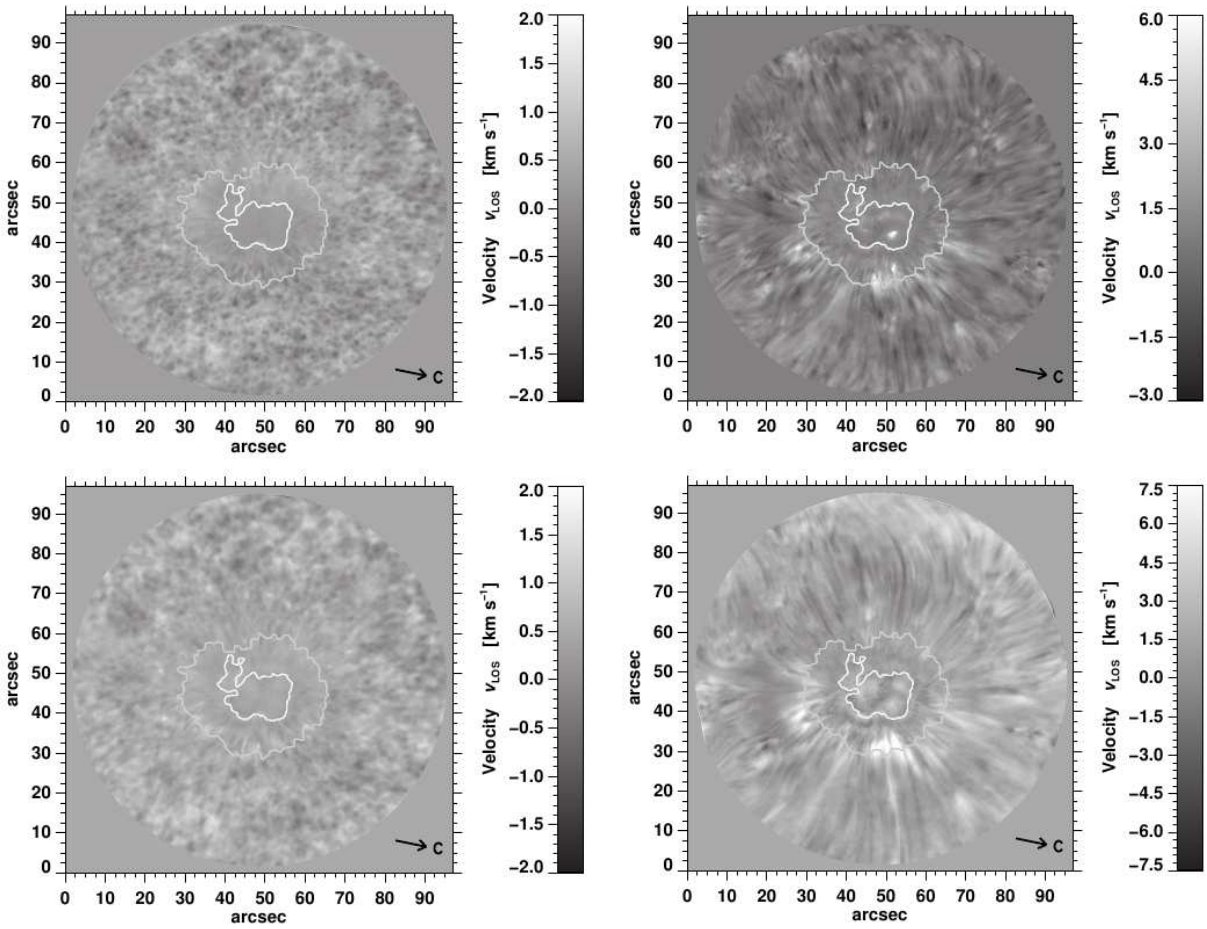

Figure 1.5: Doppler velocity maps of active region NOAA 11203 on 2011 May 4 using the spectral lines Fe I λ543.45 nm (*top-left*), Na D_1 λ589.59 nm (*bottom-left*), Ca II λ854.21 nm (*top-right*), and Hα λ656.28 nm (*bottom-right*). Doppler velocities were estimated using the Fourier phase method. The arrows indicate the direction towards disk center. Redshifts in these maps are positive (bright) and blueshifts are negative (dark). The data are courtesy of Dr. Alexandra Tritschler and were obtained with IBIS operated at the *Dunn Solar Telescope* (DST) at the *National Solar Observatory* (NSO), New Mexico.

only associated with decaying spots. They summarized the basic properties of the moat flow: (1) the moat radius is twice as large the penumbral radius, (2) the average flow speed in the moat is 0.56 km s^{-1} exceeding the supergranular velocity of 0.36 km s^{-1} by a factor of two (Giovanelli, 1980), (3) the angular extent of the moat is independent of any other property of the spot, and (4) the mean velocity of MMFs in moats is equal to the mean velocity of the surface gas in moats.

There are mainly two types of MMFs: (1) unipolar MMFs with same polarity as the sunspot and (2) bipolar MMFs of mixed polarity (Zhang *et al.*, 1992). Yurchyshyn, Wang, and Goode (2001) found that MMFs in the sunspot moat are not randomly oriented. In case of type II (bipolar) MMFs, 75% had the magnetic element of the same polarity as sunspot located farther away from the sunspot. The same polarity magnetic element of type II MMFs were stronger, compact, and appeared first. The above authors observed that the type II MMFs rotated counterclockwise if the sunspot was twisted clockwise, and viceversa. Hagenaar and Shine (2005) tracked unipolar (type I) MMFs around sunspots and found larger sunspots have a higher number of MMFs. The typical lifetime for MMFs is about one hour and the average flux contained in a MMF is 2.5×10^{18} Mx. They also showed that MMFs tend to prefer specific paths and trace a spoke-like structure around sunspots reaching out to nearest supergranular cell boundary. Filamentary magnetic features were seen in a mature sunspot moat by Sainz Dalda and Martínez Pillet (2005). They observed that many bipolar MMFs started their journey inside the sunspot penumbra, moving to the sunspot moat, and eventually following the paths outlined by moat filaments. The relation between the Evershed flow and MMFs was studied by Cabrera Solana *et al.* (2006) who analyzed spectropolarimetric measurements of a sunspot in the Fe I λ630.2 nm and λ1565 nm lines. They followed the temporal evolution of radially outward moving Evershed clouds along the same penumbral filament

and noticed their appearance as MMFs in the moat region, hence, they concluded that sometimes the penumbral Evershed flow continues as MMFs.

However, the relationship between moat flow, MMFs, and sunspot penumbra is still matter of debate. Deng *et al.* (2007) found that in a decaying sunspot, even after the penumbra had disappeared, the moat flow was still present. In contrast, Vargas Domínguez *et al.* (2008) observed no moat flow around umbral cores without penumbra. Additional evidence for moat flow and MMFs around a naked sunspot was found by Zuccarello *et al.* (2009). In a recent work, Sainz Dalda, Vargas Domínguez, and Tarbell (2012) revisited the naked spot studied by Zuccarello *et al.* (2009). They conclude that the naked sunspot had no visible penumbra in intensity maps, but its magnetic structure was similar to a sunspot with penumbra, hence, explaining the presence of MMFs around a spot lacking a visible penumbra.

1.1.7 Shear Flows in and around Active Regions

Sunspot groups with complex magnetic topology are commonly sources of solar flares, and magnetic reconnection is a well established mechanism for solar flares. However, energy buildup and release are less understood. Changes in the velocity field of an active region can be linked to changes in the magnetic field (Martres, Soru-Escaut, and Rayrole, 1973; Martres *et al.*, 1982). Often shear flows are seen along the magnetic neutral line of flare-prolific active regions. Harvey and Harvey (1976) studied fourteen flares based on Hα λ656.28 nm and Fe I λ656.9 nm data and concluded that horizontal shearing motions along the magnetic neutral line play an important role in flare production. Considering many previous studies, Henoux and Somov (1987) pointed out that in active regions horizontal flows dominate over vertical flows. In that study, they also concluded that the organized photospheric velocity fields lead to D.C. current systems in an active region which contribute to its evolution and flaring capacity. A combination of sunspot motions, strong currents, isolated polarities, and intersecting separatrices are needed to trigger flares (van Driel-Gesztelyi *et al.*, 1994). Keil *et al.* (1994) found evidence that flare kernels correspond to locations, which show shear in vertical and convergence in horizontal photospheric flows. They suggested that it is important to study the local dynamics and atmospheric flows to assess the stability of active regions.

Yang *et al.* (2004) studied the occurrence of shear flows in an active region before a major X10 flare. They observed regions with strong horizontal shear flows across the magnetic neutral line with the velocity reaching up to 1.6 km s^{-1}. They concluded that shear flows with a high velocity can cause efficient heating and results in flares (Heyvaerts and Priest, 1984). They emphasized the significance of monitoring active regions in real-time with high-resolution photospheric observations. Deng *et al.* (2006) followed the horizontal flow fields of the same active region as Yang *et al.* (2004) covering the X10 flare using G-band, white-light, and near-infrared images. They also observed persistent and strong horizontal and vertical shear flows along the magnetic neutral line until the occurrence of the X10 flare. The flow speeds in the shear motion regions decreased with increasing height in the solar atmosphere in contrast to other regions where the flow speeds increased with increasing height. However, after the flare both horizontal and vertical shear flows were enhanced. In addition, the shear angles of both magnetic field and horizontal flow field increased after the flare along the flaring neutral line. The regions undergoing rapid changes are well correlated with kernels of hard X-ray flare emission. In particular, the authors pointed out that the mechanism of the shear motion is quite different from that of the general plasma motion in an active region, which implies that the origin of the shear motion comes from a deep source below the photosphere. In their study of a moderately complex sunspot group, Denker *et al.* (2007) concluded that shear flows are a common phenomenon in complex active regions and δ-spots. However, these kind of flows are not necessarily a prerequisite condition for flaring.

Chae *et al.* (2001) observed the formation of a filament in an active region with simultaneous accumulation of magnetic helicity by the shearing motion on the solar surface. He analyzed the magnetic helicity transport rate using SoHO magnetograms and emphasized that surface motions other than differential rotation possibly play a role in accumulating magnetic helicity of coronal magnetic fields in solar active regions. Flare models (e.g., Amari *et al.*, 2000; Moore *et al.*, 2001) also take into account the role of photospheric shear motions in energy buildup. However, the origin of shear motions and how they change after flares are not yet fully included in flare models. Consequently, scrutinizing both horizontal and vertical photospheric flows is required to improve our understanding of eruptive phenomena.

- ☐ Are the outward motions detected by LCT related to the plasma velocities of the Evershed flow?
- ☐ Are moat flow and moving magnetic features related? How do they contribute to the decay of sunspots? Are the full three-dimensional flows needed to gain insight into the process of sunspot decay?
- ☐ How much flux is removed from the sunspot by MMFs?
- ☐ If we treat the sunspot and the surrounding supergranular boundaries as a system, do we then observe a flux pile-up at the boundaries while the flux contained in the spot is shrinking?
- ☐ Shear-flows are mostly observed in active regions with emerging magnetic flux, however, what role do they play during decay, (re-)distribution, or submergence of magnetic flux?
- ☐ Once a sunspot has decayed, as evidenced by its photometric and magnetic decay rates, does it still leave any signature in the photospheric flow field?

1.2 Methods to Mesasure Flows

The flows within the solar atmosphere can be measured using various methods. However, these methods can be placed in two categories: one to estimate surface velocities and another to measure LOS velocities.

The methods for estimating surface velocities can again be divided in two branches: (1) feature tracking, where individual features are tracked in time-series of images (e.g., Strous, 1995; Gonzalez and Woods, 2002) and (2) local correlation tracking, where the displacement vectors are estimated by computing the cross-correlation using consecutive images in time-series (November and Simon, 1988). The ball-tracking method developed by Potts, Barrett, and Diver (2004) can be included in the category of feature tracking. Apart from measuring surface velocities using intensity images, high-resolution magnetograms can also be used as shown in the methods developed by Schuck (2006), i.e., the differential affine velocity estimators (DAVE) and Chae and Sakurai (2008), i.e., the nonlinear affine velocity estimators (NAVE). Data from space missions such as *Hinode* provide the required seeing-free images with good temporal resolution to implement these methods and get good estimates of horizontal surface motions on the Sun. This topic is discussed in details in Chapt. 2.

The LOS velocity can be measured by computing shifts in the spectral lines and converting it to velocities using the Doppler formula given as

$$v_{\rm LOS} = \frac{\Delta\lambda}{\lambda_{\rm r}} \times {\rm c} \quad , \tag{1.1}$$

where $\lambda_{\rm r}$ is the rest wavelength, $\Delta\lambda$ is the wavelength shift, and c is the speed of light. The spectroscopic observations are multidimensional data sets covering spatial dimensions, wavelength, time, and sometimes the polarization state. Such observations can either be taken using spectrographs or imaging interferometers. The slit spectrograph captures one spatial dimension and a certain wavelength range at a time, whereas interferometers can record two-dimensional images at fixed wavelength positions. In Fig. 1.6, an example of an Hα spectrum obtained with Vacuum Tower Telescope (VTT) Echelle spectrograph is shown. The continuum image, line core image, and LOS velocity map are constructed from a scan across two decaying sunspots. An example of data recorded using an imaging interferometer is compiled in Fig. 1.4, which includes line core images of an active region in four different spectral lines taken with *Interferometric Bidimensional Spectrometer* (IBIS Cavallini, 2006). Once a spectrum is obtained, shifts in spectral lines can be computed by fitting a parabola to the core of the line profile or by implementing the Fourier phase method (Schmidt, Stix, and Wöhl, 1999), which takes into the account entire line profile (see Fig. 1.5). In both cases, the average line shifts in a quiet Sun region is used as the reference with a suitable correction for the convective blueshift.

The spectral lines emanating from the quiet Sun photosphere show asymmetries, which are detectable in high-resolution spectrophotometric data (e.g., Dravins, Lindegren, and Nordlund, 1981). In general,

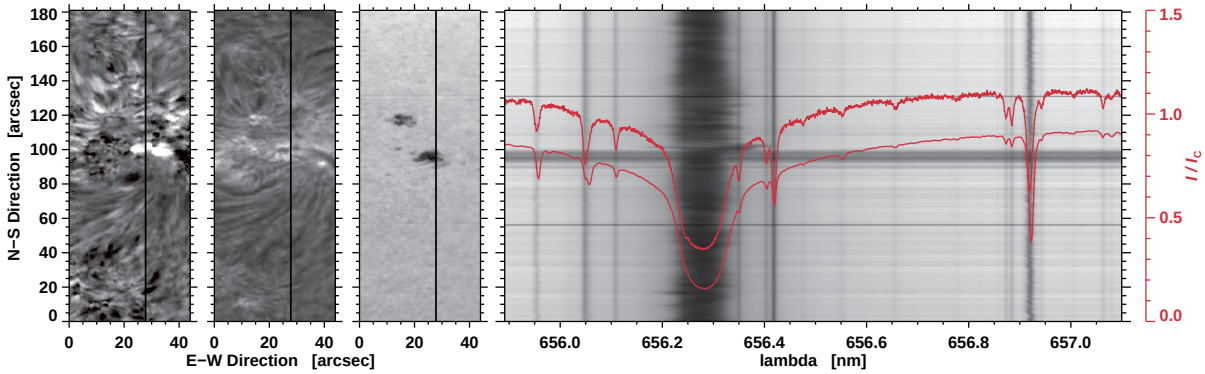

Figure 1.6: Doppler velocity map, line core intensity image, and continuum image (*left to right*) derived from a spectral scan in the strong chromospheric Hα line obtained with the VTT Echelle spectrograph on 2010 November 18. Redshifts in the Doppler velocity map are positive (bright) and blueshifts are negative (dark). The Doppler velocity is being displayed between ± 5 km s^{-1}. The straight black lines in these maps show the position of the spectrograph slit at which the spectrum (*far right*) was taken. The red atlas (*bottom*) and observed (*top*) line profiles are plotted over the spectrum. The observed spectrum was shifted upwards for clarity.

the line asymmetry is measured by computing the bisector of the line, which is the line passing through the median of points of equal intensity on the spectral line profile. Photospheric lines usually demonstrate blueshifted line asymmetries (Balthasar, 1984, 1988). Therefore, it should be noted that the even for quiet Sun convective blueshift should be corrected. Magnan and Pecker (1974) casted doubts on using bisectors to determine trend in velocities fields. However, they mentioned that the line asymmetries do show that the velocities change with the position in the photosphere. Hence, bisectors could be used as a tool to confer the height dependency of LOS velocities.

- ☐ *Hinode* G-band images are a prolific source of time-series data, which can be used to track horizontal proper motions on the solar surface. What are the design criteria for a LCT algorithm to reliably and accurately measure horizontal flow fields including divergence and vorticity maps?
- ☐ How many individual LCT maps have to be averaged to yield a reliable flow map? What should be the time cadence between consecutive images and how large should be the sampling window to reveal persistent flow patterns?
- ☐ Once LCT has been established as a quantitative tool to compute flow fields, how can these data be merged with other data sources either from telescopes on the ground or with space-borne intruments?

1.3 Applications of Cross-Correlation Techniques

Techniques to measure optical flows in solar physics have applications beyond astronomical usage. Here, three examples are presented, where cross-correlation is implemented in varying spatial scales to estimate horizontal proper motions.

1.3.1 Sea Surface Velocity

The continuous and directed movement of ocean water creates an ocean current, which is being generated and influenced by many physical factors such as temperature, wind, and salinity differences. The ocean currents have climatic as well as economic importance. Hence, studying these currents is relevant to society. The current system along the Californian shore line is one of the prominent ocean currents along the western coast of North America. The *Advanced Very High Resolution Radiometer* (AVHRR,

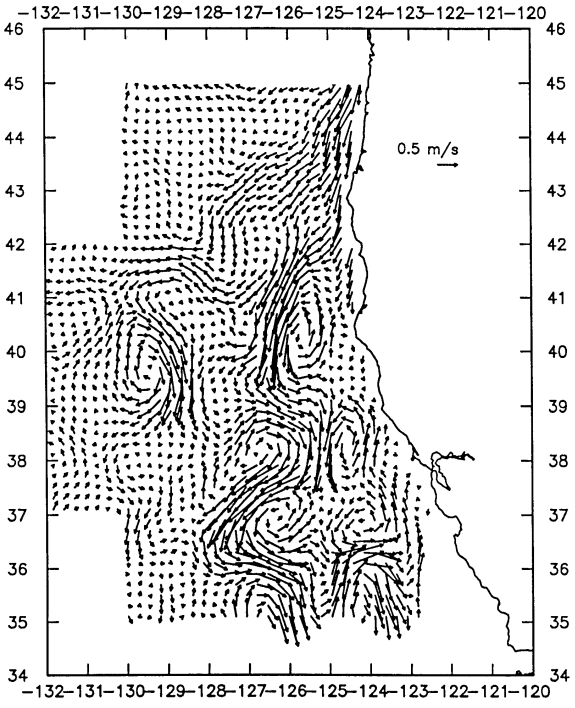

Figure 1.7: Surface velocity field computed for the California current. The solid line in the figure represents the Californian shore line starting from the Vancouver Island, Canada (upper-edge) to Pt. Conception, U.S.A. (bottom-edge). The surface velocities were computed using cross-correlations between images captured by the AVHRR and CZCS.[1]

Schwalb, 1978) and the *Coastal Zone Color Scanner* (CZCS, Hovis, 1981) are used to capture images to estimate sea surface velocities along the California current (Fig. 1.7). The method is based on the maximum cross-correlation (MCC) technique put forward by Leese, Novak, and Clark (1971) for cloud tracking and subsequently modified by Emery *et al.* (1986) for oceanic features. The underlying mathematics of LCT is very similar to MCC. Tokmakian, Strub, and McClean-Padman (1990) quantified and evaluated two MCC approaches for measuring surface velocities of California current system: (1) by applying the MCC technique to (1) simulated data and (2) to satellite data, which was then compared to in-situ measurements. This study is very similar to the evaluation of the LCT method employed in this thesis (see Chapt. 2), where we also carefully appraised the impact of the input parameters and discuss the limitations of LCT in capturing horizontal plasma motions on the solar surface. Obviously, performing in-situ measurements of surface velocities was not possible for the Sun but simulations of granulation (Chapt. 4) may serve as a substitute. Tokmakian, Strub, and McClean-Padman (1990) describe how the measurements can be affected by high-pass filtering, time-lag between consecutive images, size of the sampling window, and potential error sources mainly related to surface heating and convection in the warm water along the coast of California. In addition, they matched the measured flow field with some physical model by using the maximum correlations as a weighting function. We did not employ such approach in our LCT algorithm. However, this approach is being incorporated in some optical flows tracking algorithms such as DAVE (Schuck, 2006).

1.3.2 Cloud Motion Wind

The *Numerical Weather Prediction* (NWP) models takes the current weather information as an input to predict weather. The inputs to NWP models are collected from observations of weather satellites. One of the important ingredients is the atmospheric wind field. The global network of geostationary satellites provides the images to estimate *Cloud Motion Winds* (CMV, Schmetz *et al.*, 1993).

As the name suggests, the clouds work as tracers to measure wind velocities (Fig. 1.8). The infrared (IR) λ10.5–12.5 μm and water vapor (WV) λ5.7–7.1 μm images are used for cloud tracking and height-attribution of wind vectors, respectively. The process of estimating CMWs is a four step process: (1) From the image grid of 32 pixels, a tracer is selected and filtering is applied to enhance the tracer, i.e., upper-level clouds. (2) A height in Earth's atmosphere is assigned to the clouds, where the contributions

[1]U.S. GLOBal Ocean ECosystems Dynamics, surface velocity field estimated during mid-July 1988. Retrieved from www.usglobec.org/reports/ebcccs/ebcccs.background.html on 2012 October 31.

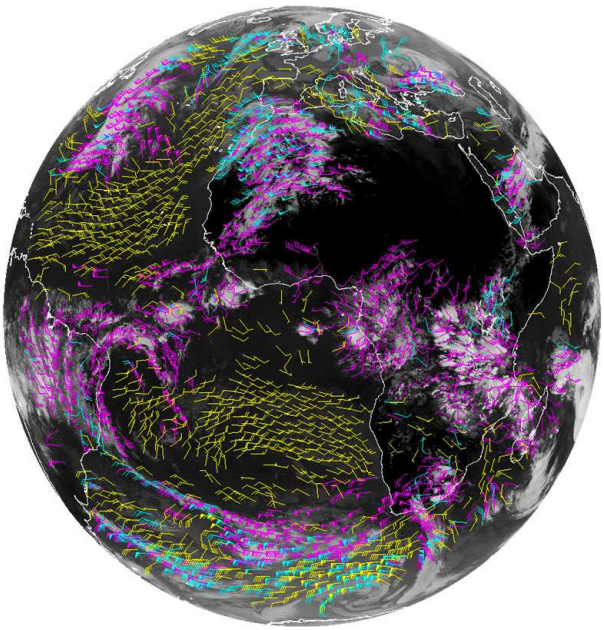

Figure 1.8: An example of CMWs derived from cloud tracking on full-disk data of Meteosat-8 in the 10.8-μm band. The colors depict high-(100–400 hPa), mid-(400–700 hPa), and low-(below 700 hPa) level winds.[2]

of both semitransparent and opaque clouds to the IR and WV radiances are used, which includes the radiative forward calculations for opaque clouds. (3) The core of the algorithm is to measure the CMWs by cloud tracking in a similar manner as solar surface motions are determined by LCT. The displacement is estimated by computing cross-correlations between successive images and divided by the time interval between images to yield the velocity. The only difference is that three images are used instead of two. (4) This provides the possibility of a symmetry check in the last step facilitating some means of quality control (Schmetz *et al.*, 1993).

1.3.3 Particle Image Velocimetry

Particle Image Velocimetry (PIV) is a technique to study the structure of flows in fluids (Adrian, 2005) by illuminating particles in the fluids and then capturing images. The two velocity vectors are computed by correlating consecutive images. The third component can also be obtained using a spectroscopic arrangement. Similar to Doppler velocities on the Sun, which are recorded by spectrographs, this provides access to the complete three-dimensional flow structure. For computing horizontal velocity vectors, the target region of the particle-infused flow is selected and the movement of particles is recorded between two light pulses. Then, the images of the sequence corresponding to two light pulses are divided into subsections, the so-called interrogation areas (IA). Pixel-by-pixel cross-correlations are computed for each IA in consecutive images. The maximum of the cross-correlation function is found using sub-pixel interpolation leading to an accurate measurement of the particle's displacement. Using the computed displacement with a time-lag between two light pulse provides the velocity flow maps. The typical particles used for air flows are oil drops ranging in size from 1–5 μm and polystyrene, polyamide, or hollow glass spheres with a size of 5–100 μm for fluids. A wide range of applications starting from tracking the flow vortex in heart valves to the flows on the wings of an airplane uses PIV techniques. The PIV technique is very similar to what is practiced in solar physics, where horizontal flow fields are obtained using cross-correlation techniques and the line-of-sight component is derived using spectroscopic methods. Interestingly, the idea of seed-particles is used in visualizing flows, where time-series data is combined with an initially equidistant grid of test particles, which are then moved forward (and sometimes backward) in time according to a prescribed flow field – one time step after the other (see the so-called cork maps in Fig. 2.2).

[2]The Geostationary Operational Environmental Satellite R-Series, derived CMWs product. Retrieved from www.goes-r.gov/products/baseline-derived-motion-winds.html on 2012 October 31.

Chapter 2

Local Correlation Tracking

Data from space do not suffer the deleterious effects of Earth's turbulent atmosphere, which blur and distort images so that features may fade into obscuration, which makes it difficult to follow them from image to image. The huge volume of the *Hinode* G-band images with good spatial resolution, cadence, and coverage provide time-series of consistent quality to quantify photospheric proper motions, which can be used in comparative studies. Various techniques have been developed in the past decades to measure horizontal proper motions on the solar surface. Basically, they can be divided into two classes: (1) Feature Tracking (FT) methods, which follow the footprints of individual features in the images of a time-series, and (2) LCT techniques, which derive displacement vectors by cross-correlating small regions in consecutive images of a time-series. The principles of LCT are laid out in the seminal work of November and Simon (1988), which is also the foundation of the algorithm that has been adapted and tailored to accommodate *Hinode* G-band images in the present work. At the outset of a comparative study the task arises to identify the most suitable technique to efficiently examine the data while reliably extracting the physical information. Therefore, a review of state-of-the-art FT and LCT techniques should provide reasons and adequate grounds for our ultimate choice.

The FT method combines a variety of techniques commonly used in modern digital image processing (e.g., Gonzalez and Woods, 2002). Individual features are tracked in a three-step procedure (see e.g., Strous, 1995): identify pixels belonging to a class of objects in each image (segmentation), label all pixels inherent to one particular object in an image (labeling), and find the relationship between the objects in consecutive images (identification). The last step might be complicated because of merging, separating, appearing, and vanishing objects. Besides establishing object properties such as size, shape, orientation, brightness, etc., the positional information can be translated into a map of horizontal proper motions. Tracking facular points of opposite magnetic polarity in an emerging flux region (Strous *et al.*, 1996) effectively demonstrated the potential of FT techniques. However, since all three image processing steps (segmentation, labeling, and identification) rely on prior knowledge about the object under investigation, FT seems to be better suited for case studies rather than bulk processing of huge data volumes, where the reduction of dimensionality is a desirable feature.

In the balltracking method developed by Potts, Barrett, and Diver (2004), the intensity information is translated into a physical surface on which tracer particles or idealized balls are placed. Bright granules correspond to hills in this representation and the dark intergranular lanes can be identified with valleys. The balls placed on such a surface will settle in a local minimum. The random motion of granules will move the balls, i.e., the position of the local minimum will change. Tracking the balls in consecutive images will map the photospheric flows with the same accuracy as LCT. However, the method is faster and very efficient so that it can be used for real-time processing of the large data sets. Even though no individual features are directly identified, ball tracking can be subsumed under FT methods, since artificial tracer particles are introduced to follow the footprints of local intensity minima. The ball tracking method works well for granulation so that it is a good choice for the characterization of supergranulation (Potts and Diver, 2008). Nevertheless, it might introduce a scale dependence, when tracking on other (small-scale) features such as bright points, penumbral grains, and umbral dots.

Since LCT basically tracks intensity contrast patterns from image to image, it is less affected by the fine structures contained in the sampling window. However, size and shape of the sampling window

play a crucial role for measuring flows on different spatial scales. The time-average of the spatially localized cross-correlations gives a measure of the local displacement, which can be identified with persistent horizontal motions of contrast features. Taking into account that LCT is the most commonly used technique for measuring horizontal proper motions, we opted for this method to create our database of photospheric flows observed in *Hinode* G-band images.

Leaving behind the underlying constant velocity assumption of LCT, Schuck (2006) developed a technique to track optical flows named DAVE. It incorporates the magnetic induction equation, i.e., the continuity equation for the magnetic flux density, keeping the velocity profile affine. Chae and Sakurai (2008) presented a formulation of the non-linear case and called it accordingly NAVE. These authors also provide a detailed parameter study of LCT, DAVE, and NAVE based on images reflecting analytical solutions of the continuity equation as well as on magnetogram data from *Hinode* and MHD simulations. They conclude that NAVE is superior to LCT techniques in more appropriately describing velocity profiles, which include, e.g., local dilation, contraction, and rotation. However, the higher computational requirements of NAVE and the more widespread use and ease of implementation led to the choice of LCT for the present study. Various other technical aspects have to be considered while implementing a technique for tracking optical flows. Since interpolations are required in the various steps of the data reduction, we refer to Potts, Barrett, and Diver (2003), who describe the systematic errors, which can be introduced by unsuitable interpolation schemes. More recently, Löfdahl (2010) discussed image-shift measurements in the context of solar wavefront sensors, which are also applicable to the LCT measurements in the present study.

In summary, there have been numerous studies focusing on flow fields. However, to the best of our knowledge no systematic study of the statistical properties of such flows has been undertaken. Data of the *Solar Optical Telescope* (SOT, Tsuneta *et al.*, 2008) onboard *Hinode* (Kosugi *et al.*, 2007) offer the opportunity for this type of research, since the uniform data quality and absence of seeing allow us to directly compare flow fields in different environments.

2.1 Observations

Images obtained in the Fraunhofer G-band (bandhead of the CH molecule at $\lambda 430.5$ nm) have high contrasts, and small-scale magnetic features can be easily identified with bright points (Berger *et al.*, 1995). Despite the observational advantages of this "proxy-magnetometry" (Leenaarts *et al.*, 2006), the theoretical description of the molecular line-formation process is far from easy (cf. Sánchez Almeida *et al.*, 2001; Steiner, Hauschildt, and Bruls, 2001; Schüssler *et al.*, 2003). The LCT techniques, however, can take full advantage of the high contrast and the rich structural contents of G-band images. On *Hinode*, these observations are carried out by the SOT instrument suite. In particular, G-band images are captured by the *Broad-band Filter Imager* (BFI). SOT is a $f/9$ Gregory telescope with a 50-cm aperture, which provides diffraction-limited resolution (0.2–0.3″) in the wavelength range from 380–670 nm with a maximum field-of-view (FOV) of $360'' \times 200''$.

Our initial selection criteria were that at least 100 G-band images had to be recorded on a given day, which should additionally have a cadence of better than 100 s. It turned out that these criteria restricted us to data with only half the spatial resolution ($0.11''$ pixel^{-1}), where 2×2 pixels were binned into one. In total 48 data sets with 2048×1024 pixels and 153 data sets with 1024×1024 pixels were selected for further analysis. The time intervals covered by these data sets range from one to 16 hours. The bulk statistical analysis will be presented later in this thesis. Here, we will discuss the LCT algorithm in detail and justify our choice of input parameters. For this purpose, we selected two data sets: one with high cadence and another one with a long duration. In addition, we picked a data set without binning to study the dependence of flow maps on the spatial resolution of the input data.

2.1.1 High-Cadence Sequence

The LCT algorithm depends on several input parameters such as the time interval between successive images and the sampling window's size and form. We analyzed a one-hour time-series with a cadence of 15 s to validate the intrinsic accuracy of the LCT algorithm. The data were captured from 14:27–

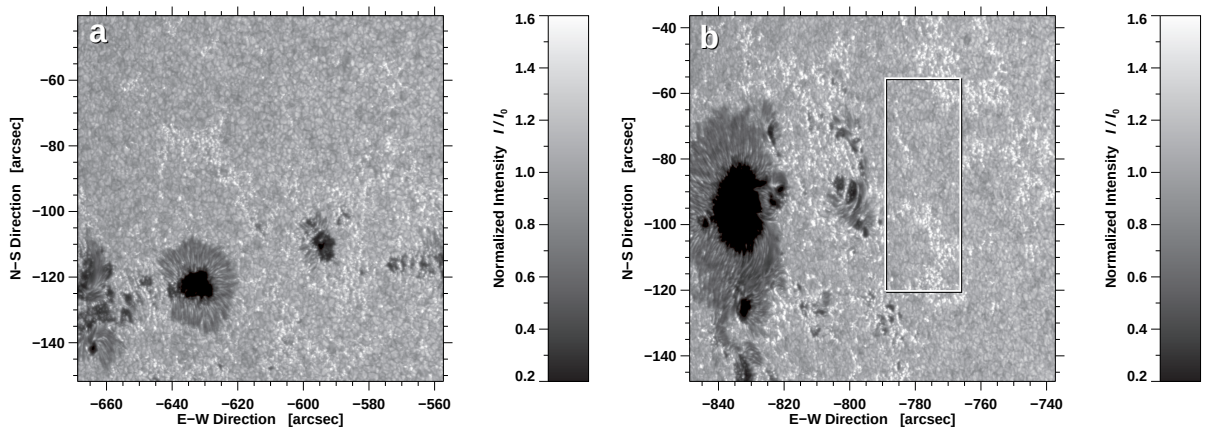

Figure 2.1: Calibrated G-band images of active regions (a) NOAA 10960 and (b) NOAA 10930 observed on 2007 June 4 and 2006 December 7, respectively. The FOV is $111'' \times 111''$. The annotation of the axes refers to heliocentric coordinates given in seconds of arc. The region in the rectangular white box is used for further analysis zooming in on a quiet Sun region containing numerous G-band bright points outlining supergranular boundaries. The images were normalized such that the mode of the quiet Sun intensity distribution corresponds to unity.

15:27 UT on 2007 June 4 (see Fig. 2.1a). The time-series contains 238 images with 1024×1024 pixels. The observations were centered on the active region NOAA 10960, which was located on the solar disk at heliocentric coordinates E630″ and S125″ ($\mu = 0.75$). The active region was in the maximum growth phase and had a complex magnetic field configuration. It was classified as a $\beta\gamma\delta$-region and was the source of many M-class flares, including a major M8.9 flare at 05:06 UT on 2007 June 4, which has been analyzed in a multi-wavelength study by Kumar *et al.* (2010). The flare originated in a conglomerate of small sunspots with mixed polarity and rudimentary penumbrae in the trailing part of the active region (lower left corner of Fig. 2.1a). The disappearance of twisted penumbral filaments as the result of the flare was associated with the activation of helical, twisted flux bundles above the active region, which become visible in the heated flare plasma. During the observing period of the high-cadence sequence, the X-ray flux settled to below C-class level. SOT was pointed towards the leading part of NOAA 10960, which had a much simpler magnetic field topology containing predominantly negative polarity flux.

2.1.2 Long-Duration Sequence

Solar features evolve on different time scales from about five minutes for granulation to several tens of hours for supergranulation. Obviously, the time over which individual LCT maps are averaged plays a decisive role in the interpretation of these average flow maps. Hence, we selected a time-series with 16 hours of continuous data captured on 2006 December 7 (see Fig. 2.1b). This long-duration sequence starts at 02:30 UT and ends at 18:30 UT. It includes 960 images with 1024×1024 pixels and has a cadence of 60 s. Owing to memory constrains imposed by the subsonic filtering, we chose an area of 210×595 pixels centered on a region with granulation and G-band bright points. This region (see Fig. 2.1b) is to the west of the active region NOAA 10930, located at heliocentric coordinates E777″and S88″ ($\mu = 0.59$). The sunspot group was classified as a $\beta\gamma\delta$-region that exhibited a complex magnetic field topology and produced numerous C-, M-, and X-class flares. This region has been extensively studied, especially around the time of an X3.4 flare on 2006 December 13 (e.g., Schrijver *et al.*, 2008). The LCT techniques were used by Tan *et al.* (2009) to study horizontal proper motions associated with penumbral filaments in a rapidly rotating δ-spot. Since this region was rapidly evolving, flows along the magnetic neutral line and global flow pattern might be present. Therefore, the selected region of granulation and G-band bright points might not be representative for horizontal proper motions of quiet Sun granulation.

2.1.3 High-Spatial Resolution Sequence

Only a few data sets of G-band images exist with the full spatial resolution of 0.055″ pixel^{-1} and a cadence suitable for LCT. We selected a one-hour time-series, which was acquired starting at 04:00 UT on

2006 November 26. This high-spatial resolution sequence contains 118 images with 2048×2048 pixels and has a time cadence of about 30 s. The observations were centered on a quiet Sun region near the disk center at heliocentric coordinates E108″ and S125″ ($\mu = 0.99$), which contains only a few G-band bright points and no major magnetic flux concentrations. This region is typical for quiet Sun granulation as encountered during the declining phase of solar cycle 23 just before reaching the solar activity minimum.

2.2 Implementation of the LCT Algorithm

2.2.1 Preprocessing of the G-band Images

The data analysis was carried out in the *Interactive Data Language* (IDL)[3]. Data sets are split in 60-minute sequences with 30 min overlap between consecutive sequences. In preparation for the LCT algorithm, basic data calibration was performed, which consists of dark current subtraction, correction of gain, and removal of spikes caused by high energy particles (e.g., flares and cosmic radiation). Figure 2.1 contains sample G-band images for the high-cadence and the long-duration data set after basic calibration. After initial data calibration, the geometric foreshortening was corrected, and the images were resampled in a regular grid with a spacing of 80 km $\times$ 80 km, i.e., the images appear as if observed at the center of the solar disk. Residual effects of projecting the surface of a sphere onto a plane are neglected, since the FOV of the G-band images is still relatively small. A grid size of 80 km was chosen so that the fine structure contents of the G-band images were not diminished. Pixels close to the solar limb were projected onto several pixels in planar coordinates. Thus, the accuracy of the flow maps at these locations is not as good as for locations close to disk center.

The calibrated, deprojected 60-minute data sequences are the basis for further data processing. In a 60-minute sequence are $l = 0, 1, 2, \ldots, L-1$ images, where L is the total number of images in a particular sequence. For an image with $N \times M$ pixels the intensity distribution is represented by $i(x,y)$ with $x = x_0, x_1, \ldots, x_{N-1}$ and $y = y_0, y_1, \ldots, y_{M-1}$ as pixel coordinates. The indices are typically dropped to ease the notation. The data processing makes extensive use of the fast Fourier transform (FFT). The FFT of the intensity distribution $i(x,y)$ is simply $\mathcal{F}(i(x,y)) = I(k_x, k_y)$, where the upper case letter indicates the FFT and $k_x = 2\pi/x$ and $k_y = 2\pi/y$ are wave numbers corresponding the spatial x- and y-coordinates.

2.2.2 Aligning the Images within a Time-Series

In principle, images could be aligned using the pointing information of the spacecraft. However, we calculate shifts between consecutive images $i_{l-1}(x,y)$ and $i_l(x,y)$ by computing the cross-correlation using only the central part of the images, which is half of the original image size. The cross-correlation between the consecutive images can be expressed as

$$\begin{aligned} c_l(x,y) &= \Re\left\{\mathcal{F}^{-1}\left[\mathcal{F}(i_{l-1}(x,y)) \cdot \mathcal{F}^*(i_l(x,y))\right]\right\} \\ &= \Re\left\{\mathcal{F}^{-1}\left[I_{l-1}(k_x,k_y) \cdot I_l^*(k_x,k_y)\right]\right\} \quad , \end{aligned} \tag{2.1}$$

where $\Re$ indicates the real part of a complex quantity, $\mathcal{F}^{-1}[\ldots]$ is the inverse FFT, and $I^*(k_x,k_y)$ refers to the complex conjugate of $I(k_x,k_y)$. The position of the maximum of the cross-correlation function is computed with subpixel accuracy. Once all $L-1$ shifts between consecutive images are computed, these shifts have to be applied in succession to align all images with respect to the first image in the sequence. Shifting the images is performed using cubic spline interpolation with subpixel accuracy.

Once the time-series of G-band images is aligned the signature of the 5-minute oscillation is removed by applying a 3D Fourier filter. This filter, sometimes called a subsonic filter, has a cut-off velocity of $c_s \approx 8$ km s^{-1} corresponding to the photospheric sound speed. This procedure can be written as

$$i'(x,y,t) = \mathcal{F}^{-1}\left(I(k_x,k_y,\omega) \cdot w(k_x,k_y,\omega)\right) \quad , \tag{2.2}$$

[3] www.ittvis.com

where $I(k_x,k_y,\omega) = \mathscr{F}(i(x,y,t))$, and

$$w(k_x,k_y,\omega) = \begin{cases} 1: & \omega/k_h \leq c_s \approx 8 \text{ km s}^{-1} \\ 0: & \omega/k_h > c_s \approx 8 \text{ km s}^{-1} \end{cases} \tag{2.3}$$

is the filter function with horizontal wave number $k_h = (k_x^2 + k_y^2)^{1/2}$ and frequency $\omega = 2\pi/t$. Because the subsonic filter uses a 3D Fourier transform, some edge effects are sometimes noted for the first few and last few images in a time-series. For this reason we decided to discard the images during the first and last two minutes of the time-series after applying the subsonic filter. Therefore, the final time-series is shortened by this amount of time (see also the discussion in Sect. 2.3.5). In the following, we drop the prime and just use $i(x,y,t)$ to simplify the notation.

2.2.3 LCT Algorithm

The LCT algorithm is based on ideas put forward by November and Simon (1988). The algorithm was adapted to subimages with sizes of 32×32 pixels corresponding to 2560 km $\times$ 2560 km speeding up the computation of the flow maps. In this way, structures with dimensions smaller than a granule will contribute to the correlation signal. Because cross-correlation techniques are sensitive to strong intensity gradients, a high-pass filter was applied to the entire image, suppressing gradients related to structures larger than granules. The high-pass filter is implemented as a Gaussian with a Full-Width-at-Half-Maximum (FWHM) of 15 pixels (1200 km). To indicate that we refer to an subimage with 32×32 pixels and not the entire image, we use the notation $i(x',y')$. The Gaussian kernel used in the high-pass filter then becomes

$$g(x',y') = \frac{1}{2\pi\sigma^2} e^{-\frac{r(x',y')^2}{2\sigma^2}} \quad , \tag{2.4}$$

where $\sigma = \text{FWHM}/(2\sqrt{2\ln 2})$ and $r(x',y') = (x'^2 + y'^2)^{1/2}$. First, a low-pass filtered version of the image is computed

$$i_{\text{low}}(x,y) = i(x,y) \otimes g(x',y') \quad , \tag{2.5}$$

where $\otimes$ denotes a convolution. In a second step, the high-pass filtered image can simply be computed as

$$i_{\text{high}}(x,y) = i(x,y) - i_{\text{low}}(x,y) \quad . \tag{2.6}$$

The result of this filtering is a detailed image, with the low spatial frequencies removed, which is ideal for estimating flow vectors using cross-correlations. Again, we drop the subscript and use $i(x,y)$ to ease notation.

After preparing the images, we put into action the core LCT algorithm. We compute the cross-correlation $c_l(x,y,x',y')$ over a 32×32 pixel region centered on the coordinates (x,y) for each pixel in image pairs $i_{l-1}(x,y)$ and $i_l(x,y)$, which can be written as

$$\begin{aligned} c_l(x,y,x',y') \quad = \quad & \Re\{\mathscr{F}^{-1}[\mathscr{F}(i_{l-1}(x,y,x',y')g(x',y')) \cdot \\ & \mathscr{F}^*(i_l(x,y,x',y')g(x',y'))]\}d(x',y') \quad , \end{aligned} \tag{2.7}$$

where $g(x',y')$ denotes a weighting function also serving as an apodising window. This function has the same form as the Gaussian kernel previously used in the high-pass filter. This ensures that the displacement vectors are computed without preference in azimuthal direction. We also multiplied the cross-correlation functions by a mask

$$d(x',y') = \begin{cases} 1: & r(x',y') \leq c_{s,\text{lim}} \\ 0: & r(x',y') > c_{s,\text{lim}} \end{cases} \tag{2.8}$$

so that the maximum of the cross-correlation function is forced to be within a distance of 12 pixels from its center. The typical time interval between consecutive images is in the range from 60–90 s, i.e., a feature moving at the photospheric sound speed of $c_s \approx 8$ km s^{-1} would travel 480–720 km. This corresponds to 6–9 pixels. This justifies our choice of $c_{s,\text{lim}} = 12$ pixels, which also takes into account

some numerical errors. The position of the maximum of the cross-correlation function is calculated with subpixel accuracy by a parabola fit to the neighboring pixels. The numerical accuracy of the parabola fit is about one fifth of a pixel or 16 km on the solar surface, which corresponds to about 200 m s^{-1} for proper motions measured from a single pair of G-band images. Therefore, many flow maps had to be averaged to determine reliable horizontal proper motions.

2.2.4 LCT Data Products

Once the individual flow maps were calculated, they were saved in binary format. In addition, average maps of horizontal speed and flow direction as well as the x- and y-components of the horizontal flow velocity (v_x, v_y) were stored in native IDL format. Some auxiliary variables were saved as well so that they can be used, e.g., in annotating plots depicting the measured flow fields. A sample of these plots for a 60-minute average flow field is shown in Fig. 2.2. In Fig. 2.2a, horizontal proper motions are plotted as red arrows with a 60-minute averaged G-band image as a background. The arrows indicate magnitude and direction of motions. An arrow with the length corresponding to the grid size indicate a velocity of 1 km s^{-1}. The moat flow starting at the sunspot penumbra and terminating at the surrounding G-band network is clearly discernible.

In Fig. 2.2b, we used an adaptive thresholding algorithm to discern between granulation, G-band bright points, and strong magnetic features. Indiscriminately, we used a fixed intensity threshold of $I_{\rm mag} = 0.8$ for strong magnetic features and an adaptive threshold for G-band bright points, which can be given as

$$I_{\rm bp} = 1.15 + 0.2(1-\mu) \quad , \tag{2.9}$$

where $\mu = \cos(\theta)$ is the cosine of the heliocentric angle θ. The darkest parts of sunspots (umbrae) and pores can be identified using another fixed threshold of $I_{\rm dark} = 0.6$, while sunspot penumbrae cover intermediate intensities from $I_{\rm dark}$ to $I_{\rm mag}$, allotting the range $I_{\rm mag}$ to $I_{\rm bp}$ to granulation. The adaptive threshold was necessary, as a first order approximation, to account for the center-to-limb variation (CLV) of the G-band bright points, which exhibit much higher contrasts near the solar limb. This adaptive thresholding algorithm allows us to study the properties of horizontal proper motions for different solar features.

Apart from the conventional way of displaying velocity vectors as arrows, we present two-dimensional high-resolution speed (Fig. 2.2c) and azimuth (Fig. 2.2d) maps. In these maps, the physical quantities are computed for each individual pixel so that the fine structure of the flow field becomes accessible. The color scale for the speed values is the same for all plots in this study. Indeed, we used the same color scale for all flow maps in the database so that flows for different scenes on the Sun can be directly compared. In the azimuth map, the direction is encoded in a 12-color compass-rose, which can be found to the very right of this panel. In principle, more colors could be used to illustrate the flow direction. However, such plots would become very crowded and are very hard to interpret. The essential features of the flow field, i.e., inward motion of the penumbral grains in the inner penumbra and outward motions related to Evershed and moat flows, can easily be identified.

In Figs. 2.2e and 2.2f, we compiled divergence and vorticity maps. The divergence of a flow field with velocity components (v_x, v_y) is simply given as

$$\nabla \cdot v = \frac{\partial v_x}{\partial x} + \frac{\partial v_y}{\partial y} \quad . \tag{2.10}$$

Similarly, the vertical component of the vorticity is given by

$$\nabla \times v = \frac{\partial v_x}{\partial y} - \frac{\partial v_y}{\partial x} \quad . \tag{2.11}$$

For comparison with other studies, we calculated these two quantities for an area containing only granulation and few G-band bright points. The maximum values for divergence (1.5×10^{-3} s^{-1}) and vorticity (0.6×10^{-3} s^{-1}) are an order of magnitude higher than values found in previous studies. Higher values are not surprising, because we calculated them for every pixel in the high-resolution maps capturing more of the small-scale motions. However, our values of the $10^{\rm th}$ percentile for divergence

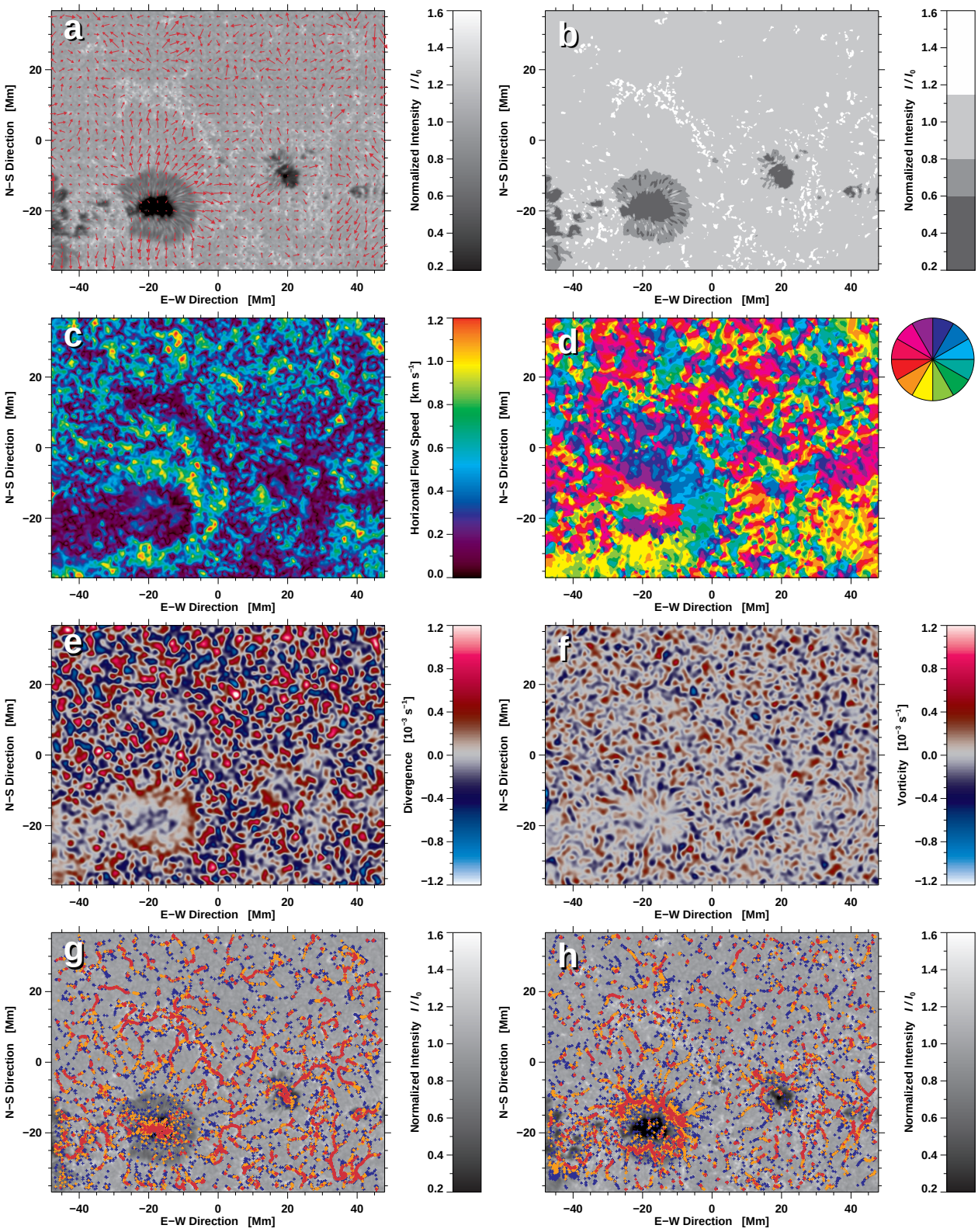

Figure 2.2: (a) The average (60-minute) G-band image after correction of geometrical foreshortening corresponding to the G-band image shown in Fig. 2.1a. The red arrows indicate the magnitude and direction of the horizontal proper motions. Arrows with a length corresponding to the grid size indicate velocities of 1 km s^{-1}. (b) Adaptive and fixed intensity thresholds are used to identify conglomerates of G-band bright points, granulation, penumbrae, umbrae, and pores. Color codes are used to point out (c) flow speed and (d) direction in high-resolution flow maps. The flow direction is encoded according to the 12 colors of the compass rose. Sources and sinks in a flow field can be identified in (e) a divergence map, whereas (f) a vorticity map imparts knowledge of rotation or spiral motion in a flow field. The (g) forward and (h) inverse cork maps provide additional means of visualizing converging and diverging motions. Test particles are displayed after they have followed the flows for two (blue), four (orange), and eight hour (red). The conspicuous network of corks is related to the spatial scales of the meso-and supergranulation.

(4.3×10^{-4} s^{-1}) and vorticity (1.9×10^{-4} s^{-1}) are essentially the same as reported by Simon *et al.* (1994), who also computed these values for a 60-minute averaged, quiet Sun flow field. On the other hand, in the present study the divergence is four times and the vorticity is two times higher than the values presented by Strous *et al.* (1996) but their values were computed in the proximity of an emerging active region. In summary, keeping in mind the different LCT parameters used in the different studies, the statistical properties of the flow fields as presented in this study agree with previous investigations.

In order to visualize the temporal evolution of the horizontal proper motions, we computed forward and inverse cork maps. In the forward cork map depicted in Fig. 2.2g, evenly spread test particles are allowed to float forward in time with a given horizontal speed for a certain time interval. We used the method described by Molowny-Horas (1994). In the inverse cork map shown in Fig. 2.2h, the particles float backward in time. This is accomplished by simply reversing the sign of the velocity components. The forward cork map is used to visualize regions of converging flows, and the inverse map is a good tool to study divergence regions. We tracked test particles for consecutively two, four, and eight hours. Test particles for these time steps are represented as blue, orange, and red colors, respectively. These particles were initially distributed on an equidistantly spaced grid with a spacing of 10 pixels, i.e., one particle was placed every 0.8 Mm. The most conspicuous feature of the forward cork map is that the tracer particles that outline the network of G-band bright points, which corresponds to the boundaries of the supergranulation. In the inverse cork map, a prominent ring of tracer particles outlines the divergence line in the middle penumbra.

All plots presented in Fig. 2.2 are production-quality PostScript files, which are converted to Portable Network Graphics (PNG) format so that they can be included in a web page serving as the entry point to the database. We prepared overview web pages for the respective dates when suitable time-series of G-band images were available, which contain eight plots of Fig. 2.2, and in addition movies in Audio Video Interleave (AVI) format of the corrected G-band images as well as auxiliary information describing the data sets. All these data products are generated using IDL routines without requiring any user interaction. The results of this study will ultimately be published as a small project within the *German Astrophysical Observatory* (GAVO)[4] as a value-added product of the *Hinode* database.

2.2.5 Timing Issues Related to the Image Capture

The LCT technique delivers localized displacements observed in image pairs. These displacements in conjunction with the time that has elapsed between the acquisition of both images yield localized velocity vectors. Therefore, accurate knowledge of the time interval between consecutive images used in the LCT algorithm is essential to provide reliable maps of the horizontal proper motions. The time interval Δt for the high-cadence image sequence observed on 2007 June 4 is shown in Fig. 2.3 as the thin sawtoothed curve at the top of the panel. It has a bimodal distribution with values Δt of 14.4 s (60.7%) and 16 s (39.3%). The average value is $\overline{\Delta t} \approx 15.0$ s. The difference of 1.6 s is an artifact of the polarization modulation. The polarization modulation unit (PMU) is located just behind the telescope exit slit within the optical telescope assembly (OTA) but in front of the tip-tilt mirror that is employed by the correlation tracker (see Tsuneta *et al.*, 2008). A common CCD camera is assigned to both the broad- and narrowband filter imagers (BFI and NFI). The critical timing between camera and PMU is handled by the focal plane package (FPP). The PMU is a continuously rotating waveplate, which is always turned on – even for non-polarimetric data such as G-band images. Its rotation period is $T = 1.6$ s and all exposure timing is controlled with the clock of the PMU. This is the reason for the non-uniformity in the observed time-interval Δt.

However, we do not find a zigzag pattern in the LCT displacements indicating that the exposures were taken at a uniform time interval is $\overline{\Delta t}$ (dash-dotted curve in Fig. 2.3). We attribute the fluctuations in the measured horizontal displacements to evolving features on the Sun and residual numerical effects of the LCT algorithm. Therefore, we opted to use a fixed time interval $\overline{\Delta t}$ in the data analysis. Note that sometimes a 'traffic jam' in the data transfer might result in even larger deviations in the time stamps recorded in the FITS headers. On the other hand, averaging individual LCT maps over an hour (or longer) will only result in velocity errors of less than a tenth of a precent, i.e., the speed measured by the

[4] www.g-vo.org

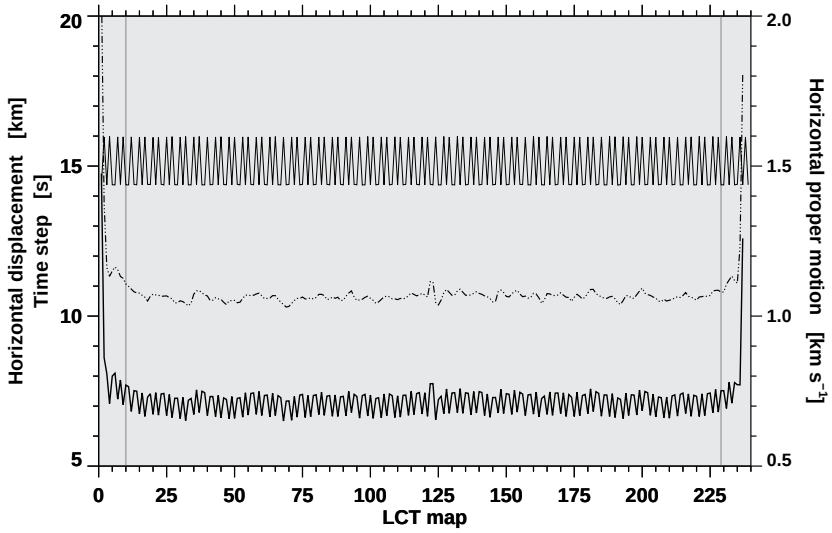

Figure 2.3: Timing issues related to the image capture of *Hinode*/SOT G-band images. The time interval between consecutive images is depicted as the thin curve. Together with the measured average horizontal displacement (*dash-dotted*), it yields the average horizontal proper motion (*thick*). Regions outside the thin gray vertical lines are affected by the subsonic filtering.

LCT algorithm varies about its mean value as can be seen in the thick curve at the bottom of Fig. 2.3. In summary, accurate timing has to be ensured to obtain reliable LCT flow maps and all data were checked for consistency between recorded time stamps and measured horizontal displacements. Because the individual flow maps during the first and last 2 min of the one-hour sequences do not reflect the true proper motions but are artifacts of the subsonic filtering, we excluded them from the calculation of the average flow maps.

2.3 Results

2.3.1 Statistical Properties of Flow Maps and Time Cadence Selection

The one-hour time-series on 2007 June 4 contains 238 G-band images, i.e., the time cadence is ≈ 15 s. This higher temporal resolution allows us to study the intrinsic accuracy of the LCT algorithm. We calculated LCT maps using seven different time intervals $\Delta t = 15$ s, 30 s, 60 s, 90 s, 120 s, 240 s, and 480 s. Note that the time interval over which flow maps are averaged is reduced to $\Delta T = 3600\ \mathrm{s} - \Delta t$, i.e., in case of the longest time cadence by as much as 8 min. However, these slightly different averaging times will not change the results discussed below. When using all individual LCT maps to compute the average horizontal proper motion, we refer to these data as the *entire sequence*. On the other hand, when we split the entire sequence into four disjunct sets, we refer to them as *interleaved data sets*, i.e., every fourth LCT map is employed to compute the average horizontal proper motion. Because these flow maps cover exactly the same period of time, differences can be directly attributed to the numerical accuracy of the LCT algorithm.

For the entire sequence and interleaved data sets we computed statistical parameters that describe the distribution of horizontal proper motions for granulation in the vicinity of active region NOAA 10960. We used the adaptive thresholding algorithm (Eqn. 2.9) to select only granulation excluding G-band bright points. The proper motions accordingly refer to plasma motions in the absence of any strong magnetic field concentrations. This selection facilitates comparing horizontal flow speeds and their distributions in all cases of the present work.

We calculated the mean $\bar{v}$, median v_{med}, maximum v_{max}, and 10$^{\mathrm{th}}$ percentile v_{10} of the horizontal flow speeds. The 10$^{\mathrm{th}}$ percentile v_{10} represents the value for which 90% of the speed values will be less and 10% will be greater than v_{10}. Since the maximum speed v_{max} is only based on a single value, it is easily influenced by numerical errors and the data calibration. The 10$^{\mathrm{th}}$ percentile v_{10} is more robust because it describes a property of the entire distribution, i.e., the high-velocity tail. Along with these quantities we also calculated the variance σ_v^2, standard deviation σ_v, skewness $\gamma_{1,v}$, and kurtosis $\gamma_{2,v}$. The last two statistical parameters describe the deviation of a distribution from the normal distribution.

We find an increase of the average velocity with increasing time cadence Δt starting from about 0.40 km s^{-1} for $\Delta t = 15$ s, arriving at a maximum value of about 0.47 km s^{-1} for $\Delta t = 60$–90 s, and then

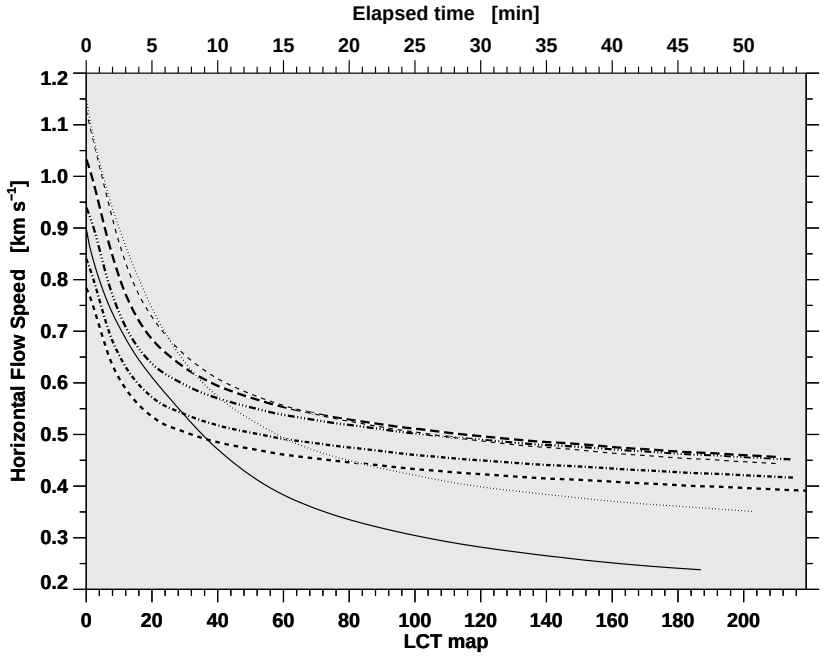

Figure 2.4: Mean horizontal flow speed as a function of averaged LCT maps for time cadences Δt of 15 s (*thick dashed*), 30 s (*thick dash-dotted*), 60 s (*thick dash-triple-dotted*), 90 s (*thick long dashed*), 120 s (*thin dashed*), 240 s (*thin dotted*), and 480 s (*thin solid*).

decreasing to about 0.45 km s^{-1} for $\Delta t = 120$ s, 0.34 km s^{-1} for $\Delta t = 240$ s and further reaching the lowest value of about 0.23 km s^{-1} for $\Delta t = 480$ s. Other statistical parameters such as $v_{\rm med}$, v_{10}, $v_{\rm max}$, σ_v^2, and σ_v follow the same trend.

The initially increasing values can be explained by the time required for a solar feature to move from one to the next pixel. Three velocity values have to be considered: (1) the photospheric sound speed of $\approx$8 km s^{-1}, (2) the maximum photospheric velocity of $\approx$2 km s^{-1} measured by LCT techniques, and (3) the average speed for the proper motion of the granulation of $\approx$0.5 km s^{-1}. For $\Delta t = 15$ s, the average displacement is around one tenth of a pixel, whereas the numerical accuracy for a single measurement is only one fifth of a pixel, because the maximum of the cross-correlation function can only be determined with this precision. Thus, in this case a solar feature has insufficient time to move, which results in underestimating its velocity.

For $\Delta t = 60$–90 s, the horizontal displacement is sufficiently large so that a feature could have moved to one of its neighboring pixels. The measured speed values in individual speed maps are now well within the range where numerical accuracy issues are negligible. Starting at $\Delta t = 120$ s, the mean velocity becomes lower, while there is sufficient time for the solar feature to move quite some distance, the feature might have evolved too much, so that the LCT algorithm might not any longer trace the same feature. This leads to diminished horizontal velocities.

Thus, 60–90 s is the good choice for measuring of horizontal flow speeds with LCT techniques. In this range of the time cadence, the mean values $\bar{v}$ of the interleaved data sets are essentially the same. Their deviations are much smaller than the previously discussed systematic trends. In summary, all flow maps for the database were calculated using $\Delta t = 60$–90 s. If the time interval Δt was shorter, a multiple of the time interval $\Delta t' = n\Delta t$ with $n = 2, 3,$ or 4 was used.

2.3.2 Determining the Duration of the Time Averages

How many individual LCT maps have to be averaged to yield a reliable flow map? As previously discussed, the parabola fit to the maximum of the cross-correlation sets one limitation. However, there are also method-independent issues to be considered. Solar features evolve over time so that a global pattern reveals itself only after averaging many individual LCT maps. We computed the mean horizontal flow speed as a function of the number of individual LCT maps that were used to arrive at an average flow map. The number of flow maps corresponds to the time interval ΔT over which the individual flow maps were averaged.

Figure 2.4 presents this functional dependence for the time cadences from $\Delta t = 15$ s to 480 s. All curves start with high velocities when only a few individual LCT maps are averaged. It takes about

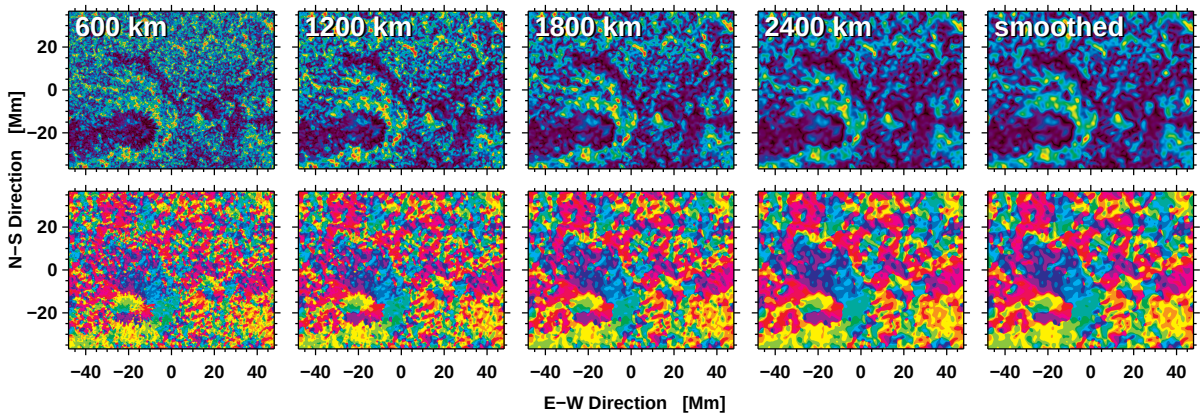

Figure 2.5: Horizontal flow speed (*top*) and azimuth maps (*bottom*) measured using Gaussian kernels with 64×64 pixels and various FWHM. The FWHM of 7.5, 15, 22.5, and 30 pixels correspond to 600, 1200, 1800, and 2400 km on the solar surface, respectively. The rightmost column depicts smoothed versions of the FWHM = 1200 km speed and azimuth maps. It is virtually impossible to distinguish these smoothed maps from the ones with a FWHM = 2400 km. The color coding is the same as in Fig. 2.2(c, d).

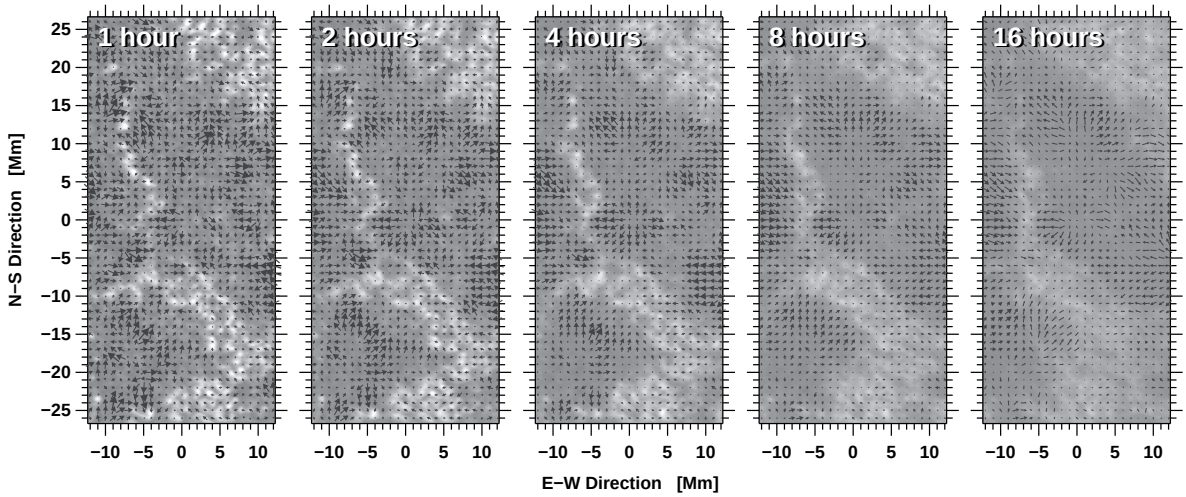

Figure 2.6: Time-averaged G-band images with horizontal flow vectors computed for $\Delta T = 1$, 2, 4, 8, and 16 h. Arrows with the length corresponding to a grid spacing indicate velocities of 1 km s^{-1}. The background images are displayed $0.5 \leq I/I_0 \leq 1.5$.

20 min before the curves level out and approach an asymptotic value, indicating that these average flow maps are still dominated by the motions of fine structure contained within the sampling window. As discussed in the context of the statistical properties of the flow maps, short time cadences Δt tend to underestimate the flow speed. If flow speeds have been computed for time intervals shorter than 20 min, feature tracking methods are more appropriate than LCT techniques, in particular for small-scale features.

We find that all curves up to $\Delta t = 90$ s are stacked on top of each other without crossing the next higher curve at any point. Starting at $\Delta t = 120$ s, we find that the curves corresponding to the longer time cadences cross the other curves after about 20–25 min. This is another indication that solar features have evolved too much so that LCT fails to properly track their motion. This behavior provides an explanation for the spread of velocity values found in literature. In particular, short time-series, as often encountered in ground-based observations, might be biased toward higher velocities. In summary, our choice of 60-minute averages for LCT maps is a conservative one that gives the solar features sufficient time to reveal the global flow pattern.

2.3.3 Selection of the Sampling Window

How do the horizontal proper motions depend on size and FWHM of the Gaussian kernel used in the LCT algorithm? To answer this question, we calculated horizontal proper motions using a Gaussian

Table 2.1: Various parameters describing the horizontal proper motions of granulation and G-band bright points calculated over time intervals $\Delta T = 1, 2, 4, 8,$ and 16 h.

	ΔT [h]	$\bar{v}$ [km s^{-1}]	$v_{\rm med}$ [km s^{-1}]	v_{10} [km s^{-1}]	$v_{\rm max}$ [km s^{-1}]	σ_v [km s^{-1}]	$\gamma_{1,v}$	$\gamma_{2,v}$
Granulation	1	0.43	0.39	0.78	1.86	0.24	0.73	0.17
	2	0.39	0.36	0.69	1.42	0.21	0.56	−0.21
	4	0.34	0.31	0.60	1.25	0.19	0.65	0.10
	8	0.30	0.29	0.50	0.87	0.15	0.46	−0.12
	16	0.23	0.22	0.38	0.74	0.12	0.53	0.01
Bright Points	1	0.22	0.22	0.37	0.70	0.10	0.35	−0.25
	2	0.22	0.22	0.35	0.55	0.10	0.18	−0.57
	4	0.17	0.17	0.27	0.52	0.08	0.41	0.10
	8	0.15	0.15	0.24	0.45	0.07	0.44	0.28
	16	0.12	0.12	0.20	0.41	0.06	0.52	0.48

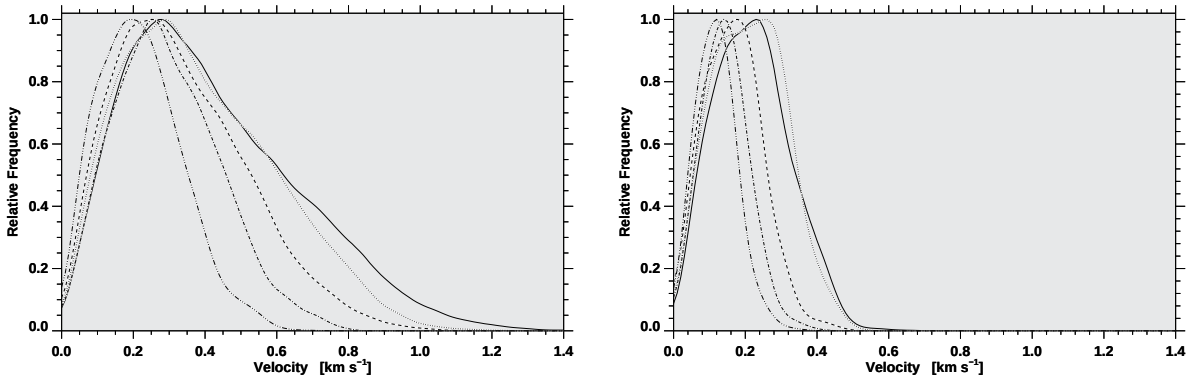

Figure 2.7: Relative frequency distributions of horizontal proper motions for quiet Sun (*left*) and G-band bright points (*right*) calculated over $\Delta T = 1$ h (*solid*), $\Delta T = 2$ h (*dotted*), 4 h (*dashed*), 8 h (*dash-dot-dotted*), and 16 h (*dash-triple-dotted*).

kernel with 64×64 pixels, which is equivalent to 5120 km $\times$ 5120 km on the solar surface. This larger kernel was chosen to encompass successively broader FWHM. We choose four FWHM of 7.5, 15, 22.5, and 30 pixels corresponding to 600, 1200, 1800, and 2400 km, respectively. The FWHM of 1200 km matches the size of a granule. Individual LCT maps are produced from image pairs separated by 60 s in time. We computed the statistical parameters relating to granulation for the entire sequence and the interleaved data sets. All statistical parameters are decreasing with increasing FWHM (except for the skewness $\gamma_{1,v}$ and kurtosis $\gamma_{2,v}$). For FWHM = 600 km the mean velocity is, $\bar{v} = 0.48$ km s^{-1} which decreases to $\bar{v} = 0.47$ km s^{-1} for FWHM = 1200 km, $\bar{v} = 0.41$ km s^{-1} for FWHM = 1800 km, and further to $\bar{v} = 0.37$ km s^{-1} for FWHM = 2400 km. Small-scale features, which exhibited the highest proper motions, are lumped together with regions of low flow speeds when the FWHM increases. This effect is displayed in Fig. 2.5, which shows the speed and azimuth maps for the four FWHM. As before, for a given FWHM all statistical parameters agree with each other for up to three significant digits, i.e., there is no indication that the algorithm's numerical accuracy depends on the FWHM of the kernel used in LCT.

In the case of FWHM = 1200 km, the statistical parameters are very close to the ones calculated for the same FWHM, but with a kernel of 32×32 pixels. This is not surprising, because the Gaussian kernel assigns a much stronger weight to features in the center of the subimage, i.e., the periphery in the 64×64 pixels FOV has only a small influence in determining the displacement vector for a pair of subimages. This of course only holds true as long as the wings of the Gaussian do not significantly extend beyond the edges of the kernel. Convolving the average flow map (FWHM = 1200 km) with a Gausssian kernel,

which had a size of 32×32 pixels and FWHM $= 26.4$ pixels (2112 km), we arrive at a smoothed version (see right column in Fig. 2.5), which is virtually identical with the flow map with FWHM $= 2400$ km.

In conclusion, it makes no difference, whether one uses a larger FWHM while computing LCT maps or one smoothes the maps after computation. In both cases, the results are virtually the same. Because only minor changes in the LCT results were observed for kernels with 32×32 pixels as compared to 64×64 pixels, the smaller kernel was chosen that significantly reduced the computing time. Furthermore, the smallest FWHM produces the most detailed flow maps. However, we chose a FWHM of 1200 km, favoring the spatial scales of granulation, which covers the largest fraction of the observed area. Additional smoothing can still be applied in the later data analysis stages to either reduce noise or to track flows on larger spatial scales. For case studies of sunspot's fine structure, a smaller FWHM might be more appropriate.

2.3.4 Numerical Errors in Calculating Flow Maps

We computed the pixel-to-pixel rms-error for the magnitude and direction of the flow velocity using the interleaved data sets for different time cadences Δt and for different FWHM of the sampling window. Six difference maps (sets $1-2$, $1-3$, $1-4$, $2-3$, $2-4$, and $3-4$) can be computed from the four interleaved data sets, thus for each pixel, we can derive the errors, which are primarily due to numerical errors inherent to the LCT algorithm. The rms-error in velocity is 15–90 m s^{-1} from shortest to longest cadence. The corresponding rms-error in direction is 5°–30°. However, for cadences in the range of 60–90 s, which is the range used to create the database, the rms-error of the velocity is typically in the range from 35–70 m s^{-1}, while the values for the direction vary by as much as 10°–15°. The largest variations in direction are observed near the boundaries of patches showing coherent flows. Even after correcting the 2π ambiguity in the difference maps, we find high values at these locations. As a side note, the rms-error in direction justifies our choice of a color wheel with only twelve segments in the display of the azimuth maps. One segment covers 30° so that pixel-to-pixel variations of about $\pm 15°$ are suppressed. Otherwise, the azimuth maps would become too crowded, and consequently, the overall flow pattern is no longer perceptible.

For a different FWHM of the sampling window, rms-errors for speed and direction decrease with increasing FWHM. The velocity error is 35 m s^{-1}, and the error in direction is about 10° for a FWHM of 1200 km. These errors decrease to 15 m s^{-1} and 5° for a FWHM = 1800 km and to 10 m s^{-1} and 4° for a FWHM = 2400 km. Here, the decreasing rms-errors can be attributed to the smoothing effect of a wider sampling window, i.e., more pixels are used with higher weights in the cross-correlation. Furthermore, the rms-error in magnitude and direction for the time cadence $\Delta t = 60$ s is nearly the same regardless of the size of the Gaussian kernel (32×32 pixels vs. 64×64 pixels).

Finally, we calculated Pearson's correlation coefficient between LCT maps of the interleaved data sets. Pearson's correlation coefficient indicates the degree of a linear relationship between two variables. A positive value of unity indicates that the data sets are identical, disregarding a linear scaling factor. The linear correlation coefficient for different time cadences Δt decreases from 0.99 to 0.93 starting at the shortest and ending at the longest cadence. The high degree of correlation indicates that all essential features of the flow field are captured by the LCT algorithm. The monotonic decrease, however, indicates that numerical errors increase when the cadences Δt become too large.

2.3.5 Long-Lived Features in Flow Maps

The one-hour time interval over which the LCT maps are averaged is insufficient to identify features that need longer to evolve, such as meso- and supergranulation. Therefore, to clearly identify the boundaries of these large-scale convective cells and to visualize the effects of longer time averages, we averaged LCT maps over $\Delta T = 1$, 2, 4, 8, and 16 h. For this purpose, we utilized the long-duration data set with 960 images and chose a time cadence $\Delta t = 60$ s.

As before, we calculated the statistical parameters for the entire sequence and the interleaved data sets for granulation. All velocity values, with exception of the skewness $\gamma_{1,v}$ and kurtosis $\gamma_{2,v}$, decrease with increasing time intervals over which the individual LCT maps are averaged. For $\Delta T = 1$ h, the mean velocity is $\bar{v} = 0.44$ km s^{-1}, which decreases to $\bar{v} = 0.38$ km s^{-1} for $\Delta T = 2$ h, $\bar{v} = 0.34$ km s^{-1}

Table 2.2: Statistical parameters describing the frequency distributions of the horizontal proper motions of various solar features (over all FOV, granulation, penumbra, umbra, and G-band bright points).

Feature	$\bar{v}$ [km s^{-1}]	$v_{\rm med}$ [km s^{-1}]	v_{10} [km s^{-1}]	$v_{\rm max}$ [km s^{-1}]	σ_v^2 [km^2 s^{-2}]	σ_v [km s^{-1}]	$\gamma_{1,v}$	$\gamma_{2,v}$
All	0.44	0.40	0.83	1.95	0.07	0.27	0.76	0.21
Granulation	0.47	0.43	0.85	1.95	0.07	0.27	0.67	0.08
Penumbra	0.30	0.24	0.62	1.43	0.05	0.23	1.46	2.07
Umbra	0.23	0.19	0.40	1.92	0.04	0.20	3.66	20.44
Bright points	0.23	0.20	0.43	1.21	0.03	0.15	1.43	2.65

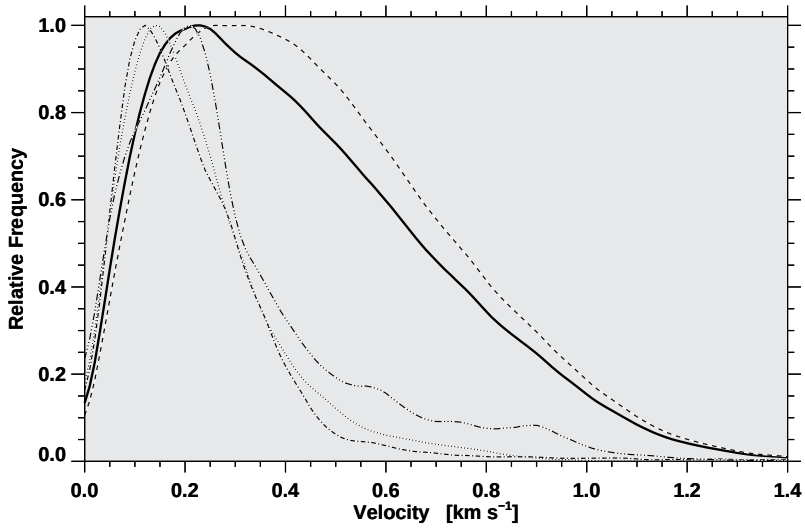

Figure 2.8: Relative frequency distributions of horizontal proper motions computed for all solar features (*solid*), G-band bright points (*dotted*), granulation (*dashed*), umbra (*dash-dotted*) and penumbra (*dash-triple-dotted*).

for $\Delta T = 4$ h, $\bar{v} = 0.30$ km s^{-1} for $\Delta T = 8$ h, and further to $\bar{v} = 0.23$ km s^{-1} for $\Delta T = 16$ h. The mean speed approaches a value for the global flow field with increasing ΔT. However, the value for $\Delta T = 1$ h is only slightly lower than previously computed for the high-cadence sequence. These small deviations (< 0.05 km s^{-1}) reflect only minute differences between the scenes on the solar surface.

Fig. 2.6 contains the time-averaged G-band images with superposed arrows indicating speed and direction of the horizontal proper motions for $\Delta T = 1$, 2, 4, 8, and 16 h. The region shows granulation and G-band bright points to the west of active region NOAA 11930. Magnetic features dominate the long-duration time averages, i.e., the flow speed is low where strong magnetic fields are present in the chromospheric network, and conversely, the speed is high where G-band bright points outline the boundaries of large-scale convective cells. The high speeds associated with the local convective pattern of granules have diminished for the long-duration flow maps and only the converging motion toward the cell boundaries remains, which explains the statistical properties of the velocity values discussed above. The overall visual impression of the vector maps is that the arrows are more ordered in the long-duration maps, whereas in the short-duration maps ($\Delta T = 1$ and 2 h) a larger scatter of the flow vectors is observed on smaller scales. Nonetheless, the imprint of the the meso- and/or supergranulation is already visible in the short-duration flow maps and becomes more prominent the longer the time interval is over which the LCT maps are averaged. Strong converging motions can be found in Fig. 2.6 near the vertical alignment of G-band bright points in the northeast corner of the FOV and at the boundary of the larger supergranular cell in the southeast corner of the FOV. The supergranule also contains substructure on smaller scale, i.e., a strong divergence center exactly in the central FOV, which can be clearly seen after averaging for at least $\Delta T = 2$ h.

We plotted the relative frequency distributions of the flow fields spanning time intervals of $\Delta T = 1$, 2, 4, 8, and 16 h in Fig. 2.7 to gain insight into the statistical properties of the long-duration data sets – this time for both granulation and for G-band bright points. The statistical parameters characterizing these distributions are provided in Tab. 2.1 for reference. The distribution describing granulation for the

Table 2.3: Statistical parameters describing the frequency distributions of the horizontal proper motions for various image scales derived from the high-spatial resolution sequence.

Image scale α		$\bar{v}$	v_{med}	v_{10}	v_{max}	σ_v^2	σ_v	$\gamma_{1,v}$	$\gamma_{2,v}$
[pixel^{-1}]	[km pixel^{-1}]	[km s^{-1}]	[km s^{-1}]	[km s^{-1}]	[km s^{-1}]	[km^2 s^{-2}]	[km s^{-1}]		
0.055″	40	0.54	0.52	0.89	1.60	0.07	0.26	0.42	−0.09
0.110″	80	0.53	0.52	0.88	1.62	0.07	0.26	0.42	−0.09
0.165″	120	0.52	0.51	0.87	1.58	0.07	0.26	0.46	−0.04
0.220″	160	0.50	0.48	0.83	1.54	0.06	0.25	0.50	0.05
0.275″	200	0.47	0.45	0.79	1.57	0.06	0.24	0.55	0.19

shortest time interval ($\Delta T = 1$ h) is the broadest and has an extended high-velocity tail. Interestingly, for velocities up to 0.6 km s^{-1} this distribution is virtually the same as the distribution for an averaging time, which is twice as long ($\Delta T = 2$ h). The only difference is the high-velocity tail. This can be interpreted that proper motions on small scales still make their presence known, if individual LCT maps are not averaged for at least two hours. The peaks of these distributions shifted towards lower velocity values (from 0.43 to 0.23 km s^{-1}) for longer ΔT. In addition, their standard deviations are progressively becoming smaller (from 0.24 to 0.12 km s^{-1}). The progression of the frequency distributions shown in the left panel of Fig. 2.7 supports the conclusion that the essential features of long-duration LCT maps have been captured for $\Delta T = 8$–16 h.

The frequency distributions for G-band bright point differ in some aspects from those for granulation. The high velocity tail is less prominent and all statistical parameters describing the distributions are reduced by about a factor of two. The two distributions with the shortest time intervals ($\Delta T = 1$ and 2 h) show a hint of a bimodal distribution, and they are skewed toward higher velocity values. However, this might be an artifact of the adaptive thresholding algorithm, because the areas covered by G-band bright points are smaller and well defined in the short-duration intensity maps. Thus, considering the FWHM = 1200 km of the sampling window, a larger contribution from granulation is expected, if more isolated G-band bright points are present in the maps, which are used for threshholding. Eqn. 2.9 was slightly modified to accommodate the longer time intervals, which lead to a fuzzier appearance of the area covered by G-band bright points and result in a diminished contrast of the G-band bright points. Because no contemporay magnetograms with a comparable spatial resolution were available, we cannot comment on the influence of flux emergence or dispersal during the observed time interval. However, active region NOAA 10930 showed pronounced activity. In particular, the penumbra of the small sunspot just to the east of the FOV decayed and resulted in continuous flaring in the active region.

Even though long-duration time averages are an important tool when studying large-scale convective patterns or the persistent motions in an active region, the scarcity of such data sets argues against their use for comprehensive and comparative studies. Since most of the characteristics of flow fields are already captured in one-hour averages, we opted for $\Delta T = 1$ h. Furthermore, selecting $\Delta T = 1$ h allows us to study changes in long-duration time-series by computing averaged flow maps every 30 min. Another consideration is that one hour is more then ten times the typical lifetime of granules, so that the proper motions of individual granules should be negligible and global motion patterns will reveal themselves.

2.3.6 Frequency Distributions for Different Solar Features

The simplest approach to describe flow fields would be to compute the overall frequency distributions for a particular FOV. However, this simplistic approach is insufficient to recover the underlying physics of plasma motions in the presence (or absence) of strong magnetic field. We used the adaptive thresholding algorithm (Eqn. 2.9) described in Sect. 2.3.4 to compute frequency distributions for granulation, penumbrae, umbrae/pores, G-band bright points, and the entire FOV regardless of the features contained in this region. For this case study, we used the high-cadence sequence (see Fig. 2.2b for thresholded image) with $\Delta t = 60$ s, $\Delta T = 1$ h, and a FWHM = 1200 km. The respective distributions are shown in Fig. 2.8, and the corresponding statistical parameters are summarized in Tab. 2.2. Similar plots and tables will be

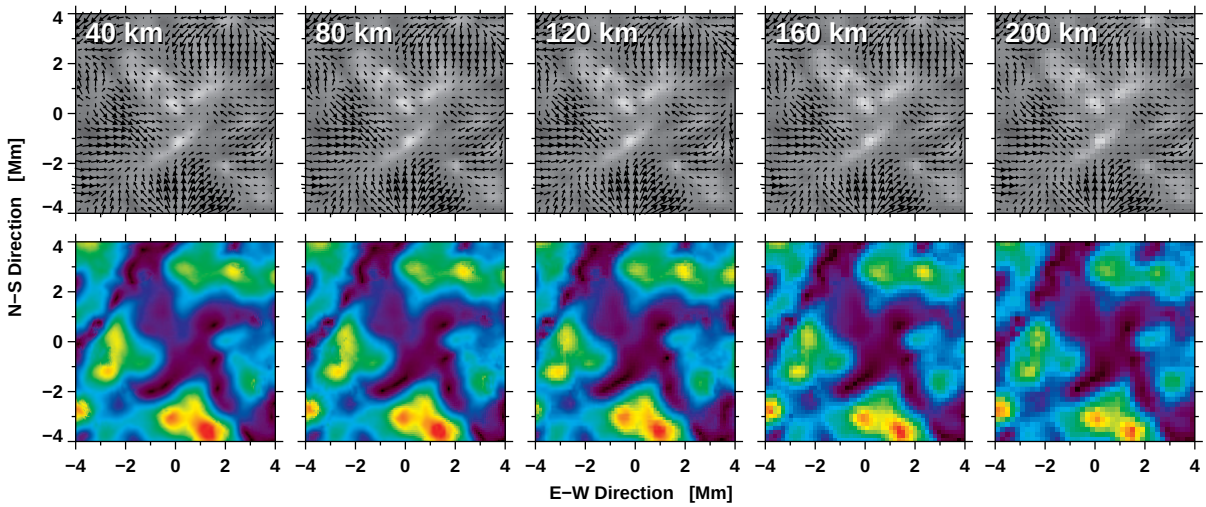

Figure 2.9: Time averaged G-band images with horizontal flow vectors (*top*) and flow speed maps (*bottom*) for different spatial resolution. Arrows with the length corresponding to the grid spacing indicate velocities of 0.5 km s^{-1}. The color coding is same as in Fig. 2.2(c).

included in the database subsuming the more than 200 data sets, that were analyzed as part of this study. We provide Fig. 2.8 and Tab. 2.2 to facilitate the comparison with other case studies. However, these data are not representative (in the sense of a mean value) for all data sets contained in the database.

A barely detectable shoulder in the frequency distribution for overall the FOV and the extended high-velocity tail already hint that this distribution contains contributions from various solar features. Its mean velocity $\overline{v} = 0.44$ km s^{-1} is only slightly lower than the corresponding value for granulation $\overline{v} = 0.47$ km s^{-1} that dominates the FOV. The distribution for granulation is broader, and a low value of kurtosis ($\gamma_{2,v} = 0.08$) leads to a flatter peak, where any indication of a shoulder is absent. There is a noticeable difference in the distributions of strong magnetic elements and granulation. The distribution curves for G-band bright points, umbral and penumbral region are narrow, with sharp peaks and are shifted toward left compared to granulation and overall FOV. The mean velocity for these region vary from $\overline{v} = 0.30$ km s^{-1} for penumbrae to $\overline{v} = 0.23$ km s^{-1} for umbrae/pores and G-band bright points. Interestingly, the distributions for the umbrae/pores and the G-band bright points are virtually identical, while that for the penumbra has significant contributions at velocities above 0.4 km s^{-1}. This is indicative of the more complex flow fields in the penumbra, where penumbral grains move preferentially in the radial direction – inward in the inner penumbra and outward in the outer penumbra. This also illustrates that some of the small-scale horizontal proper motions can be captured with the current implementation of the LCT algorithm.

2.3.7 Flow Maps for Different Spatial Resolution

Even though not at the core of our study, we will address the question of how the spatial resolution affects the determination of the horizontal proper motions before concluding this study. We used the high-spatial resolution sequence of Sect. 2.2.3 and treated it exactly as all the other data with the exception that the G-band images were sampled at 40, 80, 120, 160, and 200 km after correction of geometrical foreshortening. Multiples of 40 km were chosen to match the *Hinode* SOT/BFI pixel size of 0.55″. Obviously the number of pixels in the sampling window had to be adjusted. However, shape, size, and FWHM = 1200 km of the sampling window were not changed.

The values describing the respective frequency distributions are given in Tab. 2.3. They were computed for areas where the granulation covered the full FOV. However, to visualize the minute changes in the flow maps, we show in Fig. 2.9 only an area of 8 Mm × 8 Mm. In the top row of Fig. 2.9, the flow vectors are superposed on one-hour average G-band images with different image scales. This scene on the Sun is dominated by converging motions toward the X-shaped alignment of G-band bright points. The grid spacing corresponds to 320 km and the length of the arrows was chosen so that an arrow with a length of exactly the grid spacing corresponds to 0.5 km s^{-1}. The differences are so minute that they only

Table 2.4: Summary of LCT results in previous studies.

α [pixel^{-1}]	FWHM	d_{grid}	Δt [s]	ΔT [min]	$\bar{v} \pm \sigma_v$ [km s^{-1}]	v_{med} [km s^{-1}]	v_{max} [km s^{-1}]	**Remarks**
November and Simon (1988) and November (1989)								
0.250″	3.3″	2.0″	67	80	0.5–1.0 (for source regions)			continuum images at λ517.5 nm, Universal Birefringent Filter (UBF), 12 s exposure time, Dunn Solar Telescope/Sacramento Peak
Brandt *et al.* (1988)								
0.035″	2.4″	0.8″	60	79	0.67		1.2	broad-band (5.4 nm) images at λ469.6 nm, Solar Optical Universal Polarimeter (SOUP), 20 ms exposure time, Swedish Solar Vacuum Telescope/Observatorio del Roque de los Muchachos
Title *et al.* (1989)								
0.161″	4.0″	2.5″	60	28	0.37±0.45		$<$1.2	broad-band (100 nm) images at λ600 nm, SOUP, short-exposure images recorded on photographic film, Spacelab 2, provides also proper motion measurements for other FWHM down to 1.0″
Berger *et al.* (1998)								
0.083″	0.83″	0.4″	24	70	1.10 ± 1.30	0.70	$\sim$4.0	G-band images $\lambda 430.5 \pm 0.6$ nm, SOUP, 20 ms exposure time, SVST, LCT parameter study and comparison of proper motions between granulation and network
Shine, Simon, and Hurlburt (2000)								
0.600″	4.8″	2.4″	60	60	0.49	0.47	1.5	continuum images near the Ni I λ676.8 nm line, Michelson Doppler Imager (MDI), Solar Heliospheric Observatory (SoHO), long-duration sequence of 45.5 h

Note: α: image scale, FWHM: width of the sampling window, d_{grid}: grid spacing on which LCT flow vectors are computed, Δt: image cadence, ΔT: time interval over which individual LCT maps are averaged, $\bar{v} \pm \sigma_v$: average flow speed and standard deviation, v_{med}: median value of the frequency distribution, and v_{max}: highest observed flow speed.

show up in difference images of the LCT maps. The bottom row of Fig. 2.9 shows the flow speed at the same color scale as used in all the other figures for each pixel in the FOV. The overall appearance of the flow field is the same. However, the low-resolution maps look blockier owing to the coarser sampling, and some of the fine structure starts to fade out.

In summary, the average velocity diminishes from 0.54 km s^{-1} at the highest spatial resolution to 0.47 km s^{-1} at the lowest resolution. This trend is the same for all other parameters with the exception of kurtosis and skewness. Changes of less than 15% in velocity cannot explain the broad range of velocity values for the horizontal proper motion reported in literature. Note, however, that the *Hinode* data are not susceptible to the adverse affect of seeing, i.e., ground-based LCT measurements will be much more affected the higher the spatial resolution. Even though seeing should not introduce a systematic bias in LCT (see November and Simon, 1988), it will still affect the noise in the LCT measurements.

2.4 Conclusions

Many case studies exist in the literature that describe horizontal proper motions based on LCT or FT techniques. Even though most of them agree on the morphology of the observed flows, significant differences are found when quantifying the flow properties. Besides obvious differences inherent to the techniques, the choice of parameters such as sampling window, time cadence, and duration can significantly impact the outcome. Some results of previous studies are provided in Tab. 2.4 for convenience and to ease the comparison with the present investigation.

We presented the implementation of an LCT algorithm, which was used to create a database of flow maps derived from time-series of G-band images observed with *Hinode*/SOT. The parameter study and error analysis will also be beneficial to other studies using LCT techniques. Even for observations from the ground, our results provide guidance, since LCT techniques are not biased by seeing (see November and Simon, 1988) so that our error estimates can be understood as a lower limit.

Justifying the choice of parameters for LCT and FT algorithms is always a challenging task, which should be driven by the scientific purpose of the study. In the present study, the emphasis was on creating a database of flow maps that can be used in statistical investigations regardless of the type of solar feature, location on the Sun, or solar activity. We summarize our choice of LCT parameters.

- The flow maps are based on time-series of G-band images with cadences Δt between 60 s and 90 s. If the cadence is shorter, features with low velocities cannot be accurately tracked, whereas in longer cadences the features will have evolved too much for the algorithm to recognize them any longer. Our cadence selection is conservative in the sense that we limit our database in favor of better comparability. Note that there is a significant number of G-band time-series with cadences of about 2 min, that are not included in our database.
- The evolution of individual features (granules, bright points, penumbral grains, umbral dots, etc.) dominate flow fields on short time scales. Therefore, averaging over time scales significantly longer than the lifetime of the aforementioned features is necessary to yield the global flow field. Our choice of $\Delta T = 1$ h over which the flow maps are averaged ensures that the global flow fields has emerged from the motions of individual features and that sufficient flow maps were averaged to reduce the numerical rms-errors for magnitude and direction of the flow vectors to reasonable values of 35–70 m s^{-1} and 10–15°, respectively. Note that $\Delta T = 1$ h is not an appropriate choice for studies focusing on meso- and supergranulation because the associated flow pattern is still very noisy and could be more easily perceived in longer time averages. However, long-duration time-series are rare to facilitate these studies. Whenever time-series with longer durations were available, we computed one-hour flow maps with an overlap of 30 min so that the temporal evolution of the flow field can be monitored, which is of particular interest for the investigation of explosive events such as flares, filament eruptions, and coronal mass ejections.
- In principle, the spatial resolution of *Hinode*/SOT would allow one to track features, that are smaller than one second of arc. Our choice of a Gaussian sampling window with 32×32 pixels and a FWHM of 1200 km was again motivated by establishing a database of flow maps for statistical studies. Therefore, we used a FWHM, which corresponds approximately to the size of a granule,

which is one of the ‘largest’ elements of solar fine structures. Tracking flows on larger spatial scales can still be accomplished by smoothing the flow maps after the fact.

In forthcoming studies (e.g., Chapts. 2 and 3), we will use the database of flow maps to study the statistical properties of pores, the motions in sunspot penumbrae, and their relation to the flow pattern observed in the moat of sunspots. Several years of G-band time-series and more than 1000 individual flow maps facilitate the study of these flows during the life cycle of solar features and environment, i.e., as a function of solar activity or the complexity of the surrounding magnetic field. Once thoroughly tested, the value-added *Hinode*/SOT data will be made available as a small project within the scope of GAVO.

Chapter 3

Evaluating Local Correlation Tracking Using CO5BOLD Simulations of Solar Granulation

The interaction of flow and magnetic fields on the solar surface is intimately linked to the ever changing appearance of solar activity. Various techniques were developed to measure photospheric proper motions. November and Simon (1988) introduced the LCT technique to the solar physics community, which was previously developed by Leese, Novak, and Clark (1971) to track cloud motion from geosynchronous satellite data. Since then many variants of the LCT algorithm were used to quantify horizontal flow properties in the solar photosphere and chromosphere. Recently, Verma and Denker (2011) adapted the LCT algorithm to G-band images captured by SOT (Tsuneta *et al.*, 2008) on board the Japanese *Hinode* mission (Kosugi *et al.*, 2007) with the aim to establish a standard method for bulk-processing of such time-series data. Beauregard, Verma, and Denker (2012) modified the same algorithm for continuum images of the *Helioseismic and Magnetic Imager* (HMI, Scherrer *et al.*, 2012) on board SDO (Pesnell, Thompson, and Chamberlin, 2012).

Besides photospheric and chromospheric images, magnetograms are often used to determine horizontal proper motions. Welsch *et al.* (2007) tested and compared various techniques: minimum-energy fitting (MEF, Longcope, 2004), DAVE (Schuck, 2006), Fourier local correlation tracking (FLCT, Welsch *et al.*, 2004), the induction method (IM, Kusano *et al.*, 2002), and induction local correlation tracking (ILCT Welsch *et al.*, 2004). These algorithms were applied to simulated magnetograms using the anelastic MHD code by Lantz and Fan (1999). However, the results were not conclusive, because all methods showed considerable errors in estimating velocities. In general, MEF, FLCT, DAVE, IM, and ILCT lead to similar results with a slightly better performance of DAVE in estimating direction and magnitude of the velocities but the magnetic flux and helicity were recovered better using MEF.

The study by Welsch *et al.* (2007) was extended by Chae and Sakurai (2008), who tested three optical flow methods, i.e., LCT, DAVE, and NAVE (Schuck, 2005), using simulated, synthetic, and *Hinode* magnetograms. NAVE performed well in detecting subpixel, superpixel, and non-uniform motions, whereas LCT had problems in sensing non-uniform motions, and DAVE displayed deficiencies in estimating superpixel motions. However, LCT is the fastest and NAVE the slowest algorithm. Chae and Sakurai (2008) proposed to select smaller sampling windows to get more detailed velocity maps and to lessen the computational demands.

Simulated continuum images (Vögler *et al.*, 2005) were used by Matloch *et al.* (2010) to characterize properties of mesogranulation. However, to the best of our knowledge no systematic study has been carried out based on simulated continuum images to evaluate the reliability, accuracy, and parameter dependence of LCT. In this chapter, we present the results of rigorously testing the LCT algorithm of Verma and Denker (2011) using CO^{5}BOLD simulations of solar convection (Freytag *et al.*, 2012). Ultimately, we want to answer the question, how much of the underlying physics can be captured using optical flow methods.

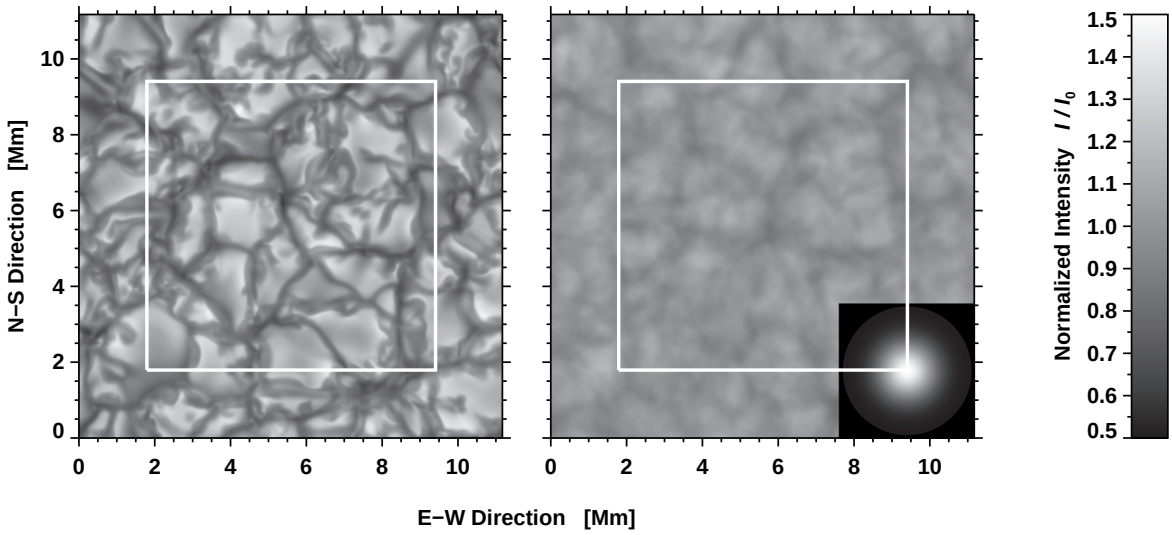

Figure 3.1: First (*left*) and one-hour averaged (*right*) images with 400 × 400 pixels and an image scale of 28 km pixel^{-1} taken from a CO^{5}BOLD time-series of solar granulation. Because of the Gaussian kernels (*inset in the lower right corner*) of 128 × 128 pixels used as sampling windows, the original image size was reduced by 128 pixels. The white squares mark the region with a size of 273 × 273 pixels that remains after the LCT computation.

3.1 CO5BOLD Simulation of Granulation

Radiation hydrodynamic simulations of solar and stellar surface convection have become increasingly realistic producing many of the observed features. The CO^{5}BOLD code (Freytag *et al.*, 2012) offers a unique opportunity to evaluate a previously developed LCT algorithm (Verma and Denker, 2011) and to explore the parameter space for tracking solar fine-structure, in particular for scrutinizing the multi-scale (time and space) nature of solar surface convection. CO^{5}BOLD simulations can be computed for a variety of solar models. The CO^{5}BOLD simulations are non-magnetic, i.e., pure radiation hydrodynamics. Here, the grid dimensions of the simulation are $400 \times 400 \times 165$ and the horizontal cell size is 28 km × 28 km with the vertical grid spacing increasing with depth from 12 km in the photosphere to 28 km in the lower part of the model, resulting in a box with a size of $11.2 \times 11.2 \times 3.1$ Mm^3. Even larger simulation boxes are needed to study convective signatures on larger spatial scales. Matloch *et al.* (2010), for example, extracted characteristic properties of mesogranulation (e.g., size and lifetime) from three-dimensional hydrodynamical simulations (MURaM code, Vögler *et al.*, 2005).

In the first part of this study, we use a time-series of snapshots of the bolometric emergent continuum intensity based on a high-resolution CO^{5}BOLD simulation of granulation. The 140-minute time-series comprises 832 images with a size of 400×400 pixels at a time cadence of $\Delta t = 10$ s. The image scale is 28 km pixel^{-1}. The first image of the time-series is shown in the left panel of Fig. 3.1. The intensity contrast of image is about 15.9%. Taking the average of 360 images (right panel of Fig. 3.1) reduces the contrast to about 5.3% but the appearance of the intensity pattern still remains granular without any indication of long-lived features.

In general, the modulation transfer function (MTF) of the telescope has to be considered when comparing simulated with observed data (Wedemeyer-Böhm and Rouppe van der Voort, 2009). However, we did not convolve the images with the point-spread-function to include the instrumental image degradation, because the fine-structure contents of an image is given by the Fourier phases and not the Fourier amplitudes. Modifying the Fourier amplitudes in granulation images or changing the shape and width of the LCT sampling window are intertwined and could be in principle disentangled but at the cost of complexity. In the second part of the data analysis, we compare the LCT results with the underlying velocity structure of the CO^{5}BOLD simulations. The time cadence of the velocity data is, however, reduced to $\Delta t = 20$ s. To maintain an impartial comparison, all LCT maps were computed first before confronting them with the intrinsic velocity field of the CO^{5}BOLD simulations.

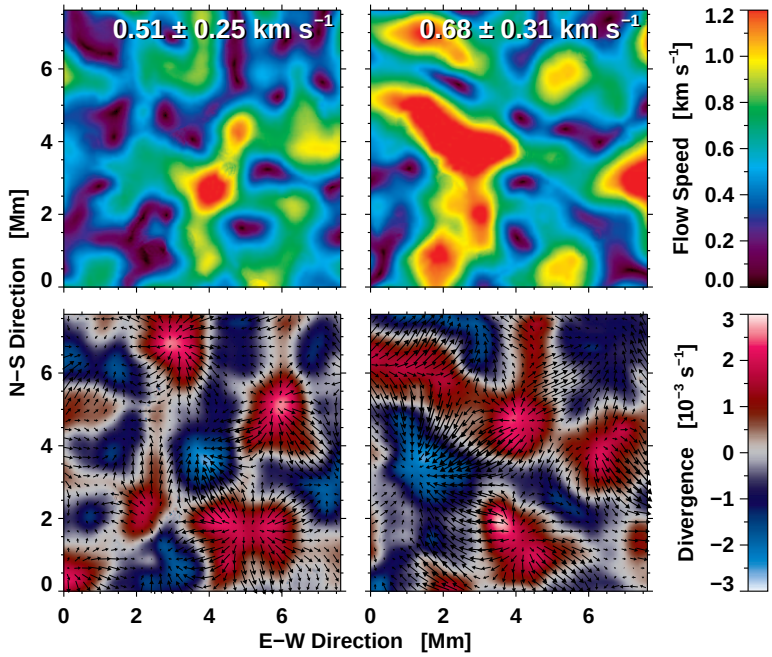

Figure 3.2: Average speed (*top*) and divergence (*bottom*) maps for the first (*left*) and last (*right*) hour of the time-series computed using a time cadence of $\Delta t = 60$ s and a Gaussian sampling window with a FWHM = 1200 km. The direction and magnitude of the horizontal flows are plotted over the divergence maps as arrows, for which a velocity of 0.5 km s^{-1} corresponds to exactly the grid spacing. The values displayed at the top are the mean speed $\bar{v}$ and its standard deviation σ_v for the one-hour averaged flow maps.

3.2 Local Correlation Tracking

Flow maps were computed using the LCT algorithm described in Verma and Denker (2011) but initial image alignment, subsonic filtering, and geometric correction were excluded. An important difference between the *Hinode* and CO^{5}BOLD data is the image scale of 80 and 28 km pixel^{-1}, respectively. Sampling windows and filter kernels of 32×32 pixels were the choice for processing *Hinode* G-band images because the computation time should be kept to a minimum for bulk-processing of time-series data. However, for this study we opted for sizes of 128×128 pixels to adapt to the higher spatial resolution of the simulated granulation images and to extend our parameter study to include broader sampling windows. The drawback is of course a much increased computation time. In principle, smaller sampling windows could have been chosen for smaller FWHM but for consistency, we decided not to change window or kernel sizes. In a direct comparison with the previous work of Verma and Denker (2011), these small differences are of no concern.

A 128×128-pixel Gaussian kernel with a FWHM = 1200 km is shown as an illustration in the lower-right corner of the right panel in Fig. 3.1. If not otherwise noted, this kernel is used as a high-pass filter, even though this is not strictly necessary in the absence of strong intensity gradients (e.g., umbra-penumbra or granulation-penumbra boundaries) and gentler slopes introduced by the limb darkening. Because of such sampling windows and kernels the size of the computed LCT maps was reduced to 273×273 pixels from the 400×400 pixels of the original images, which is indicated in Fig. 3.1 by white square boxes.

3.3 Results

3.3.1 Persistent Flows and the Duration of Time Averages

One application of LCT techniques is to uncover persistent horizontal proper motions. The imprint of solar convection results in a photospheric flow field with different spatial scales: granulation 1–2 Mm, mesogranulation 3–10 Mm, and supergranulation ∼30 Mm (Muller *et al.*, 1992). The LCT method recovers the corresponding flow features from time-series of photospheric images. This raises the question, if similar signatures are present in the simulated time-series of granulation.

In Fig. 3.2, we computed flow (top row) and divergence (bottom row) maps for the first (left column) and last (right column) hour of the time-series. We chose a time cadence of $\Delta t = 60$ s and a Gaussian sampling window with a FWHM = 1200 km and then averaged the individual flow maps over $\Delta T = 1$ h to facilitate easier comparison with the study of Verma and Denker (2011). This choice of input parameters

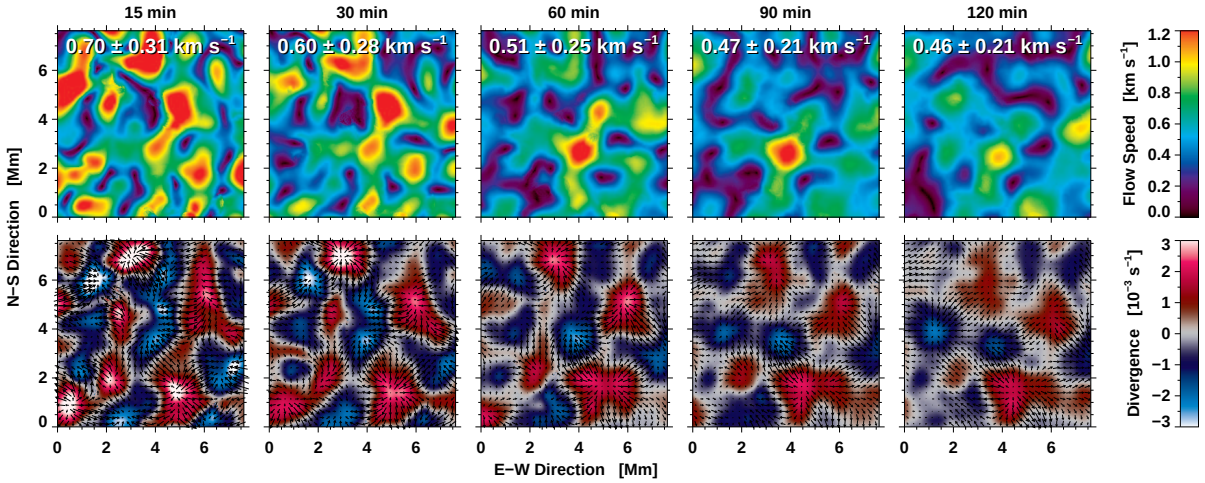

Figure 3.3: Speed (*top*) and divergence (*bottom*) maps averaged over time intervals of $\Delta T = 15$–120 min. The LCT maps were computed using a time cadence of $\Delta t = 60$ s and a Gaussian sampling window with a FWHM = 1200 km.

produced the most reliable results when previously applied to *Hinode* G-band images. The mean speeds $\bar{v}$ and their standard deviations σ_v are 0.51 ± 0.20 km s^{-1} and 0.68 ± 0.31 km s^{-1} for the first and last hour, respectively. The mean speed in the later case is higher by 33% because of a large structure with high velocities in the top-left quarter of the flow map. The divergence of a flow field with velocity components (v_x, v_y) is computed as $\nabla \cdot \mathbf{v} = \partial v_x/\partial \mathbf{x} + \partial v_y/\partial \mathbf{y}$. On average the divergence values are two times higher than the ones for *Hinode* G-band images discussed in Verma and Denker (2011). The superimposed flow vectors clearly indicate the locations of the diverging and converging flows.

Neither the two flow nor the two divergence maps bear any resemblance to another suggesting that after about one hour persistent flow features are no longer present in the CO^{5}BOLD time-series. The absence of meso- or supergranular features is, however, expected considering both the horizontal dimensions and the depth of the simulation box. Interestingly, strong flow features will still be present even after averaging for one hour, which points to the necessity of longer time-series for assessing convective flow properties on larger spatial scales.

The time dependence of the average flow field is depicted in Fig. 3.3 along with the corresponding divergence maps. These maps were computed with the same input parameters as in Fig. 3.2 but in this case with different time intervals $\Delta T = 15$–120 min over which the individual flow maps were averaged. Proper motions of single granules are well captured when flow maps are averaged over $\Delta T = 15$ and 30 min, which is evident from the speed maps containing mostly features of typical granular size. However, contributions to the flow field from separate granules are averaged out over longer time intervals ΔT, but some long-lived features might survive the averaging process. Most notably, a high-velocity feature with negative divergence (converging flows) remains in the central part of the maps. It first appears at 15 min as an appendage to a stronger flow kernel, then separates from the kernel (30–60 min), before becoming the only strong flow kernel at 90 min, and fading away after about 120 min. This behavior resembles flow patterns encountered at the vertices of supergranular cells. However, in real observations the lifetime of such a flow kernel with converging horizontal motions is much longer. Despite the tendency of lower divergence values for increasing ΔT, the divergence values are still significantly higher than the values given by Verma and Denker (2011).

The more than 30% decrease of the average flow speed from 0.70 km s^{-1} in the 15-minute map to 0.46 km s^{-1} in the 120-minute map is of the same order as the 25% difference found for the two one-hour averaged flow maps in Fig. 3.2. Furthermore, the extended flow feature in the right panel of Fig. 3.2 is absent in the 120-minute map of Fig. 3.3 pointing to the importance of the vectorial summation (constructive and destructive) of the individual flow maps. Taken together, both facts serve as a reminder that we must treat the mean speed values of different sequences with caution when comparing them. In addition, the large variance of reported speed values in literature might also have its origin in the stochastic nature of granulation and not only in the choice of LCT input parameters. In the following, only data for the first hour of the time-series were analyzed.

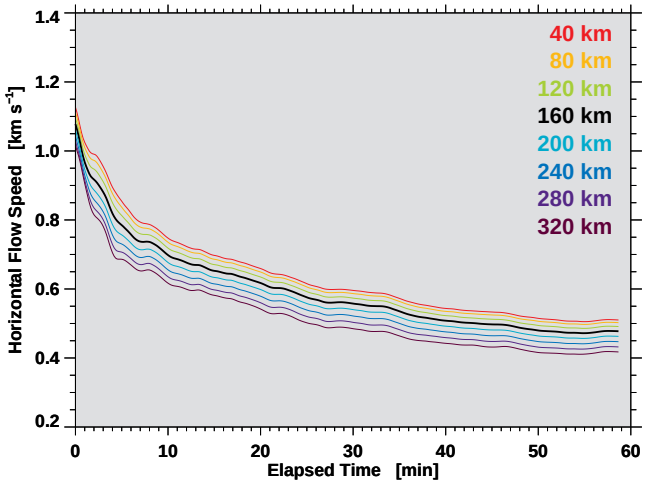

Figure 3.4: Average horizontal flow speed as a function of the elapsed time. The maps were computed using a Gaussian sampling window with a FWHM = 1200 km and time cadence $\Delta t = 60$ s. Before computing the cross-correlations, the images were convolved with a Gaussian kernel FWHM = 40–320 km to degrade the spatial resolution of the images. The increasing FWHM values are presented in rainbow colors. The black solid line is used to depict result for the FWHM = 160 km, which is the typical spatial resolution of most *Hinode* G-band images (see Verma and Denker, 2011).

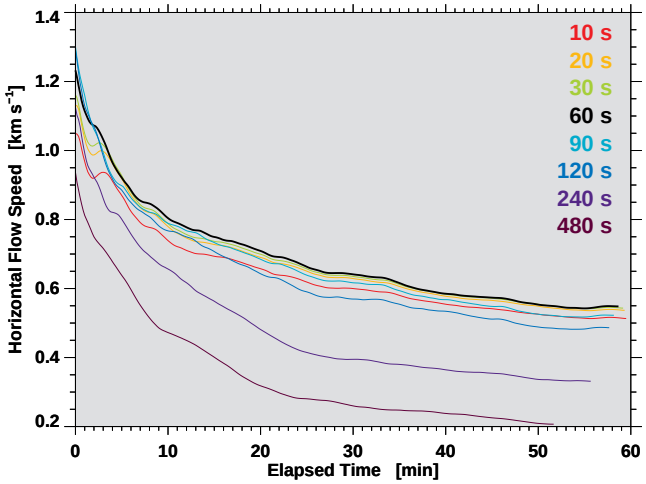

Figure 3.5: Average horizontal flow speed as a function of the elapsed time. The maps were computed using a Gaussian sampling window with a FWHM = 1200 km and time cadence $\Delta t = 10$–480 s. The increasing time cadences Δt are presented in rainbow colors. The black solid line is depicting the result for the time cadence $\Delta t = 60$ s, which has been identified in Verma and Denker (2011) as an optimal choice for tracking horizontal proper motions in *Hinode* G-band time-series data.

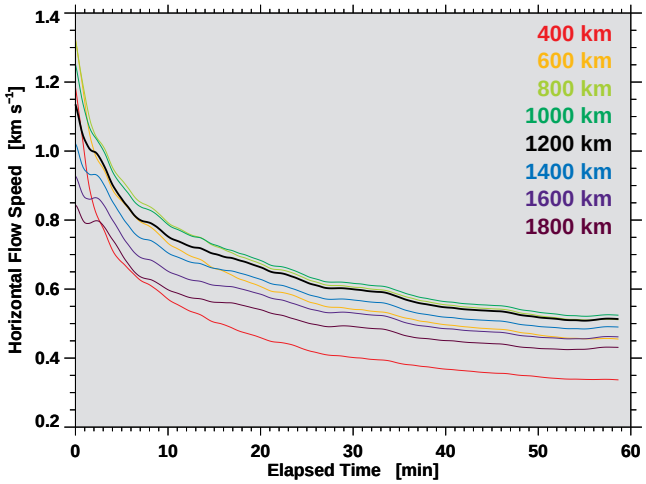

Figure 3.6: Average horizontal flow speed as a function of the elapsed time. The maps were computed using a time cadence $\Delta t = 60$ s and Gaussian sampling window with various FWHM = 400–1800 km. The increasing FWHM values are presented in rainbow colors. The black solid line is used to depict the result for a Gaussian sampling window with a FWHM = 1200 km, which has been identified in Verma and Denker (2011) as an optimal choice for tracking horizontal proper motions in *Hinode* G-band time-series data.

3.3.2 Convergence Properties of the Mean Flow Speeds

Hinode is the most prolific data source for high-resolution solar images, and G-band images with 2×2-pixel binning and an image scale of about 80 km pixel^{-1} are the most common image type. Hence, the LCT algorithm of Verma and Denker (2011) was developed for bulk-processing of these images leading to an optimal set of LCT input parameters: time cadence $\Delta t = 60$–90 s, Gaussian sampling window with a FWHM = 1200 km, and averaging time $\Delta T = 1$ h. Beauregard, Verma, and Denker (2012) showed that this algorithm is easily adaptable to images with a coarser spatial sampling, e.g., continuum images of the SDO/HMI. In the following, we use CO^{5}BOLD simulation data to cross-check the aforementioned input parameters.

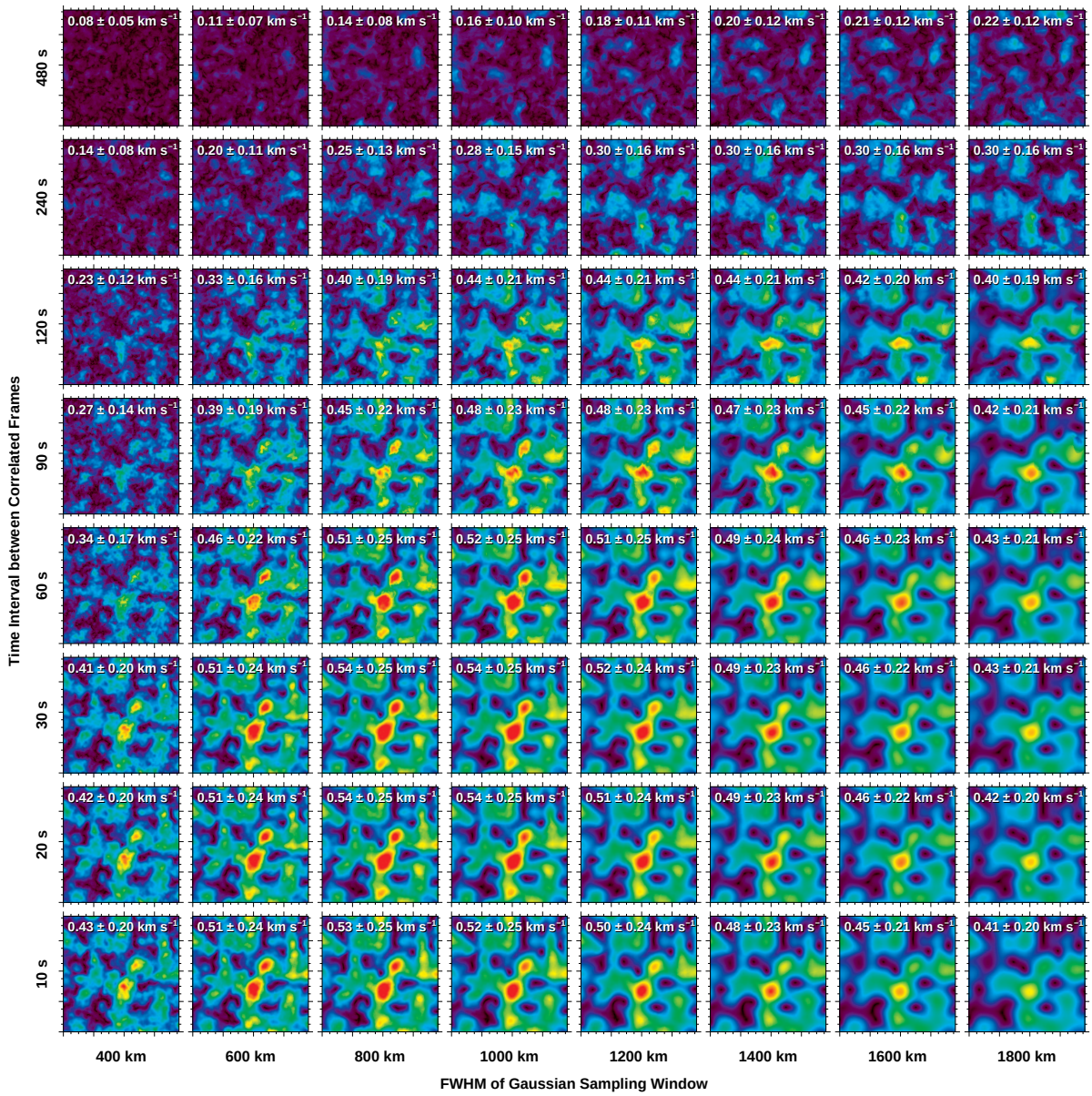

Figure 3.7: Horizontal flow speed maps (one-hour averages) computed with time cadences $\Delta t = 10$–480 s (*bottom to top*) and Gaussian kernels with a FWHM = 400–1800 km (*left to right*). Displayed at the top of the panels are the mean speed $\bar{v}$ and its standard deviation σ_v averaged over the FOV. The speed maps are scaled between 0.0–1.2 km s^{-1}, which corresponds to the scale used in Figs. 3.2 and 3.3. Axes are in megameters with the major tickmarks separated by 2 Mm.

First, to study the effects of spatial resolution, we degraded the original images with an image scale of 28 km pixel^{-1} by convolving them with Gaussian kernels of FWHM = 40–320 km but without correcting the telescope's MTF (cf., Wedemeyer-Böhm and Rouppe van der Voort, 2009). We computed the mean horizontal flow speed as a function of the elapsed time (see Fig. 3.4). This time corresponds to the number of flow maps averaged. These temporal averages were carried out up to $\Delta T = 1$ h. The Gaussian sampling window with a FWHM = 1200 km and time cadence $\Delta t = 60$ s were kept constant. Rainbow colors from red to violet indicate increasingly larger FWHM. The black curve (FWHM = 160 km) corresponds to the spatial resolution of the *Hinode* G-band images. The diffraction-limited resolution of the 0.5-meter *Hinode*/SOT according to the Rayleigh criterion is $1.22 \cdot \lambda / D = 0.22''$ at λ430 nm or 160 km on the solar surface. Therefore, even with 2×2-binning, *Hinode* G-band images are still critically sampled (Nyquist theorem). In the following, we use v_{28} to indicate velocities, which were derived from the full-resolution simulated images, while v_{80} refers to velocities refers to velocities based on smoothed simulated images, which provide the link to G-band images (see Verma and Denker, 2011).

It takes about 5–10 min before the slope of the curves changes, and after 15–20 min the curves level out and approach an asymptotic value. Changing the slope is directly related to the lifetime of individual

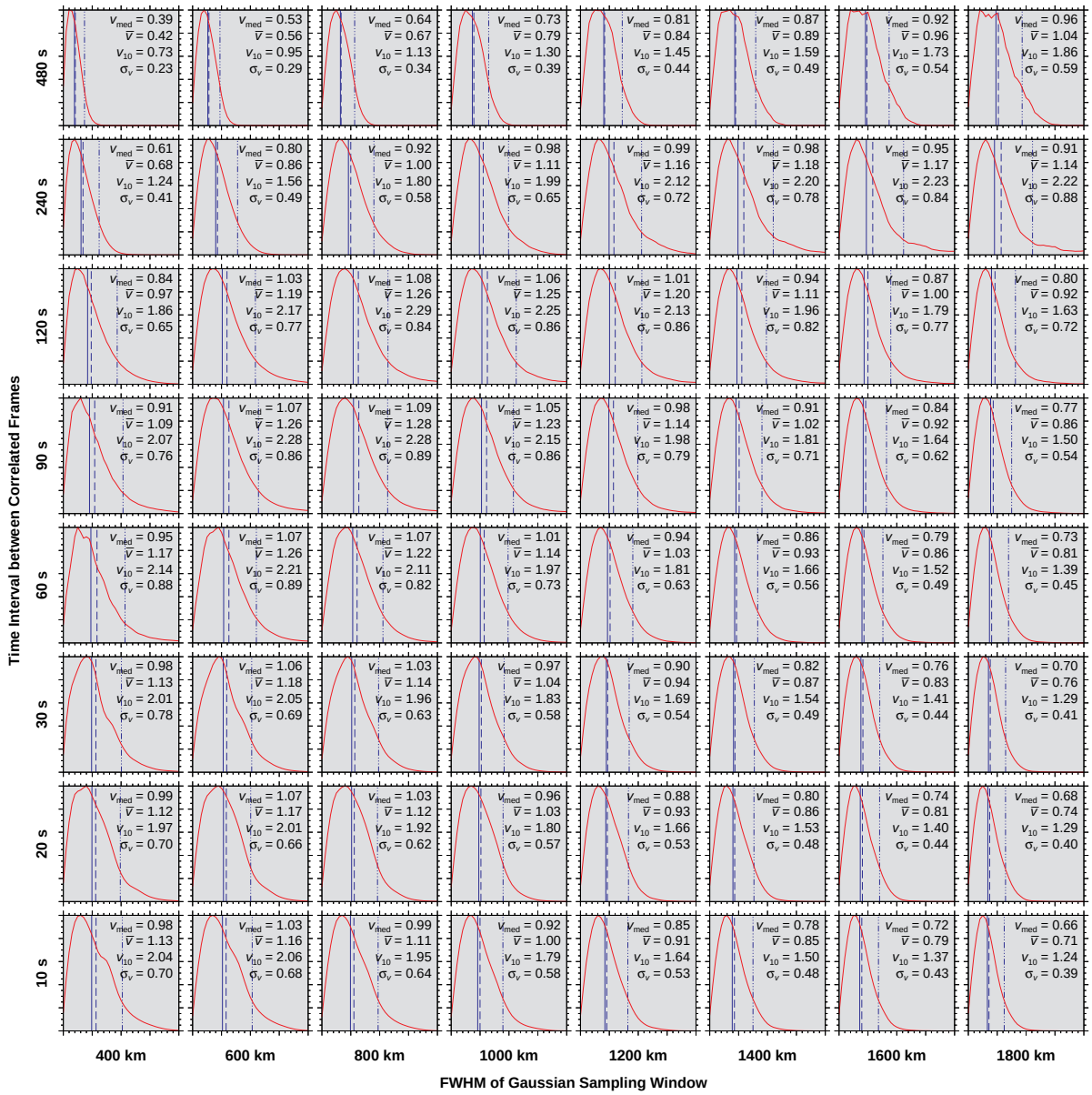

Figure 3.8: Relative frequency distributions of horizontal flow speeds computed with time cadences $\Delta t = 10$–480 s (*bottom to top*) and Gaussian sampling windows with a FWHM = 400–1800 km (*left to right*). The three vertical lines mark the position of median $v_{\rm med}$ (*solid*), mean $\overline{v}$ (*long-dashed*), and 10$^{\rm th}$ percentile v_{10} (*dash-dotted*) values of speed. The frequency distributions were normalized such that the modal values correspond to unity, i.e., major tickmarks are separated by 0.2 on the ordinate. The speed distributions cover the range 0.0–4.0 km s^{-1}, i.e., major tickmarks are separated by 1.0 km s^{-1} on the abscissae.

granules, and it takes several lifetimes to reveal any longer-lasting flow features. In addition, all the curves are stacked on top of each other without crossing any other curve at any point. The mean flow speed decreases monotonically by about 0.1 km s^{-1} when reducing the FWHM of the Gaussian filter kernel from 40 to 320 km. Evidently, in images with high spatial resolution, the LCT algorithm picks up fine-structure such as the corrugated boundaries of granules, fragments of exploding granules, and the occasional bright points. These feature have either intrinsically higher speeds or high contrasts, thus biasing the cross-correlation algorithm to higher velocities.

Second, we change the time cadences in the range of $\Delta t = 10$–480 s while keeping the FWHM = 1200 km of the Gaussian sampling window and the spatial resolution of 28 km pixel^{-1} constant (see Fig. 3.5). Again, rainbow colors from red to violet indicate longer time cadences. The black curve corresponds to the optimal LCT parameter $\Delta t = 60$ s for G-band images. This curve exhibits the highest mean speed except for very short averaging times. For shorter time cadences $\Delta t = 10$–30 s, the mean velocity profiles differ only slightly and monotonically approach the 60-second profile. Starting already with the 90-second profile, the mean velocities drastically drop. If the time cadence is too short, then granules

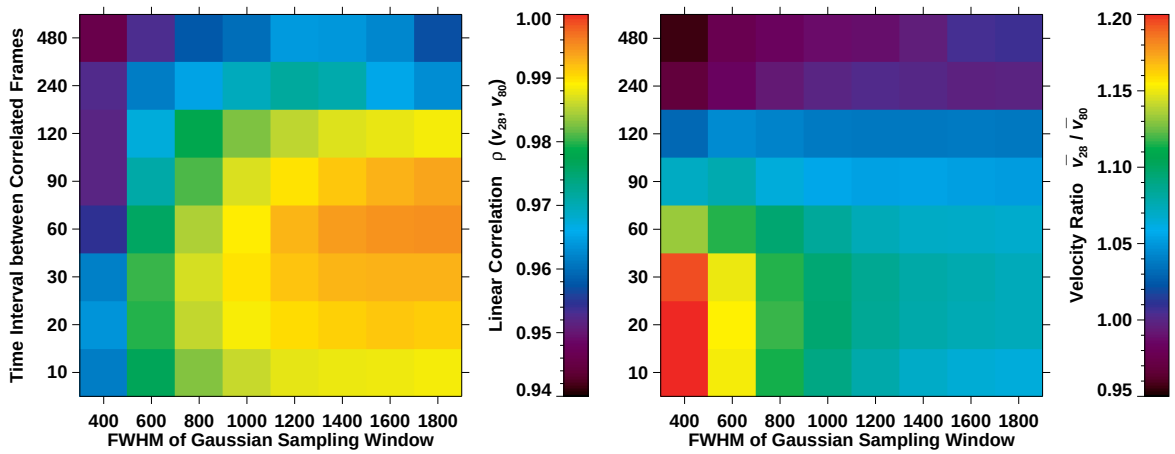

Figure 3.9: Correlation $\rho(v_{28}, v_{80})$ (*left*) and mean velocity ratio v_{28}/v_{80} (*right*) between the flow maps computed from full-resolution images (v_{28}) and from images convolved with a Gaussian of FWHM = 160 km (v_{80}) to match the spatial resolution of *Hinode* G-band images. For both cases, flow maps were computed with time cadence Δt = 10–480 s and Gaussian sampling windows with a FWHM = 400–1800 km, shown here as 8×8 square blocks.

have not evolved sufficiently to provide a strong cross-correlation signal. If, on the other hand, the time cadence becomes too long, then granules have either evolved too much or completely disappeared so that their horizontal proper motions are no longer properly measured. Already a time cadence of $\Delta t = 90$ s is a compromise, but many G-band time-series are acquired with more than 60 s between successive images. These findings are consistent with a similar parameter study for *Hinode* G-band images (see Fig. 3 of Verma and Denker, 2011) and independently corroborate that the CO^{5}BOLD simulation reproduces essential flow characteristics of solar granulation.

Third, the last important input parameter is the FWHM of the Gaussian sampling window, which was adjusted in the range from 400 to 1800 km (see Fig. 3.6), while maintaining a constant time cadence (Δt = 60 s) and image scale (28 km pixel^{-1}). The reference profile (FWHM = 1200 km) is once more shown as a black curve. Interestingly, profiles with small FWHM = 400 and 600 km start at high velocities, then quickly drop, while intersecting all other profiles. These sampling windows track fine-structures with high velocities but the lack of large, coherent structures (i.e., at least one entire granule) rapidly diminishes the mean flow speed. The highest flow speeds in the asymptotic part of the mean speed profiles are found for FWHM = 800 and 1000 km. These profiles are very similar but cut across each other at an averaging time of $\Delta T \approx 14$ min. Starting at a FWHM = 1200 km, the mean speed profiles are again systematically arranged without any intersection. Once the sampling window is sufficiently large to encompass several granules, their stochastic motions tend to reduce the average flow speed.

In summary, the mean speed profiles in Figs. 3.4, 3.5, and 3.6 confirm that for an image scale of 80 km pixel^{-1} the LCT input parameters (averaging time $\Delta T = 1$ h, time cadence $\Delta t = 60$ s, and a Gaussian sampling window with a FWHM = 1200 km) are indeed a very good choice to derive horizontal proper motions from *Hinode* G-band images.

3.3.3 Morphology of Flow Maps and Frequency Distributions of Flow Speeds

Two-dimensional maps of the flow speed offer another approach to evaluate the influence of the LCT input parameters. In Fig. 3.7, we compiled 8×8 one-hour averaged speed maps for time cadences of Δt = 10–480 s and Gaussian sampling windows with a FWHM = 400–1800 km. Mean and standard deviation of the flow speed are given at the top of each panel. This 8×8 matrix of flow maps facilitates an easy visual comparison of flow features.

Narrow sampling windows track only small-scale features such as the corrugated borders of granules, fragmenting granules, and bright points. The flow speeds are significantly diminished for a FWHM = 400 km indicating that narrow sampling windows miss an important part of the horizontal proper motions related to granules. If small-scale features are short-lived or travel fast, significant velocity contributions are only expected for short time-cadences. Already at a time cadence $\Delta t = 60$ s corresponding velocity

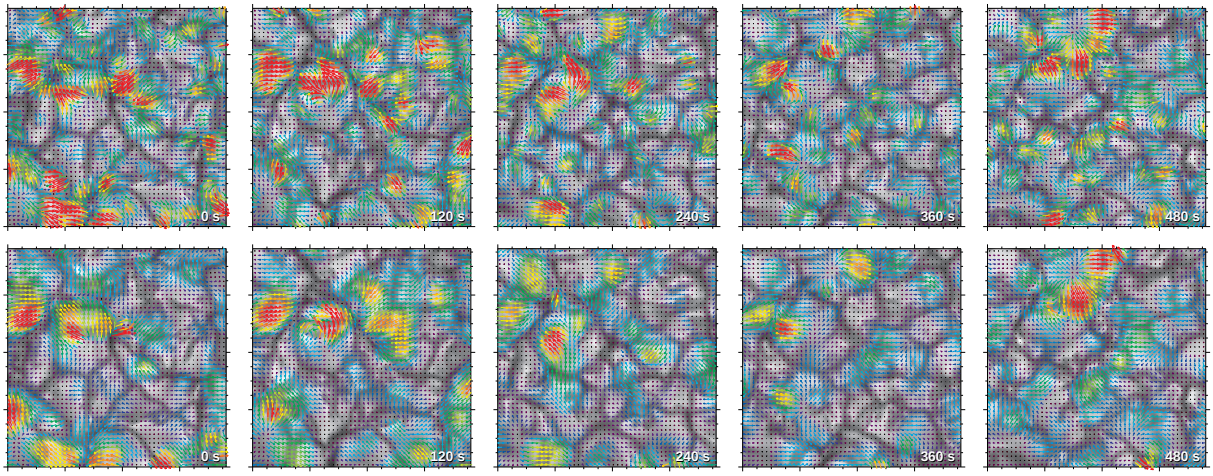

Figure 3.10: Temporal evolution of flow fields for different time intervals between successive images and sampling window sizes: $\Delta t = 20$ s and FWHM $= 600$ km (*top*) and $\Delta t = 60$ s and FWHM $= 1200$ km (*bottom*). The time stamp in the lower right corner indicates the time, which has elapsed since the beginning of the time-series. The original flow maps were derived from just one pair of correlated images per time step. These maps with 273×273 pixels were then resampled to 50×50 pixels before applying a sliding average over the leading and trailing four flow maps. Speed and direction of the horizontal proper motions are given by rainbow-colored arrows (dark blue corresponds to speeds lower than 0.2 km s^{-1} and red to larger than 2.0 km s^{-1}), which were superposed on the corresponding gray-scale intensity images of the CO^{5}BOLD simulation. Major tickmarks are separated by 2 Mm.

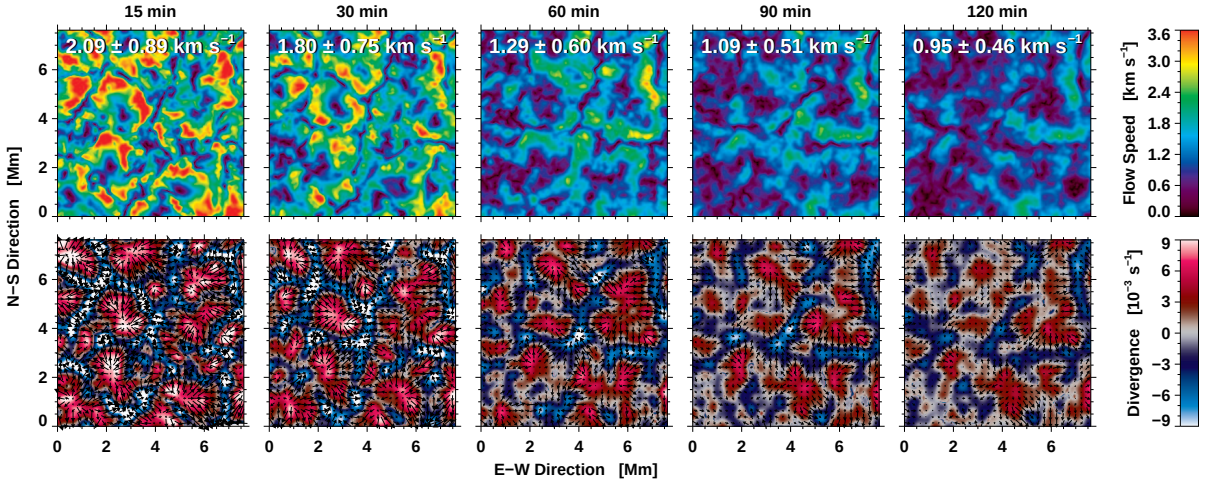

Figure 3.11: Speed (*top*) and divergence (*bottom*) maps averaged over time intervals of $\Delta T = 15$–120 min of the horizontal plasma velocities corresponding to an optical depth of $\log \tau = 0$. The speed and divergence values are larger roughly by a factor of three as compared to Fig. 3.3.

signals have vanished. The same argument related to the lifetime of granules holds for the longest time cadence that we examined on all spatial scales. At $\Delta t = 480$ s, granules have evolved too much to leave a meaningful cross-correlation signal.

Wider sampling windows with short time cadences ($\Delta t = 20$–30 s) start to show higher velocities for a FWHM $= 600$–1200 km. As the FWHM increases, the flow maps become smoother, and the flow speed starts to decrease. Broader sampling windows contain more small-scale features exhibiting jumbled proper motions, and also the number of enclosed granules increases, which results in weaker flows. Similar results were found for *Hinode* G-band images (see Fig. 4 and Sect. 4.4 in Verma and Denker, 2011). For higher time cadences $\Delta t = 120$–240 s, the overall appearance of the flow maps has not changed but the flow speeds are now much lower reflecting the lifetime (5–10 min) of solar granulation.

Based on the high resolution images of the CO^{5}BOLD simulations with an image scale of 28 km pixel^{-1}, the "sweet-spot" with the highest flow speeds is found for LCT input parameters $\Delta t = 20$–30 s and FWHM $= 800$–1000 km. The parameter pair $\Delta t = 60$ s and FWHM $= 1200$ km yields slightly lower

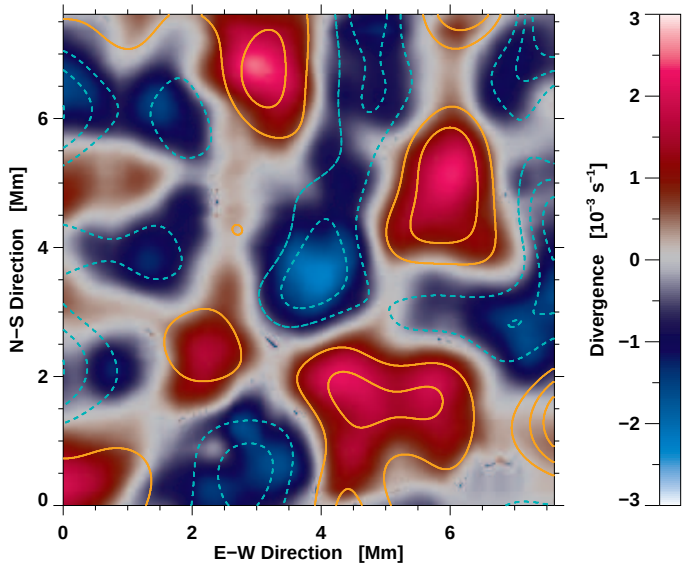

Figure 3.12: LCT divergence map computed for input parameters: image scale 80 km pixel^{-1}, time cadence $\Delta t = 60$ s, Gaussian sampling window with a FWHM = 1200 km, and averaging time $\Delta T = 1$ h. Overplotted are the contours of the corresponding one-hour averaged divergence of the actual flow velocity smoothed by a Gaussian with a FWHM = 1266 km. Orange (*solid*) and blue (*dashed*) lines indicate positive and negative (± 1, ± 2 and $\pm 3 \times 10^{-3}$ s^{-1}) divergence, respectively.

flow speeds but the corresponding flow maps are virtually identical to the ones within the sweet-spot. Considering the lower spatial resolution (image scale of 80 km pixel^{-1}) of *Hinode* G-band images and the typical cadences of time-series of $\Delta t = 60$ s or slightly more, the above parameter pair is still a very good selection.

The frequency distributions in Fig. 3.8 correspond to the 8×8 flow maps shown in Fig. 3.7. However, the flow speeds were derived from individual flow maps, i.e., the flow vectors were not averaged before computing the frequency distributions. This approach might not be suitable for observational data, which are not free from telescope jitter and seeing. Thus, only contributions from numerical errors of the LCT method will affect flow maps based on simulated data.

Apart from the distributions, we calculated median v_{med}, mean $\bar{v}$, 10$^{\mathrm{th}}$ percentile v_{10}, and the standard deviation σ_v of the speed. The first three values are depicted in each panel as solid, long-dashed, and dash-dotted vertical lines, respectively. All the values describing the frequency distribution are significantly higher than the ones displayed in Fig. 3.7, because they were obtained from individual flow maps and not the one-hour averaged data. The first and second moments of the distributions follow the trend already discussed above for Fig. 3.7. A high-velocity tail (parametrized by v_{10}) and a positive skewness is found for all distributions, likewise $\bar{v}$ is always larger than v_{med}.

Each frequency distribution is comprised of more than 25 million flow vectors and no smoothing was applied. Thus, not only their overall shape but also the minute detail is significant. Small ripples become visible around the maximum of the distributions for $\Delta t = 480$ s and a FWHM ≥ 1200 km suggesting that the initial feature is no longer tracked. Furthermore, the high-velocity tail has vanished in all distributions with the longest time cadence. Another interesting feature is the shoulder at the high-velocity side of the distributions for short time cadences and narrow sampling windows, which hints at a contribution from smaller features with higher velocities. Exploding or fragmenting granules and bright points, thus, might have a different velocity spectrum distinguishing them from regular granules.

In summary, Figs. 3.7 and 3.8 can also be taken as a point of reference for many other LCT studies with various input parameters, hopefully providing a more cohesive description of horizontal proper motions in the photosphere and chromosphere, or where ever time-series of images are available.

As a corollary to the above parameter study, we repeated the LCT measurements but now with smoothed simulation data (Gaussian kernel with a FWHM = 160 km) to have the same spatial resolution (image scale of 80 km pixel^{-1}) as *Hinode* G-band images. In Fig. 3.9, we use the linear correlation coefficient $\rho(v_{28}, v_{80})$ and the ratio of the velocities v_{28}/v_{80} for both image scales to quantify how a coarser spatial resolution affects the flow maps. The correlation coefficients are lowest for narrow sampling windows (FWHM = 400 km) and long time cadences $\Delta \geq 240$ s because much of the fine structure (with high velocities) has been blurred. The highest correlations are found for FWHM ≥ 1200 km and $\Delta t = 20$–90 s. Only a very small deviation of less than 0.001 from a perfect correlation is observed for the LCT input parameters chosen in Verma and Denker (2011).

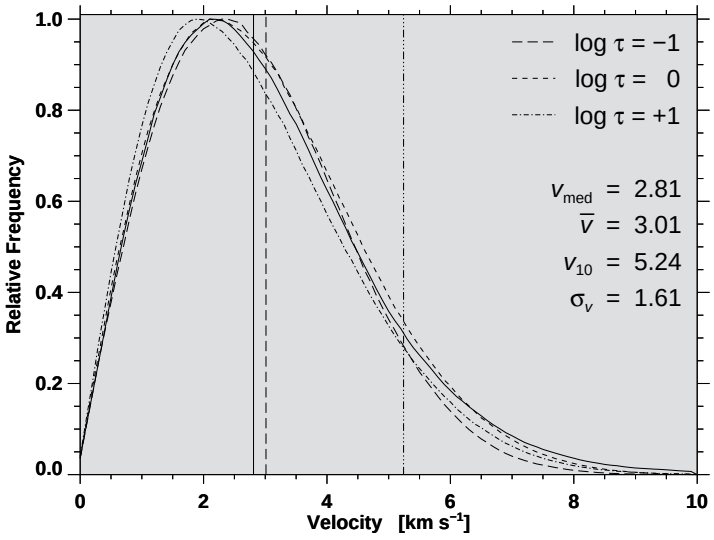

Figure 3.13: Relative frequency distributions for the horizontal plasma velocities corresponding to different optical depths of $\log\tau = -1$, 0, and $+1$, which are depicted as long-dashed, dashed, and dash-dotted curves, respectively. The three vertical lines mark the position of median $v_{\rm med}$ (*solid*), mean $\bar{v}$ (*long-dashed*), and $10^{\rm th}$ percentile v_{10} (*dash-dotted*) values of speed at an optical depth of $\log\tau = 0$. A frequency distribution (*solid*) for LCT flow velocities was stretched by a factor of about three so that the root-mean-square deviation from the profile with $\log\tau = 0$ was minimal. The LCT input parameters were image scale 80 km pixel^{-1}, time cadence $\Delta t = 60$ s, and a Gaussian sampling window with a FWHM = 1200 km.

The right panel in Fig. 3.9 demonstrates that flow speeds could be underestimated by as much as 8% in the case of G-band images (neglecting so far the comparison with the plasma velocities in Sect. 3.3.5). However, such strong deviations are only observed for very narrow sampling windows and very short time cadences. In general, the velocities in both cases differ by less than 2%. Interestingly, if the time cadence is high, then there are not many traceable features left in the sampling window, but by additional smoothing, more coherent features are created that are long-lived, which explains the slightly higher velocities v_{80} for G-band images in the $\Delta t = 240$–400 s range. Considering that HMI continuum images have an image scale of about 360 km pixel^{-1} and a cadence of $\Delta t = 45$ s, broad sampling windows (FWHM $\geq$ 1600 km) might be needed to build up a reliable cross-correlation signal. Even though the flow speeds might be underestimated by 10–20% as compared to high-resolution simulation data (see Figs. 3.7 and 3.8), the overall morphology of the flow field will still be reliably recovered with correlation coefficients close to unity (see top panel of Fig. 3.9). This was also demonstrated by Beauregard, Verma, and Denker (2012) for complex flows along the magnetic neutral line of active region NOAA 11158 at the time of an X2.2 flare.

3.3.4 Dynamics of Horizontal Proper Motions

Besides quantifying persistent flow fields, LCT techniques can also capture the dynamics of horizontal proper motions. In Fig. 3.10, we compare snapshots from two movies with two different sets of LCT input parameters: $\Delta t = 20$ s and FWHM = 600 km (top row) and $\Delta t = 60$ s and FWHM = 1200 km (bottom row). The snapshots are separated by 120 s in time and show the continuum intensity with a 50×50 grid of superposed, color-coded flow vectors. The flow maps were smoothed both in space (5×5-pixel neighborhood) and time (sliding average of nine individual flow maps). These values were chosen such that watching the movies leaves a smooth and continuous visual impression. Less smoothing will result in jittering arrows in some places. We counterpoint the narrow sampling window/high cadence case with our typical choice of LCT input parameters. In the first case, much higher flow speeds are apparent, and the flow vectors in regions with high flow speeds show indications of vortex or twisting motions, which are absent in the latter case, where the flow vectors are more uniformly arranged. Comparing the flow fields at 0 s and 360 s clearly demonstrates that periods with many strong flow kernels are followed by much quieter flow fields. The high flow speeds have their origin in the borders of rapidly expanding or fragmenting granules.

3.3.5 Comparison with Plasma Velocities

The actual plasma velocities are given for three optical depths $\log\tau = -1$, 0, and $+1$. The time dependence of the average flow field along with the corresponding divergence maps are depicted in Fig. 3.11 for plasma velocities at a depth of $\log\tau = 0$. Both speed and divergence values are higher by a factor of two to three as compared to the maps in Fig. 3.3. The highest factor between average LCT and

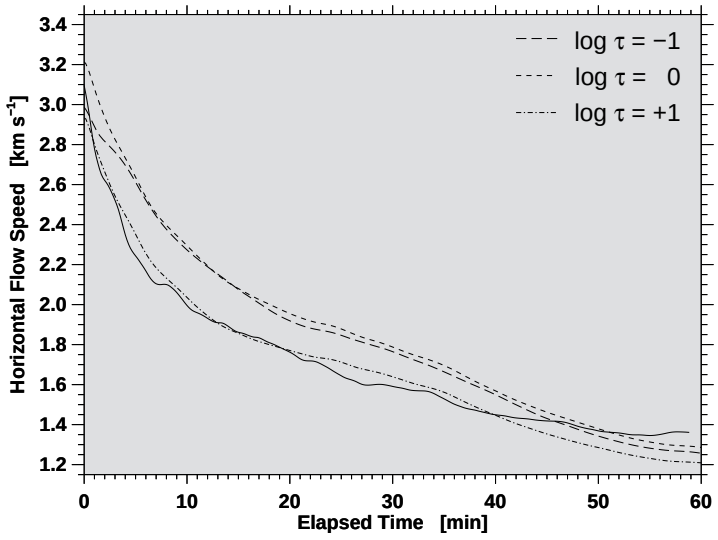

Figure 3.14: Average horizontal flow speeds as a function of the elapsed time for the horizontal plasma velocities corresponding to optical depths of $\log\tau = -1$, 0, and $+1$ are depicted as long-dashed, dashed, and dash-dotted curves, respectively. The solid curve, as in Fig. 3.13, has to be multiplied by a factor of three to match the profile for $\log\tau = +1$.

plasma velocities is encountered for shorter time averages. For averaging times of $\Delta T = 15$–30 min, the speed maps exhibit more fast-moving, small-scale features associated with the boundaries of expanding or fragmenting granules. Increasing the averaging time results in smoother speed maps with much reduced speed values. By visually comparing Figs. 3.3 and 3.11, it becomes apparent that significant spatial smoothing has to be applied to the speed and divergence maps of the plasma velocities. This is a direct consequence of the sampling windows employed in LCT.

Figure 3.12 shows the divergence map for LCT flow fields computed for a one-hour time-series of images, which were smoothed to match the spatial resolution of *Hinode* G-band images, a time cadence of $\Delta t = 60$ s, and a Gaussian sampling window with a FWHM = 1200 km. We overplotted the divergence of the actual flow velocity from an optical depth of $\log\tau = 0$ averaged over one hour and smoothed it with a Gaussian kernel with a FWHM = 1266 km. The size of the smoothing kernel was chosen such that linear correlation between the LCT and plasma maps was maximized (ρ =0.90). The position of positive and negative divergence corresponding to the plasma flows roughly matches with the LCT divergence extrema. Even though the correlation between LCT and plasma divergence maps is significant (once properly smoothed), there are still morphological differences not to mention the drastic difference in the absolute values of speed and divergence. In general, our findings are in good agreement with Matloch *et al.* (2010), e.g., their Fig. 2, but the lack of a more quantitative description prevents us from a more detailed comparison. In Fig. 3.9, we found a negligible dependence of the LCT results on the image scale (28 vs. 80 km pixel^{-1}) or in this context equivalently the spatial resolution. Hence, for the further discussion, we use G-band-type LCT flow maps.

The frequency distributions of the actual plasma velocities are shown in Fig. 3.13. The distributions are assembled from the 180 velocity maps covering about one-hour. The mode of the distributions is shifted to higher velocities for higher atmospheric layers. For comparison, we show the LCT-based velocity distribution. The LCT input parameters were a time cadence of $\Delta t = 60$ s and a Gaussian sampling window with a FWHM = 1200 km. Similar to Fig. 3.8, the flow speeds were derived from the individual flow maps, i.e., the flow vectors were not averaged before computing the frequency distributions. The stretched LCT and actual velocity distributions have very similar shapes. We scaled the LCT frequency distribution by the factor of ≈ 3.01 in velocity to match it with the distributions for the actual plasma velocities. For an optical depth of $\log\tau = 0$, it had the lowest χ^2-error. However, the differences in the χ^2-error for all three optical depth are not significant.

In Figure 3.14, we plotted the mean flow speed as a function of elapsed time for the actual plasma velocities at optical depths $\tau = -1$, 0, and $+1$. We overplotted the same relation for the LCT-computed flow speed. This curve was scaled by a factor of ≈ 2.85 to match it with the curve for optical depth $\log\tau = +1$ as it had the lowest χ^2-error. The profiles for plasma and scaled LCT velocities are very similar up to about 40 min, when the LCT velocities level out at higher velocities, which can be attributed to the LCT method rather than a physical cause. However, the fact that the curves track each other for the first 40 min is a strong indicator that LCT reliably detects the time-dependence of the actual plasma

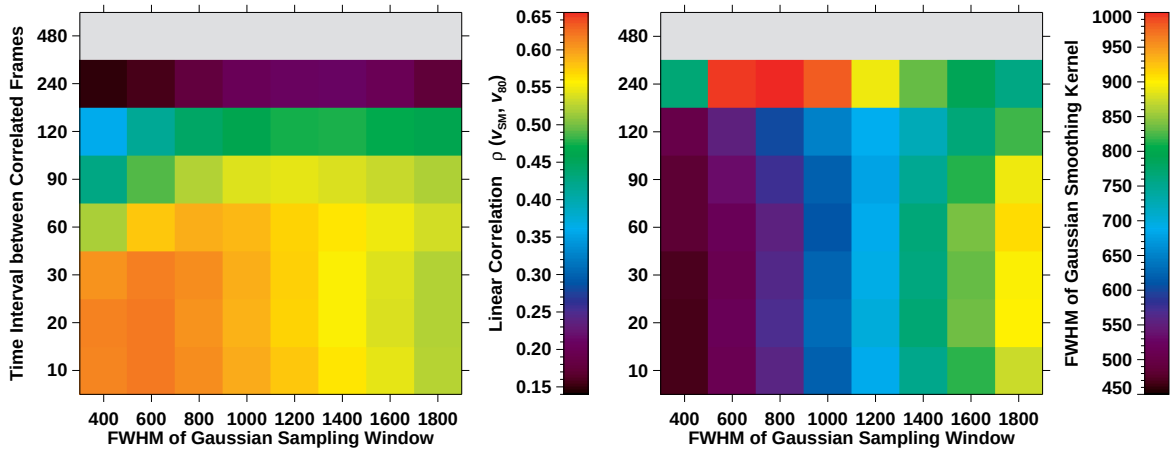

Figure 3.15: Maximum correlation $\rho(v_{\rm sm}, v_{80})$ (*left*) and corresponding FWHM of Gaussian kernel (*right*) used to smooth the actual flow map $v_{\rm sm}$. For both cases, the maps were averaged over one hour. The LCT flow maps were computed for images with an image-scale of 80 km pixel^{-1} matching *Hinode* G-band images, using time cadences of $\Delta t = 10$–480 s and Gaussian sampling windows with a FWHM = 400–1800 km, shown here as 8×8 square blocks. Gray blocks indicate parameters, where the linear correlation did not deliver meaningful results.

flows. Although the differences in the χ^2-error are of the same order of magnitude for all three optical depths, the lower χ^2-error at an optical depth of $\log\tau = +1$ indicates that LCT is picking up velocities at deeper layers in the photosphere.

Matloch *et al.* (2010) just used the same Gaussian kernel for smoothing the plasma flows as they used for computing the LCT flow maps. In principle, this is a free parameter and it has to be determined how much smoothing is required to get the highest correlations between plasma and LCT flow maps. We smoothed the one-hour averaged actual flow speed $v_{\rm sm}$ and divergence maps with a Gaussian kernel of size 64×64 pixels and with varying FWHM = 100–1500 km. We correlated it with the one-hour averaged LCT speed v_{80} and divergence maps for time cadences $\Delta t = 10$–480 s and Gaussian sampling windows with a FWHM = 400–1800 km. We performed this smoothing-correlation evaluation for plasma speeds at all three optical depths. However, only the results for the speed corresponding to optical depth $\log\tau = +1$ and the corresponding FWHM of the Gaussian smoothing kernel are shown in Fig. 3.15. The top rows for both correlation coefficient and FWHM are empty because we found no meaningful correlation between LCT maps computed with a time cadence of $\Delta t = 480$ s and the smoothed plasma flow maps. One can notice this lack of correlation already in the row for the time cadence $\Delta t = 240$ s, which shows a different behavior as compared to the remaining rows. This strongly substantiates earlier results indicating that time cadences in excess of 4 min are too long to deliver meaningful LCT results at least in the case of photospheric continuum images.

The mean correlations $\bar{\rho}$ between the smoothed plasma $v_{\rm sm}$ and LCT v_{80} velocities are 0.25, 0.41, and 0.49 at optical depths of $\log\tau = -1$, 0, and $+1$, respectively. The highest correlations are found at $\log\tau = +1$ indicating that LCT speed correlates better with plasma flows emerging from deeper layer irrespective of the LCT input parameters. Speed maps show the best correlations for smaller time cadences and narrow sampling windows. The actual plasma velocities were smoothed with kernels that are in general narrower than the LCT sampling windows (the only exception arises for the smallest FWHM = 400 km). The divergence maps again match best with flows from deeper layers. However, the FWHM of the Gaussian kernels are about twice the size of kernels used for speed maps. At the moment, we do not have a physical interpretation why much stronger smoothing has to be applied to the plasma divergence.

All our previous findings and the difficulties in interpreting LCT flow and divergence maps have their origin in the instantaneous flow field. In the left panel of Fig. 3.16, the local plasma velocities are superposed as color-coded arrows on top of the first continuum image in the time-series. Only minor spatial smoothing over a 5×5-pixel neighborhood was applied. The strongest horizontal flows are encountered near the boundaries of the expanding and fragmenting granules. The center of granules is almost always a divergence center and the velocity at these locations is significantly reduced. The visual appearance of this flow map is quite different from what is found in the LCT analysis. In the right

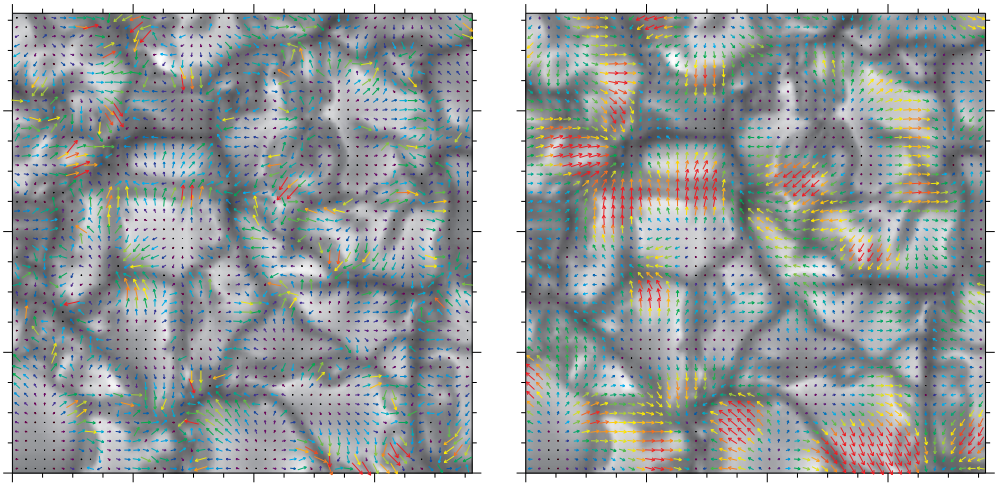

Figure 3.16: First gray-scale intensity image of the time-series overplotted with the actual (*left*) and smoothed plasma velocity vectors (see left most panel in Fig. 3.10 for the corresponding LCT flow vectors). The flow field was smoothed using a Gaussian kernel with FWHM = 686 km (see Fig. 3.15) corresponding to the maximum correlation coefficient between plasma and LCT (time cadence $\Delta t = 60$ s and Gaussian sampling window with a FWHM = 1200 km) velocities. The speed and direction of the flow field are given by rainbow-colored arrows, where dark blue corresponds to low and red to high velocities within the range of 0.75–7.5 km s^{-1} and 0.3–3.0 km s^{-1} for the actual and smoothed flow fields, respectively.

panel of Fig. 3.16, we smoothed the plasma velocities using a Gaussian kernel with a FWHM = 686 km, which produced the highest linear correlation $\rho \approx 0.57$ for the time cadence $\Delta t = 60$ s and a Gaussian sampling window with a FWHM = 1200 km. As a result, velocity vectors reflecting different plasma properties (high/low speeds and convergent/divergent motions) become intermingled. The final flow map is additionally modulated by the morphology of the granular cells, which are included in the sampling window. Even by using narrower sampling windows and higher time cadences it is doubtful that the original plasma velocities can be recovered, once having been scrambled in the LCT algorithm. On the other hand, any average property of the plasma flows, which does not depend on the spatial location should remain unaffected (see Figs. 3.13 and 3.14).

3.4 Conclusions

Applying LCT techniques to simulated data of solar granulation has proven as an excellent diagnostic to evaluate the performance of the algorithm. By contrasting LCT velocities with the plasma velocities of the simulation, some of the inherent troubles with optical flow techniques became apparent. Based on the previous analysis, we draw the following conclusions:

- ☐ One-hour averaged LCT flow and divergence maps differ significantly, if separated by more than one hour in time. The simulation of granulation does not contain any systematic persistent flow features. However, some strong flow kernels might still survive the averaging process but they can still be of intermittent nature.

- ☐ The time over which individual flow maps are averaged critically determines, if the LCT flow field reflects either instantaneous proper motions by individual granules or longer lasting flow features. The functional dependence of the mean flow speed on the elapsed time indicates that an averaging time of at least 20 min (several times the life time of a granule) is needed to raise persistent flows to the state of being significant.

- ☐ Time cadences $\Delta t = 240$–480 s are not suitable for LCT because the features (granules) in the tracking window have either evolved too much or moved outside the sampling window so that the cross-correlations become meaningless.

- ☐ Smaller sampling windows track fast-moving fine structures, if high-cadence images are available, but lack the ability to measure horizontal proper motions of coherent features, which results in an

underestimation of the flow speed. However, the morphology of the flow field is recovered better with narrower sampling windows.

- ☐ Frequency distributions of flow speeds for short time cadences and narrow sampling windows indicate that exploding or fragmenting granules and bright points have a different velocity spectrum distinguishing them from regular granules.

- ☐ LCT yields the highest speed values for sampling windows with a FWHM = 800–1000 km and short time cadences Δt = 20–30 s.

- ☐ The input parameters time cadence Δt = 60 s, Gaussian sampling window with a FWHM = 1200 km, and averaging time ΔT = 1 hr are a very good choice for bulk-processing of *Hinode* G-band images.

- ☐ Both the stochastic nature of granulation and the choice of LCT input parameters might be responsible for the often conflicting values in literature concerning flow speed, divergence, and vorticity.

- ☐ Significant smoothing has to be applied to the actual plasma velocities to match the LCT flow and divergence maps. The typical velocity pattern – high velocities at the border and low speeds in the center of granules – will however be lost in the smoothing process. Thus, even with very narrow sampling windows, short time cadences, and images free of aberrations and distortions, recovering details of the plasma flows might prove a futile undertaking.

Although the current study focuses only on granulation, in principle a similar study could be performed based on simulated data of active regions. Realistic MHD simulations of sunspots (e.g., Rempel *et al.*, 2009; Cheung *et al.*, 2010) could provide the basis for such a study, which will potentially aid in the interpretation of persistent flow features such as the divergence line in the mid-penumbra (e.g., Denker, 1998) or the distinct flow channels of moving magnetic features connecting the sunspot's penumbra to the surrounding supergranular cell boundary (Verma *et al.*, 2012).

Chapter 4

Flow Fields in the Final Stages of Sunspot Decay

Sunspots are a thought-provoking aspect of solar activity because of the close interaction between plasma motions and magnetic fields. Recent progress in MHD simulations (e.g., Rempel, 2011) provide a comprehensive framework for the interpretation of high-resolution sunspot observations. The formation of a penumbra around a sunspot is a rapid phenomenon, i.e., within a few hours a sunspot can develop a penumbra (Leka and Skumanich, 1998; Yang *et al.*, 2003), which is intimately linked to more inclined magnetic field lines and the onset of the Evershed flow. Schlichenmaier *et al.* (2010) observed the growth of a penumbra where only the newly formed penumbra contributed to the increase in spot size while the umbra remained stable. The formation of a penumbra, which would surround the entire spot, was hindered by continuous flux emergence between the spots of the bipolar region.

Quite the opposite, the decay of a sunspot is a slow process. Decay rates for stable leading sunspots and irregular follower spots are different (Martínez Pillet, 2002). A number of decay laws were proposed such as a linear decay law described by Bumba (1963) and a parabolic decay law proposed by Petrovay and van Driel-Gesztelyi (1997). Martínez Pillet (2002) critically reviews various diffusion models, concludes that they explain well how flux is spread over larger areas while the spot is decaying, but they fail to satisfactorily describe the flux removal process. The initial stages of sunspot decay, i.e., when the spot looses its penumbra, are exemplary described in Bellot Rubio, Tritschler, and Martínez Pillet (2008), who discovered finger-like structures, which are neither related to penumbral filaments nor the Evershed flow. These features might be penumbral field lines rising to the chromosphere, thus contributing to the decay of the sunspot penumbra. When a sunspot looses its penumbra, its decay reaches a critical point. Magnetic field lines become more vertical and convective motions in its vicinity begin to change. These ideas of a critical inclination angle and convective motions were put together by Rucklidge, Schmidt, and Weiss (1995), who explain in a simple model why small sunspots can have a penumbra while larger pores do not possess one.

The moat flow is a large-scale flow pattern commonly observed around sunspots (Meyer *et al.*, 1974). However, flux removal and dispersal can only be understood in the context of the moat flow's fine structure. Moving magnetic features (MMFs) play a major role in the flux dispersal process and they are only associated with decaying sunspots (Harvey and Harvey, 1973). The total flux carried by MMFs is several times larger than the flux contained within the sunspot itself. Thus, the polarity of MMFs has to be considered for a balance of the net flux. MMFs move radially outward with a velocity of 1 km s^{-1} before they reach and dissolve within the network, i.e., at the boundaries of the supergranular cell containing the sunspot. Zuccarello *et al.* (2009) showed evidence that MMFs and moat flow are present even in the vicinity of pores, i.e., in the absence of penumbral filaments and Evershed flow (cf., Cabrera Solana *et al.*, 2006). Deng *et al.* (2007) also detected a persistent moat flow after the penumbra around a spot disappeared leaving only a pore. Even though the moat flow might not be closely tied to the Evershed flow, the sub-photospheric interaction of magnetic field lines and flows can still produce the observed flow patterns.

Verma and Denker (2011) described a LCT method to measure horizontal flows based on *Hinode* G-band images. In this study, we perform a case study, where we put such horizontal flow fields in

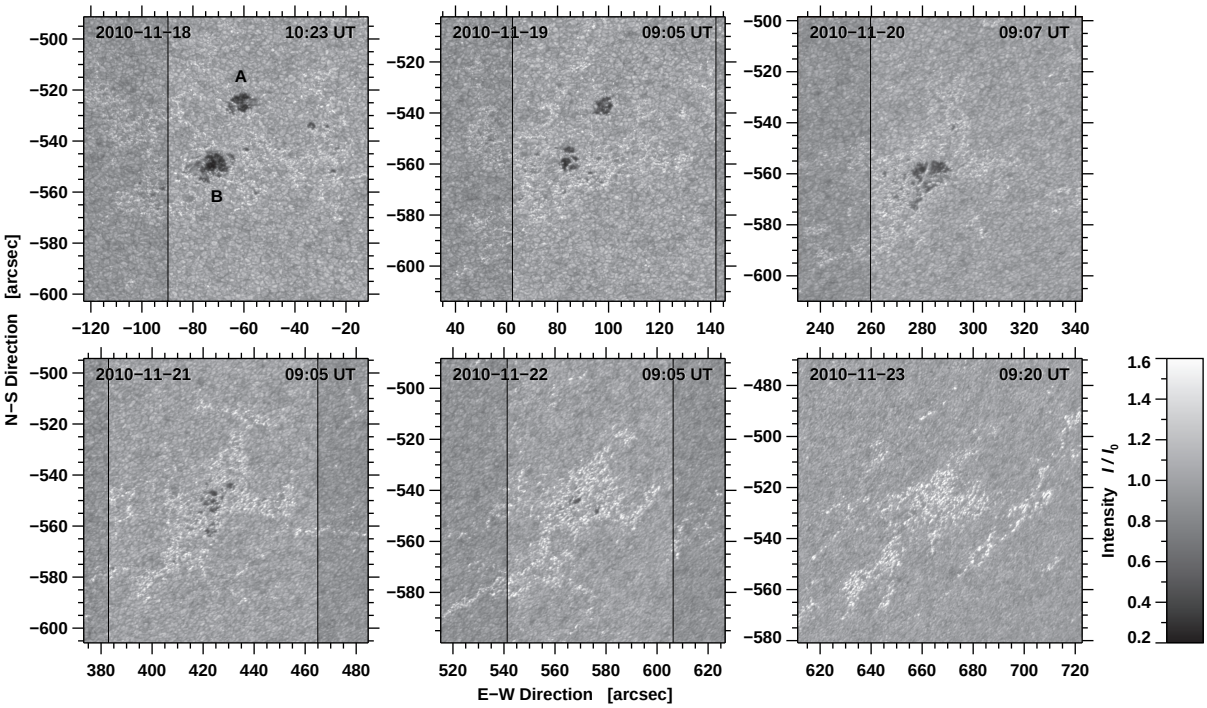

Figure 4.1: Calibrated *Hinode* G-band images showing the decay of active region NOAA 11126 observed during the period from 2010 November 18–23 (*from top-left to bottom-right*). The FOV is $111'' \times 111''$. The annotation of the axes refers to heliocentric coordinates given in seconds of arc. Brighter areas delineated by vertical black lines correspond to regions, which were covered by spectral scans obtained with the VTT Echelle spectrograph. The intensity scale to the right applies to these regions, while areas not covered by Echelle data are displayed with an offset of $0.1 I_0$. On 2010 November 23, only few *Hinode* G-band images were available. The limb darkening has been subtracted from the G-band images, which were then normalized so that the mean of the quiet Sun intensity distribution corresponds to unity.

the context of other photospheric and chromospheric data. In particular, we are interested in the final stages of sunspot decay. In Sect. 4.1, we present a subset of multi-wavelengths observations, which were obtained within the scope of *Hinode Operation Plan* (HOP) 0176. The temporal evolution of active region NOAA 11126 in terms of intensity, morphology, and flow as well as magnetic fields is described in Sect. 4.2 and discussed in Sect. 4.3.

4.1 Observations

The disk passage of active region NOAA 11126 started on 2010 November 12 and ended on November 24. NOAA 11126 was classified as a β-region, while it crossed the solar disk. No major flaring was associated with the region. Only a few B-class events were reported on 2010 November 15. As part of HOP 0176 "*High-resolution multi-wavelength study of small-scale jets on the solar disk*", we observed the decay of two small follower sunspots in the active region for five days from 2010 November 18–22. A time-series of *Hinode* G-band images is shown in Fig. 4.1, where we labeled the northern and southern spots with A and B, respectively. In the following, we will simply refer to these magnetic features as *spots*, even if the proper classification should be *pores*, i.e., sunspots lacking a penumbra. Spectral scans with different FOVs and cadences were observed for three hours every day. Since we are only focusing on the general properties of sunspot decay, we chose the first scan on the given day, which covered the largest FOV. The settings for the VTT Echelle data and data of *Hindoe/Spectro-Polarimeter*- were chosen as to obtain the best spatial and spectral match. The general observing characteristics are listed in Tab. 4.1.

4.1.1 SDO/HMI Full-Disk Images

The discussion of the temporal evolution and morphology of active region NOAA 11126 is based on full-disk images and LOS magnetograms obtained with the HMI (Schou *et al.*, 2012; Couvidat *et al.*,

Table 4.1: Observing characteristics and physical parameters

November		18	19	20	21	22
B		S32.6°	S32.6°	S32.6°	S32.6°	S32.6°
L		E5.5°	W6.3°	W20.5°	W31.5°	W44.1°
μ		0.81	0.81	0.77	0.70	0.58
$t_{0,\mathrm{GB}}$	UT	10:23	09:05	09:07	09:05	09:05
$t_{0,\mathrm{SP}}$	UT	11:46	09:05	09:07	09:04	09:04
$t_{0,\mathrm{ES}}$	UT	10:22	08:59	14:16	09:31	08:47
$A_{\mathrm{Spot\ A}}$	Mm^2	33.8	21.5			
$v_{\mathrm{Spot\ A}}$	$\mathrm{km\ s}^{-1}$	0.22 ± 0.19	0.15 ± 0.15			
		0.20 ± 0.25	0.15 ± 0.14			
$v_{\mathrm{Ring\ A}}$	$\mathrm{km\ s}^{-1}$	0.44 ± 0.23	0.37 ± 0.19			
	$\mathrm{km\ s}^{-1}$	0.44 ± 0.23	0.38 ± 0.19			
$\lvert\nabla v\rvert_{\mathrm{Ring\ A}}$	$10^{-3}\ \mathrm{s}^{-1}$	0.83 ± 0.78	0.65 ± 0.54			
		1.28 ± 1.33	1.13 ± 1.06			
$A_{\mathrm{Spot\ B}}$	Mm^2	54.7	21.6	54.2	17.5	2.7
$v_{\mathrm{Spot\ B}}$	$\mathrm{km\ s}^{-1}$	0.22 ± 0.15	0.15 ± 0.15	0.16 ± 0.07	0.18 ± 0.05	0.28 ± 0.06
		0.20 ± 0.14	0.11 ± 0.05	0.15 ± 0.08	0.25 ± 0.06	0.37 ± 0.06
$v_{\mathrm{Ring\ B}}$	$\mathrm{km\ s}^{-1}$	0.31 ± 0.19	0.20 ± 0.12	0.28 ± 0.14	0.25 ± 0.14	0.30 ± 0.09
		0.32 ± 0.20	0.20 ± 0.12	0.29 ± 0.15	0.28 ± 0.13	0.40 ± 0.09
$\lvert\nabla v\rvert_{\mathrm{Ring\ B}}$	$10^{-3}\ \mathrm{s}^{-1}$	0.63 ± 0.68	0.37 ± 0.36	0.46 ± 0.49	0.47 ± 0.51	0.28 ± 0.33
		0.91 ± 1.20	0.47 ± 0.59	0.76 ± 1.04	0.63 ± 0.81	0.44 ± 0.44
A_{mag}	Mm^2	136.9	83.5	98.9	44.7	22.2
N_{mag}		10	5	9	6	2
v_{mag}	$\mathrm{km\ s}^{-1}$	0.22 ± 0.12	0.15 ± 0.09	0.16 ± 0.07	0.18 ± 0.05	0.28 ± 0.06
v_{bp}	$\mathrm{km\ s}^{-1}$	0.27 ± 0.19	0.27 ± 0.16	0.28 ± 0.16	0.23 ± 0.12	0.26 ± 0.10
v_{gran}	$\mathrm{km\ s}^{-1}$	0.40 ± 0.24	0.35 ± 0.20	0.37 ± 0.20	0.34 ± 0.19	0.34 ± 0.18
$\lvert\nabla v\rvert_{\mathrm{gran}}$	$10^{-3}\ \mathrm{s}^{-1}$	0.88 ± 0.89	0.72 ± 0.67	0.85 ± 0.79	0.95 ± 0.88	1.04 ± 0.98
$\lvert v\rvert_{\mathrm{mag,LOS}}$	$\mathrm{km\ s}^{-1}$	0.03 ± 0.17	0.02 ± 0.12	0.04 ± 0.20	0.02 ± 0.12	0.00 ± 0.02
$\lvert v\rvert_{\mathrm{bp,LOS}}$	$\mathrm{km\ s}^{-1}$	0.43 ± 0.37	0.44 ± 0.37	0.44 ± 0.38	0.41 ± 0.38	0.34 ± 0.30
$\lvert v\rvert_{\mathrm{gran,LOS}}$	$\mathrm{km\ s}^{-1}$	0.51 ± 0.41	0.50 ± 0.41	0.55 ± 0.45	0.57 ± 0.47	0.55 ± 0.45

Note: The parameters in the first column of the table refer to heliographic latitude B, heliographic longitude L, cosine of the heliocentric angle $\mu = \cos\theta$, start of the G-band (GB), spectro-polarimeter (SP), and Echelle spectrograph (ES) observing sequences t_0, spot area A, horizontal velocity v, mean divergence $|\nabla v|$, number of magnetic elements N_{mag}. The indices refer to G-band bright points (bp), granulation (gran), magnetic elements (mag), the two sunspots (Spot A and Spot B), and the four-megameter wide annuli around both spots (Ring A and Ring B). If two rows are given for a physical parameter, then the top row refers to G-band data, whereas the bottom row was derived from Ca II H data. If present, the standard deviation refers to the variation of the physical parameters within the specified regions rather than to any formal error.

2012; Scherrer *et al.*, 2012) on board the *Solar Dynamics Observatory* (SDO Pesnell, Thompson, and Chamberlin, 2012). Since the *Hinode* FOV is too small to cover the entire active region and to give an overview of the magnetic field topology, we show in Fig. 4.2 the limb-darkening corrected HMI continuum image and magnetogram for November 18.

We selected from the SDO/HMI database one image/magnetogram with 4096×4096 pixels every 15 min for the period from 2010 November 13–23, i.e., a total of 1056 full-disk images. The image scale is about $0.5''$ pixel^{-1}, so that even finer details of penumbra and umbra can be captured. The average limb-darkening function was computed for this time interval and subtracted from the full-disk images to yield contrast enhanced images (see e.g., Denker *et al.*, 1999), which can then be used for feature identification. The photometric temporal evolution for the entire active region as shown in Fig. 4.2 is depicted in the left panel of Fig. 4.3. The corresponding changes of the magnetic flux are shown in the right panel of Fig. 4.3. Since HMI data cover the whole solar disk, it is straightforward to compute the

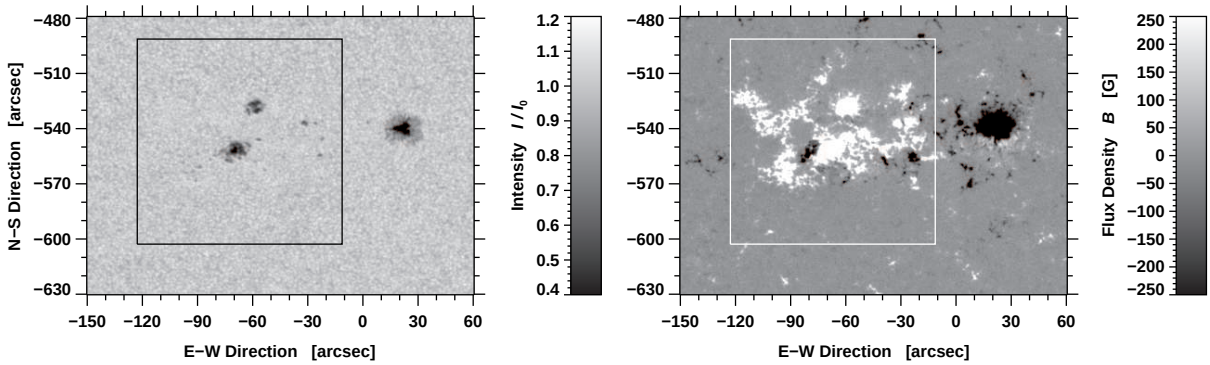

Figure 4.2: Limb-darkening corrected HMI continuum image (*left*) and magnetogram (*right*) of active region NOAA 11126 on November 18. The square box in both images shows the FOV covered by *Hinode*/BFI. The axes are labeled in heliographic coordinates.

cosine of the heliocentric angle μ on a pixel-by-pixel basis. Thus, a geometrical correction is applied to the measured areas and flux values of Fig. 4.3, which are discussed in detail in Sects. 4.2.1 and 4.2.5, respectively.

4.1.2 Hinode G-band and Ca II H Images

We applied LCT (for details see Verma and Denker, 2011) to image sequences captured in G-band λ430.5 nm and Ca II H λ396.8 nm to compare horizontal flows in the photosphere and chromosphere. Note that the Ca II H images do not purely represent the chromosphere, but contain contributions from both the upper photosphere and lower chromosphere. These observations were carried out by the BFI of the SOT on board *Hinode* (Kosugi *et al.*, 2007). Data sequences were captured every day from 09:00 UT to 12:00 UT with an average time cadence of 120 s (with some jumps in the data sequences). In both wavelengths the images are 2×2-pixel binned with an image scale of $0.11''$ pixel^{-1}. Images have a size of 1024×1024 pixels and a FOV of $111'' \times 111''$.

After basic data calibration, the images were corrected for geometrical foreshortening and resampled onto a regular grid of 80 km $\times$ 80 km. The signature of the five-minute oscillation was removed from the images by using a three-dimensional Fourier filter with a cut-off velocity of 8 km s^{-1} corresponding roughly to the photospheric sound speed. For measuring horizontal proper motions, we applied the LCT algorithm described in Verma and Denker (2011), which computes cross-correlations over 32×32-pixel regions with a Gaussian kernel having a FWHM of 15 pixels (1200 km) corresponding to the typical size of a granule. In two aspects, we deviated from the aforementioned algorithm, the time cadence was $\Delta t = 120$ s and the flow maps were averaged over $\Delta T = 3$ h.

4.1.3 Hα Echelle Spectra

The observations in Hα λ656.28 nm and Fe I λ656.92 nm were carried out with the VTT Echelle spectrograph. Spectral data were acquired with a slit width of 80 μm and an exposure time of 300 ms. The image-scale of the spectrograph is $8.99''$ mm^{-1}. We did not use a predisperser, hence, to suppress overlapping in spectral orders, we placed a broad-band interference filter directly behind the spectrograph slit. The infrared grating with a blaze angle of 51.6° and 200 grooves mm^{-1} was used to record spectra in the 12$^{\text{th}}$ order. In this configuration, we achieved a dispersion of 0.60 pm pixel^{-1}. The spectra covered a wavelength range of 1.2 nm from λ655.9 nm to λ657.1 nm. We employed a PCO.4000 CCD camera that has a quantum efficiency of about 30% at Hα. After 2×2-pixel binning the images have a size of 2004×1336 pixels. The pixel size of the CCD detector is 18 μm $\times$ 18 μm. The Echelle data were intended to match the *Hinode* observations, which was mostly achieved except for a few interruptions because of deteriorating seeing conditions. The two-dimensional FOV was scanned with a spatial step of $0.32''$ and 200–250 spectra were recorded in a sequence. A sequence of 240 spatial steps took about 12 min and covered a FOV of $72.0'' \times 182.6''$.

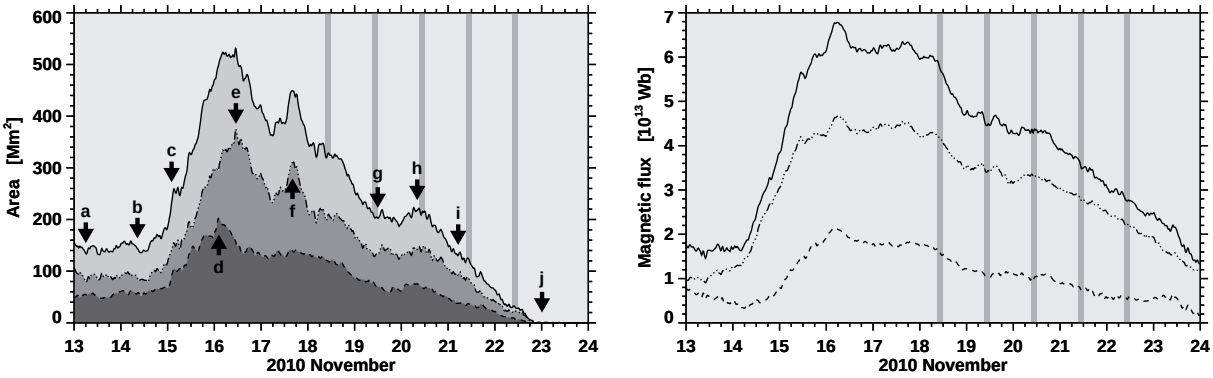

Figure 4.3: Temporal evolution of the area (*left*) covered by active region NOAA 11126 while it crossed the solar disk. The area enclosed by umbral cores and pores is displayed with dashed line. The dash-dotted line refers to the penumbra, whereas solid line denotes the total area. Some smoothing was applied to the time-series to suppress features on temporal scales below one hour. The vertical gray bars refer to the observing periods of HOP 0176 (2010 November 18–22). The labels indicate different stages of active region evolution, which are explained in Sect. 4.2.1. The temporal evolution of the magnetic flux (*right*) contained in the active region is depicted with solid, dash-dotted, and dashed lines refering to the total, positive, and negative flux, respectively.

The common FOVs of the G-band images and Hα Echelle spectra are shown in Fig. 4.1 for each observing day. We first matched the image scale of the Echelle data to that of the *Hinode* data. We then aligned *Hinode* G-band images and continuum images derived from Echelle spectra. After this procedure, the heliocentric coordinates for G-band images and Hα spectra differ by less than $1''$ in the periphery of the FOV. Furthermore, the Echelle scan direction is not perfectly aligned with the *Hinode* BFI detector. Hence, we computed an offset angle (smaller than $\pm 2°$) for each date and applied it to the spectral data. On 2010 November 20, the time difference between G-band images and Echelle spectra was about five hours.

4.1.4 Hinode Spectro-Polarimeter

The photospheric magnetic topology and evolution of the active region were studied using high-resolution spectral data from the *Hinode/Spectro-Polarimeter* (SP, Ichimoto *et al.*, 2008), which uses two magnetically sensitive Fe I lines at $\lambda 630.15$ nm and $\lambda 630.25$ nm and the nearby continuum (Tsuneta *et al.*, 2008) to obtain Stokes *IQUV* spectral profiles. We used spectral data captured in the fast mapping mode with a FOV of $58'' \times 122''$ and an average scan time of 12 min. On November 18, we also used ten continuous high cadence scans with a FOV of $32'' \times 123''$ and a scan time of 7 min. The dispersion is about 2.155 pm pixel^{-1}. The region was scanned with a spatial step of about $0.3''$ and an image scale of $0.32''$ pixel^{-1}. The basic data reductions such as subtraction of dark current, flat fielding, and polarization and wavelength correction were performed using procedures available in SolarSoft (SSW, Bentley and Freeland, 1998; Freeland and Handy, 1998).

4.2 Results

4.2.1 Photospheric Evolution

Contrast-enhanced HMI full-disk continuum images were used to study the evolution and decay of active region NOAA 11126 during its disk passage. The curves in Fig. 4.3 correspond to the areas of umbral cores/pores, penumbrae, and the sum of both types of features. These strong magnetic features are identified according to intensity thresholds of 75% and 92%, respectively, where the quiet Sun intensity was normalized to unity. Some spatial smoothing and minimum-size criteria were applied to binary masks of identified features using morphological image processing techniques, thus ensuring unwrinkled boundaries and contiguous structures. Note that this algorithm only provides a rough estimate of the above areas. Some (small) features could be misclassified. In particular, the borders of pores will be classified as penumbra.

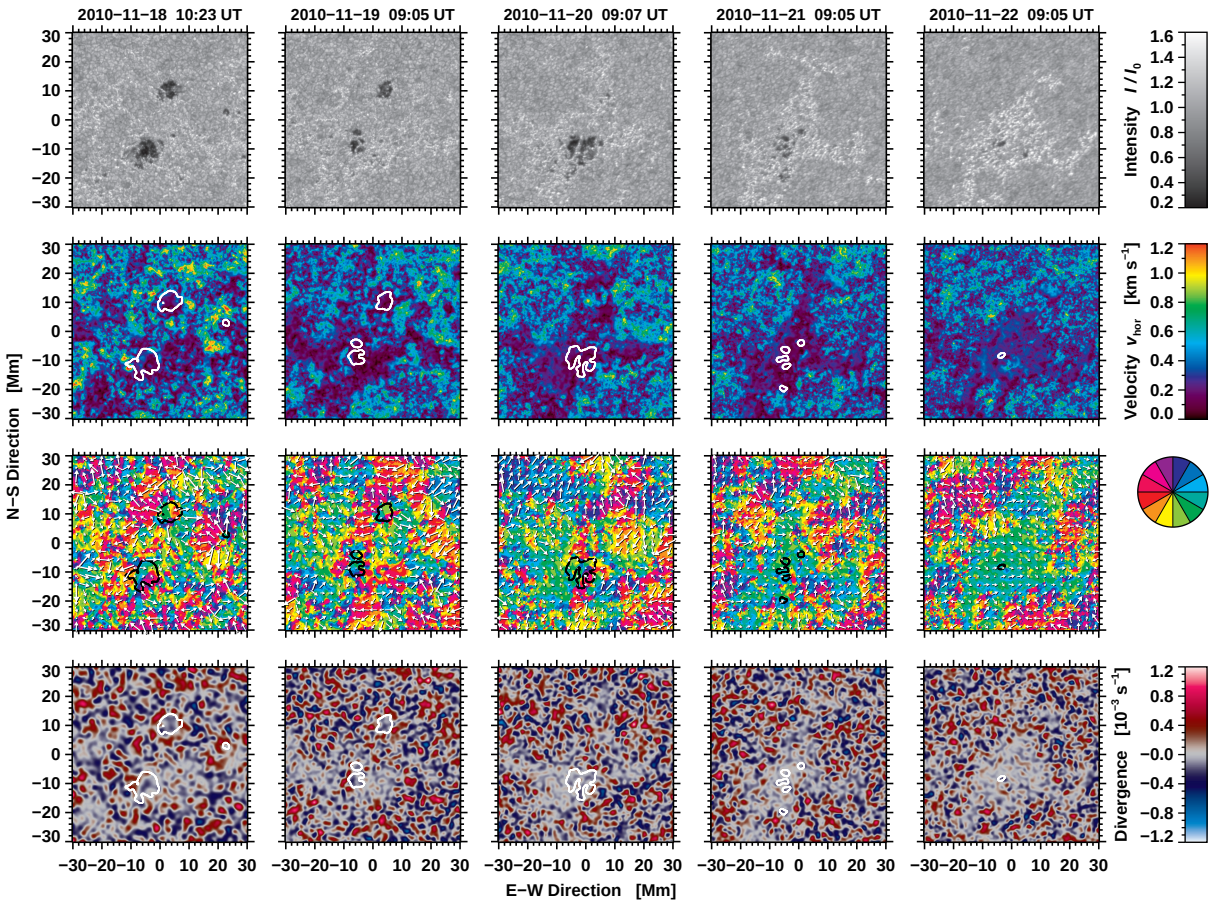

Figure 4.4: G-band images (*top*) after correction of geometrical foreshortening tracing the photospheric evolution of the central part of active region NOAA 11126 (*from left to right* 2010 November 18–22). The horizontal flow speeds (2nd *row*) are given by the velocity scale to the right. The direction of the horizontal flows (3rd *row*) are displayed according to the color-wheel and arrows for which a velocity of 1 km s^{-1} corresponds to exactly the grid spacing. The divergence of the horizontal flow field (*bottom*) are presented according to the scale on the right, where gray indicates divergence values close to zero. All G-band images and LCT maps were aligned so that the center of the panels coincides with a latitude of 31.9° South. The white and black contours outline the location of the small sunspots/pores. Times refer to the first image of the time-series, which was used to compute the flow maps.

The most important stages of the active region evolution are labeled in Fig. 4.3: (a) Initially, two tightly spaced sunspots of positive polarity were present early on November 13. The leading spot was larger and had a well established penumbra. (b) New flux emerged towards the south-east of these spots at 8:30 UT on November 14. Numerous (more than ten) magnetic knots and pores appeared to the south-west forming a bipolar magnetic region. (c) The umbral core of the leading sunspot of the new group established at 2:00 UT on November 15. (d) The leading sunspot of the new group continuously grew by advecting magnetic knots and small pores. The umbral cores/pores occupied the largest area at 2:20 UT on November 16. (e) The penumbra of the leading spot reached its maximum about nine hours later. At this time, active region NOAA 11126 started its decay phase. (f) Some further flux emergence occurred in the trailing part of the region at about 16:00 UT on November 17, which strengthened spot B and produced thin elongated dark lanes. These typical features of flux emergence (see e.g., Strous *et al.*, 1996) were labeled erroneously as penumbrae by the thresholding algorithm.

HOP 0176 focused on the two trailing spots/pores, of which the northern one (spot A) was already decaying, while the southern one (spot B) had just reached its maximum. This sunspot also showed strong indications of rotation. (g) This spot then fragmented into numerous magnetic knots until about 19:30 UT on November 19. (h) At this time, the fragments started to converge again forming a small sunspot, which reached its maximum at 8:00 UT on November 20. Interestingly, the northern pore faded away in parallel to this growths spurt. (i) Most of the penumbra in the leading spot had disappeared by 5:00 UT on November 21. (j) Finally, on November 23, all spots, pores, and magnetic knots had vanished and only a bright plage region remained until it rotated off the visible hemisphere.

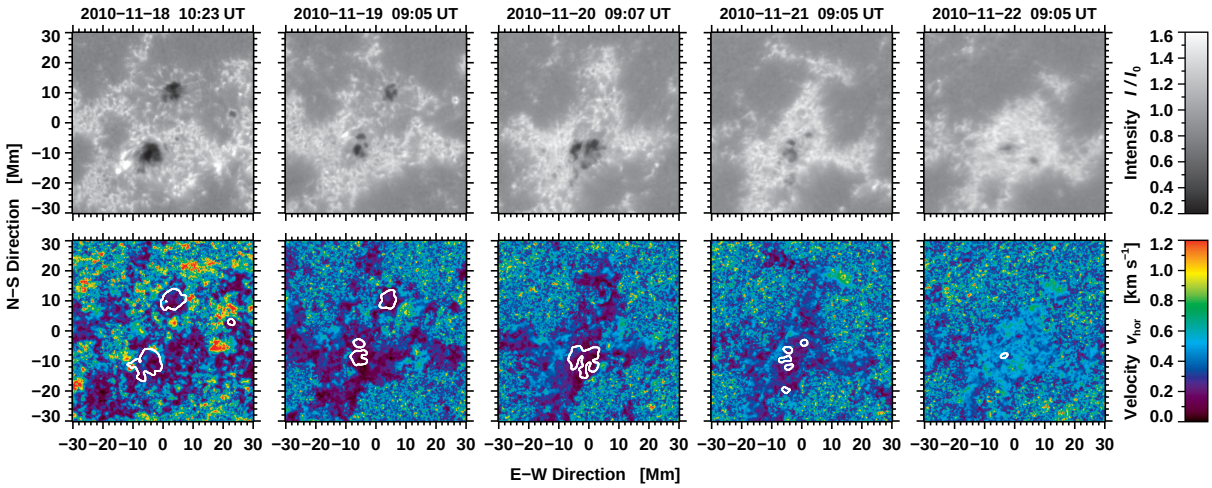

Figure 4.5: Ca II H average images tracing the evolution of active region NOAA 11126 in the chromosphere. The horizontal proper motions were derived from time-sequences of Ca II H images. Otherwise, data processing and display are the same as in Fig. 4.4.

In summary and neglecting all details of active region evolution, active region decay rates can be computed using a linear fit for time periods when the area coverage reached its maximum to the point when the area fell below 5 Mm^2. The overall decay rate of the active region is 72.6 Mm^2 per day. The values for penumbrae and umbral cores/pores are 48.3 and 25.1 Mm^2 per day, respectively. Similarly, we computed the growth rate of umbrae and penumbrae starting at 21:00 UT on November 14. The values are 171.4 and 104.8 Mm^2 per day, respectively. This is about four times faster than the corresponding decay times but less than one half of the penumbral growth rate of about 400 Mm^2 per day presented by Schlichenmaier *et al.* (2010).

Hinode G-band images allow us to zoom in on the two trailing spots. The region-of-interest (ROI) is shown in the top row of Fig. 4.4. The data of 2010 November 18–22 are corrected for geometrical foreshortening and the center-to-limb variation. The ROI with a size of 756×756 pixels or 60 Mm $\times$ 60 Mm was centered at a heliographic latitude of S31.9°. The first G-band image of the daily observing sequences was used as a reference to align all other data.

Various solar features are identified using intensity thresholds and morphological image processing. We indiscriminately used a fixed intensity threshold of $I_{\rm mag} = 0.8 I_0$ for strong magnetic features and an adaptive threshold for G-band bright points of $I_{\rm bp} = (1.37 - 0.08\mu) I_0$, where μ is the cosine of the heliocentric angle θ, and I_0 refers to the average quiet Sun intensity. Intensity values between $I_{\rm bp}$ and $I_{\rm mag}$ consequently enclose granulation. The measured spot areas for HMI and *Hinode* agree with each other, and the remaining differences can be attributed to different spectral characteristics of the observed passbands, image scales, and threshold/selection criteria. In general, the temporal evolution within the ROI follows the same trend as discussed in the context of SDO observations (Fig. 4.3). Areas, velocities, and other physical quantities based on high-resolution data are included in Tab. 4.1.

In the following, we present a chronology of the important phases of sunspot decay based on the high-spatial resolution G-band images. On November 18, the two trailing sunspots were embedded in a network of G-band bright points hinting at widely dispersed, weak magnetic fields. Both spots were filled with numerous umbral dots. Spot A had three umbral cores separated by faint light bridges and a small penumbral segment pointing westward. Spot B had two umbral cores with a few associated magnetic knots. It possessed curved penumbral filaments pointing eastwards, which are indicative of twisted magnetic field lines. These kind of non-radial penumbral filaments are frequently observed in flaring sunspots with horizontal shear flows (Denker *et al.*, 2007; Deng *et al.*, 2006). On November 19, the faint light-bridges had disappeared and the penumbra had vanished leaving only a single pore, which was filled with conglomerates of umbral dots. Spot B also lost its penumbra leaving four umbral cores separated by faint light-bridges, which, however, were more pronounced in comparison to the previous day. Magnetic knots were still surrounding spot B. Spot A had decayed on November 20 with only two faint magnetic knots remaining at its location. Interestingly, at this point of time, spot B started to grow

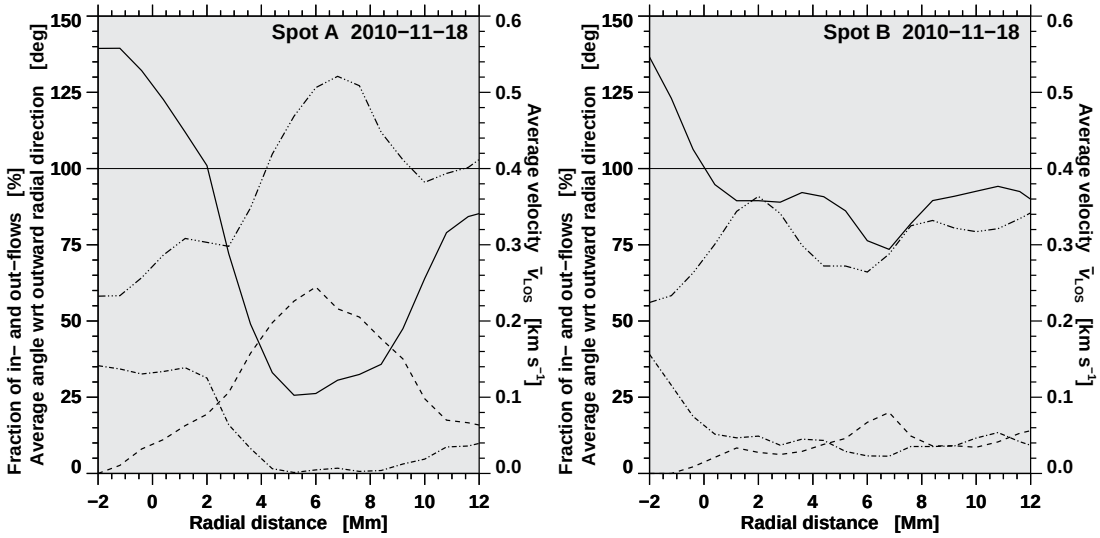

Figure 4.6: Radial dependence of parameters characterizing the flow fields of spots A (*left*) and B (*right*). Radial distances are measured from the outer boundary of the spots, i.e., 0.0 Mm marks the transition from penumbra to granulation. The thick black curves indicate the average angle of horizontal flow vectors with respect to the outward radial direction. High values refer to inward flows and low values indicate outward flow vectors. Fractions of in-/outward flow vectors as defined in the text are shown as a dash-dotted and dashed lines, respectively. The horizontal straight lines denotes the 100%-level. The average flow speed is displayed as a dash-triple-dotted line.

in area and a penumbral filament became visible on its western side. It consisted of three umbral cores, which were now separated by strong light-bridges, which split the spot in two halves along its north-south axis. The presence of strong light-bridges might suggest the initiation of the spot's decay phase (see Sobotka, Bonet, and Vazquez, 1993). Once spot A had disappeared on November 21, it did not leave any significant trace within the network of G-band bright points. By this time, spot B had dissolved into multiple tiny pores and magnetic knots, which roughly covered the same region as on the previous day. By November 22, only two tiny pores were left from spot B, which disappeared on November 23 just leaving G-band bright points at its point of disappearance. Two observations are noteworthy: (1) The area covered by the G-band bright points remained almost constant during the disk passage of the active region, which suggests that flux decays more or less in place and is not redistributed over a larger area. The time scale of flux removal or dispersal extends well beyond the photometric decay time of strong magnetic features such as sunspots, pores, and magnetic knots. (2) The two trailing spots have different histories of flux emergence and decay.

4.2.2 Chromospheric Evolution

The description of the chromospheric evolution is based on Ca II H (top row of Fig. 4.5) and Hα line core intensity maps (top row of Fig. 4.7). The Ca II H images were averaged over three hours to highlight some of the long-lived chromospheric features. On November 18, the lower quarter of the Ca II H image showed the undisturbed pattern of inverse granulation (Rutten, de Wijn, and Sütterlin, 2004). Ca II H brightenings cover a larger area, since their filling factor is significantly greater than that of G-band bright points. Spot A was encircled by individual brightenings at a radial distance of 5 Mm. These individual brightenings coalesced into a wagon-wheel-like Ca II H intensity structure in the three-hour average image pointing to the presence of MMFs. A similar feature was noticeable around a much smaller pore with a diameter of about 2 Mm located to the west of spot A. This conspicuous Ca II intensity structure was first described by Shine *et al.* (1996), who identified the bright ridges with azimuthal convergence regions, whereas the dark regions between the spokes correspond to azimuthal divergence zones. Spot A resides in the middle of a supergranular cell with a diameter of about 20 Mm. In contrast, spot B is embedded in an area of much more pronounced Ca II H brightenings. The exterior tips of its penumbral filaments appeared bright because a low-level B-class flare occurred at the time of observations.

On November 19, the average Ca II H image showed evidence that the moat flow around spot A survived the initial stages of sunspot decay, even after its penumbra had disappeared (see e.g., Deng

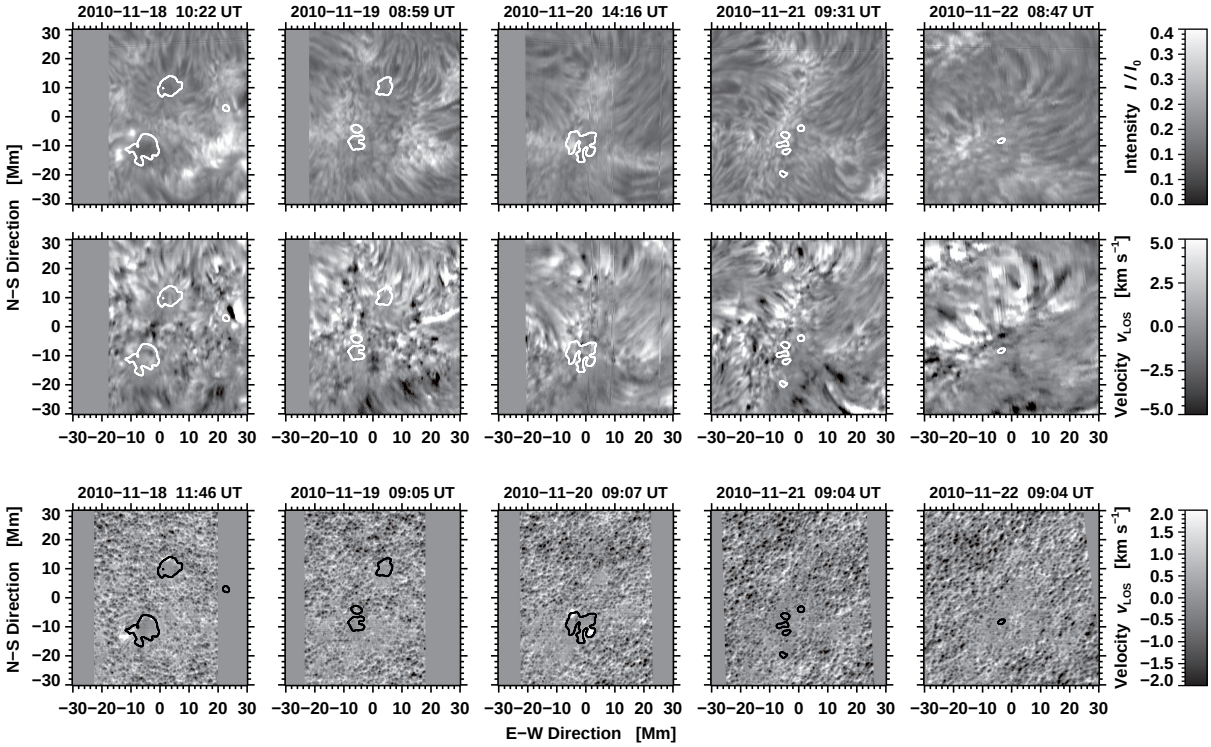

Figure 4.7: VTT Echelle spectra were used to study the chromospheric evolution of active region NOAA 11126 during the period from 2010 November 18–22. The chromospheric fibril structure surrounding the decaying sunspots can be traced in Hα λ656.28 nm line core intensity (*top*) and LOS velocity (*middle*) maps. In addition, photospheric LOS velocities (*bottom*) were derived from *Hinode*/SP Fe I λ630.25 nm spectra. The FOV matches those of Figs. 4.4 and 4.5. Regions not covered by the spectral data are shown in medium gray. The times above the panels refer to the start of a spectral scan.

et al., 2007). Spot A had completely dissolved by November 20. Assuming that spot A was located in the center of a supergranular cell as indicated by the surrounding Ca II H brightenings on November 18 and 19, we conclude that this supergranular cell ceased to exist on November 20, when the strong magnetic fields of spot A where no longer present. The Ca II H brightenings are now squeezed together by two supergranular cells to east and to the west, which could already be identified on November 19 and remained visible until November 22.

At the time when spot A vanished, spot B had already fragmented into two umbral cores, which were separated by a strong light-bridge with a noticeable dark lane along its axis (Rouppe van der Voort, Bellot Rubio, and Ortiz, 2010). This dark core was even more clearly discernible in the three-hour average Ca II H image. The presence of the strong light-bridge can be taken as a first indication of the spot entering the decay phase. During the next two days on November 21–22, spot B decayed further.

The Hα line core intensity map of November 18 exposed a radial pattern of fibrils around spot A reminiscent of a superpenumbra. Strong brightenings in the Hα line core in the vicinity of spot B are related to the aforementioned small B-class flare. We did not notice any significant Hα intensity features on the following days, except that after the decay of both spots the Hα plage became more prominent. By the end of our observations with the Echelle spectrograph, only a very compact plage region with a length of about 8 Mm remained within ROI.

4.2.3 Horizontal Proper Motions

The LCT flow maps displayed in Figs. 4.4 and 4.5 were computed using the time-sequence of *Hinode* G-band and Ca II H images. As mentioned in Section 4.2.1, we distinguished various solar features (e.g., G-band bright points, granulation, strong magnetic features, and sunspot penumbrae) by morphological and adaptive thresholding. For comparison, we refer to the typical flow speeds of granulation $v_{\mathrm{gran}} = 0.47 \pm 0.27$ km s^{-1} and G-band bright points $v_{\mathrm{bp}} = 0.23 \pm 0.15$ km s^{-1} as reported by Verma and Denker (2011), who also presented values for longer time intervals ΔT (Tab. 1 therein) and cadences Δt (Fig. 3 therein).

Their values for granulation are in very good agreement with the mean values $\bar{v}_{\rm gran} = 0.36 \pm 0.20$ km s^{-1} of the present study. The mean values for bright points $\bar{v}_{\rm bp} = 0.26 \pm 0.15$ km s^{-1} in the neighborhood of active region NOAA 11126 are within the range of expected values. Daily values of flow speeds for granulation and G-band bright points are given in Tab. 4.1. The standard deviation of the aforementioned horizontal flow speeds refers to the variance in the data for a particular solar feature rather than to a formal error. The intrinsic error of the LCT algorithm is 50 m s^{-1} and 15° for flow speed and direction, respectively (see Verma and Denker, 2011).

We computed the flow vectors for strong magnetic elements, i.e., spots A and B. We identified spots by smoothing the geometrically corrected G-band images using a Gaussian kernel with a FWHM of 1280 km and subsequently applied an intensity threshold of $0.83 I_0$. We plotted contours based on these binary masks in Figs. 4.4 and 4.5 to provide some visual guidance in identifying the spot positions in the physical maps. The mean flow speeds $\bar{v}_{\rm Spot\ A} = 0.19 \pm 0.17$ km s^{-1} and $\bar{v}_{\rm Spot\ B} = 0.18 \pm 0.11$ km s^{-1} are virtually identical for both spots. While computing the mean velocity $\bar{v}_{\rm SpotB}$ for spot B, we discarded November 22, because on that day only a tiny pore with a diameter of 4 Mm was left at the location of spot B. Therefore, adjacent regions with G-band bright points and granulation would bias the flow speed towards higher values.The overall flow pattern for the Ca II H data is very similar as compared to G-band data, and the average values $\bar{v}_{\rm Spot\ A} = 0.18 \pm 0.20$ km s^{-1} and $\bar{v}_{\rm Spot\ B} = 0.18 \pm 0.08$ km s^{-1} are virtually identical with a tendency to be slightly lower on individual days.

The moat flow around sunspots and pores reveals itself as radially, outward-directed vectors in flow maps, which point to a ring-like structure with kernels of elevated flow speeds. In the speed and azimuth maps on November 18 and 19 (Figs. 4.4 and 4.5) indications of moat flow were visible around spot A and a small pore located to the west of spot A. There was no clear signature of the moat flow detectable around spot B. To express the characteristics of the moat flow in more quantitative terms, we plotted in Fig. 4.6 the angle of the flow vectors, the fraction of in- and outward flow vectors, and the horizontal velocities for spots A and B. These quantities are radial averages and the zero point of the radial distance was placed at the penumbra/granulation boundary of the spots. We considered a flow vector to point in-/outward, if the tip of the arrow aims in-/outward and if the angle with the radial direction is less than 20°. Therefore, the fractions of in-/outward flow vectors presented in Fig. 4.6 do not add up to 100%, since more tangential flows are neglected. At a radial distance of 6 ± 2 Mm from the boundary of spot A, more than 50% of the flow vectors point outward. The average flow speed in this region is about 0.5 km s^{-1}. The region with high-speed outward flows marks the location, where the moat flow around spot A terminates. An exact determination of where the moat flow starts and where it ends strongly depends on the underlying criteria, e.g., photometric or magnetic features, or horizontal proper motions. In Sect. 4.2.5, we will discuss some properties of moat flow based on the proper motions of MMFs. Sobotka and Roudier (2007) determine that the moat radius is independent of the spot size. However, Balthasar and Muglach (2010) find that the moat flow terminates at a distance of four times the spot radius – in contrast to three times the spot radius in the present study. Extended statistical studies will help to clarify this issue.

We created two ring-like structures by morphological dilation with a width of 4 Mm, which encircled both spots at a distance of 2 Mm. This ring-like structure starts, where inflows turn to outflows 2 Mm beyond the boundary of spot A, and terminates, where the outflows reach the highest speed. We used these templates to calculate the flows in the immediate neighborhood of spots A and B. These regions were labeled as rings A and B. The velocities for these regions are included in Tab. 4.1. The flow speed $v_{\rm Ring\ A}$ was more than double than that of $v_{\rm Spot\ A}$ because of the suppressed convective motions in the spot's interior. The flow speeds in the immediate vicinity of spot B was higher by 30–40% on November 18 and 19. However, on November 22 during the final decay stage of spot B, no major difference between the spot and its closest surroundings was observed.

To effectively visualize the plasma motions, we presented high resolution maps of flow speed and azimuth (see Figs. 4.4 and 4.5). The speed maps of G-band and Ca II H images are virtually the same. The region with G-band bright points exhibits suppressed velocities in both cases. The regions around spot A and the small pore to the west are surrounded by a ring of high velocities (around 0.5 km s^{-1}), where the ordered moat flow terminates. In the azimuth maps of November 18 and 19, outward plasma motions are traceable in these regions. In addition, to gain more insight into inflows and outflows around

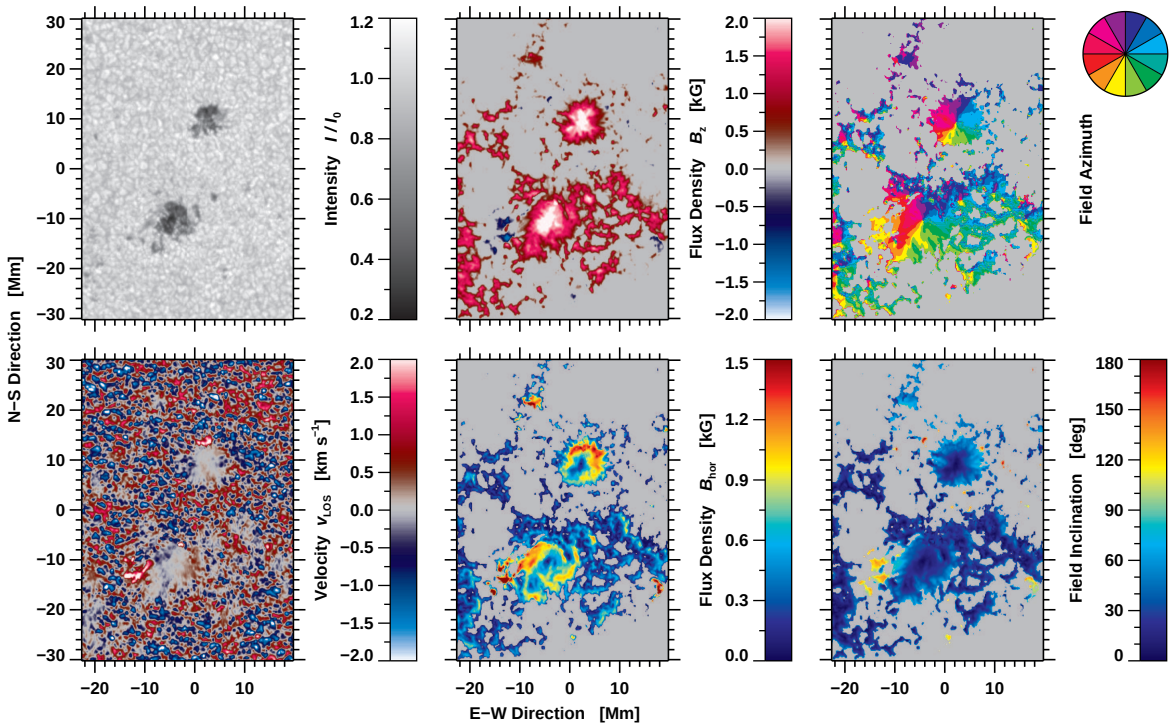

Figure 4.8: Maps of physical parameters derived using the SIR-code for a *Hinode*/SP scan on 2010 November 18: (*from top-left to bottom-right*) normalized intensity I/I_0, vertical component of magnetic flux density B_z, magnetic field azimuth ϕ, Doppler velocity v_{LOS}, horizontal component of magnetic flux density B_{hor}, and magnetic field inclination to the vertical γ.

the spots, we computed the divergence of the flow field. The divergence maps are included in the bottom row of Fig. 4.4. The positive values of divergence refer to outflows, whereas negative values indicate inflows. Negative divergence values are encountered within the boundaries of the sunspots. In contrast, small patches of positive divergence encircle the spots. This is indicative of inflows in the sunspots and outflows at their periphery. The area with low divergence values is increasing as the active region is decaying. The presence of a low divergence region could be a signature of the final stages of decay.

4.2.4 Line-of-sight Velocities

The LOS velocities were derived using *Hinode*/SP Fe I spectral data and Hα spectra of the VTT Echelle spectrograph. LOS velocities for the Fe I spectral line were calculated using the Fourier phase method (Schmidt, Stix, and Wöhl, 1999). This method makes use of entire line profile and is less sensitive to noise, along with this it takes into account the spectral line asymmetry. To compute the LOS velocity for Hα spectra, we calculated shifts using parabola fits to the central 50 pixels (0.03 nm), because the Hα spectral line is too wide to identify the real continuum. The calculated shifts in both cases were converted to velocities using the Doppler formula. The average photospheric velocity of dark umbral cores was used as the frame of reference. The Fe I λ656.92 nm line served as the reference for the Hα velocities. The Doppler velocity maps are displayed in the bottom and middle rows of Fig. 4.7. Redshifts in these maps are positive and blueshifts are negative, hence, areas moving away from the observer are bright, while areas moving toward the observer are dark.

To compute velocities for various solar features, we used an intensity mask generated using G-band images. The values are compiled in Tab. 4.1. On November 18 and 20 in the Fe I Doppler velocity maps, strong photospheric downflows were observed at edges of spot B. The average downflow velocity in these regions is about 2.5 km s^{-1}. In all maps a gray patch of near zero velocity was observed in the central FOV, which became more prominent on the last two days of observation. We identify this region with abnormal granulation (see e.g., de Boer and Kneer, 1992), in which convection is still strongly inhibited by the presence of (dispersed) magnetic fields.

In case of Hα LOS velocities, no conspicuous features were visible in the velocity maps, except on November 18 when we observed a radial filamentary structure around spot A in Hα line core intensity

maps, which resembled a superpenumbra. At the footpoints of the dark Hα filaments, we measure downflows from about 3.5 up to 4.5 km s^{-1}, which we interpret as an inverse Evershed flow (Maltby, 1975). Tightly wound superpenumbral spirals are only predicted for spots with radii larger than 8 Mm, whereas spot A was compact with a radius of 4 Mm. The downward chromospheric velocities at the edge of spot A are compatible with the MHD model of superpenumbral flows presented by Peter (1996).

4.2.5 Magnetic Fields

In addition to the photometric evolution shown in Fig. 4.3, we also computed the flux contained in the active region as shown in Fig. 4.3. Since only HMI LOS magnetograms were available (processing of the vector magnetograms is still under way). We took the measured magnetic field strength at face value and only carried out a geometrical correction to yield the proper average values of the magnetic flux. The geometrical correction only applies to the surface area covered by a pixel, which can simply be achieved by dividing the magnetic field strenght by $\mu = \cos\theta$. Signatures of geometric projection effects can be seen when the active region was close to the east limb, and the angle between LOS and shallow penumbral field lines leads to an apparent polarity reversal. Consequently, the positive and negative flux gradients have opposite signs, while the total flux remained almost constant for the first 30 hours until projection effects become less severe. To compute the temporal evolution of magnetic flux, we created a binary template, which only contained pixels above/below $\pm$50 Gauss in the HMI magnetograms. Morphological erosion with a 1-Mm kernel was applied to the template three times to eliminate small, isolated flux concentrations. Finally, we used morphological dilation with a 5-Mm kernel to include the strong magnetic fields in the immediate neighborhood of active region NOAA 11126. In this way, we avoided a bias, which could be introduced by weak magnetic fields, which do not belong to the active region but are contained within the FOV shown in Fig. 4.2.

The growth rates of the magnetic flux are 2.66, 1.98, and 1.09×10^{13} Wb day^{-1} for the total, positive, and negative flux, respectively. The negative flux showed a monotonous rise until about 06:00 UT on November 16, whereas the positive flux increased with a twice steeper slope, stopped a day earlier, and turned to a shallower slope until the end of November 17. On average, the positive flux was three times larger than the negative one. However, using adaptive thresholding and morphological image processing tools, we only measured the flux in the immediate vicinity of the sunspots. The missing negative flux required for flux balance has to be contained in flux concentration beyond the immediate neighborhood of the sunspots. The decay rates of the magnetic flux are four to five times lower than the growth rates and amount to 0.66, 0.47, and 0.23×10^{13} Wb day^{-1} for the total, positive, and negative flux, respectively. A linear fit to the data was used and despite some deviations from a linear trend, there is no indication for a parabolic (or any other) decay law. The decay rates of the present study are in agreement with Kubo *et al.* (2008) who report rates on the order of 10^{13} Wb day^{-1} and discusses the magnetic flux loss rate in a decaying active region.

The SIR-code (Stokes Inversion based on Response functions) developed by Ruiz Cobo and del Toro Iniesta (1992) was used to invert the *Hinode*/SP spectra. We restrict ourselves to the more sensitive line Fe I λ630.25 nm ($g_{\rm eff} = 2.5$). The starting model covers the optical depth range $+1.0 \leq \log\tau \leq -4.4$. A limb-darkening factor is considered according to Eq. 10 of Pierce and Slaughter (1977). We assume a constant macroturbulence of 1 km s^{-1} and a fixed straylight contribution of one percent. The inversions deliver the temperature stratification with four nodes $T(\tau)$, the total magnetic flux density $B_{\rm tot}$, the magnetic inclination γ and azimuth ϕ, and the Doppler velocity $v_{\rm LOS}$ constant with height (one node for each of these physical parameters).

The magnetic azimuth ambiguity must be solved after the inversions. For the first two days when we observed two major pores/small sunspots, we assumed two azimuth centers (see Balthasar, 2006). For the other days, it is sufficient to assume one azimuth center away from the pores in the direction towards disk center. The magnetic field in such small pores is more or less vertical to the solar surface so that on these days the field is sufficiently inclined with respect to the LOS that such an assumption is justified. If the expected azimuth ϕ deviates by more than 90° and less than 270° from the calculated one, we correct it by 180°. Finally, we rotate the magnetic vector with respect to the local solar frame. For a few locations, it happens that there is a sudden change of sign in the Cartesian components of the magnetic vector. This problem is solved by an additional correction of the LOS-azimuth. To be on the safe side,

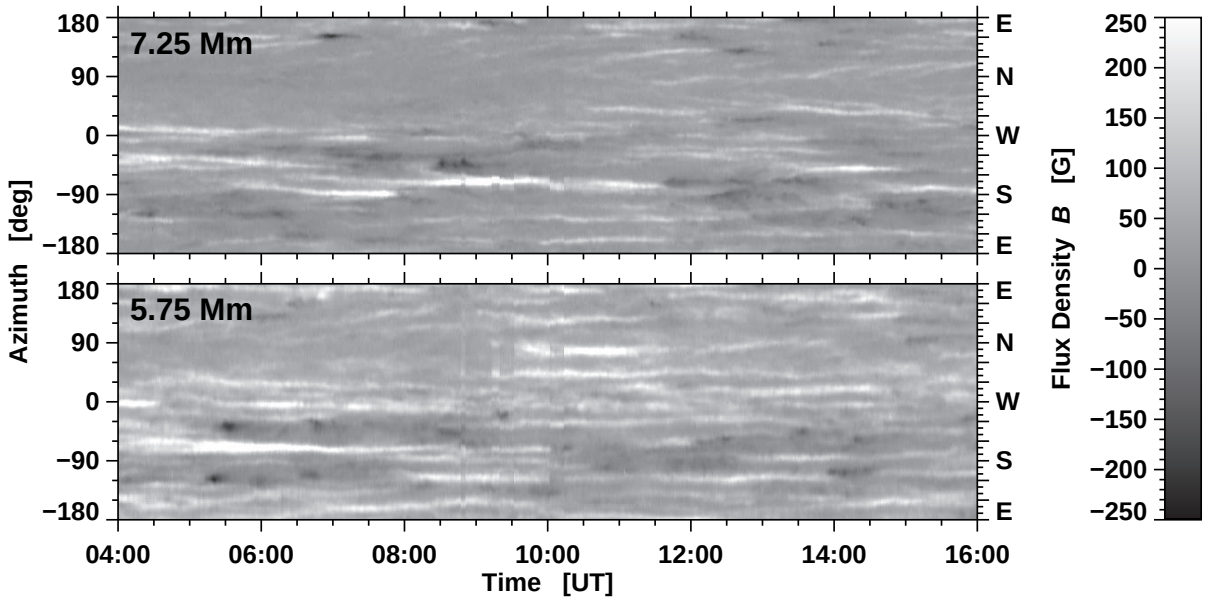

Figure 4.9: Space-time slices showing the temporal evolution of the magnetic flux along annuli with radii of 5.75 Mm (*bottom*) and 7.25 Mm (*top*), respectively, which are centered on spot A. HMI magnetograms with a cadence of 45 s covered a period of 12 hours starting at 04:00 UT on 2010 November 18. The annulus with a widths of 0.5 Mm was cut open in the East and then transformed to a straight line so that the southern part of the spot is mapped to the lower half of the space-time map. The heliographic direction is indicated on the axis to the right.

we additionally apply to data of November 18 the code provided by Leka *et al.* (2009), which minimizes $|J_z| + |\nabla B|$ to solve the azimuth ambiguity. Pixels, where the integrated circular and the integrated linear polarization are below 0.006, are excluded from the further analysis of the magnetic field. We finally use the magnetic vector field in the local solar frame. The results of the SIR-inversion for November 18 are depicted in Fig. 4.8.

The vertical magnetic flux density B_z in the ROI is predominantly positive and points outwards. The only significant patches of negative polarity were found on November 18 on the eastern side of spot B. Penumbral filaments connect spot B to several magnetic knots of negative polarity. In addition, we measure Evershed flows with velocities $v_{\rm LOS} > 2$ km s^{-1}. On smaller spatial scales, we find MMFs in the vicinity of spot A. They are mostly of type II (unipolar with the same polarity as the spot) but a few scattered U-shaped type I MMFs (bipolar with the inner footpoint of opposite polarity of the spot) were observed as well. No type I MMFs were observed near spot B.

Since the time cadence of *Hinode*/SP scans is about 12 min, we used SDO/HMI magnetograms with a cadence of 45 s to study the dynamics of MMFs. Space-time slices are an option to visualize local changes of the magnetic flux in a time-series. The continuous coverage of HMI magnetograms allowed us to depict in Fig. 4.9 the temporal evolution of the magnetic flux around spot A during a 12-hour period on 2010 November 18. The magnetic flux changes were recorded within two 0.5-Mm wide annuli of 5.75 Mm (bottom panel) and 7.25 nm (top panel) radius, respectively. Note that the linear scale of the ordinate in Fig. 4.9 is 38 Mm and 47 Mm for the inner and outer ring, respectively. The inner ring corresponds to the location, where the strongest outflows were observed (see Fig. 4.6). The outer ring marks the site, where the largest fraction (about 8%) of the annulus is covered by negative-polarity features.

Within a radial distance from 4–10 Mm from the center of spot A, only about 5% of the magnetic flux observed during 12-hour period is of negative polarity. Negative-polarity MMFs are weaker by about 20% as compared to MMFs of opposite polarity. Negative flux elements are most prominent in the southern half of spot A and absent in the northern half. The most notable difference between positive- and negative-polarity features is the morphology. Negative-polarity features can be tracked in space-time slices for only about 15–30 min, i.e., they are strongly localized. Time-lapse movies show that these negative-polarity features are mostly type I MMFs. The positive polarity appears first in the space-time slices (to the left) followed by the negative polarity. The appearance of the positive-polarity features is

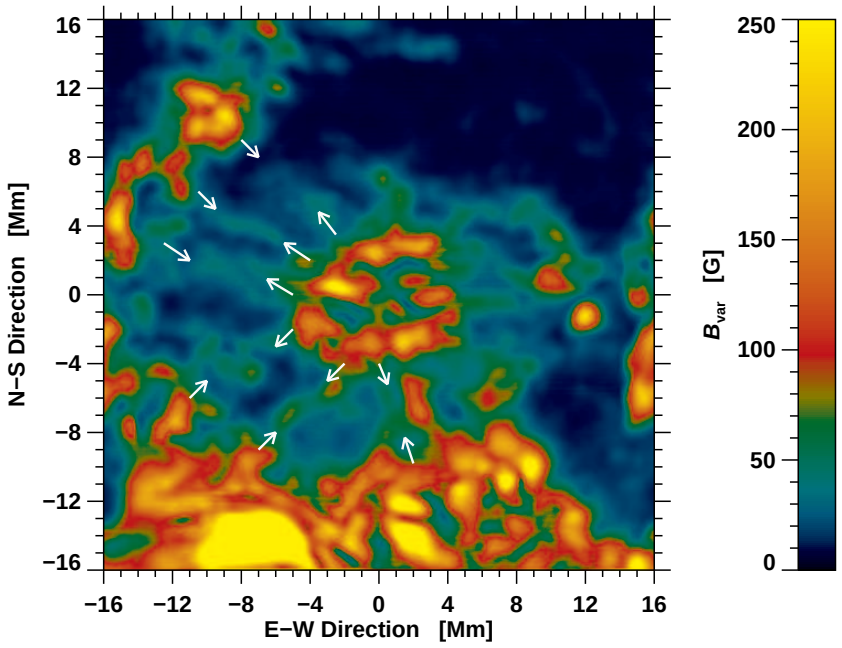

Figure 4.10: Local, background-subtracted variation of the magnetic flux B_{var} around spot A on 2010 November 18.

very different. Horizontal striation can be seen for several hours. These bands can abruptly (dis-)appear and in a few cases merging as well as splitting of the striae can be observed. In time-lapse movies, type II MMFs are moving away from spot A along radial paths on top of a background of positive flux.

The temporal variation of the magnetic flux above/below the local background is given by $B_{var} = \langle |B - \langle B \rangle| \rangle$, where $\langle \ldots \rangle$ indicates a temporal average. To compute the temporal average in Fig. 4.10, we used the same 12-hour time-series of HMI magnetograms that was used to create Fig. 4.9. The strongest changes occur at the periphery of spot A, where also the horizontal magnetic field B_{hor} is strongest as can be seen in Fig. 4.8. This correspondence also applies to the feature of strong horizontal field to the north-east of spot A, which belongs to the (chromospheric) network. The most notable features in Fig. 4.10 are, however, several spoke-like structures with a length of about 10 Mm, which extend from spot A all the way out to the border of the supergranule surrounding the spot. These elongated structures are the signatures of MMFs streaming from the spot along identical paths (Harvey and Harvey, 1973) towards the supergranular boundary. However, the distance traveled is much shorter as Harvey and Harvey (1973) observed for mature sunspots. Therefore, we conclude that the preferred paths of MMFs are a phenomenon, which can be observed even in the final stages of sunspot decay. The traces left by MMFs in the variance of the magnetic field around its background B_{var} are most prominent on the eastern side of the spot. They also match the wagon-wheel structure discussed in the context of the time-averaged Ca II H images in Sect. 4.2.2. Finally, the preference of MMFs for distinct radial channels connecting the sunspots' magnetic fields to the strong network fields was also noticed by Hagenaar and Shine (2005).

Maps similar to Fig. 4.8 were computed for each day so that we could study the evolution of the magnetic field. The strongest horizontal magnetic flux densities B_{hor} are observed in the immediate surroundings of spots A and B as long as the spots are compact (November 18 and 19). They symmetrically enclose the entire boundary of the spots. Once spot A had disappeared and spot B started to fragment, this symmetry is broken most evidently on November 20, when strong horizontal fields were present at the western side of spot B. This corresponds to a time when a rudimentary penumbra was present. Whenever indications of penumbral filaments were observed during the decay of the sunspots, inclined magnetic field lines and Evershed flows were present at the same time (cf., Leka and Skumanich, 1998; Yang *et al.*, 2003).

The magnetic field lines spread out symmetrically from the center of the spots on November 18 and 19. Such well defined azimuth centers can still be found in the later decay stages of spot B. Even though these region are no longer circular and become elongated. Smaller azimuth centers are also observed to the east of spot B on November 19. These centers are associated to several magnetic knots.

The Doppler velocity v_{LOS} is suppressed in the presence of strong magnetic features. Starting on November 20, the velocity pattern associated with the magnetic fields changes. Positive Doppler ve-

locities occupy more and more of the magnetic region. This coherent pattern was also observed in the divergence maps (bottom row of Fig. 4.4) and the horizontal flow maps (Figs. 4.4 and 4.5). Indeed, considering that the region is approaching the limb, some of the Doppler velocities can be interpreted as a coherent proper motion of the magnetic region towards the south-west (cf. the azimuth maps of the horizontal proper motions). In summary, during the final stages of sunspot decay, the three-dimensional flow field, in regions previously occupied by strong magnetic fields, significantly differs from granular flow patterns or regions of reduced velocities in the presence of G-band bright points. Since we are only presenting a case study, the question remains, if this intriguing flow pattern is a typical feature of sunspot decay.

4.3 Conclusions

We have presented a detailed account of the final stages in the decay of the active region NOAA 11126, which did not obey the Hale-Nicholson polarity law (e.g., Zirin, 1988). Since only one out of ten active regions shows such a behavior (Howard, 1990) and we only present a case study, our results might not be representative for sunspot decay in general. However, space missions such as *Hinode* and SDO provide nowadays data of sufficient coverage, resolution, and cadence that statistical properties of sunspot decay become accessible. Furthermore, previous studies of non-Hale regions (e.g., López Fuentes *et al.*, 2000, and reference therein) were centered on flux emergence, δ-spots, and strong solar flares. The present study can consequently be considered as an extension of these studies with a focus on a much quieter magnetic field topology, which might be representative for the lower solar activity during cycle No. 24 (Petrovay, 2010; Nielsen and Kjeldsen, 2011).

The major findings of our study can be summarized as follows:

- MMFs were observed in the vicinity of spot A until it decayed. Mostly type II and a few interspersed U-shaped type I MMFs contributed to the observed moat flow, which also left a clear signature in the time-averaged Ca II H images (Martínez Pillet, 2002).

- Even though penumbral filaments had almost completely disappeared in photospheric G-band images of spot A on November 18, Hα line core images clearly exhibited a structure reminiscent of a superpenumbra. Thus, filamentary structures including the inverse Evershed flow (Maltby, 1975; Georgakilas and Christopoulou, 2003) might be more persistent in the chromosphere.

- We have also observed MMFs in the vicinity of a tiny pore with a diameter of about 2 Mm, which did not show any indication of penumbral filaments. Such an observation argues strongly against a close tie between Evershed flows and MMFs (cf., Vargas Domínguez *et al.*, 2008, 2010; Cabrera Solana *et al.*, 2006). Rempel (2011) argues based on MHD simulations of sunspots that penumbral flows can be separated in two components, where the shallow one corresponds to the Evershed flow and the deeper one is related to moat flow.

- The strong rotation and twist seen in spot B might explain, why this trailing spot never advected sufficient magnetic flux to establish more than a rudimentary penumbra and remained highly fragmented during its entire life cycle.

- The photospheric and chromospheric maps of horizontal flows show a peculiar pattern, once the last dark feature of the active region has disappeared. In general, the flow field in this region is less structured than regions covered by granulation, i.e., the dispersed magnetic field still significantly affects the convective pattern. Chromospheric flows have increased notably compared to times when spots and pores were still present. Most prominently, a contiguous area of low divergence appears towards the end of sunspot decay.

Chapter 5

The Decay of a Satellite Sunspot and the Role of Magnetic Flux Removal in Flaring

A theoretical description of flares has to explain their underlying cause and the origin of the various observed features (e.g., flare ribbons, loops, emissions across all wavelength regimes, and particle acceleration). Priest and Forbes (2002) review recent flare models, starting with some type of MHD catastrophe followed by magnetic reconnection. They place an emphasis on three-dimensional models, which are required for a full appreciation of the dynamics in complex magnetic field topologies. In addition to modeling efforts, a wealth of new data became available by space missions such as RHESSI, Yohkoh, TRACE, and SoHO. Observations in the EUV and in soft/hard X-rays revealed a plethora of transition region and coronal arcades and loops as summarized by Benz (2008), who discusses energetic and eruptive events as well as the nature of energy release and particle deposition. More recently, the relevant MHD processes such as flux emergence, formation of a current sheet, rapid dissipation of electric current, shock heating, mass ejection, and particle acceleration have been recounted by Shibata and Magara (2011).

Newly emerging flux has been linked to solar flares, whereas flares related to sunspot decay are not broadly discussed in the literature. Simultaneous emergence and submergence of magnetic flux has been explored by Kálmán (2001) for the two (recurring) active regions NOAA 6850 (6891) and 7220 (7222). Based on X-ray observations, no direct interaction of new and old magnetic flux was evident. However, flaring was observed for active region NOAA 6891, where only one magnetic polarity submerged. The magnetic field evolution was comparatively slow in these cases, with time scales ranging from several hours to days. An intermediate case has been discussed by Wang *et al.* (2002), who observed an M2.4 flare associated with rapid penumbral decay (within a time period of just a few minutes) immediately after the flare, which was followed by the slow decay (three hours) of the remaining umbral core. The first phase of sunspot decay, i.e., rapid penumbral decay, has been established as an important signature of flare-related photospheric magnetic field changes (e.g., Wang *et al.*, 2004; Deng *et al.*, 2005; Liu *et al.*, 2005; Sudol and Harvey, 2005; Ravindra and Gosain, 2012). In our study of the flaring active region NOAA 10930, we focus on the gradual decay of a satellite sunspot and discuss its relationship to a developing δ-spot of opposite polarity.

Active region NOAA 10930 was the first complex sunspot group producing X-class flares that was observed by the Japanese *Hinode* mission. The region was the source of the well-studied X3.4 solar flare on 2006 December 13 (e.g., Schrijver *et al.*, 2008). For this highly active time period Tan *et al.* (2009), applied LCT to study horizontal proper motions related to penumbral filaments in a rapidly rotating δ-spot (Min and Chae, 2009). Both studies found twisted penumbral filaments, shear flows, sunspot rotation, and emerging flux at various locations within the active region. However, fewer studies were published for the time just after the region rotated onto the solar disk, which mostly focused on the X6.5 flare on 2006 December 6 (e.g., Wang, Deng, and Liu, 2012).

Balasubramaniam *et al.* (2010) described a prominent Moreton wave having an angular extent of almost 270°, which was initiated by the X6.5 flare. The radiant point of the Moreton wave appeared to be located at a small satellite sunspot to the west of the major sunspot, whereas X-ray, white-light, and G-band emissions were centered on the developing δ-spot to the south. The strongest changes of

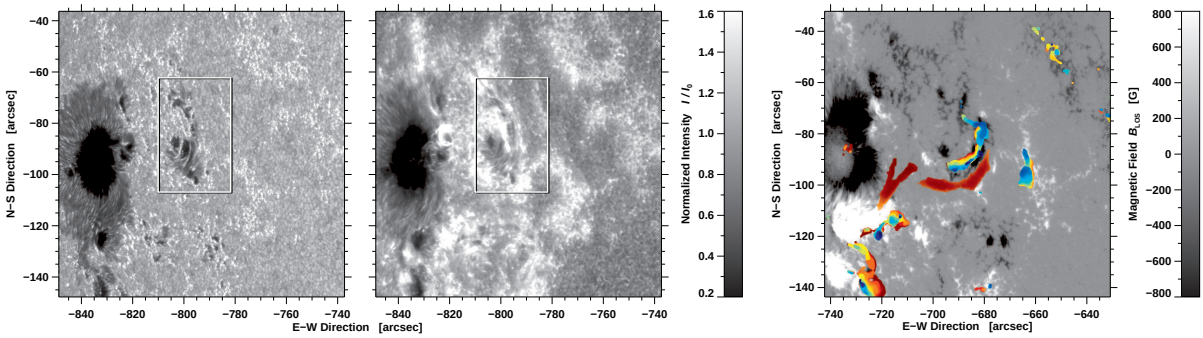

Figure 5.1: First calibrated G-band (*left*) and Ca II H (*middle*) image in a 16-hour time-series of active region NOAA 10930 at 2:30 UT on 2006 December 7. The region in the white rectangle is the region-of-interest, i.e., a small satellite sunspot. SOT/NFI magnetogram (*right*) captured at 18:46 UT on 2006 December 7. The rainbow-colored regions are the flare kernels derived from 32 Ca II H images covering the M2.0 flare for 16 min from 18:47 UT to 19:03 UT. The time progresses from blue to red. A Big Bear Solar Observatory full-disk Hα (Denker *et al.*, 1999) image taken at 18:39 UT is used to trace a small filament (reddish colors), which consists of a V- and sickle-shaped region. The annotation of the axes refers to heliocentric coordinates given in seconds of arc.

the magnetic force also occurred at this location (cf., Fisher *et al.*, 2012). Rapid penumbral decay and changes in the horizontal flow fields associated with the X6.5 flare were discussed by Deng *et al.* (2011a). After observing the enhanced and sheared Evershed flow along the magnetic neutral line separating the main and δ-spots, they concluded that increased flow speed is not associated with new flux emergence in the active region. In the present study, we follow up the evolution of active region NOAA 10930 after the X6.5 flare leading up to a homologous M2.0 flare on 2006 December 7.

5.1 Observations

Active region NOAA 10930 appeared on the eastern solar limb on 2006 December 5. The sunspot group was classified as a $\beta\gamma\delta$-region exhibiting a complex magnetic field topology, and it produced numerous C-, M-, and X-class flares. On 2006 December 7, we analyzed 16 hours of data from 02:30 UT to 18:30 UT about eight hours after the X6.5 flare. The region was located at heliocentric coordinates E800″ and S85″ ($\mu = 0.56$, where $\mu = \cos(\theta)$ is the cosine of the heliocentric angle θ). The sequence with a cadence of 30 s comprises 1920 G-band and Ca II H images (left and middle panels of Fig. 5.1) captured by the SOT (Tsuneta *et al.*, 2008) on board the Japanese *Hinode* mission (Kosugi *et al.*, 2007). We dropped every second image from the time-series because a cadence of 60 s is sufficient for measuring horizontal proper motions. A SOT/NFI magnetogram (right panel of Fig. 5.1) serves as reference to illustrate the magnetic configuration of NOAA 10930, which is later used in the discussion of the M2.0 flare at 18:47 UT (see Sect. 5.2.5). The G-band and Ca II H images are 2×2-pixel binned with an image scale of 0.11″ pixel^{-1}. Thus, the 1024×1024-pixel images have a FOV of $111'' \times 111''$. After basic data calibration, the images were corrected for geometrical foreshortening and resampled onto a regular grid of 80 km $\times$ 80 km (see Verma and Denker, 2011).

The ROI with a size of 40 Mm $\times$ 40 Mm was centered on a small decaying sunspot in the western part of the active region (see the white rectangular region in Fig. 5.1 before geometrical correction). This satellite spot significantly evolved over the course of 16 hours. Accompanied by C- and M-class flares (Tab. 5.1), the penumbra of the small spot almost completely vanished. The X-ray flux over three days as measured by the Geostationary Operational Environmental Satellite (GOES) is shown in Fig. 5.2, where the shaded region indicates the 16-hour observing period. Before measuring horizontal proper motions, we removed the signature of the five-minute oscillation from the images by using a three-dimensional Fourier filter with a cut-off velocity of 8 km s^{-1}, which corresponds roughly to the photospheric sound speed. To scrutinize flow fields associated with slow penumbral decay and its relationship to flaring, we used the LCT method described in Verma and Denker (2011). The technique computes cross-correlations over 32×32-pixel regions with a Gaussian sampling window having a FWHM of 15 pixels (1200 km), corresponding to the typical size of a granule.

Table 5.1: Flare list for 2006 December 7 with starting, peak, and end times as well as flare sites in heliocentric coordinates and X-ray flare class.

Start Time	Peak Time	End Time	Position		X-Ray Class
03:32 UT	03:36 UT	03:39 UT	E766″	S86″	C2.0
04:27 UT	04:45 UT	05:09 UT	E764″	S120″	C6.1
10:49 UT	11:48 UT	12:57 UT	E720″	S120″	C1.1
14:49 UT	15:15 UT	15:33 UT	E709″	S120″	C1.2
18:20 UT	19:13 UT	19:33 UT	E687″	S103″	M2.0

Note: Figure 5.2 provides a graphical representation of flare timing and the GOES X-ray flux. Data were provided by NOAA's National Geophysical Data Center (NGDC).

5.2 Results

In the following, we will describe the decay of the satellite sunspot, compute the photometric decay rates of its umbra and penumbra, and study the impact of the decay process on photospheric and chromospheric horizontal flows. The photometric observations together with a temporal analysis of the flow maps yields estimates of decay times of various solar features. Finally, we relate these findings to an M2.0 flare, which occurred towards the end of the time-series.

5.2.1 Morphology

The temporal evolution of the decaying satellite sunspot is shown at two-hour intervals in Fig. 5.3. Note that after geometric correction, the axis labels no longer refer to heliographic coordinates on the solar disk. They are more readily provided for easier identification and comparison of intensity or flow features. As a convenient reference to photometric and magnetic components of the satellite spot, we provided numbered labels P and N in Figs. 5.3 and 5.4 referring to positive- and negative-polarity features, respectively. Initially, the ROI contains a few umbral cores with rudimentary penumbrae, which are embedded in regions covered by G-band bright points. The strongest umbral core N3 is located close to the center of the ROI, where it is separated from an elongated umbral core N2 by a faint light-bridge. The south side of the light-bridge flares out in a strand of penumbral filaments, which wind around the strong umbral core. Nonradial penumbral filaments are indicative of shear flows (e.g., Denker *et al.*, 2007; Jiang *et al.*, 2012). These filaments became significantly weaker in response to a C6.1 flare at 04:45 UT, which can be considered as a form of 'rapid' penumbral decay (Wang *et al.*, 2004; Liu *et al.*, 2005). However, in this case the observed decay was very localized and veiwed at high spatial resolution. In addition to shear flows, we observed an umbral core N5 drifting away eastward from the dominant umbral core N3. The separation of these umbral cores grew by 6 Mm over the course of 14 hours, i.e., the separation speed is about 120 m s^{-1}. Three small 1-Mm wide pores of positive and negative polarity (P1, P2, and N1) are located to the south of the strong umbral core. All three pores disappeared by the end of the time-series. In addition, penumbral regions started decaying across the entire ROI at about 10:00 UT. At 12:00 UT only weak penumbral signatures were present, so that only scattered pores were left by 14:00 UT. This period of 'slow' penumbral decay was accompanied by several B-class flares and a C1.1 flare at 11:48 UT.

In addition to the photometric evolution shown in Fig. 5.3, we also trace in Fig. 5.4 the reduction of magnetic complexity in the satellite sunspot, which is based on *Hinode* NFI magnetograms taken in the photospheric Fe I λ630.25 nm line. The Stokes-V/I magnetograms have 1024×1024 pixels and an image scale of 0.16″ pixel^{-1}. From the Stokes-V and I signal, the approximate LOS magnetic field was calculated as

$$B_{\text{LOS}} = -\frac{C_V}{0.798 C_I} \times 10^4 \text{ Mx cm}^{-2} \tag{5.1}$$

given in Isobe *et al.* (2007). We scaled the magnetograms displayed in Figs. 5.1 and 5.4 using this relation. However, no attempt was made to translate the LOS magnetic fields into the field component B_z

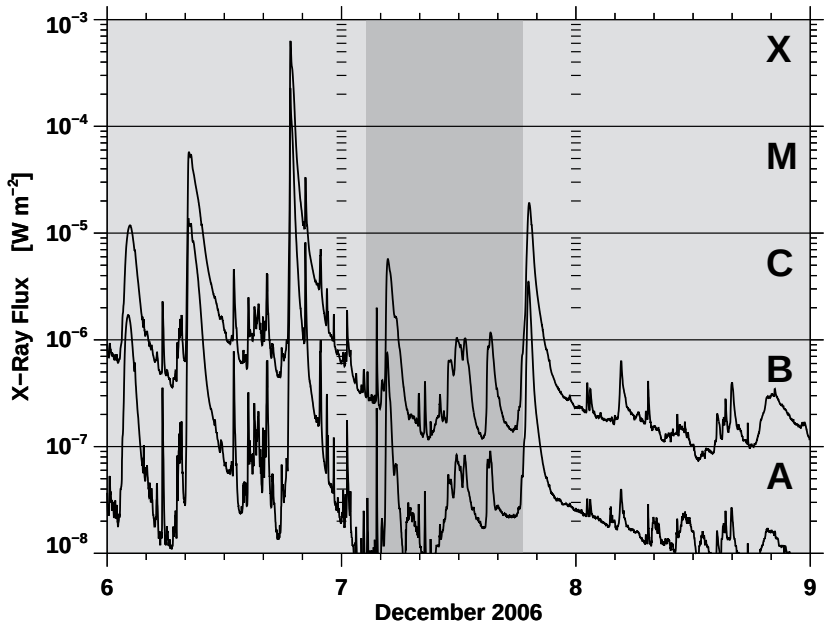

Figure 5.2: One-minute GOES-11 X-ray flux on 2006 December 6–9 obtained in the 0.05–0.40 nm (*bottom*) and 0.1–0.8 nm (*top*) energy channels. The shaded region indicates the time interval of 16 hours covered by *Hinode* data analyzed in the present study.

normal to the solar surface. These data were only corrected for geometrical foreshortening and carefully matched to the G-band images. Unfortunately, no magnetograms were available until 06:30 UT, so that we substituted a Ca II H image in the first panel of Fig. 5.4 and had to resort to a magnetogram taken about 30 min later than the G-band companion in the second panel. Note that the proximity of the active region to the solar limb casts doubt on simply associating the sign of the circular polarization with the sign of the magnetic field component that is normal to the solar surface. In particular, we observe in the NFI magnetograms at the begining of the time-series apparent polarity reversals in limbward penumbral regions for both the major and satellite sunspots, which are clearly related to the almost horizontal magnetic field lines in these regions.

At the beginning of the time-series, the satellite sunspot was much more complex than either the main spot or the developing δ-spot. Four magnetic features with negative polarity and three features with positive polarity play a role in the decay of the satellite sunspot. Over a period of 16 hours, the complexity of the magnetic fields was much reduced. The dominant umbra N3 is separated by a light-bridge from a curved and elongated umbra N2. Brightening of the small-scale features along the light-bridge around 06:00 UT can be taken as an indication that convection penetrates the strong magnetic fields, thus contributing to the decay of the satellite spot. During this decay, the satellite sunspot slowly rotates counterclockwise ($\approx 3.6^\circ$ h^{-1}), as can be seen in Fig. 5.2, using the light-bridge as a tracer. This slow rotation adds up to more than 50° over the course of the observations.

The core of the satellite spot, i.e., N2, N3, and the light-bridge, survive until the end of the time-series. The curved, nonradial penumbral filaments associated with this core can be traced not just in intensity but also in magnetograms. The observed alternating polarities of the filaments could just be projection effects of nearly horizontal magnetic fields. This effect is likewise visible at the limb-side penumbra of the main spot and for the magnetic element N5. Despite its strong proper motion (see above), the photometric and magnetic decay of N5 is slow. Only towards the end of the time-series the pore starts to break up. A conspicuous bright umbral dot appears in the center of the pore around 18:00 UT. Together with two protrusions from the periphery of the pore, it forms a structure like a light-bridge, indicating further erosion of the pore. This erosive process is easier to follow in intensity than in the magnetic field evolution, where N5 remains compact.

Two small pores N1 and P1 are located to the south of the dominant umbra. Magnetic cancellation characterizes the evolution of this small magnetic bipole. Because it is the minority polarity, N1 disappeared earlier than P1. At 10:00 UT only P1 was left. In general, the photometric decay proceeds faster than the decline of the magnetic flux. This also holds true for the third small pore P2, which survived somewhat longer than P1 and can still be detected as a tiny magnetic knot in the G-band image at 18:00 UT.

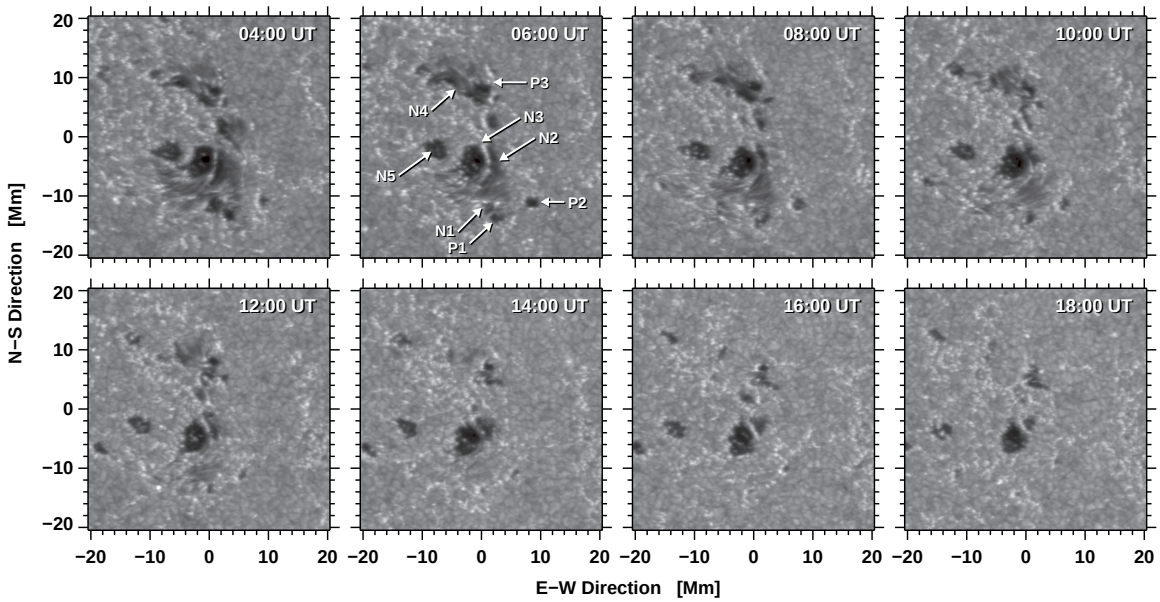

Figure 5.3: Time-series of calibrated and geometrically corrected G-band images of the satellite sunspot in active region NOAA 10930 depicting various stages of its decay. The labels N and P refer to magnetic features with negative and positive polarities, respectively.

To the east of a small umbral core P3, we observe a rudimentary penumbra of opposite polarity, which had dissolved by 14:00 UT. The underlying magnetic field N4 of the rudimentary penumbra was elongated stretching over a distance of about 18 Mm and connecting to the likewise elongated umbral core N2. Together, N2 and N4 define the magnetic neutral line of the satellite sunspot, with strong positive fields at the extremities to the south (P1 and P2) and north (P3). The slow cancellation of flux associated with P3 continues over the 16-hour period and results in long-lived flow features in the decorrelation maps (see Sect. 5.2.4).

5.2.2 Decay Rates

We used morphological thresholding for discerning various solar features in intensity. Images were normalized using eight quiet-Sun regions evenly spread over the time-series. Thus, a weak trend in mean intensity (center-to-limb variation related to solar rotation) was removed from the data. We used a fixed-intensity threshold of $I_{\rm mag} < 0.85$ for strong magnetic features and an adaptive threshold for G-band bright points (see Verma and Denker, 2011), which is given as

$$I_{\rm bp} = 1.15 + 0.2(1-\mu)\,. \tag{5.2}$$

The umbrae were identified using a fixed threshold of $I_{\rm dark} = 0.6$, while sunspot penumbrae cover intermediate intensities from $I_{\rm mag}$ to $I_{\rm dark}$ and granulation lies between $I_{\rm mag}$ to $I_{\rm bp}$. The adaptive threshold was used as a first-order approximation to take into account the center-to-limb variation of G-band bright points because they exhibit an enhanced contrast near the solar limb. The thresholding algorithm also allows us to compute the area for different solar features. The algorithm provides in general a good estimate of the area, except for a few small features and towards the end of the sequence, when only pores are left (for which the borders are erroneously classified as penumbra). If many small pores are present, then their periphery with intensities like penumbra can be significantly larger than the cores of the pores themselves.

The curves in Fig. 5.5 represent the temporal evolution of areas subsumed by umbral cores/pores, penumbrae, and the entire satellite spot (sum of pores, umbra, and penumbra). At the beginning of the time-series, the area of all magnetic features was about 200 Mm^2, of which approximately two thirds were classified as penumbra and the remaining third corresponded to umbral cores/pores. By the end of the time-series only, the latter features stayed on; they covered little over 50 Mm^2, i.e., only one quarter of the area initially covered by the strong magnetic features. The features' decay rates were computed

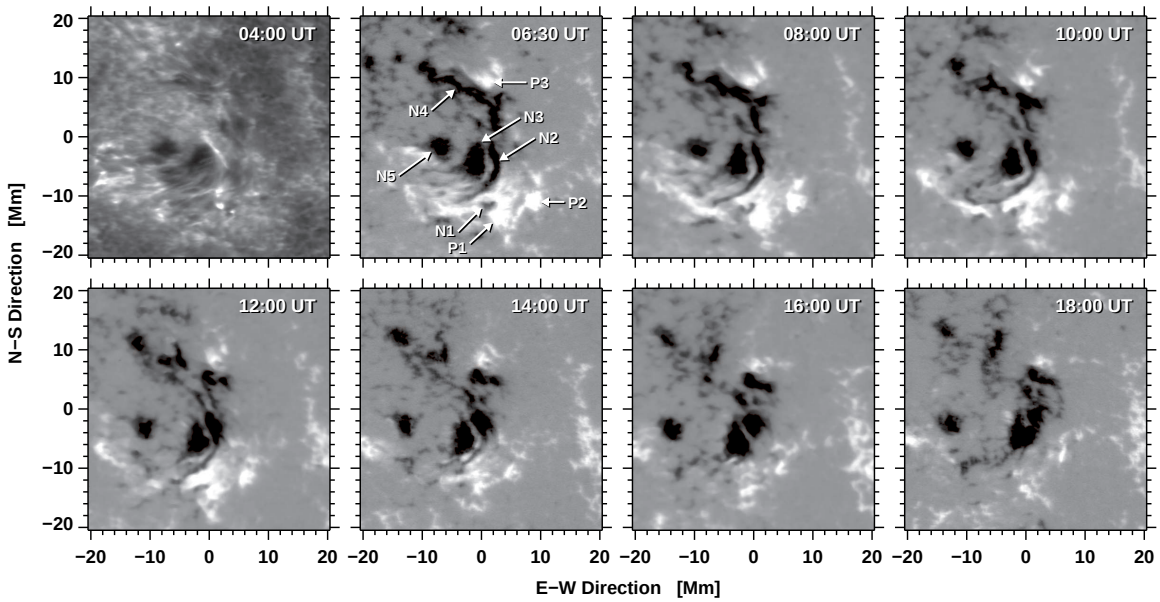

Figure 5.4: Time-series of calibrated and geometrically corrected *Hinode*/NFI magnetograms corresponding to the G-band images in Fig. 5.3. The line-of-sight magnetic field B_{LOS} is displayed in the range of ±800 G as in Fig. 5.1.

using linear regression. We divided the time-series into four time intervals $t_0 - t_1, t_1 - t_2, t_2 - t_3$, and $t_0 - t_3$, because the penumbral decay curve has two peaks at t_0 and t_1, and the penumbra had completely vanished at t_2. The time t_3 was chosen just eight images before the end of the time-series so that artifacts from the subsonic filtering become negligible, and it marks the onset of the M2.0 flare.

Slow penumbral decay is the distinctive feature of the satellite sunspot's temporal evolution. Table 5.2 provides the respective photometric decay rates for the above-mentioned time intervals. The penumbral decay rate significantly increases from $t_0 - t_1$ to $t_1 - t_2$, almost doubling its value to 244.2 Mm^2 day^{-1}. A linear regression might not be the best choice for the penumbral decay rate (130.2 Mm^2 day^{-1}) during the first time interval because there is a sudden decay in the area after the C6.1 flare at 04:45 UT. During the time interval $t_2 - t_3$, the penumbral area decayed by 4.7 Mm^2 in 3.6 h, which corresponds to a decay rate of 31.3 Mm^2 day^{-1}. However, this is just an artifact of the intensity-thresholding algorithm used in classifying penumbral areas, which erroneously labels the boundaries of pores as penumbra. The 1-σ uncertainties for the decay rates are about 2.5 Mm^2 day^{-1}.

Therefore, computing a penumbral decay rate for the entire time period $t_0 - t_3$ is not meaningful. The umbral decay rates do not vary much. The overall value of 73.7 Mm^2 day^{-1} during $t_0 - t_3$ closely represents the decay rates for the shorter intervals. Hence, the penumbra decayed three times faster than the umbral cores. The decay rate of the spot is just the sum of the umbral and penumbral decay rates. The overall spot decay rate in the current study (225.8 Mm^2 day^{-1} for t_0–t_3) is well within the range of previously reported values, e.g., Bumba (1963) found a decay rate of 180 Mm^2 day^{-1} for nonrecurrent groups. Spot decay rates in other studies range from 10–125 Mm^2 day^{-1} (e.g., Moreno-Insertis and Vazquez, 1988; Martínez Pillet, Moreno-Insertis, and Vazquez, 1993; Hathaway and Choudhary, 2008).

5.2.3 Flow Fields in Photosphere and Chromosphere

The two-hour averaged LCT flow maps shown in Fig. 5.6 were computed using the 16-hour time-series of *Hinode* G-band and Ca II H images. We used the satellite sunspot as a reference and aligned all images in the time-series accordingly. These flow maps provide insight into horizontal proper motions in the photosphere and chromosphere. We quantified horizontal proper motions for various solar features (e.g., bright points, granulation, sunspot penumbrae, and strong magnetic features) by applying morphological and adaptive thresholds to G-band images (see Sect. 5.2.1). We applied the same indexing to the Ca II H flow maps to have one-to-one correspondence comparing photospheric and chromospheric flow fields, while neglecting morphological differences. We calculated the mean $\bar{v}$, median v_{med}, maximum v_{max}, 10$^{\mathrm{th}}$ percentile v_{10}, and standard deviation σ_v of the horizontal flow speeds (see Tab. 5.3). The standard

Table 5.2: Decay rates [Mm^2 day^{-1}] of penumbra, umbra, and the entire satellite sunspot (pores, umbrae, and penumbrae) for four time intervals.

Feature	Decay rate [Mm^2 day^{-1}] for four time intervals			
	$t_0 - t_1$	$t_1 - t_2$	$t_2 - t_3$	$t_0 - t_3$
Penumbra	130.2	244.2	31.3	
Umbra	86.4	68.4	67.9	73.7
Spot	216.6	312.6	99.3	225.8

Note: The time intervals are t_0= 03:07 UT, t_1= 08:36 UT, t_2= 14:46 UT, t_3= 18:20 UT.

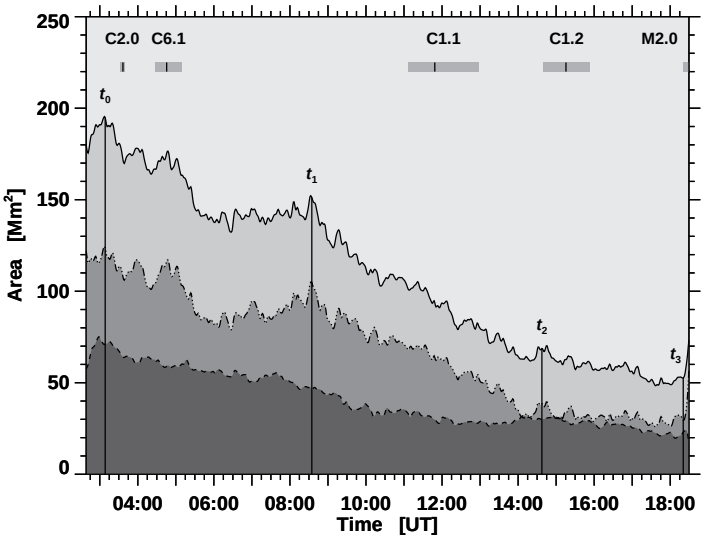

Figure 5.5: Temporal evolution of the area covered by active region NOAA 10930 over the 16-hour period from 02:30–18:30 UT. The area enclosed by umbral cores and pores is displayed with a dashed line. The dash-dot-dotted line refers to the penumbra, whereas the solid line denotes the total area. The times t_0, t_1, t_2, and t_3 delimit time intervals over which the linear photometric decay rates were computed (see Tab. 5.2). The gray bars depict the duration of flares (Tab. 5.1), where the thin black line marks the peak time for flares.

deviation in the flow speed refers to the variance in the data rather than to a formal error. Typical flow characteristics of solar features were reported by Verma and Denker (2011), who also presented values for other time intervals ΔT and cadences Δt. Here, we computed the flow parameters for four time-series with $\Delta T = 2$ h and afterwards averaged them. The average flow parameters of the various solar features are within the expected ranges, except for granulation. Here $\bar{v} = 0.35 \pm 0.21$ km s^{-1}, which is lower than the value of $\bar{v} = 0.47 \pm 0.27$ km s^{-1} mentioned in Verma and Denker (2011). However, the granular flow speed could be lower because of the presence of strong magnetic flux concentrations. Regions of granulation, which are not in close proximity to strong magnetic fields, often showed strong divergence centers, e.g., in the south-west corner of the FOV towards the end of the time-series. In general, photospheric and chromospheric flow parameters are virtually the same. The only notable dissimilarity between the G-band and Ca II H flow maps relates to post-flare loops straddling the dominant pore N3. These loops are most prominent in Ca II H images and result in strong flows of more than 1.14 km s^{-1} (Fig. 5.6: 06:30–08:30 UT). The signature of these post-flare loops is still visible at later time periods. However, the associated flows are much weaker. Other than that, differences in the frequency distributions exist only for the high-speed tail, i.e., the maximum speed v_{max} and, to a lesser extent, the 10^{th} percentile speed v_{10}.

In the two-hour averaged LCT flow maps, the overall impression of flow vectors for G-band and Ca II H images is indistinguishable. The flow patterns around the satellite sunspot are different from regular sunspots (e.g., Balthasar and Muglach, 2010) because of its nonradial penumbra and location within a complex active region. The most intriguing feature in the G-band flow maps is the anticlockwise spiral motion around the dominant umbral core N3. The light-bridge between N2 and N3 marks the location of shear flows, where stronger flows (≈ 0.45 km s^{-1}) linked to the elongated umbra N2 move past weaker flows (≈ 0.17 km s^{-1}) spiraling around the dominant umbra N3. The spiral motion and shear flows were most conspicuous in the first flow map (02:30–04:30 UT), but faded out once the penumbra had decayed. Strong outward motions were present at the outer tips of penumbral filaments associated

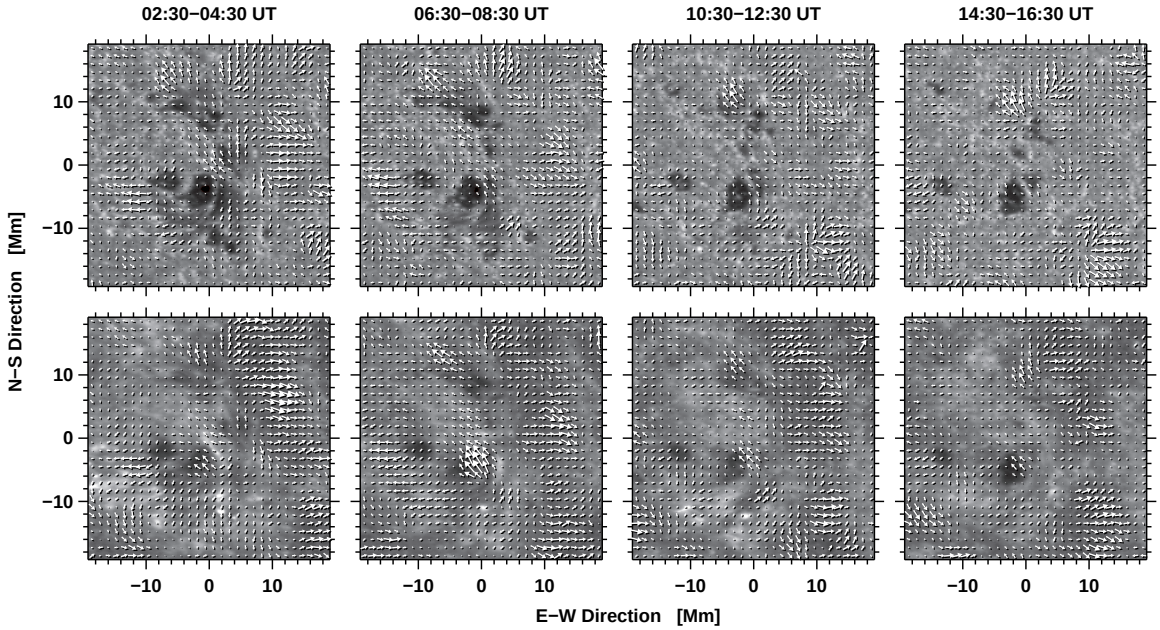

Figure 5.6: Horizontal flow fields averaged over two hours are depicted as arrows overlaid on geometrically corrected G-band (*top*) and Ca II H (*bottom*) images of four time-series. The arrows indicate magnitude and direction of the horizontal proper motions. Arrows with a length corresponding to the grid size indicate velocities of 0.5 km s^{-1}.

with N3 and P3 in the northern part of the FOV. These strong outward motions associated with P3 continue to exist until the end of the time-series and appear as long-lived features in the decorrelation maps of the flow speed (see Sect. 5.2.4).

5.2.4 Decorrelation Times

The lifetime of solar features can be estimated by selecting a reference map at an instance t_i and computing how consecutive maps decorrelate with time. As put forward by Welsch *et al.* (2012), we computed linear Pearson and rank-order Spearman's correlation coefficients for G-band intensity and the corresponding horizontal flow speed. The flow speed maps were computed as sliding one-hour averages centered on each point in time t_i. Pearson's correlation coefficient ρ measures the strength of a linear dependence of two variables x and y, and is computed by dividing the covariance of the two variables by the product of their standard deviations:

$$\rho = \frac{\sum_{i=1}^{N} (x_i - \bar{x})\,(y_i - \bar{y})}{\sqrt{\sum_{i=1}^{N} (x_i - \bar{x})^2 \cdot \sum_{i=1}^{N} (y_i - \bar{y})^2}} \quad \text{with} \quad \bar{x} = \frac{1}{N}\sum_{i=1}^{N} x_i \quad \text{and} \quad \bar{y} = \frac{1}{N}\sum_{i=1}^{N} y_i\,. \tag{5.3}$$

The Spearman's correlation coefficient r_s is similarly defined as the Pearson correlation coefficient between two ranked variables $\mathrm{r}(x)$ and $\mathrm{r}(y)$. We used an IDL algorithm based on the recipe provided in Press *et al.* (1992):

$$r_s = \frac{\sum_{i=1}^{N} \left(\mathrm{r}(x_i) - \overline{\mathrm{r}(x)}\right)\left(\mathrm{r}(y_i) - \overline{\mathrm{r}(y)}\right)}{\sqrt{\sum_{i=1}^{N} \left(\mathrm{r}(x_i) - \overline{\mathrm{r}(x)}\right)^2 \cdot \sum_{i=1}^{N} \left(\mathrm{r}(y_i) - \overline{\mathrm{r}(y)}\right)^2}} \quad \text{with} \quad \bar{x} = \frac{1}{N}\sum_{i=1}^{N} \mathrm{r}(x_i) \quad \text{and} \quad \bar{y} = \frac{1}{N}\sum_{i=1}^{N} \mathrm{r}(y_i)\,. \tag{5.4}$$

The 16-hour time-series was divided into two parts. The first eight-hour time-series covers the phase of penumbral decay, whereas toward the second half the penumbra had already vanished. Autocorrelation functions $r_s(t)$ were computed for intensity and flow maps over circular areas with a diameter of about

Table 5.3: Parameters describing horizontal proper motions for various solar features based on the four G-band and Ca II H time-series with $\Delta T = 2$ h and $\Delta t = 60$ s for four time-series shown in Fig. 5.6.

Feature	Image Type	$\bar{v}$ [km s^{-1}]	$v_{\rm med}$ [km s^{-1}]	v_{10} [km s^{-1}]	$v_{\rm max}$ [km s^{-1}]	σ_v [km s^{-1}]
All	G-Band	0.33	0.29	0.63	1.46	0.21
	Ca II H	0.35	0.28	0.69	2.31	0.25
Granulation	G-Band	0.35	0.31	0.65	1.43	0.21
	Ca II H	0.36	0.30	0.71	2.31	0.25
Penumbra	G-Band	0.28	0.24	0.51	1.22	0.19
	Ca II H	0.30	0.24	0.60	1.36	0.21
Umbra	G-Band	0.20	0.19	0.33	0.60	0.10
	Ca II H	0.30	0.23	0.66	1.19	0.23
Bright Points	G-Band	0.18	0.17	0.32	0.71	0.10
	Ca II H	0.19	0.18	0.32	0.82	0.10

Note: For computing the characteristic parameters of the penumbral flow field, we neglected the last time interval t_2–t_3, since by that time the penumbra had decayed and the features detected as penumbra were just artifacts of the thresholding algorithm. The time period t_0–t_2 was excluded from calculating Ca II H flow parameters of the umbra, since motions along post-flare loops resulted in high flow speeds.

5 Mm and for lag times of up to 300 min. We used 16 and 10 reference frames for the intensity and speed maps, respectively. The number of reference frames had to be reduced to ten in the case of the flow maps because of the 60-minute sliding average. We averaged the autocorrelation functions to have different instances of surface features contributing to our sample. In both cases, the averages are based on 460 min of data, i.e., either $16\times10+300$ min or $10\times10+300+60$ min, where the last term results from the sliding averages. The thus averaged autocorrelation functions are fitted with decaying exponential functions

$$\begin{aligned} r_s(t) &= \Big[r_s\big(f(t_0),f(t_1)\big),\, r_s\big(f(t_0),f(t_2)\big),\, \ldots,\, r_s\big(f(t_0),f(t_{n-1})\big),\, r_s\big(f(t_0),f(t_n)\big)\Big] \\ &\approx \exp\left(-\frac{1}{\tau}t^{\gamma}\right), \end{aligned} \tag{5.5}$$

where the constants τ and γ are derived from a least-squares fit to the measured $r_s(t)$. The function $f(t)$ is either an intensity or a horizontal flow speed map. The lifetimes (or decorrelation times) were calculated for $r_s(t) = 1/2$, i.e.,

$$t_{1/2} = (\tau \ln 2)^{1/\gamma}. \tag{5.6}$$

The case $\gamma = 1$ corresponds to a simple exponential decay, and τ simply refers to the lifetime of the feature. While this is the standard approach for determining lifetimes of solar granulation, this simple decay law no longer holds in the presence of (strong) magnetic fields. Using also γ as a free-fit parameter results in a much improved χ^2-statistics, independent of the magnetic environment. If $\gamma \neq 1$, then τ can no longer be interpreted as lifetime. Therefore, we chose Eq. 6.6 to determine how long solar features last because it removes the entanglement of τ and γ by emphasizing the quality of the fit.

A more detailed analysis shows that $\gamma \approx 1$ in regions with granulation and $\gamma \approx 1/2$ in sunspots are representative values for the autocorrelation functions of intensity features. The autocorrelation functions of flow features are characterized by $\gamma \approx 3/2$, with no major differences between sunspots and granulation. However, the exponent can approach $\gamma \approx 3$ for some long-lived features, e.g., stationary G-band bright points. In these cases, the τ values become very large and can no longer be interpreted as a lifetime.

In Figs. 5.7 and 5.8, we depict the decorrelation-time maps for the intensity and flow speed, respectively. Linear and rank-order correlations qualitatively produce the same decorrelation times. Our type of presentation differs from Welsch *et al.* (2012) because our decorrelation times were computed either for

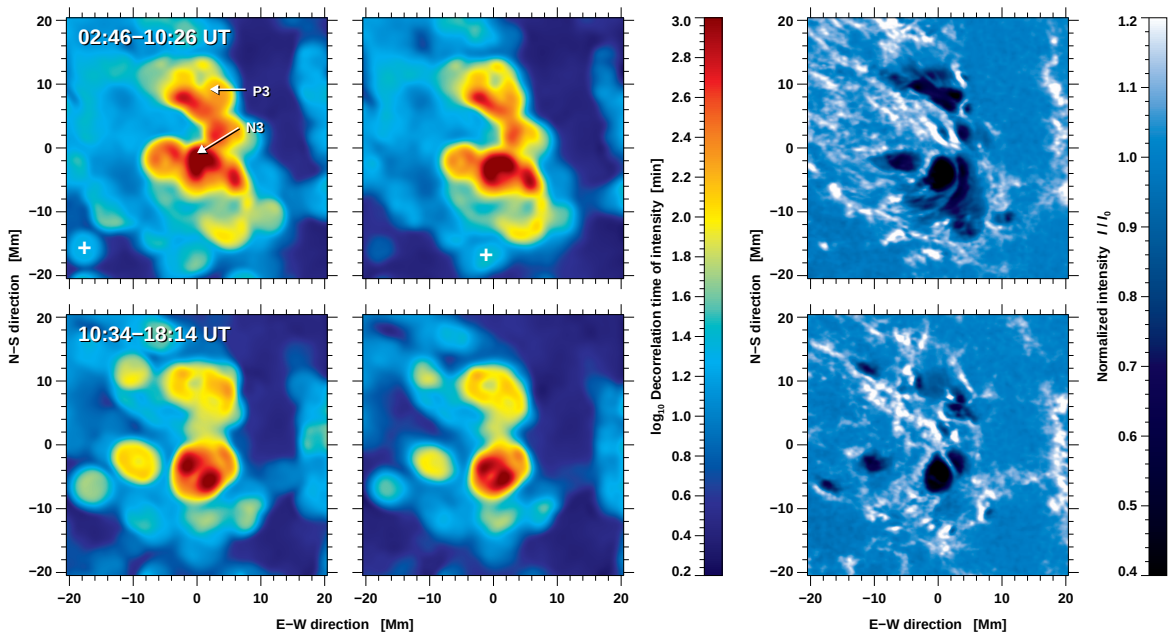

Figure 5.7: Decorrelation times computed using the linear Pearson (*left*) and Spearman's rank order (*middle*) correlation coefficients for the intensity of G-band images. The time-series was divided into two parts, from 02:46–10:26 UT (*top*) and 10:34–18:14 UT (*bottom*). Average G-band images for these time intervals (*right*) clearly show the penumbral decay of the satellite sunspot.

each pixel in the FOV (Pearson's ρ) or for a 4×4-pixel grid (Spearman's r_s). The coarser sampling is required because of the computational overhead in ranking the variables. These maps were then smoothed by a Gaussian with a FWHM of 1200 km. We inferred from the decorrelation maps of the intensity that the magnetic features have longer lifetimes than granulation, which is expected.

Regions of granulation can be extracted from the average G-band images shown in the right panels of Fig. 5.7, where they correspond to the dark blue regions to the west of the satellite sunspot. Typical granular lifetimes derived from the linear and rank-order decorrelation maps are about 3.1 min and 4.6 min, respectively. In the rank-order case, we find a standard deviation of the frequency distributions of about 1 min. Because of a pronounced tail towards longer lifetimes, the standard deviation of the linear case is much higher. However, the median is close to 3 min in both cases. There is no significant difference in the granular lifetimes during the first and second halves of the time-series. Our findings are in good agreement with the original work of Bahng and Schwarzschild (1961) and match accurately the findings of Title *et al.* (1989).

G-band bright points show two types of behavior: either they remain stationary as at the supergranular boundary at the western periphery of the FOV or they stream away from the satellite sunspot towards the main spot. In the long-duration G-band images, the bright points coalesce into strands indicating preferential paths taken by small-scale magnetic features. Similar motion patterns were observed for the moat flow of the decaying sunspot (Verma *et al.*, 2012). However, thread-like concentrations of magnetic field were also observed by Strous *et al.* (1996) for an emerging active region. Thus, preferential paths for the migration of small-scale magnetic elements might be a common property of flux emergence, removal, and dispersal. The factor that G-band bright points are either stationary or moving does not have an impact on their lifetimes. The light-blue to turquoise colors denote lifetimes of about 35 min in linear and 25 min in rank-order decorrelation maps. The distributions in both cases have a pronounced high-lifetime tail. Note that individual, long-lived, and stationary G-band bright points can create artifacts, which appear as disk-shaped features (e.g., marked with white + in Fig. 5.7) in the smoothed decorrelation maps. This is because as long as they are fully contained in the circular correlation window, their presence outweighs any other contribution to the correlation function.

The typical lifetime of strong magnetic features (pores, umbrae, and penumbrae) is about 200 min and 235 min using linear and rank-order correlations. There is virtually no difference in the respective distributions of magnetic features, except that the area covered by extremely long-lived feature (lifetimes

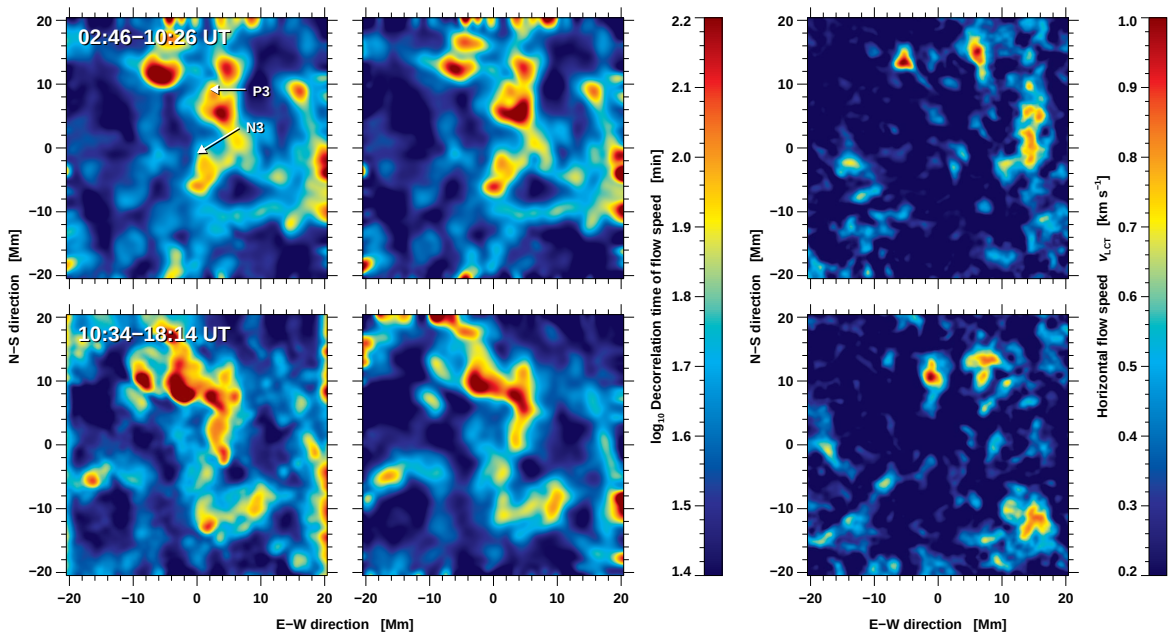

Figure 5.8: Decorrelation times computed using the linear Pearson (*left*) and Spearman's rank order (*middle*) correlation coefficients for the horizontal flow speed. The time-series was divided into two parts from 02:46–10:26 UT (*top*) and 10:34–18:14 UT (*bottom*). Average flow speed maps (*right*) show several small regions with enhanced flows in the vicinity of long-lasting flow features.

$>$ 500 min) is moderately higher (1.8 Mm^2) in the case of rank-order correlations as compared to linear correlations (1.2 Mm^2). The photometric decay of the satellite sunspot also leaves its mark on the decorrelation maps. The area covered by features living longer than 100 min decreased from 160 Mm^2 to 80 Mm^2, while in parallel the complexity of the long-lived features decreased. The lifetime in the vicinity of the umbral core P3 was about 300 min during the first half of the time-series. In the second half, erosion of the rudimentary penumbra and slow cancellation of magnetic flux near P3 led to significantly shorter lifetimes (about 100 min) in that region. The only conspicuous feature that remained in the latter decorrelation map is a compact oval region associated with the dominant umbral core N3. In two small kernels with an area of about 2 Mm^2, the lifetime exceeds 1000 min.

Decorrelation maps of the flow speed are presented in Fig. 5.8. The right panels show the averaged, long-duration flow maps. Flow speeds are suppressed in regions containing strong and weak magnetic fields. Typical values are 0.24 ± 0.15 km s^{-1}, where the standard deviation refers to the variance within the region covered by the satellite sunspot and the surrounding G-band bright points. Higher flow speeds (0.52 ± 0.11 km s^{-1}) are encountered in quieter areas. Especially in proximity to supergranular boundaries near the western periphery of the FOV, flow speeds approaching 1 km s^{-1} are measured. For example, a strong divergence region (see Fig. 5.6 at time periods 10:30–12:30 UT and 14:30–16:30 UT) becomes apparent in the lower-right corner of the FOV in the second half of the time-series.

Two small flow kernels of about 1 Mm^2 possessing high-speed values approaching 1 km s^{-1} are related to the decay of the rudimentary penumbra near the umbral core P3 as well as to slow flux cancellation in that region. These flow kernels also leave an imprint in the decorrelation maps. Note that the logarithmic scale of the decorrelation times significantly differs for G-band intensities and horizontal flow speeds. Surprisingly, the lifetimes associated with the dominant umbral core N3 are much lower than the ones for P3, i.e., horizontal flows are more persistent near P3. Thus, flows contribute to the decay of the satellite sunspot most noticeably in regions with weaker and less compact magnetic fields. Persistent flows have lifetimes typically over 80 min and survive up to 160 min. The frequency distributions of flow lifetimes derived from linear and rank-order decorrelation maps are virtually same. In both cases, distributions are broad and do not have a high-velocity tail. In comparison to Fig. 5.7, higher fine-structure contents become immediately apparent in Fig. 5.8, which might be explained by the shorter lifetimes of horizontal flow patterns.

5.2.5 Homologous M2.0 Flare

An M2.0 flare started in active region NOAA 10930 at 18:20 UT towards the end of the time-series. Time-resolved Ca II H flare kernels are shown in the right panel of Fig. 5.1. The color-coded flare kernels are based on images with the full cadence of 30 s. The first indications of this two-ribbon flare were associated with the remnants of the negative polarity features around N2 and N3 in the satellite sunspot. The second ribbon is located some 10–15 Mm away in a network region to the west with positive polarity. Flare brightenings related to the δ-spot appear delayed by a few minutes. Furthermore, remote brightenings appear in a negative-polarity Ca II H plage region towards the north-west. A small filament above the neutral line formed by the remnants of N2/N3 and P1/P2 erupted during the flare. The location of this filament was extracted from BBSO Hα full-disk images and carefully matched with the magnetogram of Fig. 5.1.

The X6.5 flare on 2006 December 6 was also a two-ribbon flare. Here, the flare ribbons were located inside the umbra of the main spot and along the neutral line separating the main and δ spots. A filament located above this neutral line (see F1 in Fig. 11 of Balasubramaniam *et al.*, 2010) erupted as a result of the flare and produced an impressive Moreton wave. The latter flare ribbon extended all the way to the satellite sunspot, which at that time was still connected to the main spot by a wide band of penumbral filaments. Rapid penumbral decay initiated by the X6.5 flare characterize this penumbral region. Deng *et al.* (2011a) find no indications for flux emergence in this regions, but attribute the initiation of the flare to (shear) flows along the magnetic neutral line, which were enhanced just before the onset of the flare. The rapid penumbral decay within the band connecting main and satellite sunspots (Wang, Deng, and Liu, 2012) also marks the beginning of the demise of the satellite sunspot.

Even though separated by more than one order of magnitude in X-ray flux, the X6.5 and M2.0 flares share a variety of traits, so that they can be considered as homologous flares: both are two-ribbon flares, filament eruption is observed in both cases, the reconfiguration of the magnetic field topology involves the satellite sunspot, and flux removal rather than emergence is a decisive means in the flare process.

Nonetheless, the X6.5 and M2.0 flares also deviate in some aspects. While rapid penumbral decay is a characteristic of the X6.5 flare, it only plays a very localized role in the M2.0 flare, where slow penumbral decay is the most prominent feature. Balasubramaniam *et al.* (2010) found that the centroid of the high-energy radiation during the X6.5 flare is associated with the developing δ-spot, whereas the Moreton wave has its origin in the satellite sunspot. The absence of a wave for the M2.0 flare does not preclude the characterization of X6.5 and M2.0 flares as homologous because, even though Moreton waves have been observed for M-class flare (Warmuth *et al.*, 2004a,b), their frequency of occurrence drops with diminishing X-ray flux. In summary, all observations agree with the scenario that while the M2.0 flare is initiated at the satellite sunspot, the strong magnetic field gradients in the vicinity of the δ-spot are responsible for the stronger flare emission.

5.3 Conclusions

We have presented a case study involving the flare-prolific active region NOAA 10930, where a satellite sunspot decayed and flux removal during the decay was causally linked to two homologous X6.5 and M2.0 flares. Our major findings with respect to this slowly decaying sunspot are:

- Nonradial penumbral filaments indicate the presence of twisted magnetic fields in the satellite sunspot.
- Shear flows were observed along a light-bridge between two umbral cores in the center of the satellite sunspot, which is in close proximity to the magnetic neutral line. The shear flows continue as long as penumbral filaments exist in proximity to the central umbral cores.
- Slow rotation of the satellite sunspot ($\approx 50^\circ$ in 14 hours), as marked by the tilt angle of the light-bridge, contributes to the alteration of the magnetic field topology.
- The light-bridge is becoming stronger while the sunspot is decaying, indicating that it is now easier for convective motions to penetrate strong magnetic fields.

- Photometric decay rates observed in the satellite sunspot are in good agreement with other studies (Bumba, 1963; Moreno-Insertis and Vazquez, 1988; Martínez Pillet, Moreno-Insertis, and Vazquez, 1993; Hathaway and Choudhary, 2008).

- We find evidence for localized 'rapid' penumbral decay (Wang *et al.*, 2004; Deng *et al.*, 2005; Liu *et al.*, 2005) near the central umbral core in response to a C6.1 flare. However, 'slow' penumbral decay is the more prominent characteristic of the decaying satellite sunspot, particularly near the northern part of the spot.

- We find persistent flow kernels with velocities up to 1 km s^{-1} close to the region of slow penumbral decay. The decorrelation times in this region range from 80–160 min, which are among the longest-lasting flow structures of the time-series.

- Even though the intensity-based decorrelation times are high for the dominant umbral core (typical values of about 200 min, but exceeding 1000 min in some small kernels), the flow-based decorrelation times are significantly lower compared to the region with slow penumbral decay. Therefore, the satellite sunspot decays most noticeably in regions with weaker and less compact magnetic fields.

In summary, we conclude that the decay of the satellite sunspot led to a substantial restructuring of the magnetic field topology. Thus, flux removal has to be considered an important ingredient in triggering flares, as we have discussed in the context of the homologous X6.5 and M2.0 flare. We used the phrase "flux removal" because even though flux submergence might be the more likely scenario, we cannot exclude that flux cancellation is a contributing factor. Ultimately, only results from local helioseismology can answer this question (e.g., Kosovichev, 2011). The presence of the δ-spot provided the environment for even stronger flare emissions. However, rotation, twist, and rapid proper motions of this δ-spot will soon become the hallmark of the flare-prolific active region NOAA 10930.

In addition, we adapted and extended the autocorrelation analysis of Welsch *et al.* (2012) to study the lifetime of intensity and flow features. The novel approach of aggregating decorrelation times into two-dimensional maps will be a valuable tool for investigating other dynamic processes of the active and quiet Sun.

Chapter 6

Statistical Properties of the Dynamical Environment around Pores

The magnetic flux on the solar surface appears in many forms starting from the inter-granular dark lanes to azimuth centers (ACs, Keppens and Martinez Pillet, 1996), over magnetic knots to pores, and finally to the magnificent sunspots. Azimuth centers are magnetic structures, which have the size of a pore with a central magnetic field of up to 1400 Gauss and a filling factor of about 50%. They are characterized by a horizontal magnetic field component that covers all horizontal angles with respect to a central point. No darkening of the continuum intensity is observed for ACs, which indicates that the magnetic flux is not strong enough to suppress convection. There are indications that ACs represent the nascent stage of pore formation. Pores, which are often described as sunspots lacking a penumbra (Bray and Loughhead, 1964), are formed by the advection of magnetic flux and clustering of magnetic elements. Once the size becomes larger than 300 km, pores appear dark, because the magnetic field is now sufficient to suppress the energy transport by convection (Keller, 1992). The magnetic flux linked to pores at their periphery provides a mechanism for keeping them in their existing state and for contributing to further growth. If magnetic flux from the surroundings is constantly added to pores, then their growth can be maintained (Wang and Zirin, 1992).

Pores demarcate the transitory state between small-scale magnetic elements and sunspots. The transition from a pore to a sunspot is driven by changes of the enclosed magnetic flux. According to Rucklidge, Schmidt, and Weiss (1995), there is an overlap between large pores and small sunspots. The convective mode responsible for this overlap sets in suddenly and rapidly. The consequence of this convective interchange is the filamentary penumbra, which is responsible for the energy transport across the boundary of the spot into the external plasma. The new mode of filamentary convection sets in, when the inclination θ to the vertical of the photospheric magnetic field exceeds some critical value. Thus, pores and sunspots form a single family parametrized by θ, and the two branches are linked by an unstable branch (see Fig. 2 in Rucklidge, Schmidt, and Weiss, 1995). Hence, pores as penumbra-lacking features are ideally suited to study the interaction between the vertical magnetic field and the surrounding convective motions.

Keil *et al.* (1999) observed in an active region with newly emerging magnetic flux that pores are formed by an increased concentration of magnetic fields at the supergranular boundaries, and that the surface motions are responsible for the increased magnetic field concentration. They found that downflows appear in annular, ring-like structures around most of the pores and that the LOS component of the magnetic flux increases with the downflow velocity. The strength of the LOS velocity component in pores increases as one moves down from the upper to the lower photosphere. Downflows around pores are reported in many studies (e.g., Hirzberger, 2003; Sankarasubramanian and Rimmele, 2003). In addition, Keil *et al.* (1999) applied LCT to calculate horizontal surface velocities. They found a decrease in the horizontal surface velocity inside the pore, which they related to an increase of the magnetic field strength. This finding was later confirmed by Hirzberger (2003).

Roudier, Bonet, and Sobotka (2002) observed that inside the pore the horizontal plasma velocities are smaller by a factor of two to three compared to velocities outside of the pore. The highest velocities inside the pore are located near the pore's border, which are contaminated by flows penetrating from the outside. This motion at the periphery of a pore is instigated by external plasma flows deposited by explosive

Table 6.1: List of active regions containing pores observed in *Hinode* G-band images. Apart from active regions, date, and time of observations, the number of one-hour sequences N_s and number of pores N_p in the FOV are also listed.

Active region	Date	Time	N_s	N_p
NOAA 10921	20061103	16:41 UT	3	54
	20061104	17:11 UT	4	51
	20061104	17:41 UT	2	18
	20061105	12:39 UT	2	23
NOAA 10926	20061130	13:09 UT	6	30
	20061203	13:39 UT	6	16
	20061204	14:09 UT	15	23
NOAA 10930	20061207	21:05 UT	30	242
NOAA 10933	20070110	22:05 UT	6	29
NOAA 10938	20070115	19:49 UT	7	57
	20070116	20:19 UT	5	51
	20070116	08:09 UT	10	79
	20070117	08:39 UT	5	19
	20070117	09:09 UT	3	4
	20070118	09:40 UT	6	7
	20070119	10:10 UT	6	23
	20070120	10:39 UT	9	46
	20070120	20:19 UT	2	1
NOAA 10940	20070201	21:19 UT	5	26
	20070201	21:50 UT	2	17
	20070202	22:20 UT	3	29
	20070202	22:49 UT	3	31
	20070203	00:29 UT	5	45
	20070203	01:00 UT	4	58
	20070204	01:30 UT	5	19
	20070204	02:00 UT	6	21
	20070205	02:30 UT	4	16
	20070205	02:59 UT	3	7
no region No.	20070308	03:29 UT	3	3
NOAA 10953	20070427	04:00 UT	3	16
	20070428	04:30 UT	10	90
	20070428	05:00 UT	9	63
	20070429	05:30 UT	9	51
	20070429	05:59 UT	7	19
	20070430	06:29 UT	1	6
	20070430	07:00 UT	3	17
	20070501	07:30 UT	2	7
	20070501	03:30 UT	2	3
	20070502	04:30 UT	6	3

Active region	Date	Time	N_s	N_p
NOAA 10953	20070503	05:00 UT	4	11
	20070503	05:30 UT	5	3
	20070504	06:00 UT	1	3
	20070504	06:29 UT	3	3
	20070505	07:00 UT	7	8
	20070505	07:30 UT	5	10
	20070506	08:00 UT	2	2
NOAA 10956	20070516	08:30 UT	1	9
	20070517	09:00 UT	1	2
	20070517	09:30 UT	1	4
	20070518	10:00 UT	1	6
	20070518	10:30 UT	1	8
	20070519	11:00 UT	1	7
	20070521	11:30 UT	1	5
	20070521	12:00 UT	1	8
	20070522	12:30 UT	1	1
	20070522	13:00 UT	1	1
NOAA 10960	20070604	13:30 UT	1	4
	20070604	14:00 UT	1	4
	20070609	14:30 UT	1	2
	20070609	15:00 UT	1	3
	20070612	15:30 UT	1	1
NOAA 10969	20070824	16:30 UT	2	2
	20070831	17:30 UT	4	9
NOAA 10978	20071207	18:00 UT	4	41
	20071208	04:43 UT	6	71
	20071209	05:13 UT	9	87
	20071209	05:43 UT	7	69
	20071210	06:13 UT	9	90
	20071210	06:43 UT	4	44
	20071211	07:13 UT	3	22
	20071212	11:25 UT	1	34
	20071212	11:56 UT	8	263
	20071213	12:25 UT	9	264
	20071214	12:55 UT	4	129
	20071214	13:25 UT	8	183
	20071215	13:55 UT	9	124
NOAA 10978	20080106	14:25 UT	5	6
Total			**357**	**2863**

events. These authors also found ring-like structures of positive divergence around the pore, which they related to continuous explosive events in the granulation around the pore. Thus, they confirmed the results of Sobotka, Brandt, and Simon (1999), i.e., the existence of so-called rosettas – a typical diverging velocity pattern related to mesogranulation. Hirzberger (2003) found that the horizontal flow fields are asymmetric and that the absolute values of horizontal flow velocities are much smaller than the velocities observed by Roudier, Bonet, and Sobotka (2002). Furthermore, positive divergence structures are observed surrounding the pores, i.e., horizontal inflows were observed, which can be explained in terms of the continuous downflows detected in LOS velocity maps. Hirzberger (2003) also described the formation of a proto-pore or magnetic knot, which he explained by convective collapse (Stein and Nordlund, 2006).

Deng *et al.* (2007) observed a decaying sunspot in white-light to investigate the evolution of flows and horizontal proper motions in an active region. LCT was used for the computation of horizontal flow fields. The study confirmed the existence of a divergence line inside the penumbra (Denker, 1998). The moat flow, which is a characteristic of sunspots, was also observed around a residual pore. Zuccarello *et al.* (2009) found evidence of MMFs and moat flow in the vicinity of a naked sunspot, i.e., even when penumbral filaments and the Evershed flow were not present (cf., Cabrera Solana *et al.*, 2006). Verma

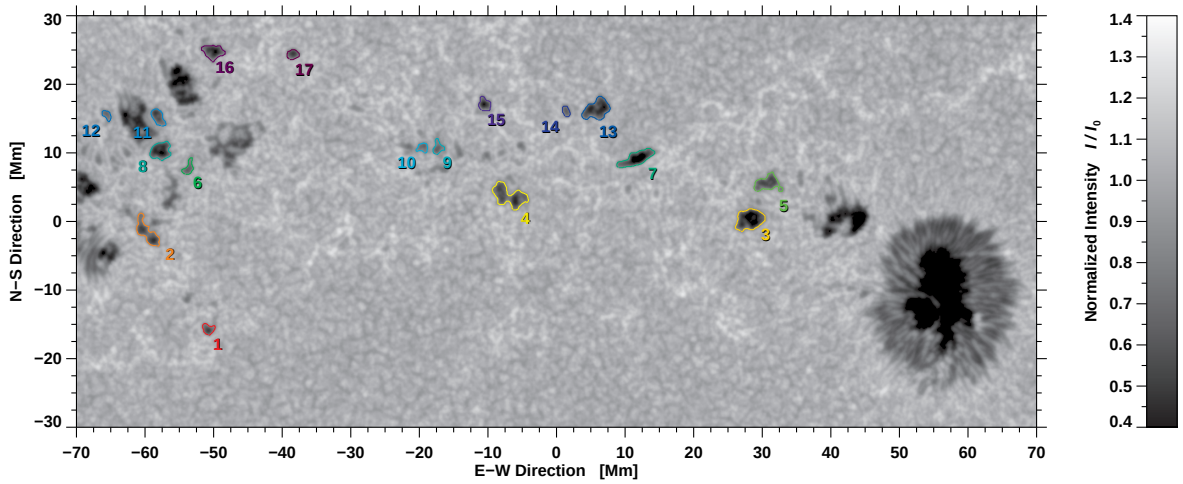

Figure 6.1: *Hinode*/SOT time-averaged (one-hour) G-band image of active region NOAA 10921 observed on 2006 November 3. Pores selected for further analysis are marked by rainbow-colored contours.

et al. (2012) also observed MMFs and moat flow around a spot with almost no filamentary penumbra. Vargas Domínguez *et al.* (2010) studied flow fields around seven pores by computing horizontal proper motions using G-band images and found no trace of moat flow around pores. They do observed inward and outward motion around pores related to exploding granules. Sainz Dalda, Vargas Domínguez, and Tarbell (2012) studied the same naked sunspot as Zuccarello *et al.* (2009) and concluded that MMFs around this spot can be explained in the same way as for sunspots with penumbral filaments, because the naked sunspot despite has almost the same magnetic structure as a sunspot with penumbra. The connection between moat flow and MMFs around pores is still an open question.

In summary, all these research efforts are just case studies focusing on individual pores, which have different evolutionary paths. To generalize and to make the picture complete, one has to perform a detailed statistical analysis, including the pore's morphology, horizontal flows, evolutionary stage (young, mature, or decaying), complexity of the surrounding magnetic field, and proximity to sunspots or cluster of G-band bright points. *Hinode*/SOT data offer the opportunity for this type of research, because of the uniform data quality and the absence of seeing, which allows us to directly compare pores in different environments and at various stages of their evolution.

6.1 Observations

Tracking horizontal proper motions works best on images with high-contrast and rich structural details. G-band (λ430.5 nm) images fulfill these requirements. On *Hinode*, G-band images are captured by SOT/BFI. In Verma and Denker (2011), the data selection and analysis steps, were described in detail. However, in the following, we briefly recapitulate the most important facts, which are relevant to this statistical study. The initial data selection criterion was that there should be at least a one-hour sequence with a time cadence better than 100 s. For the time period from November 2006 – January 2008, we found about 153 datasets with 1024×1024 pixels and 48 with 2048×1024 pixels. The paucity of full-resolution data limited us to images with only half the spatial resolution ($0.11''$ pixel^{-1}) and 2×2 pixels binning. The typical time-cadence was between 30–90 s. In total, we had about 557 one-hour sequences covering various scenes on the solar surface, out of which 410 contained active regions. However, *Hinode* mostly observed the same set of active regions over a period of several days. Hence, we have only twelve distinct active regions in the database, which introduces a bias into the statistical study. In Tab. 6.1 all the observed active regions are listed. Nevertheless, the present study is the first attempt to use the *Hinode* data base to establish a statistically meaningful characterization of the horizontal flow fields associated with solar pores.

Before applying LCT, the selected datasets were divided into one-hour time-sequences. Basic image-calibration steps were performed on the images such as subtraction of dark current, correction of gain, and removal of spikes caused by high-energy. After that the images were corrected for geometrical-

Table 6.2: Parameters describing the morphology and the associated flow field of pores shown in Fig. 6.1.

N_{pore}	A_{pore} [Mm^2]	L_{pore} [Mm]	$A_{\mathrm{pore}}/L_{\mathrm{pore}}$ [Mm]	I_{min}	I_{mean}	ε	θ [°]	v_{mean} [km s^{-1}]	$\nabla \cdot v$ [10^{-3} s^{-1}]	$\nabla \times v$ [10^{-3} s^{-1}]
1	1.99	5.95	0.33	0.50	0.70	0.60	−20.44	0.12	−0.22	0.05
2	6.60	14.66	0.45	0.45	0.69	0.94	−54.54	0.19	−0.24	0.11
3	9.95	13.12	0.76	0.30	0.57	0.73	17.96	0.19	−0.18	−0.03
4	10.44	17.71	0.59	0.42	0.67	0.86	−24.30	0.17	−0.19	−0.02
5	6.19	13.26	0.47	0.52	0.69	0.80	7.48	0.22	−0.17	0.02
6	1.99	7.01	0.28	0.63	0.75	0.87	66.60	0.09	−0.13	0.00
7	7.56	14.02	0.54	0.28	0.59	0.95	23.54	0.28	−0.28	0.09
8	6.00	10.16	0.59	0.39	0.60	0.59	24.81	0.13	−0.11	0.01
9	2.07	6.75	0.31	0.63	0.77	0.71	87.17	0.09	−0.10	0.02
10	1.60	5.42	0.30	0.65	0.77	0.58	5.84	0.18	−0.11	0.02
11	3.32	7.73	0.43	0.49	0.69	0.85	−58.43	0.11	−0.14	−0.03
12	1.27	4.87	0.26	0.67	0.77	0.83	−54.08	0.06	−0.01	−0.01
13	8.58	12.91	0.66	0.40	0.62	0.76	29.23	0.20	−0.22	−0.01
14	1.30	4.53	0.29	0.63	0.74	0.80	−68.86	0.10	−0.19	0.11
15	2.68	6.65	0.40	0.40	0.67	0.64	−62.26	0.12	−0.20	0.08
16	5.03	9.82	0.51	0.38	0.64	0.74	−8.75	0.18	−0.19	0.02
17	1.94	5.37	0.36	0.49	0.68	0.61	9.78	0.13	−0.06	−0.11

Note: The area A_{pore} covered by the pore, the length L_{pore} of the circumference, the ratio $A_{\mathrm{pore}}/L_{\mathrm{pore}}$, the minimum I_{min} and the mean I_{mean} intensities, the average flow speed v_{mean}, the mean divergence $\nabla \cdot v$, and the mean vorticity $\nabla \times v$.

foreshortening and resampled in a regular grid of 80 km × 80 km. Images were aligned with respect to the first image in a sequence by applying the shifts between consecutive images in succession using cubic spline interpolation with subpixel accuracy. These shifts were calculated using the cross-correlation over the central part of the images. The signature of the five-minute oscillation was removed from the images by using a three-dimensional Fourier filter with a cut-off velocity of 8 km s^{-1} corresponding roughly to the photospheric sound speed. A high-pass filter in form of a Gaussian kernel with a FWHM of 15 pixels (1200 km) was applied to all images. The application of such a filter was required to suppress strong intensity gradients. The LCT algorithm of (Verma and Denker, 2011) was based on the seminal work of November and Simon (1988). The algorithm operates on subimages with a size of 32×32 pixels corresponding to 2560 km × 2560 km on the solar surface. A Gaussian similar to the kernel used in the high-pass filter was used as an apodization/sampling window constraining the cross-correlation to structures with a size of 1200 km i.e., roughly the size of a granule. After computation of the cross-correlation function, the position of its maximum is found using a parabolafit to the neighboring pixels. The calculated and averaged flow maps build the foundation of this study.

6.2 Selection of Pores

To prepare the data, a CLV correction to the G-band images using a linear regression in $\mu = \cos(\theta)$ was applied, where μ is the cosine of the heliocentric angle θ. While computing the LCT flow maps, the images were not CLV-corrected, because the high-pass filter takes care of any large-scale intensity variation. The corrected and averaged image was then normalized so that the quiet Sun intensity I_0 equals to unity. Pores are dark features on the solar surface. Therefore, we required that at least one dark core ($I_{\mathrm{core}} < 0.6 I_0$) consisting of 10 pixels is contained within a pore. In foreshortening-corrected G-band images, we restricted the size of pores to 125 pixels (0.8 Mm^2) and 15625 pixels (100 Mm^2). We considered features smaller than the lower limit as magnetic knots and features larger than the higher limit as sunspots while neglecting a certain overlap towards higher end. Going beyond the limitations of 'simple' thresholding, we used an anisotropic diffusion filter (see Perona and Malik, 1990) instead of simple Gaussian smoothing. The Perona-Malik filter uses the anisotropic diffusion equation, which smoothes the image without blurring the boundaries of an object, hence making the automatic selection of pores by intensity thresholds more efficient (Fig. 6.1). However, to finally confirm, if the selected

Table 6.3: Parameters describing the morphology of pores and the associated flow field.

Parameters	Isolated	Residual
A_{pore} [Mm^2]	3.11	16.90
L_{pore} [Mm]	6.73	16.49
$A_{\text{pore}}/L_{\text{pore}}$ [Mm]	1.02	1.10
ε	0.25	0.58
θ [°]	−43.6	85.20
I_{min}	0.37	0.24
I_{mean}	0.60	0.48
v_{mean} [km s^{-1}]	0.18	0.29
$\nabla\, v$ [10^{-3} s^{-1}]	−0.05	−0.14
$\nabla \times v$ [10^{-3} s^{-1}]	0.01	0.10

feature is a pore, we resorted to visual inspection. We deselected all features with any signature of penumbral filaments. In total, we ended up with 2863 pores for further analysis (Tab.6.2).

6.3 Results

6.3.1 Parameters Describing Morphology of Pores and Associated Flow Fields

The selection procedure results in binary masks containing all pixels belonging to pores. The masks provide easy access to many physical quantities. Using the standard tools for blob analysis (Fanning, 2003), parameters describing the morphology of pores and the associated flow field were derived. We measured area covered by pores A_{pore}, the length of the circumference L_{pore}, the mean intensity I_{mean}, the average flow speed v_{mean}, the divergence $\nabla \cdot v$, and the vorticity $\nabla \times v$ within pores. Fitting an ellipse to each pore yields among other parameters the numerical eccentricity $\varepsilon = \sqrt{1-(b/a)^2}$, where a is the semimajor axes and b is the semiminor axes. The angle of the major axis with the horizontal θ corresponds to lines of equal latitude because of the chosen deprojection method. In Fig. 6.1, the one-hour averaged and corrected image of active region NOAA 10921 observed on 2006 November 3 is shown. The rainbow-colored contours mark pores selected by using the above described intensity threshold. All 17 pores were fitted with ellipses, and all the discussed parameters were computed, which are compiled in Tab. 6.2.

6.3.2 Illustrative Examples of the Data Analysis

In Fig. 6.2, two pores out of 2863 pores are presented as an example to explain the data analysis and parameters obtained for further study. We compared two pores with different histories and backgrounds: an isolated pore in the vicinity of a sunspot and a residual pore, i.e., the end product of a decaying sunspot. The isolated pore was located in a supergranular cell within active region NOAA 10940 observed on 2007 February 3, close to a fully developed sunspot, whereas the residual pore was the end product of a satellite sunspot in the vicinity of the highly active and flare-prolific region NOAA 10930 observed on 2006 December 7. We used the one-hour averaged image as background with the averaged flow vectors overlaid on it. As seen in the averaged image, both pores are surrounded by a bright intensity ring. However, in case of the residual pore, the bright ring is not regular. An annular structure of positive divergence (not shown in the figure) envelops the bright intensity ring like an onion peel. The positive divergence structure contained respective divergence centers, which can be related to exploding granules. A similar ring of divergence centers around a pore was previously observed by Roudier, Bonet, and Sobotka (2002). Inflows inside and outflows in the exterior are found in pores, which are not necessarily symmetric. Around the isolated pore the outflows are rather stronger than the inflows.

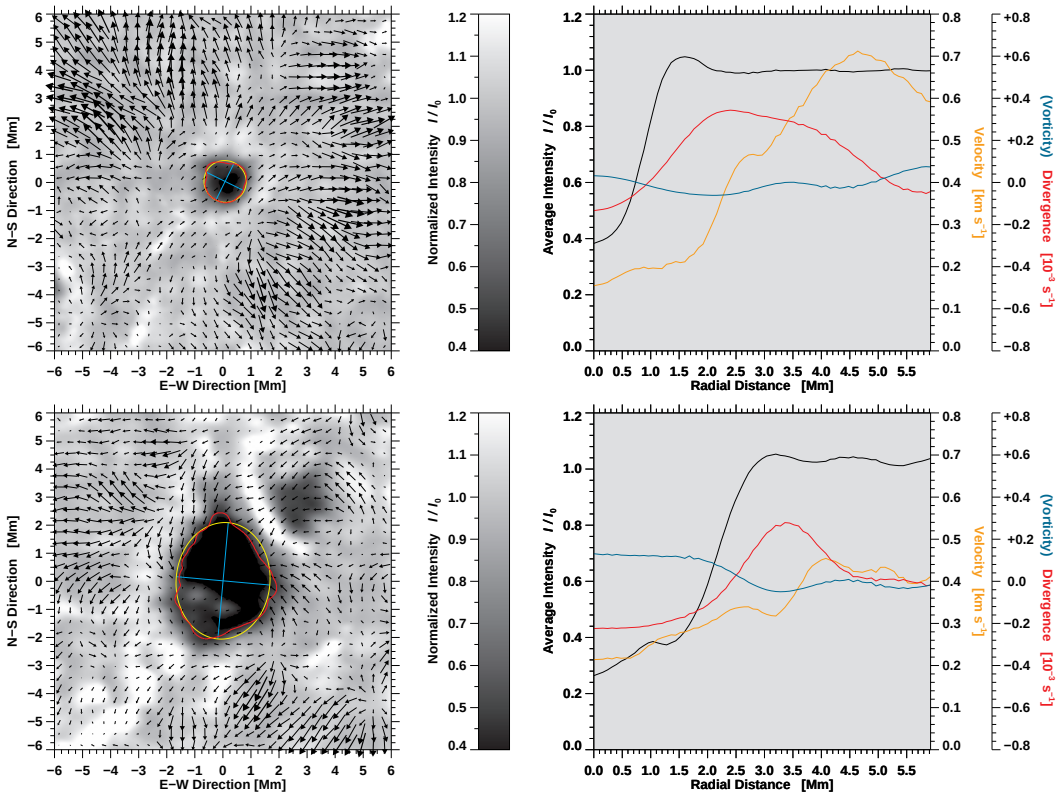

Figure 6.2: Average (60-minute) G-band image (*left*) of an isolated pore (*top*) observed on 2007 February 3 and an residual pore (*bottom*) observed on 2006 December 7. The arrows indicate magnitude and direction of the horizontal proper motions. An arrow with the length of the grid spacing indicates a speed of 0.5 km s^{-1}. Azimuthally averaged profiles (*right*) are presented for the time-averaged G-band intensity (*black*), the horizontal flow velocities (*orange*), the divergence (*red*), and the vorticity (*cyan*).

The parameters describing the morphology for both pores are compiled in Tab. 6.3. As expected, from a visual inspection, the isolated pore, has a smaller eccentricity than the residual pore, i.e., it is more circular. The value of the minimum intensity $I_{\rm min}$ is lower in the residual pore. The mean divergence within both pores are negative, indicating the converging flows, as seen in the overlaid flow vectors in the averaged G-band images. Apart from computing parameters inside pores, we computed radial averages for intensity, velocity, divergence, and vorticity over a radial distance of 6 Mm for all pores. Radial averages beyond the pore's boundary are only computed, if there are segments covering at least 180° in azimuth which are free of any other dark features. In right-panel of Fig. 6.2, the radial averages for both pores are compiled. For both pores, the intensity is low inside and increases to unity, i.e. to the quiet Sun value. However, near the boundary of both pores, we see a maximum of the intensity, which corresponds to the bright ring that we observed around pores. The divergence changes sign at the boundary of pores and the location of its maximum is well outside the pores. Interestingly, the divergence maximum extends even beyond the bright circular ring surrounding pores. The high speed values outside the isolated pore are also evident in the radial averages with speed values reaching up to 0.7 km s^{-1}. These two examples of pores befittingly describe the diversity in the database. In the current study, we will discuss only some of the statistical results. A detailed analysis will be provided in an upcoming publication.

6.3.3 Area vs. Perimeter

A scatter plot of perimeter length $L_{\rm pore}$ vs. area $A_{\rm pore}$ for all pores is depicted in Fig. 6.3. The ratio $L_{\rm pore}/A_{\rm pore}$ is minimal for a perfectly circular pore, i.e., $\alpha = 1$ in

$$L_{\rm pore} = 2\alpha\sqrt{\pi A_{\rm pore}}. \tag{6.1}$$

In the scatter plot, the lower solid curve represents the relation for $\alpha = 1$. Most perimeter lengths are above the curve representing circular objects, suggesting that the majority of pores are elongated and not

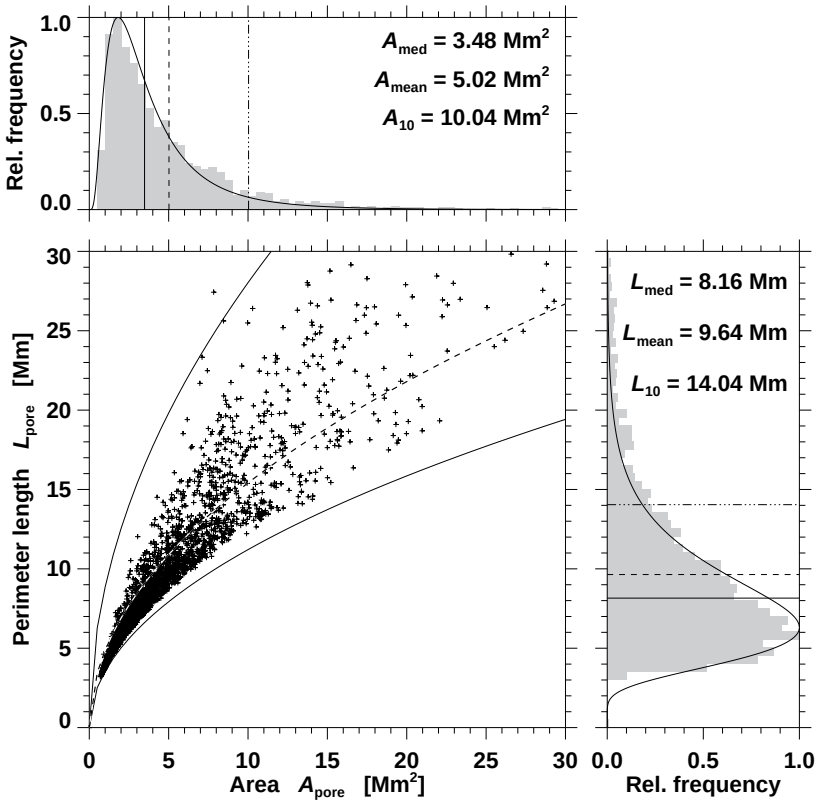

Figure 6.3: Scatter plot of perimeter length $L_{\rm pore}$ vs. area $A_{\rm pore}$, which also includes the respective frequency distributions. The lower envelope (*solid*) of the scatter plot refers to perfectly circular pores ($\alpha = 1$ in Eqn. 6.1), while the upper envelope (*solid*) is given by a scaling factor of $\alpha = 2.5$. A non-linear least squares fit (*dashed*) using Eqn. 6.1 leads to a scaling factor of $\alpha = 1.37$. Median, mean, and 10$^{\rm th}$ percentile of the frequency distributions are given by solid, dashed, and dash-dotted lines, respectively. The quantitative values are given in the panels for both the perimeter length $L_{\rm pore}$ and area $A_{\rm pore}$.

perfectly circular. As the area of the pores becomes larger, the farther the points are located from the curve. Using Eqn. 6.1 and a non-linear least squares fit over all values of area and perimeter, we obtained scaling factor of $\alpha = 1.37$. As an upper envelope for the scatter plot a scaling factor of $\alpha = 2.5$ is a used.

Figure 6.3 also contains the frequency distributions for perimeter length $L_{\rm pore}$ and area $A_{\rm pore}$, which are plotted as gray histogram bars. Their respective parameters are included in each panel. In addition, log-normal frequency distributions were fitted to the histograms

$$f(x,\mu,\sigma) = \frac{1}{x\sigma\sqrt{2\pi}} e^{-\frac{(\ln x-\mu)^2}{2\sigma^2}} \quad \text{with} \quad x > 0, \tag{6.2}$$

where μ and σ are the mean and standard deviation of the variable's x (i.e., $L_{\rm pore}$ or $A_{\rm pore}$) natural logarithm, respectively. In Tab. 6.4, the mean μ and standard deviation σ for $A_{\rm pore}$ and $L_{\rm pore}$ are given, along with the moments of the distributions, e.g., median, mean, and 10$^{\rm th}$ percentile. For the fitted distributions, the median, mean, and 10$^{\rm th}$ percentile are smaller than for the observed distributions, because there are significant numbers of pores larger than 3 Mm^2 and with perimeter lengths above 10 Mm, which do not follow the log-normal frequency of occurrence. The positive values of skewness exhibited by distributions points to the extended tail, showing the relative prevalence of larger pores. More than 66% of all pores (2863) are smaller than 5 Mm^2, which corresponds to a region with the size of just a few granules. Hence, overall observations and log-normal fits are in good agreement.

6.3.4 Frequency Distributions

The relative frequency distribution of the G-band intensity within all pores is given in Fig. 6.4. The mean, median, and 10$^{\rm th}$ percentile of the frequency distribution are $I_{\rm mean} = 0.65 I_0$, $I_{\rm med} = 0.67 I_0$, and $I_{10} = 0.83 I_0$, respectively. The distribution is skewed to higher-intensities with an extended shoulder on the low intensity side. The most striking feature of the distribution is almost linear increase of the intensity from 0.58 to to $0.80 I_0$. We fitted the frequency distribution with two Gaussians, one representing dark and the other referring to bright components. Two Gaussians are chosen to take into account the appearance of bright intrusions in dark pores, which can be for example the counterparts of umbral dots in sunspots.

Table 6.4: Parameters and moments of the frequency distributions for $L_{\rm pore}$ and area $A_{\rm pore}$.

Log-normal distributed variable x		$A_{\rm pore}$	$L_{\rm pore}$
Mean $\ln x$	μ	1.13	2.03
Standard deviation $\ln x$	σ	0.73	0.43
Median	e^{μ}	3.09	7.62
Mean	$e^{\mu+\sigma^2/2}$	4.03	8.37
Mode	$e^{\mu-\sigma^2}$	1.82	6.31
$10^{\rm th}$ percentile		7.76	13.22
Variance	$(e^{\sigma^2}-1)\,e^{2\mu+\sigma^2}$	11.38	14.55
Skewness	$(e^{\sigma^2}+2)\sqrt{e^{\sigma^2}-1}$	3.10	1.69
Kurtosis	$e^{4\sigma^2}+2e^{3\sigma^2}+3e^{2\sigma^2}-6$	20.86	4.03

The respective frequency distribution is given by

$$p(I/I_0) = \frac{P_1}{\sqrt{2\pi}\sigma_1} e^{-\frac{(I/I_0-\mu_1)^2}{2\sigma_1^2}} + \frac{P_2}{\sqrt{2\pi}\sigma_1} e^{-\frac{(I/I_0-\mu_2)^2}{2\sigma_2^2}} \quad , \tag{6.3}$$

where $P_{1,2}$ are the probabilities of occurrence and $P_1+P_2=1$. Bright features cover about 21.6% of the pore's area, i.e., $P_2=0.216$. Means $\mu_{1,2}$ and standard deviations $\sigma_{1,2}$ of the two Gaussians are given in the caption of Fig. 6.4. Optimal thresholds $T_{1,2}$ can be computed (e.g., Gonzalez and Woods, 2002), which separate the bright and dark components, using the quadratic equation

$$AT^2+BT+C=0 \tag{6.4}$$

with

$$\begin{aligned} A &= \sigma_1^2-\sigma_2^2 \\ B &= 2\left(\mu_1\sigma_2^2-\mu_2\sigma_1^2\right) \\ C &= \sigma_1^2\mu_2^2-\sigma_2^2\mu_1^2+2\sigma_1^2\sigma_2\ln\left(\sigma_2 P_1/\sigma_1 P_2\right). \end{aligned} \tag{6.5}$$

Two thresholds $T_1=0.76\,I_0$ and $T_2=0.87\,I_0$ are required to separate the dark and bright components because of the strong overlap. However, the combination of two Gaussians leads to a bimodal frequency distribution, which is not observed, because the averaged intensities were computed over a wide range of heliocentric angles θ. Accordingly, both the means and the standard deviations will exhibit a CLV. Hence, by incorporating this functional dependence of intensity on the heliocentric angle θ, one could reproduce the general shape of the distribution in Fig. 6.4.

Along with frequency in Fig. 6.4, the frequency distributions for the speed, the divergence, and the vorticity within all pores are shown. The distribution for the speed is broad and has a high-velocity tail. As expected, the mean speed is low $v_{\rm mean}=0.18$ km s^{-1} inside pores. However, because LCT follows intensity contrasts, the dark core could lead to low speed inside pores in the absence of contrast-rich structures. The frequency distributions for the divergence and the vorticity have almost the same shape. We fitted the divergence distribution with a Gaussian curve

$$f(x,\mu,\sigma) = \frac{1}{\sigma\sqrt{2\pi}} e^{-\frac{(x-\mu)^2}{2\sigma^2}} \quad , \tag{6.6}$$

with $\sigma=0.11\times10^{-3}$ s^{-1} and $\mu=-0.14\times10^{-3}$ s^{-1}. The negative mean value of the divergence within the pore indicates inflows inside pores, which we also observed in the two pores presented as examples in Fig. 6.2. A normal distribution is also a valid representation for the vorticity. We fitted the vorticity distribution with a Gaussian centered at $\mu=-0.00\times10^{-3}$ s^{-1} and having $\sigma=0.10\times10^{-3}$ s^{-1}. The mean value of vorticity inside pores is approaching zero, suggesting that there is not much twist and spiralling motion in the horizontal flow fields within a pore.

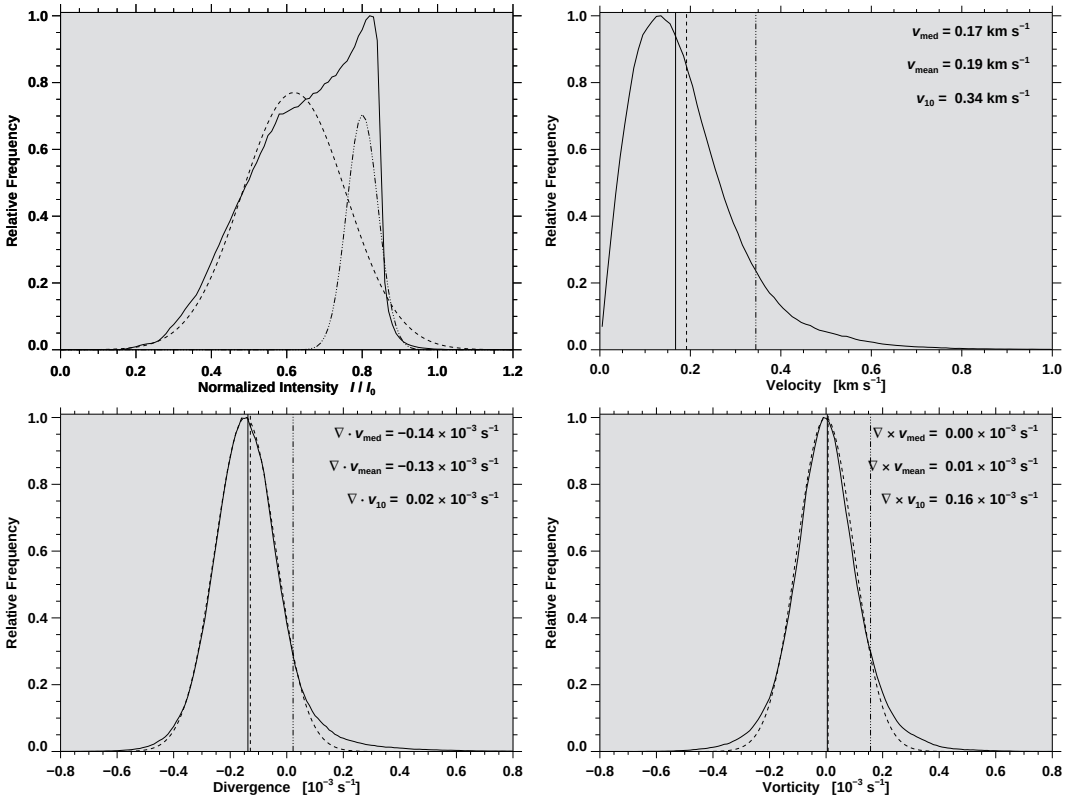

Figure 6.4: The intensity distribution (*top-left*) of all pores (*solid*) can be fitted with two Gaussians, i.e., a dark component with $\mu = 0.62\,I_0$ and $\sigma = 0.14\,I_0$ (*dashed*) and a bright component with $\mu = 0.80\,I_0$ and $\sigma = 0.04\,I_0$ (*dash-dotted*). The frequency distributions are also given for the flow speed (*top-right*), the divergence (*bottom-left*), and the vorticity (*bottom-right*) within all pores. The three vertical lines mark the position of the median (*solid*), mean (*long-dashed*), and 10^{th} percentile (*dash-dotted*) of the the speed v, the divergence $\nabla \cdot v$, and $\nabla \times v$ the vorticity. The divergence and vorticity distributions are fitted with Gaussians (*dashed*) having a mean value of $\mu = -0.14 \times 10^{-3}$ s^{-1} and -0.00×10^{-3} s^{-1}, respectively.

6.4 Conclusions

We showed that the newly created LCT database facilitates statistical studies of flows around solar features in a straightforward manner. In this study, we concentrated on the flows in the vicinity of pores. In total, 2863 pores contributed to the statistical analysis. We computed perimeters and areas describing the morphology of pores, and we provided the radial averages for intensity, velocity, divergence and vorticity. We presented two pores as an example to illustrate the data analysis strategy and the parameters that can be used in a more detailed analysis. The study has not reached its culmination. The complete analysis and discussion has to be deferred to a future publication. Nevertheless, here we present some preliminary findings:

- Most of the pores have a small area. About 66% of the observed pores have an area smaller than 5 Mm^2, which is comparable to an area covered by just a few granules. Interestingly, smaller pores tend to be more circular. This might be partially explained by the tendency of pores to align in chains and sometimes even ring-like structures. The feature identification algorithm might not always break up these elongated features.

- The intensity distribution has a very distinct shape, which can be reproduced by using Gaussians for dark and bright components inside the pore with a dependence on the heliocentric angle θ. The CLV of the dark component might not be as strong as the one for bright features (umbral dots and faint light-bridges), if the CLV of G-band bright-point is taken as a guide.

- The frequency distributions of the divergence and the vorticity within pores were easily fitted with a normal-distributions. The divergence is mainly negative within pores strongly suggesting inflows. The mean value of the vorticity is about zero, showing the lack of twisted or spiralling motions within pores.

Pores can represent two stages in the evolution of sunspots: during the formation as an umbral core without penumbra and following the decay again as an umbral core where the penumbra had already decayed. Since pores represent a transitory state, the statistical analysis of the flow fields related to pores will allow us to improve our knowledge of how sunspots form and decay.

Chapter 7

Conclusions

In the introduction of the thesis (Chapt. 1), many aspects of flow fields on the solar surface were discussed and several questions were raised. In the first part of the conclusions, we provide answers to these questions and present the major findings of this work.

Design Criteria for LCT Algorithms. The LCT technique produces reliable results when a Gaussian sampling window with a FWHM =1200 km is used for G-band images with a time cadence of 60 s, and when the flow maps are averaged over an hour. The LCT speed values for various solar features are in good agreement with previous studies. The newly developed algorithm is able to retrieve almost all global properties of flow fields related to granulation. However, the results should be interpreted with a proper understanding of the technique. When compared with CO^{5}BOLD simulations of granulation, the estimated flow speeds are almost a factor of three smaller than the actual plasma flows and correspond more closely to the plasma flows encountered in the deeper photosphere. However, irrespective of small or large sampling windows, it is nearly impossible to retrieve the actual plasma motions because in any case, the computed flow fields will be averaged over many pixels resulting in smoothed flow maps. The real challenge will be to conceptualize an inversion technique to attain actual from estimated flow fields, i.e., untangling the smoothing process and capturing the actual plasma motions, which are strongest in close proximity to the intergranular cell boundaries. Nevertheless, the LCT algorithm was able to match the frequency distributions and the functional dependence of the mean flow speed with the elapsed time, thus establishing LCT as an effective method to estimate horizontal proper motions (Chapters 2 and 3).

Synergies between Horizontal Flow Fields and Other Data from Ground and Space. The LCT results can be easily complemented with data from various instruments, as shown in Chapt. 4, where *Hinode* data were presented together with SDO and VTT observations. Using the VTT Echelle spectra, LOS velocities were computed. Continuum images and LOS magnetograms provided the temporal evolution of area and flux growth and decay rates. *Hinode*/SP data furnished the high-resolution magnetic configuration of the region. This study serves as a perfect example of the cooperation between various observing facilities. The synergy of multi-wavelength observations potentiates the scientific reach of individual instruments. Phenomena can be observed in various atmospheric layers, and knowledge about plasma flows and magnetic fields in three dimensions facilitates a comprehensive description of physical processes on the Sun.

Moving Magnetic Features in Decaying Sunspots. Studying flow fields of decaying sunspots, we found that MMFs follow preferred paths, travel across the gap from the sunspot border to the nearest supergranular boundary and create a spoke-like structure around the spot. The MMFs were visible around the sunspot even after its penumbra had decayed. Most of the MMFs were type II, i.e., unipolar with same polarity as the sunspot, which is in good agreement with the result of Yurchyshyn, Wang, and Goode (2001) who found that 75% of MMFs streaming out from the sunspot are of type II (Chapt.4).

Coherent Patch of Granulation as the Final Stage of Sunspot Decay. Once the two spots of active region NOAA 11126 had decayed on 2010 November 22 as evidenced by their photometric and magnetic evolution, a patch of abnormal granulation remained at that place, which was characterized by low flow speeds, low divergence, and a coherent direction of motion. This kind of flow pattern differed from the usual horizontal granular flow pattern. The patch of altered granulation in flow maps could be an indication magnetic flux dispersal and signifies the final stages of sunspot decay (Chapt.4).

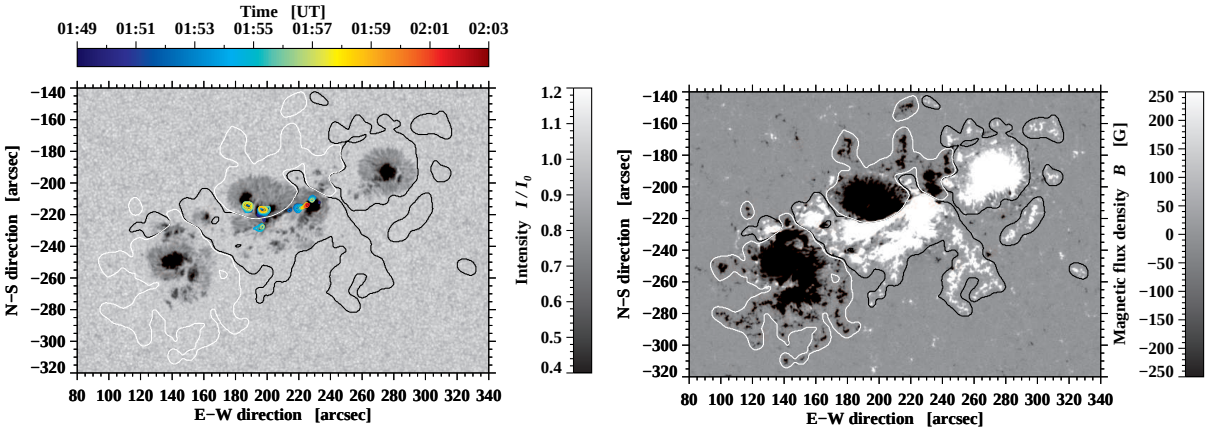

Figure 7.1: Limb-darkening corrected HMI continuum image (*left*) and LOS magnetogram (*right*) of active region NOAA 11158, which were observed at 01:33 UT just before the onset of the X2.2 flare on 2012 February 15. The black and white contour lines enclose strong (above/below ±10 G) positive and negative flux concentrations, respectively. Strong polarity inversion lines exist in regions where the contour lines overlap. The color-coded contour lines indicate kernels of white-light flare emission at different times. The axes are labeled in heliographic coordinates (Fig. 2 in Beauregard, Verma, and Denker, 2012).

Shear Flows and the Role of Flares in Sunspot Decay. In the decaying satellite sunspot residing in active region NOAA 10930, shear flows played an important role in its evolution. The spiral motions along non-radial penumbral filaments pointed to the existence of twisted magnetic fields. The satellite sunspot underwent shear motions until a rudimentary penumbra was established. We also observed rapid penumbral decay near the central umbral core after C6.1 flare, however, it was highly localized and not widespread. The overall spot decay was slow, and the decay rates were in good agreement with previous studies. From the decorrelation time maps, we noticed that the features with longer lifetimes in intensity images did not correspond to long-lived features in flow maps. The long-lived flow features were related to the slowly decaying penumbra. During the 16 hours of observations, the magnetic flux topology of the decaying satellite spot was altered and simplified, which was followed by a M2.0 flare. This points to the less explored possibility of flux submergence or removal as the origin of flares (Chapt.5).

Prospects and Future Research Directions

In this thesis, we presented an extensive investigation of LCT techniques and their application to sunspot observations. However, this work could be considered as the terminus a quo for further scientific studies. Some of the future projects are listed below.

Application of LCT to SDO Data. The launch of SDO in 2010 enabled uninterrupted access to full-disk images of the Sun in various wavelengths. This provides the opportunity to follow the evolution of active regions during their disk-passage. However, the huge amount of data generated by space missions such as SDO requires data analysis techniques which are reliable and tested for bulk-processing. In Beauregard, Verma, and Denker (2012), we presented a case study related to the horizontal flow fields around active region NOAA 11158, which was source of the first X-class flare of solar cycle 24 (Fig. 7.1). For that study, the LCT algorithm was adapted to HMI continuum images. With the application of our LCT algorithm, we were able to even capture weak photospheric shear flows (a few 100 m s^{-1}) along the polarity inversion line (see Fig. 7.2). This one case study showed already that our algorithm could be easily extended to perform the real-time analysis of photospheric shear flows around active regions. Shear flows contribute to the energy buildup and increase the likelihood of magnetic reconnection leading up to solar flares. Following the time evolution of photospheric motions along magnetic neutral lines in continuum images and magnetograms will be a valuable aid in predicting flare-prone active regions, which is one of the important tasks of space weather forecasting. Currently, space weather forecasting is limited to data of high energy proton and X-ray flux as well as real-time images and magnetograms. The value-added LCT data products will surely augment the already available tools for space weather forecasting.

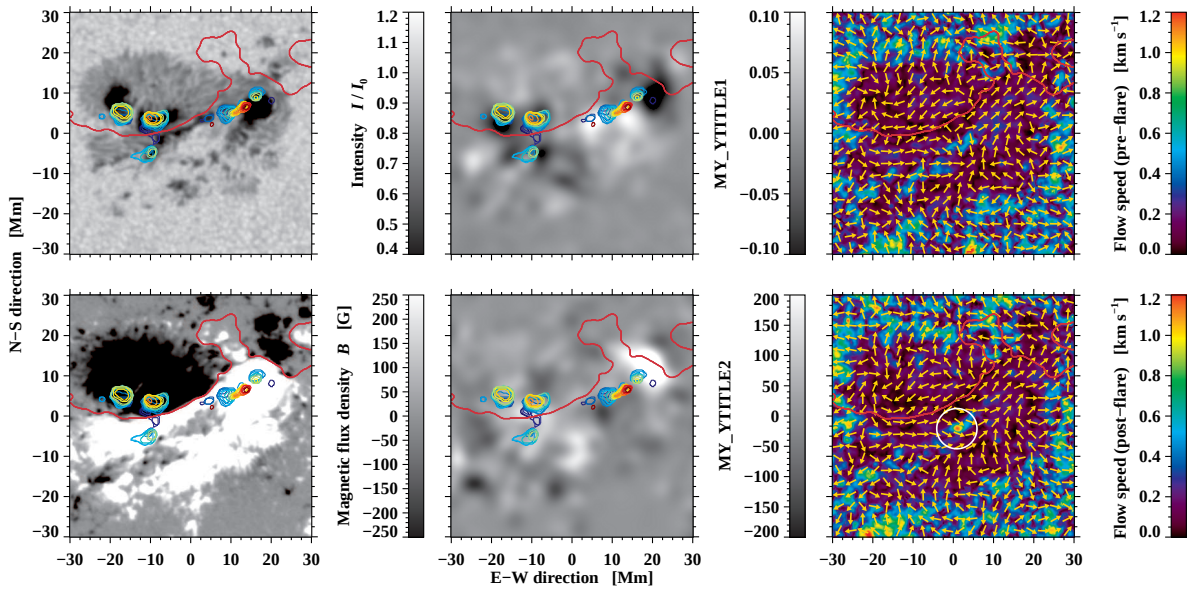

Figure 7.2: The ROI depicting the central region of active region NOAA 11158 where the X2.2 flare occurred on 2012 February 15. The left column shows a continuum image (*top*) and a magnetogram (*bottom*) at the peak of the flare (01:58 UT). The middle column contains difference maps (1-hour post- minus pre-flare phase, i.e., 02:18-03:18 UT and 00:33-01:33 UT) of the continuum intensity (*top*) and LOS magnetic flux density (*bottom*), respectively. These maps were smoothed with a Gaussian kernel FWHM = 4.0 Mm to emphasize regions of flare-induced changes in the photosphere. Superposed on all these maps are white-light flare kernels, which are depicted in the same way as in Fig. 7.1. Finally, the right column compares the horizontal flow speeds before (*top*) and after (*bottom*) the flare, respectively. The white circle encompasses a circular area of enhanced flow speed, which appeared after the flare. Orange arrows indicate the direction of the horizontal proper motions. The red curve in all panels refers to the flaring polarity inversion line. In the left and middle column are the data which are directly accessible, whereas the flow fields shown in the right column are the value-added product of LCT application (Fig. 4 in Beauregard, Verma, and Denker, 2012).

Horizontal Proper Motions at High-Spatial Resolution. The future prospects of high-resolution solar physics are very promising. *Solar Orbiter* (SO, Marsden and Fleck, 2007) is one of the key European space missions of this decade. On the ground, a network for high-resolution solar observations is on the horizon with the GREGOR solar telescope (Denker *et al.*, 2012; Schmidt *et al.*, 2012) on Tenerife, the *New Solar Telescope* (NST, Cao *et al.*, 2010) at Big Bear Solar Observatory in California, the U.S. *Advanced Technology Solar Telescope* (ATST, Rimmele *et al.*, 2010) on Hawaii, the *European Solar Telescope* (EST, Collados, 2008) on the Canary Islands, and the *National Large Solar Telescope* (NLST, Hasan *et al.*, 2010a) in India. Almost evenly spread in longitude, these telescopes could track solar activity in all its intricate detail without being limited by Earth's day-and-night cycle. The resolution attained by solar observations will soon be comparable or even higher than the currently available resolution of sunspot simulations (Rempel *et al.*, 2009; Rempel, 2011). For example, GREGOR with a mirror of $D = 1.5$ m (the Rayleigh criterion is $1.22 \cdot \lambda/D$ at $\lambda 500$ nm) will be delivering images with a resolution of 50 km at $\lambda = 500$ nm, and features smaller than 20 km can be resolved in ATST images ($D = 4$ m) which is half the resolution of sunspot simulation presented in Rempel (2011). As mentioned in the Chapt. 1.1.4, the flows in and around sunspots are mainly related to fine structures, which necessitate data with high-spatial and temporal resolution. The goal will be to adapt the LCT algorithm developed during the doctoral thesis to meticulously follow horizontal proper motions in high-spatial resolution data. Careful monitoring of the flow fields in and around sunspots will provide critical conditions for the formation and decay of penumbrae. Finding the exact parameters for these transitions will also furnish important boundary conditions for sunspot and penumbra models.

Evaluating LCT Based on Sunspot Simulations. In the past few years, MHD models have emerged to produce realistic simulations of sunspots and active regions (e.g., Rempel *et al.*, 2009; Cheung *et al.*, 2010). We have already evaluated our LCT algorithm based on simulations of granulation (Chapt.3). The future emphasis will be to quantify the flows in sunspots, which range from the moat flow to the complex penumbrae with specific characteristics such as the distinct divergence line in the mid-penumbra.

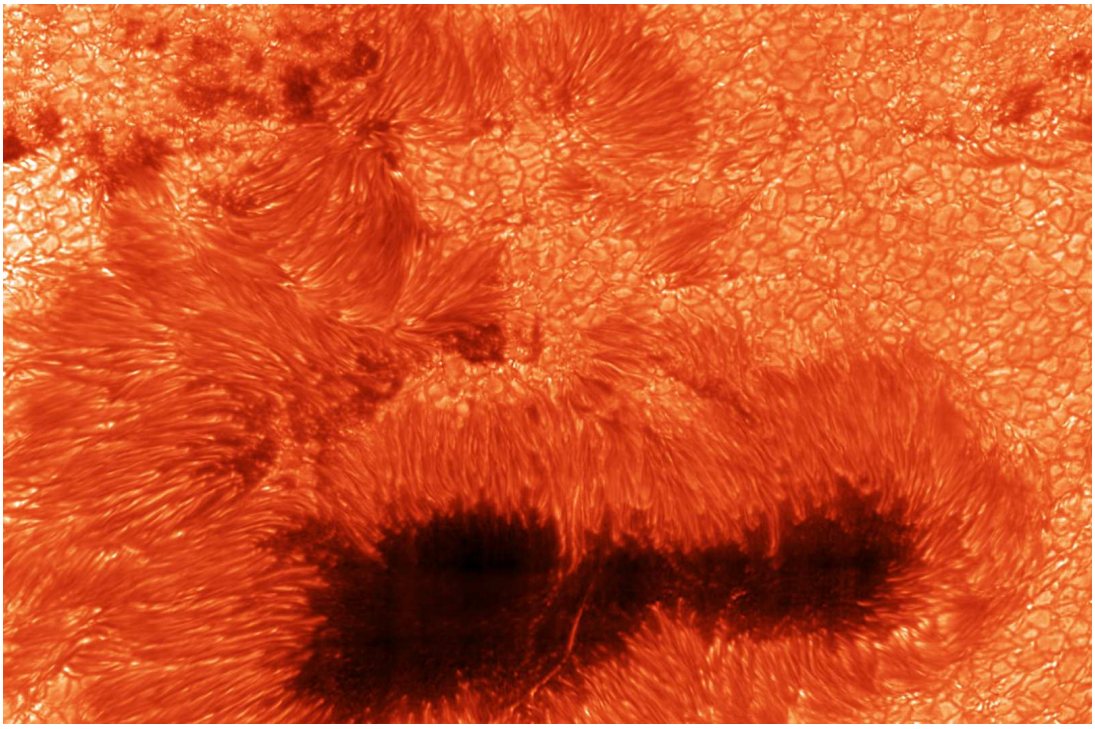

Figure 7.3: Broad-band speckle-restored image at $\lambda 656$ nm a major sunspot in active region NOAA 11520 observed on 2012 July 14. The data were taken with the *Broad-band Imager* (BBI, von der Lühe *et al.*, 2012) of the GREGOR solar telescope (Denker *et al.*, 2012; Schmidt *et al.*, 2012). The FOV is $110'' \times 67''$, and the image scale is $0.0283''$ pixel^{-1}. The sunspot was approaching west limb. Many fine structures are clearly visible in the complex penumbra (overlapping filaments, filament at almost 90° to each other, and filaments protruding into the umbra) and the highly structured umbra (many umbral dots and faint light-bridges). This kind of high-resolution data is required to study sunspots in fine details to finally understand the intricate flows of the penumbra.The image is courtesy of Dr. Oskar von der Lühe.

However, MHD simulations are limited to simple sunspots, complex sunspots (for example the one in Fig. 7.3) might still be beyond the reach of current MHD models.

Statistical Studies Related to the Moat Flow. The most valuable outcome of this thesis is the database of LCT flow maps containing more than 200 days of data and around 200 sunspots at various evolutionary stages. The database consists of already computed flow vectors. Hence, making it easy to carry out a statistical study of the moat flows. Deng *et al.* (2011b) studied the horizontal proper motions in the vicinity of nine regular sunspots. However, most of the sunspots reside in active regions exhibiting very complex magnetic topology like the sunspot shown in Fig. 7.3. Only with a statistically significant sample one can address question such as: Is the moat flow more evident in newly formed, mature, or decaying sunspots? How is this related to the presence/absence of a penumbra? What is the typical flow speed in the moat and does it change with distance from the sunspot? Are there external factors such as flux emergence that hinder setting up a moat flow around a sunspot? Almost 200 flow maps will enable us to compile statistically meaningful results, which are adequate to answer these questions.

Lifetime of Supergranular Boundaries. While creating the flow field database, we encountered a 22-hour-long time-series of *Hinode*/SOT LOS magnetograms and Ca II H, G-band, and blue continuum images observed on 2007 August 30–31. The dataset is ideally suited for computing the lifetime of meso- and supergranular cells, which live significantly longer than granules. The NFI magnetograms would facilitate a comparison with optical flow techniques specifically adapted to magnetic elements and flux concentrations. We will use the decorrelation time technique introduced by Welsch *et al.* (2012) and extended in Verma *et al.* (2012) to measure the decorrelation times of long-lived convective features in intensity, flow speed, and magnetic field maps.

This thesis was aimed at a better understanding of the changes in flow fields in the vicinity of sunspots during their growth and decay. We carefully evaluated and quantified the LCT algorithm. Two case studies related to flows in a decaying sunspots were carried out. One focusing on the quiet disintegration of two spots, which evolved differently, and another describing a decaying sunspot in a more complex and flare-prolific active region. These case studies will soon culminate in statistical studies related to flows

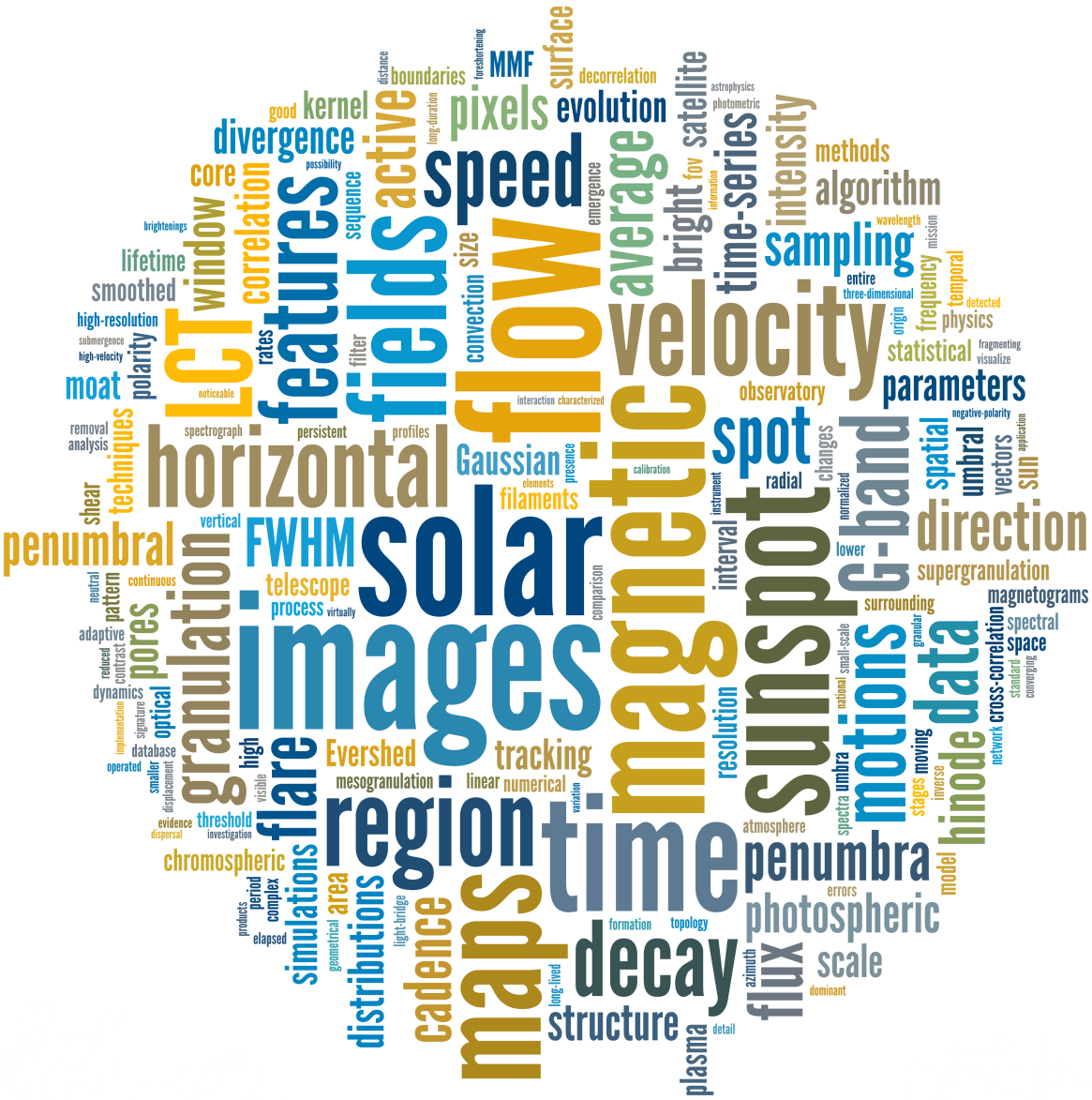

Figure 7.4: Word cloud created online[5] showing a graphical representation of the word frequency in the doctoral thesis.

surrounding sunspots and pores. The outcome of this thesis offered new information and confirmed some previously established facts, providing new insight into the complicated relation between solar magnetic and flow fields. The prospect of database-oriented research work is very promising and will help to know the Sun better. In Fig. 7.4, a word cloud is presented as the visual summary of the thesis. The word cloud is an image, which compiles a frequency-weighted list of keywords that appeared in the doctoral thesis. The frequency of the keywords relates directly to the font size. Usually word clouds are used to make reader quickly aware of the prominent terms in the text or to summarize the contents of web pages or web blogs. The many figures and graphical representations in this thesis certainly support the notion that "a picture is worth more than a thousand words" but before concluding the thesis, we turn this saying around by summarizing the thesis in a picture of just over 100 words.

[5] www.tagxedo.com

Bibliography

Adrian, R.: 2005, Twenty Years of Particle Image Velocimetry. *Exp. Fluids* **39**, 159 – 169.

Amari, T., Luciani, J.F., Mikic, Z., Linker, J.: 2000, A Twisted Flux Rope Model for Coronal Mass Ejections and Two-Ribbon Flares. *Astrophys. J. Lett.* **529**, L49 – L52, 2000ApJ...529L..49A.

Bahng, J., Schwarzschild, M.: 1961, Lifetime of Solar Granules. *Astrophys. J.* **134**, 312 – 322, 1961ApJ...134..312B.

Balasubramaniam, K.S., Cliver, E.W., Pevtsov, A., Temmer, M., Henry, T.W., Hudson, H.S., Imada, S., Ling, A.G., Moore, R.L., Muhr, N., Neidig, D.F., Petrie, G.J.D., Veronig, A.M., Vršnak, B., White, S.M.: 2010, On the Origin of the Solar Moreton Wave of 2006 December 6. *Astrophys. J.* **723**, 587 – 601, 2010ApJ...723..587B.

Balthasar, H.: 1984, Asymmetries and Wavelengths of Solar Spectral Lines and the Solar Rotation Determined from Fourier-Transform Spectra. *Solar Phys.* **93**, 219 – 241, 1984SoPh...93..219B.

Balthasar, H.: 1988, The Center-to-Limb Variation of Solar Spectral Lines. *Astron. Astrophys. Suppl. Ser.* **72**, 473 – 495, 1988A&AS...72..473B.

Balthasar, H.: 2006, Vertical Current Densities and Magnetic Gradients in Sunspots. *Astron. Astrophys.* **449**, 1169 – 1176, 2006A&A...449.1169B.

Balthasar, H., Muglach, K.: 2010, The Three-Dimensional Structure of Sunspots. II. The Moat Flow at Two Different Heights. *Astron. Astrophys.* **511**, A67, 2010A&A...511A..67B.

Bappu, M.K.V., Sivaraman, K.R.: 1971, K Emission-Line Widths and the Solar Chromosphere. *Solar Phys.* **17**, 316 – 330, 1971SoPh...17..316B.

Beauregard, L., Verma, M., Denker, C.: 2012, Horizontal Flows Concurrent with an X2.2 Flare in Active Region NOAA 11158. *Astron. Nachr.* **333**, 2012AN....333..125B.

Bellot Rubio, L.R., Tritschler, A., Martínez Pillet, V.: 2008, Spectropolarimetry of a Decaying Sunspot Penumbra. *Astrophys. J.* **676**, 698 – 703, 2008ApJ...676..698B.

Bentley, R.D., Freeland, S.L.: 1998, SOLARSOFT – An Analysis Environment for Solar Physics. In: *Crossroads for European Solar and Heliospheric Physics. Recent Achievements and Future Mission Possibilities, ESA Special Publication* **417**, 225 – 228, 1998ESASP.417..225B.

Benz, A.O.: 2008, Flare Observations. *Living Rev. Solar Phys.* **5**, 5 – 64, 2008LRSP....5....1B.

Berger, T.E., Schrijver, C.J., Shine, R.A., Tarbell, T.D., Title, A.M., Scharmer, G.: 1995, New Observations of Subarcsecond Photospheric Bright Points. *Astrophys. J.* **454**, 531 – 544, 1995ApJ...454..531B.

Berger, T.E., Löfdahl, M.G., Shine, R.S., Title, A.M.: 1998, Measurements of Solar Magnetic Element Motion from High-Resolution Filtergrams. *Astrophys. J.* **495**, 973 – 993, 1998ApJ...495..973B.

Berrilli, F., Consolini, G., Pietropaolo, E., Caccin, B., Penza, V., Lepreti, F.: 2002, 2-D Multiline Spectroscopy of the Solar Photosphere. *Astron. Astrophys.* **381**, 253 – 264, 2002A&A...381..253B.

Bhatnagar, A., Tanaka, K.: 1972, Intensity Oscillation in Hα-Fine Structure. *Solar Phys.* **24**, 87 – 97, 1972SoPh...24...87B.

Bhattacharyya, J.C.: 1970, The Solar Magnetometer of Kodaikanal Observatory. *Kodaikanal Obs. Bull.* **205**, 203, 1970KodOB.205..203B.

Borrero, J.M., Ichimoto, K.: 2011, Magnetic Structure of Sunspots. *Living Rev. Solar Phys.* **8**, 4, 2011LRSP....8....4B.

Brandt, P.N., Scharmer, G.B., Ferguson, S., Shine, R.A., Tarbell, T.D.: 1988, Vortex Flow in the Solar Photosphere. *Nature* **335**, 238 – 240, 1988Natur.335..238B.

Bray, R.J., Loughhead, R.E.: 1964, *Sunspots*, The International Astrophysics Series, Chapman & Hall, London, 1964suns.book.....B.

Brickhouse, N.S., Labonte, B.J.: 1988, Mass and Energy Flow near Sunspots. I. Observations of Moat Properties. *Solar Phys.* **115**, 43 – 60, 1988SoPh..115...43B.

Bumba, V.: 1963, Development of Spot Group Areas in Dependence on the Local Magnetic Field. *Bull. Astron. Inst. Czech.* **14**, 91 – 97, 1963BAICz..14...91B.

Cabrera Solana, D., Bellot Rubio, L.R., Beck, C., del Toro Iniesta, J.C.: 2006, Evershed Clouds as Precursors of Moving Magnetic Features around Sunspots. *Astrophys. J. Lett.* **649**, L41 – L44, 2006ApJ...649L..41C.

Cao, W., Gorceix, N., Coulter, R., Ahn, K., Rimmele, T.R., Goode, P.R.: 2010, Scientific Instrumentation for the 1.6 m New Solar Telescope in Big Bear. *Astron. Nachr.* **331**, 636 – 639, 2010AN....331..636C.

Cavallini, F.: 2006, IBIS: A New Post-Focus Instrument for Solar Imaging Spectroscopy. *Solar Phys.* **236**, 415 – 439, 2006SoPh..236..415C.

Chae, J., Sakurai, T.: 2008, A Test of Three Optical Flow Techniques – LCT, DAVE, and NAVE. *Astrophys. J.* **689**, 593 – 612, 2008ApJ...689..593C.

Chae, J., Wang, H., Qiu, J., Goode, P.R., Strous, L., Yun, H.S.: 2001, The Formation of a Prominence in Active Region NOAA 8668. I. SOHO/MDI Observations of Magnetic Field Evolution. *Astrophys. J.* **560**, 476 – 489, 2001ApJ...560..476C.

Cheung, M.C.M., Rempel, M., Title, A.M., Schüssler, M.: 2010, Simulation of the Formation of a Solar Active Region. *Astrophys. J.* **720**, 233 – 244, 2010ApJ...720..233C.

Chou, D.Y., Chen, C.S., Ou, K.T., Wang, C.C.: 1992, Power Spectra of Median- and Small-Scale Solar Convection. *Astrophys. J.* **396**, 333 – 339, 1992ApJ...396..333C.

Cloutman, L.D.: 1979, The Supergranulation – Solar Rip Currents. *Astron. Astrophys.* **74**, L1 – L3, 1979A&A....74L...1C.

Collados, M.: 2008, European Solar Telescope (EST): Project Status. In: Stepp, L.M., Gilmozzi, R. (eds.) *Ground-Based and Airborne Telescopes II, Proc. SPIE* **7012**, 70120J, 2008SPIE.7012E..17C.

Couvidat, S., Schou, J., Shine, R.A., Bush, R.I., Miles, J.W., Scherrer, P.H., Rairden, R.L.: 2012, Wavelength Dependence of the Helioseismic and Magnetic Imager (HMI) Instrument onboard the Solar Dynamics Observatory (SDO). *Solar Phys.* **275**, 285 – 325, 2012SoPh..275..285C.

Danilovic, S., Gandorfer, A., Lagg, A., Schüssler, M., Solanki, S.K., Vögler, A., Katsukawa, Y., Tsuneta, S.: 2008, The Intensity Contrast of Solar Granulation: Comparing Hinode SP Results with MHD Simulations. *Astron. Astrophys.* **484**, L17 – L20, 2008A&A...484L..17D.

Dawes, W.R.: 1864, Results of Some Recent Observations of the Solar Surface, with Remarks. *Mon. Not. R. Astron. Soc.* **24**, 161, 1864MNRAS..24..161D.

de Boer, C.R., Kneer, F.: 1992, Speckle Observations of Abnormal Solar Granulation. *Astron. Astrophys.* **264**, L24 – L26, 1992A&A...264L..24D.

De Rosa, M., Duvall, T.L. Jr., Toomre, J.: 2000, Near-Surface Flow Fields Deduced Using Correlation Tracking and Time-Distance Analyses. *Solar Phys.* **192**, 351 – 361, 2000SoPh..192..351D.

Del Moro, D., Berrilli, F., Duvall, T.L. Jr., Kosovichev, A.G.: 2004, Dynamics and Structure of Supergranulation. *Solar Phys.* **221**, 23 – 32, 2004SoPh..221...23D.

Deng, N., Liu, C., Yang, G., Wang, H., Denker, C.: 2005, Rapid Penumbral Decay Associated with an X2.3 Flare in NOAA Active Region 9026. *Astrophys. J.* **623**, 1195 – 1201, 2005ApJ...623.1195D.

Deng, N., Xu, Y., Yang, G., Cao, W., Liu, C., Rimmele, T.R., Wang, H., Denker, C.: 2006, Multiwavelength Study of Flow Fields in Flaring Super Active Region NOAA 10486. *Astrophys. J.* **644**, 1278 – 1291, 2006ApJ...644.1278D.

Deng, N., Choudhary, D.P., Tritschler, A., Denker, C., Liu, C., Wang, H.: 2007, Flow Field Evolution of a Decaying Sunspot. *Astrophys. J.* **671**, 1013 – 1021, 2007ApJ...671.1013D.

Deng, N., Liu, C., Prasad Choudhary, D., Wang, H.: 2011a, Rapid Enhancement of Sheared Evershed Flow Along the Neutral Line Associated with an X6.5 Flare Observed by Hinode. *Astrophys. J.* **733**, L14, 2011ApJ...733L..14D.

Deng, N., Shimizu, T., Choudhary, D.P., Wang, H.: 2011b, What Determines the Penumbral Size and Evershed Flow Speed? In: Prasad Choudhary, D., Strassmeier, K.G. (eds.) *Physics of Sun and Star Spots*, *IAU Symp.* **273**, 216 – 220, 2011IAUS..273..216D.

Denker, C.: 1998, Speckle Masking Imaging of Sunspots and Pores. *Solar Phys.* **180**, 81 – 108, 1998SoPh..180...81D.

Denker, C., Verma, M.: 2011, Velocity Fields in and around Sunspots at the Highest Resolution. In: Prasad Choudhary, D., Strassmeier, K.G. (eds.) *Physics of Sun and Star Spots*, *IAU Symp.* **273**, 204 – 211, 2011IAUS..273..204D.

Denker, C., Johannesson, A., Marquette, W., Goode, P.R., Wang, H., Zirin, H.: 1999, Synoptic Hα Full-Disk Observations of the Sun from Big Bear Solar Observatory. I. Instrumentation, Image Processing, Data Products, and First Results. *Solar Phys.* **184**, 87 – 102, 1999SoPh..184...87D.

Denker, C., Deng, N., Tritschler, A., Yurchyshyn, V.: 2007, Two-Dimensional Spectroscopy of Photospheric Shear Flows in a Small δ Spot. *Solar Phys.* **245**, 219 – 238, 2007SoPh..245..219D.

Denker, C., von der Lühe, O., Feller, A., Arlt, K., Balthasar, H., Bauer, S.M., Bello González, N., Berkefeld, T., Caligari, P., Collados, M., Fischer, A., Granzer, T., Hahn, T., Halbgewachs, C., Heidecke, F., Hofmann, A., Kentischer, T., Klvaňa, M., Kneer, F., Lagg, A., Nicklas, H., Popow, E., Puschmann, K.G., Rendtel, J., Schmidt, D., Schmidt, W., Sobotka, M., Solanki, S.K., Soltau, D., Staude, J., Strassmeier, K.G., Volkmer, R., Waldmann, T., Wiehr, E., Wittmann, A.D., Woche, M.: 2012, A Retrospective of the GREGOR Solar Telescope in Scientific Literature. *Astron. Nachr.* **333**, 810 – 815, 2012AN....333..810D.

DeRosa, M.L., Toomre, J.: 2004, Evolution of Solar Supergranulation. *Astrophys. J.* **616**, 1242 – 1260, 2004ApJ...616.1242D.

Domínguez Cerdeña, I.: 2003, Evidence of Mesogranulation from Magnetograms of the Sun. *Astron. Astrophys.* **412**, L65 – L68, 2003A&A...412L..65D.

Dravins, D., Lindegren, L., Nordlund, Å.: 1981, Solar Granulation – Influence of Convection on Spectral Line Asymmetries and Wavelength Shifts. *Astron. Astrophys.* **96**, 345 – 364, 1981A&A....96..345D.

Emery, W.J., Thomas, A.C., Collins, M.J., Crawford, W.R., Mackas, D.L.: 1986, An Objective Method for Computing Advective Surface Velocities from Sequential Infrared Satellite Images. *J. Geophys. Res.* **91**, 12865 – 12878, 1986JGR....9112865E.

Evershed, J.: 1909, Radial Movement in Sunspots. *Mon. Not. R. Astron. Soc.* **69**, 454 – 457, 1909MNRAS..69..454E.

Fanning, D.W.: 2003, *IDL Programming Techniques*, Fanning Software Consulting, Fort Collins, Colorado, 2003idlp.book.....F.

Fisher, G.H., Bercik, D.J., Welsch, B.T., Hudson, H.S.: 2012, Global Forces in Eruptive Solar Flares: The Lorentz Force Acting on the Solar Atmosphere and the Solar Interior. *Solar Phys.* **277**, 59 – 76, 2012SoPh..277...59F.

Freeland, S.L., Handy, B.N.: 1998, Data Analysis with the SolarSoft System. *Solar Phys.* **182**, 497 – 500, 1998SoPh..182..497F.

Freytag, B., Steffen, M., Ludwig, H.G., Wedemeyer-Böhm, S., Schaffenberger, W., Steiner, O.: 2012, Simulations of Stellar Convection with CO5BOLD. *J. Comp. Phys.* **231**, 919 – 959, 2012JCoPh.231..919F.

Georgakilas, A.A., Christopoulou, E.B.: 2003, Temporal Behavior of the Evershed Effect. *Astrophys. J.* **584**, 509 – 523, 2003ApJ...584..509G.

Ginet, G.P., Simon, G.W.: 1992, On the Evidence for Mesogranules in Solar Power Spectra. *Astrophys. J.* **386**, 359 – 363, 1992ApJ...386..359G.

Giovanelli, R.G.: 1980, The Supergranule Velocity Field. *Solar Phys.* **67**, 211 – 228, 1980SoPh...67..211G.

Gonzalez, R.C., Woods, R.E.: 2002, *Digital Image Processing*, Prentice-Hall, Upper Saddle River, New Jersey, 2002dip..book.....G.

Hagenaar, H.J., Shine, R.A.: 2005, Moving Magnetic Features around Sunspots. *Astrophys. J.* **635**, 659 – 669, 2005ApJ...635..659H.

Hart, A.B.: 1954, Motions in the Sun at the Photospheric Level. IV. The Equatorial Rotation and Possible Velocity Fields in the Photosphere. *Mon. Not. R. Astron. Soc.* **114**, 17 – 38, 1954MNRAS.114...17H.

Hart, A.B.: 1956, Motions in the Sun at the Photospheric Level. VI. Large-Scale Motions in the Equatorial Region. *Mon. Not. R. Astron. Soc.* **116**, 38 – 55, 1956MNRAS.116...38H.

Harvey, K., Harvey, J.: 1973, Observations of Moving Magnetic Features near Sunspots. *Solar Phys.* **28**, 61 – 71, 1973SoPh...28...61H.

Harvey, K.L., Harvey, J.W.: 1976, A Study of the Magnetic and Velocity Fields in an Active Region. *Solar Phys.* **47**, 233 – 246, 1976SoPh...47..233H.

Hasan, S.S., Soltau, D., Kärcher, H., Süß, M., Berkefeld, T.: 2010a, NLST: India's National Large Solar Telescope. *Astron. Nachr.* **331**, 628 – 635, 2010AN....331..628H.

Hasan, S.S., Mallik, D.C.V., Bagare, S.P., Rajaguru, S.P.: 2010b, Solar Physics at the Kodaikanal Observatory: A Historical Perspective. In: Hasan, S.S., Rutten, R.J. (eds.) *Magnetic Coupling between the Interior and Atmosphere of the Sun*, *Springer, Berlin*, 12 – 36, 2010mcia.conf...12H.

Hathaway, D.H., Choudhary, D.P.: 2008, Sunspot Group Decay. *Solar Phys.* **250**, 269 – 278, 2008SoPh..250..269H.

Hathaway, D.H., Beck, J.G., Bogart, R.S., Bachmann, K.T., Khatri, G., Petitto, J.M., Han, S., Raymond, J.: 2000, The Photospheric Convection Spectrum. *Solar Phys.* **193**, 299 – 312, 2000SoPh..193..299H.

Hathaway, D.H., Beck, J.G., Han, S., Raymond, J.: 2002, Radial Flows in Supergranules. *Solar Phys.* **205**, 25 – 38, 2002SoPh..205...25H.

Heinemann, T., Nordlund, Å., Scharmer, G.B., Spruit, H.C.: 2007, MHD Simulations of Penumbra Fine Structure. *Astrophys. J.* **669**, 1390 – 1394, 2007ApJ...669.1390H.

Henoux, J.C., Somov, B.V.: 1987, Generation and Structure of the Electric Currents in a Flaring Activity Complex. *Astron. Astrophys.* **185**, 306 – 314, 1987A&A...185..306H.

Herschel, W.: 1801, Observations Tending to Investigate the Nature of the Sun, in Order to Find the Causes or Symptoms of its Variable Emission of Light and Heat; With Remarks on the Use that May Possibly be Drawn from Solar Observations. *R. Soc. Lon. Phil. Trans. Ser. I* **91**, 265 – 318, 1801RSPT...91..265H.

Heyvaerts, J., Priest, E.R.: 1984, Coronal Heating by Reconnection in DC Current Systems – A Theory Based on Taylor's Hypothesis. *Astron. Astrophys.* **137**, 63 – 78, 1984A&A...137...63H.

Hirzberger, J.: 2002, On the Brightness and Velocity Structure of Solar Granulation. *Astron. Astrophys.* **392**, 1105 – 1118, 2002A&A...392.1105H.

Hirzberger, J.: 2003, Imaging Spectroscopy of Solar Pores. *Astron. Astrophys.* **405**, 331 – 340, 2003A&A...405..331H.

Hirzberger, J., Vazquez, M., Bonet, J.A., Hanslmeier, A., Sobotka, M.: 1997, Time Series of Solar Granulation Images. I. Differences between Small and Large Granules in Quiet Regions. *Astrophys. J.* **480**, 406 – 419, 1997ApJ...480..406H.

Hirzberger, J., Gizon, L., Solanki, S.K., Duvall, T.L.: 2008, Structure and Evolution of Supergranulation from Local Helioseismology. *Solar Phys.* **251**, 417 – 437, 2008SoPh..251..417H.

Hovis, W.A.: 1981, The Nimbus-7 Coastal Zone Color Scanner (CZCS) Program. In: Gower, J. F. R. (ed.) *Oceanography from Space*, 213 – 225.

Howard, R.F.: 1990, The Magnetic Fields of Active Regions. II. Rotation. *Solar Phys.* **126**, 299 – 309, 1990SoPh..126..299H.

Ichimoto, K., Lites, B., Elmore, D., Suematsu, S. Y. andTsuneta, Katsukawa, Y., Shimizu, T., Shine, R., Tarbell, T., Title, A., Kiyohara, J., Shinoda, K., Card, G., Lecinski, A., Streander, K., Nakagiri, M., Miyashita, M., Noguchi, M., Hoffmann, C., Cruz, T.: 2008, Polarization Calibration of the Solar Optical Telescope onboard Hinode. *Solar Phys.* **249**, 233 – 261, 2008SoPh..249..233I.

Isobe, H., Kubo, M., Minoshima, T., Ichimoto, K., Katsukawa, Y., Tarbell, T.D., Tsuneta, S., Berger, T.E., Lites, B., Nagata, S., Shimizu, T., Shine, R.A., Suematsu, Y., Title, A.M.: 2007, Flare Ribbons Observed with G-Band and Fe I 6302 Å Filters of the Solar Optical Telescope on Board Hinode. *PASJ* **59**, 807 – 813, 2007PASJ...59S.807I.

Janssen, J.: 1896, *Ann. Obs. Paris, Meudon* **1**, 91.

Jiang, Y., Zheng, R., Yang, J., Hong, J., Yi, B., Yang, D.: 2012, Rapid Sunspot Rotation Associated with the X2.2 Flare on 2011 February 15. *Astrophys. J.* **744**, 50, 2012ApJ...744...50J.

Kálmán, B.: 2001, Submergence of Magnetic fFlux in Interaction of Sunspot Groups. *Astron. Astrophys.* **371**, 731 – 737, 2001A&A...371..731K.

Keil, S.L., Balasubramaniam, K.S., Bernasconi, P., Smaldone, L.A., Cauzzi, G.: 1994, Observations of Active Region Dynamics: Preflare Flows and Field Observations. In: Balasubramaniam, K.S., Simon, G.W. (eds.) *Solar Active Region Evolution: Comparing Models with Observations, ASP Conf. Ser.* **68**, 265 – 282, 1994ASPC...68..265K.

Keil, S.L., Balasubramaniam, K.S., Smaldone, L.A., Reger, B.: 1999, Velocities in Solar Pores. *Astrophys. J.* **510**, 422 – 443, 1999ApJ...510..422K.

Keller, C.U.: 1992, Resolution of Magnetic Flux Tubes on the Sun. *Nature* **359**, 307 – 308, 1992Natur.359..307K.

Keppens, R., Martinez Pillet, V.: 1996, The Magnetic Structure of Pores and Sunspots Derived from Advanced Stokes Polarimeter Data. *Astron. Astrophys.* **316**, 229 – 242, 1996A&A...316..229K.

Kosovichev, A.G.: 2011, Helioseismic Response to the X2.2 Solar Flare of 2011 February 15. *Astrophys. J. Lett.* **734**, L15, 2011ApJ...734L..15K.

Kosugi, T., Matsuzaki, K., Sakao, T., Shimizu, T., Sone, Y., Tachikawa, S., Hashimoto, T., Minesugi, K., Ohnishi, A., Yamada, T., Tsuneta, S., Hara, H., Ichimoto, K., Suematsu, Y., Shimojo, M., Watanabe, T., Shimada, S., Davis, J.M., Hill, L.D., Owens, J.K., Title, A.M., Culhane, J.L., Harra, L.K., Doschek, G.A., Golub, L.: 2007, The Hinode (Solar-B) Mission: An Overview. *Solar Phys.* **243**, 3 – 17, 2007SoPh..243....3K.

Krieg, J., Kneer, F., Koschinsky, M., Ritter, C.: 2000, Granular Velocities of the Sun from Speckle Interferometry. *Astron. Astrophys.* **360**, 1157 – 1162, 2000A&A...360.1157K.

Kubo, M., Lites, B.W., Shimizu, T., Ichimoto, K.: 2008, Magnetic Flux Loss and Flux Transport in a Decaying Active Region. *Astrophys. J.* **686**, 1447 – 1453, 2008ApJ...686.1447K.

Kumar, P., Srivastava, A.K., Filippov, B., Uddin, W.: 2010, Multiwavelength Study of the M8.9/3B Solar Flare from AR NOAA 10960. *Solar Phys.* **266**, 39 – 58, 2010SoPh..266...39K.

Kusano, K., Maeshiro, T., Yokoyama, T., Sakurai, T.: 2002, Measurement of Magnetic Helicity Injection and Free Energy Loading into the Solar Corona. *Astrophys. J.* **577**, 501 – 512, 2002ApJ...577..501K.

Lantz, S.R., Fan, Y.: 1999, Anelastic Magnetohydrodynamic Equations for Modeling Solar and Stellar Convection Zones **121**, 247 – 264, 1999ApJS..121..247L.

Leenaarts, J., Rutten, R.J., Carlsson, M., Uitenbroek, H.: 2006, A Comparison of Solar Proxy-Magnetometry Diagnostics. *Astron. Astrophys.* **452**, L15 – L18, 2006A&A...452L..15L.

Leese, J.A., Novak, C.S., Clark, B.B.: 1971, An Automated Technique for Obtaining Cloud Motion from Geosynchronous Satellite Data Using Cross Correlation. *J. Appl. Meteor.* **10**, 118 – 132, 1971JApMe..10..118L.

Leighton, R.B.: 1963, The Solar Granulation. *Ann. Rev. Astron. Astrophys.* **1**, 19 – 40, 1963ARA&A...1...19L.

Leighton, R.B., Noyes, R.W., Simon, G.W.: 1962, Velocity Fields in the Solar Atmosphere. I. Preliminary Report. *Astrophys. J.* **135**, 474 – 510, 1962ApJ...135..474L.

Leka, K.D., Skumanich, A.: 1998, The Evolution of Pores and the Development of Penumbrae. *Astrophys. J.* **507**, 454 – 469, 1998ApJ...507..454L.

Leka, K.D., Barnes, G., Crouch, A.D., Metcalf, T.R., Gary, G.A., Jing, J., Liu, Y.: 2009, Resolving the 180°Ambiguity in Solar Vector Magnetic Field Data: Evaluating the Effects of Noise, Spatial Resolution, and Method Assumptions. *Solar Phys.* **260**, 83 – 108, 2009SoPh..260...83L.

Liu, C., Deng, N., Liu, Y., Falconer, D., Goode, P.R., Denker, C., Wang, H.: 2005, Rapid Change of δ Spot Structure Associated with Seven Major Flares. *Astrophys. J.* **622**, 722 – 736, 2005ApJ...622..722L.

Löfdahl, M.G.: 2010, Evaluation of Image-Shift Measurement Algorithms for Solar Shack-Hartmann Wavefront Sensors. *Astron. Astrophys.* **524**, A90, 2010A&A...524A..90L.

Longcope, D.W.: 2004, Inferring a Photospheric Velocity Field from a Sequence of Vector Magnetograms: The Minimum Energy Fit. *Astrophys. J.* **612**, 1181 – 1192, 2004ApJ...612.1181L.

López Fuentes, M.C., Demoulin, P., Mandrini, C.H., van Driel-Gesztelyi, L.: 2000, The Counterkink Rotation of a Non-Hale Active Region. *Astrophys. J.* **544**, 540 – 549, 2000ApJ...544..540L.

Magnan, C., Pecker, J.C.: 1974, Asymmetry in Solar Spectral Lines. *Highlight Astron.* **3**, 171 – 203, 1974HiA.....3..171M.

Maltby, P.: 1975, The Chromospheric Evershed Flow. *Solar Phys.* **43**, 91 – 105, 1975SoPh...43...91M.

Marsden, R.G., Fleck, B.: 2007, Solar Orbiter: A Mission Update. In: Heinzel, P., Dorotovič, I., Rutten, R.J. (eds.) *The Physics of Chromospheric Plasmas*, *ASP Conf. Ser.* **368**, 645, 2007ASPC..368..645M.

Martínez Pillet, V.: 2002, Decay of Sunspots. *Astron. Nachr.* **323**, 342 – 348, 2002AN....323..342M.

Martínez Pillet, V., Moreno-Insertis, F., Vazquez, M.: 1993, The Distribution of Sunspot Decay Rates. *Astron. Astrophys.* **274**, 521 – 533, 1993A&A...274..521M.

Martres, M.J., Soru-Escaut, I., Rayrole, J.: 1973, Relationship between Some Photospheric Motions and the Evolution of Active Centers. *Solar Phys.*, 365 – 378, 1973SoPh...32..365M.

Martres, M.J., Rayrole, J., Semel, M., Soru-Escaut, I., Tanaka, K., Makita, M., Moriyama, F., Unno, W.: 1982, Magnetic and Velocity Fields of Emerging Flux Regions on the Sun. *PASJ* **34**, 299 – 310, 1982PASJ...34..299M.

Matloch, Ł., Cameron, R., Shelyag, S., Schmitt, D., Schüssler, M.: 2010, Mesogranular Structure in a Hydrodynamical Simulation. *Astron. Astrophys.* **519**, A52, 2010A&A...519A..52M.

Meyer, F., Schmidt, H.U.: 1968, Magnetisch Ausgerichtete Strömungen Zwischen Sonnenflecken. *Zeitschrift für angewandte Mathematik und Mechanik* **48**, 218 – 221, 1968ZaMM...48..218M.

Meyer, F., Schmidt, H.U., Wilson, P.R., Weiss, N.O.: 1974, The Growth and Decay of Sunspots. *Mon. Not. R. Astron. Soc.* **169**, 35 – 57, 1974MNRAS.169...35M.

Min, S., Chae, J.: 2009, The Rotating Sunspot in AR 10930. *Solar Phys.* **258**, 203 – 217, 2009SoPh..258..203M.

Molowny-Horas, R.: 1994, Proper Motion Measurements of Umbral and Penumbral Structure. *Solar Phys.* **154**, 29 – 39, 1994SoPh..154...29M.

Montesinos, B., Thomas, J.H.: 1997, The Evershed Effect in Sunspots as a Siphon Flow along a Magnetic Flux Tube. *Nature* **390**, 485 – 487, 1997Natur.390..485M.

Moore, R., Rabin, D.: 1985, Sunspots. *Ann. Rev. Astron. Astrophys.* **23**, 239 – 266, 1985ARA&A..23..239M.

Moore, R.L., Sterling, A.C., Hudson, H.S., Lemen, J.R.: 2001, Onset of the Magnetic Explosion in Solar Flares and Coronal Mass Ejections. *Astrophys. J.* **552**, 833 – 848, 2001ApJ...552..833M.

Moreno-Insertis, F., Vazquez, M.: 1988, A Statistical Study of the Decay Phase of Sunspot Groups from 1874 to 1939. *Astron. Astrophys.* **205**, 289 – 296, 1988A&A...205..289M.

Muller, R., Auffret, H., Roudier, T., Vigneau, J., Simon, G.W., Frank, Z., Shine, R.A., Title, A.M.: 1992, Evolution and Advection of Solar Mesogranulation. *Nature* **356**, 322 – 325, 1992Natur.356..322M.

Namba, O., Diemel, W.E.: 1969, A Morphological Study of the Solar Granulation. *Solar Phys.* **7**, 167 – 177, 1969SoPh....7..167N.

Nielsen, M.L., Kjeldsen, H.: 2011, Is Cycle 24 the Beginning of a Dalton-Like Minimum? *Solar Phys.* **270**, 385 – 392, 2011SoPh..270..385N.

Nordlund, Å., Stein, R.F., Asplund, M.: 2009, Solar Surface Convection. *Living Rev. Solar Phys.* **6**, 1 – 117, 2009LRSP....6....2N.

November, L.J.: 1989, Proper Motion Measurements of Solar Granulation: The Case for Mesogranulation. In: von der Lühe, O. (ed.) *High Spatial Resolution Solar Observations, Proc.* 10th *Sacramento Peak Summer Workshop*, 457, 1989hsrs.conf..457N.

November, L.J., Simon, G.W.: 1988, Precise Proper-Motion Measurement of Solar Granulation. *Astrophys. J.* **333**, 427 – 442, 1988ApJ...333..427N.

November, L.J., Toomre, J., Gebbie, K.B., Simon, G.W.: 1981, The Detection of Mesogranulation on the Sun. *Astrophys. J. Lett.* **245**, L123 – L126, 1981ApJ...245L.123N.

Ortiz, A., Bellot Rubio, L.R., Rouppe van der Voort, L.: 2010, Downflows in Sunspot Umbral Dots. *Astrophys. J.* **713**, 1282 – 1291, 2010ApJ...713.1282O.

Perona, P., Malik, J.: 1990, Scale-Space and Edge Detection Using Anisotropic Diffusion. *IEEE Trans. Pattern Anal. Mach. Intell.* **12**, 629 – 639.

Pesnell, W.D., Thompson, B.J., Chamberlin, P.C.: 2012, The Solar Dynamics Observatory (SDO). *Solar Phys.* **275**, 3 – 15, 2012SoPh..275....3P.

Peter, H.: 1996, Superpenumbral Vortices. *Mon. Not. R. Astron. Soc.* **278**, 821 – 828, 1996MNRAS.278..821P.

Petrovay, K.: 2010, Solar Cycle Prediction. *Living Rev. Sol. Phys.* **7**, 6, 2010LRSP....7....6P.

Petrovay, K., van Driel-Gesztelyi, L.: 1997, Making Sense of Sunspot Decay. I. Parabolic Decay Law and Gnevyshev-Waldmeier Relation. *Solar Phys.* **176**, 249 – 266, 1997SoPh..176..249P.

Pierce, A.K., Slaughter, C.D.: 1977, Solar Limb Darkening. I. At Wavelengths of 3033–7297 Å. *Solar Phys.* **51**, 25 – 41, 1977SoPh...51...25P.

Ploner, S.R.O., Solanki, S.K., Gadun, A.S., Hanslmeier, A.: 1998, Temporal Evolution of Artificial Solar Granules. *Space Science Rev.* **85**, 261 – 268, 1998SSRv...85..261P.

Potts, H.E., Diver, D.A.: 2008, Automatic Recognition and Characterisation of Supergranular Cells from Photospheric Velocity Fields. *Solar Phys.* **248**, 263 – 275, 2008SoPh..248..263P.

Potts, H.E., Barrett, R.K., Diver, D.A.: 2003, Reduction of Interpolation Errors When Using Local Correlation Tracking for Motion Detection. *Solar Phys.* **217**, 69 – 78, 2003SoPh..217...69P.

Potts, H.E., Barrett, R.K., Diver, D.A.: 2004, Balltracking: An Highly Efficient Method for Tracking Flow Fields. *Astron. Astrophys.* **424**, 253 – 262, 2004A&A...424..253P.

Press, W.H., Teukolsky, S.A., Vetterling, W.T., Flannery, B.P.: 1992, *Numerical Recipes in C. The Art of Scientific Computing*, Cambridge University Press, New York, 1992nrca.book.....P.

Priest, E.R., Forbes, T.G.: 2002, The Magnetic Nature of Solar Flares. *Astron. Astrophys. Rev.* **10**, 313 – 377, 2002A&ARv..10..313P.

Rast, M.P.: 2003, The Scales of Granulation, Mesogranulation, and Supergranulation. *Astrophys. J.* **597**, 1200 – 1210, 2003ApJ...597.1200R.

Ravindra, B., Gosain, S.: 2012, Rapid Disappearance of Penumbra-Like Features near a Flaring Polarity Inversion Line: The Hinode Observations. *Adv. Astron.* **2012**, 735879, 2012AdAst2012E..24R.

Rempel, M.: 2011, Penumbral Fine Structure and Driving Mechanisms of Large-Scale Flows in Simulated Sunspots. *Astrophys. J.* **729**, 5 – 27, 2011ApJ...729....5R.

Rempel, M., Schlichenmaier, R.: 2011, Sunspot Modeling: From Simplified Models to Radiative MHD Simulations. *Living Rev. Solar Phys.* **8**, 3, 2011LRSP....8....3R.

Rempel, M., Schüssler, M., Cameron, R.H., Knölker, M.: 2009, Penumbral Structure and Outflows in Simulated Sunspots. *Science* **325**, 171 – 174, 2009Sci...325..171R.

Richardson, R.S., Schwarzschild, M.: 1950, On the Turbulent Velocities of Solar Granules. *Astrophys. J.* **111**, 351 – 361, 1950ApJ...111..351R.

Rieutord, M., Rincon, F.: 2010, The Sun's Supergranulation. *Living Rev. Solar Phys.* **7**, 2, 2010LRSP....7....2R.

Rieutord, M., Roudier, T., Malherbe, J.M., Rincon, F.: 2000, On Mesogranulation, Network Formation and Supergranulation. *Astron. Astrophys.* **357**, 1063 – 1072, 2000A&A...357.1063R.

Rieutord, M., Ludwig, H.G., Roudier, T., Nordlund, Å., Stein, R.: 2002, A Simulation of Solar Convection at Supergranulation Scale. *II Nuovo Cimento C.* **25**, 523 – 529, 2002NCimC..25..523R.

Rimmele, T.R.: 1995, Sun Center Observations of the Evershed Effect. *Astrophys. J.* **445**, 511 – 516, 1995ApJ...445..511R.

Rimmele, T.R.: 1997, Evidence for Magnetoconvection in a Sunspot Light Bridge. *Astrophys. J.* **490**, 458, 1997ApJ...490..458R.

Rimmele, T.R., Marino, J.: 2006, The Evershed Flow. Flow Geometry and its Temporal Evolution. *Astrophys. J.* **646**, 593 – 604, 2006ApJ...646..593R.

Rimmele, T.R., Wagner, J., Keil, S., Elmore, D., Hubbard, R., Hansen, E., Warner, M., Jeffers, P., Phelps, L., Marshall, H., Goodrich, B., Richards, K., Hegwer, S., Kneale, R., Ditsler, J.: 2010, The Advanced Technology Solar Telescope: Beginning Construction of the World's Largest Solar Telescope. In: Stepp, L.M., Gilmozzi, R., Hall, H.J. (eds.) *Ground-Based and Airborne Telescopes III*, *Proc. SPIE*, **7733**, 2010SPIE.7733E..14R.

Roudier, T., Bonet, J.A., Sobotka, M.: 2002, Properties of Horizontal Flows Inside and Outside a Solar Pore. *Astron. Astrophys.* **395**, 249 – 255, 2002A&A...395..249R.

Roudier, T., Malherbe, J.M., Vigneau, J., Pfeiffer, B.: 1998, Solar Mesogranule Lifetime Measurements. *Astron. Astrophys.* **330**, 1136 – 1144, 1998A&A...330.1136R.

Roudier, T., Rieutord, M., Malherbe, J.M., Vigneau, J.: 1999, Determination of Horizontal Velocity Fields at the Sun's Surface with high Spatial and Temporal Resolution. *Astron. Astrophys.* **349**, 301 – 311, 1999A&A...349..301R.

Rouppe van der Voort, L., Bellot Rubio, L.R., Ortiz, A.: 2010, Upflows in the Central Dark Lane of Sunspot Light Bridges. *Astrophys. J.* **718**, L78 – L82, 2010ApJ...718L..78R.

Royds, T.: 1926, Unusual Bright Filaments on the Sun on 1926 February 22. *Mon. Not. R. Astron. Soc.* **86**, 380 – 381, 1926MNRAS..86..380R.

Royds, T.: 1935, Oxygen in the Sun's Chromosphere. *Nature* **136**, 606 – 607, 1935Natur.136..606R.

Rucklidge, A.M., Schmidt, H.U., Weiss, N.O.: 1995, The Abrupt Development of Penumbrae in Sunspots. *Mon. Not. R. Astron. Soc.* **273**, 491 – 498, 1995MNRAS.273..491R.

Ruiz Cobo, B., del Toro Iniesta, J.C.: 1992, Inversion of Stokes Profiles. *Astrophys. J.* **398**, 375 – 385, 1992ApJ...398..375R.

Rutten, R.J., de Wijn, A.G., Sütterlin, P.: 2004, DOT Tomography of the Solar Atmosphere. II. Reversed Granulation in Ca II H. *Astron. Astrophys.* **416**, 333 – 340, 2004A&A...416..333R.

Sainz Dalda, A., Martínez Pillet, V.: 2005, Moving Magnetic Features as Prolongation of Penumbral Filaments. *Astrophys. J.* **632**, 1176 – 1183, 2005ApJ...632.1176S.

Sainz Dalda, A., Vargas Domínguez, S., Tarbell, T.D.: 2012, Magnetic Topology of a Naked Sunspot: Is it Really Naked? *Astrophys. J. Lett.* **746**, L13, 2012ApJ...746L..13S.

Sánchez Almeida, J., Asensio Ramos, A., Trujillo Bueno, J., Cernicharo, J.: 2001, G-Band Spectral Synthesis in Solar Magnetic Concentrations. *Astrophys. J.* **555**, 978 – 989, 2001ApJ..555..978S.

Sánchez Cuberes, M., Bonet, J.A., Vázquez, M., Wittmann, A.D.: 2000, Center-to-Limb Variation of Solar Granulation from Partial Eclipse Observations. *Astrophys. J.* **538**, 940 – 959, 2000ApJ...538..940S

Sankarasubramanian, K., Rimmele, T.: 2003, Properties of Magnetic and Velocity Fields in and around Solar Pores. *Astrophys. J.* **598**, 689 – 699, 2003ApJ...598..689S.

Scharmer, G.B., Gudiksen, B.V., Kiselman, D., Löfdahl, M.G., Rouppe van der Voort, L.H.M.: 2002, Dark Cores in Sunspot Penumbral Filaments. *Nature* **420**, 151 – 153, 2002Natur.420..151S.

Scherrer, P.H., Schou, J., Bush, R.I., Kosovichev, A.G., Bogart, R.S., Hoeksema, J.T., Liu, Y., Duvall, T.L., Zhao, J., Title, A.M., Schrijver, C.J., Tarbell, T.D., Tomczyk, S.: 2012, The Helioseismic and Magnetic Imager (HMI) Investigation for the Solar Dynamics Observatory (SDO). *Solar Phys.* **275**, 207 – 227, 2012SoPh..275..207S.

Schlichenmaier, R.: 2002, Penumbral Fine Structure. Theoretical Understanding. *Astron. Nachr.* **323**, 303 – 308, 2002AN....323..303S.

Schlichenmaier, R., Jahn, K., Schmidt, H.U.: 1998a, A Dynamical Model for the Penumbral Fine Structure and the Evershed Effect in Sunspots. *Astrophys. J. Lett.* **493**, 121 – 124, 1998ApJ...493L.121S.

Schlichenmaier, R., Jahn, K., Schmidt, H.U.: 1998b, Magnetic Flux Tubes Evolving in Sunspots. A Model for the Penumbral Fine Structure and the Evershed Flow. *Astron. Astrophys.* **337**, 897 – 910, 1998A&A...337..897S.

Schlichenmaier, R., Rezaei, R., Bello González, N., Waldmann, T.A.: 2010, The Formation of a Sunspot Penumbra. *Astron. Astrophys.* **512**, L1, 2010A&A...512L...1S.

Schmetz, J., Holmlund, K., Hoffman, J., Strauss, B., Mason, B., Gaertner, V., Koch, A., Van De Berg, L.: 1993, Operational Cloud-Motion Winds from Meteosat Infrared Images. *J. Appl. Meteor.* **32**, 1206 – 1225, 1993JApMe..32.1206S.

Schmidt, W., Stix, M., Wöhl, H.: 1999, Center-to-Limb Variation of the Solar Oscillation. New Results from MDI Data. *Astron. Astrophys.* **346**, 633 – 640, 1999A&A...346..633S.

Schmidt, W., von der Lühe, O., Volkmer, R., Denker, C., Solanki, S.K., Balthasar, H., Bello Gonzalez, N., Berkefeld, T., Collados, M., Fischer, A., Halbgewachs, C., Heidecke, F., Hofmann, A., Kneer, F., Lagg, A., Nicklas, H., Popow, E., Puschmann, K.G., Schmidt, D., Sigwarth, M., Sobotka, M., Soltau, D., Staude, J., Strassmeier, K.G., Waldmann , T.A.: 2012, The 1.5 Meter Solar Telescope GREGOR. *Astron. Nachr.* **333**, 796 – 809, 2012AN....333..796S.

Schou, J., Scherrer, P.H., Bush, R.I., Wachter, R., Couvidat, S., Rabello-Soares, M.C., Bogart, R.S., Hoeksema, J.T., Liu, Y., Duvall, T.L., Akin, D.J., Allard, B.A., Miles, J.W., Rairden, R., Shine, R.A., Tarbell, T.D., Title, A.M., Wolfson, C.J., Elmore, D.F., Norton, A.A., Tomczyk, S.: 2012, Design and Ground Calibration of the Helioseismic and Magnetic Imager (HMI) Instrument on the Solar Dynamics Observatory (SDO). *Solar Phys.* **275**, 229 – 259, 2012SoPh..275..327S.

Schrijver, C.J., DeRosa, M.L., Metcalf, T., Barnes, G., Lites, B., Tarbell, T., McTiernan, J., Valori, G., Wiegelmann, T., Wheatland, M.S., Amari, T., Aulanier, G., Démoulin, P., Fuhrmann, M., Kusano, K., Régnier, S., Thalmann, J.K.: 2008, Nonlinear Force-Free Field Modeling of a Solar Active Region around the Time of a Major Flare and Coronal Mass Ejection. *Astrophys. J.* **675**, 1637 – 1644, 2008ApJ...675.1637S.

Schröter, E.H.: 1967, The Evershed-Effect in Sunspots. In: Xanthakis, J.N. (ed.) *Solar Physics, Proc. NATO Adv. Study Inst. Solar Phys.*, Interscience Publication, London, 1967sp...conf..325S.

Schuck, P.W.: 2005, Local Correlation Tracking and the Magnetic Induction Equation. *Astrophys. J. Lett.* **632**, L53 – L56, 2005ApJ...632L..53S.

Schuck, P.W.: 2006, Tracking Magnetic Footpoints with the Magnetic Induction Equation. *Astrophys. J.* **646**, 1358 – 1391, 2006ApJ...646.1358S.

Schüssler, M., Vögler, A.: 2006, Magnetoconvection in a Sunspot Umbra. *Astrophys. J. Lett.* **641**, L73 – L76, 2006ApJ...641L..73S.

Schüssler, M., Shelyag, S., Berdyugina, S., Vögler, A., Solanki, S.K.: 2003, Why Solar Magnetic Flux Concentrations are Bright in Molecular Bands. *Astrophys. J. Lett.* **597**, L173 – L176, 2003ApJ...597L.173S.

Schwalb, A.: 1978, The TIROS-N/NOAA A-G Satellite Series. Technical Report 95, National Oceanic and Atmospheric Administration.

Sheeley, N.R. Jr.: 1972, Observations of the Horizontal Velocity Field Surrounding Sunspots. *Solar Phys.* **25**, 98 – 103, 1972SoPh...25...98S.

Shibata, K., Magara, T.: 2011, Solar Flares: Magnetohydrodynamic Processes. *Living Rev. Solar Phys.* **8**, 6, 2011LRSP....8....6S.

Shine, R.A., Simon, G.W., Hurlburt, N.E.: 2000, Supergranule and Mesogranule Evolution. *Solar Phys.* **193**, 313 – 331, 2000SoPh..193..313S.

Shine, R.A., Title, A., Frank, Z., Scharmer, G.: 1996, Photospheric Surface Flows and Small Magnetic Structures in Sunspot Moats, *Bull. Am. Astron. Soc.* **28**, 871, 1996AAS...188.3501S.

Simon, G.W., Leighton, R.B.: 1964, Velocity Fields in the Solar Atmosphere. III. Large-Scale Motions, the Chromospheric Network, and Magnetic Fields. *Astrophys. J.* **140**, 1120, 1964ApJ...140.1120S.

Simon, G.W., Title, A.M., Weiss, N.O.: 1991, Modeling Mesogranules and Exploders on the Solar Surface. *Astrophys. J.* **375**, 775 – 788, 1991ApJ...375..775S.

Simon, G.W., Brandt, P.N., November, L.J., Scharmer, G.B., Shine, R.A.: 1994, Large-Scale Photospheric Motions: First Results from an Extraordinary Eleven-Hour Granulation Observation. In: Rutten, R.J., Schrijver, C.J. (eds.) *Solar Surface Magnetism, NATO Adv. Sci. Inst. Ser. C*, Kluwer Academic Publishers, Dordrecht, The Netherlands, 261 – 270, 1994ssm..work..261S.

Singh, J., Bappu, M.K.V.: 1981, A Dependence on Solar Cycle of the Size of the Ca Network. *Solar Phys.* **71**, 161 – 168, 1981SoPh...71..161S.

Singh, J., Ravindra, B.: 2012, Twin Telescope Observations of the Sun at Kodaikanal Observatory. *Bull. Astron. Soc. India* **40**, 77, 2012BASI...40...77S.

Sobotka, M., Hanslmeier, A.: 2005, Photometry of Umbral Dots. *Astron. Astrophys.* **442**, 323 – 329, 2005A&A...442..323S.

Sobotka, M., Roudier, T.: 2007, Properties of Sunspot Moats Derived from Horizontal Motions. *Astron. Astrophys.* **472**, 277 – 282, 2007A&A...472..277S.

Sobotka, M., Bonet, J.A., Vazquez, M.: 1993, A High-Resolution Study of Inhomogeneities in Sunspot Umbrae. *Astrophys. J.* **415**, 832 – 846, 1993ApJ...415..832S.

Sobotka, M., Brandt, P.N., Simon, G.W.: 1999, Fine Structure in Sunspots. III. Penumbral Grains. *Astron. Astrophys.* **348**, 621 – 626, 1999A&A...348..621S.

Sobotka, M., Bonet, J.A., Vazquez, M., Hanslmeier, A.: 1995, On the Dynamics of Bright Features in Sunspot Umbrae. *Astrophys. J. Lett.* **447**, L133, 1995ApJ...447L.133S.

Solanki, S.K.: 2003, Sunspots: An Overview. *Astron. Astrophys. Rev.* **11**, 153 – 286, 2003A&ARv..11..153S.

Spruit, H.C., Nordlund, Å., Title, A.M.: 1990, Solar Convection. *Ann. Rev. Astron. Astrophys.* **28**, 263 – 301, 1990ARA&A..28..263S.

Stanchfield, D.C.H. II, Thomas, J.H., Lites, B.W.: 1997, The Vector Magnetic Field, Evershed Flow, and Intensity in a Sunspot. *Astrophys. J.* **477**, 485 – 494 1997ApJ...477..485S.

Stein, R.F., Nordlund, Å.: 2000, Realistic Solar Convection Simulations. *Solar Phys.* **192**, 91 – 108, 2000SoPh..192...91S.

Stein, R.F., Nordlund, Å.: 2006, Solar Small-Scale Magnetoconvection. *Astrophys. J.* **642**, 1246 – 1255, 2006ApJ...642.1246S.

Steiner, O., Hauschildt, P.H., Bruls, J.: 2001, Radiative Properties of Magnetic Elements. I. Why are G-Band Bright Points Bright? *Astron. Astrophys.* **372**, L13 – L16, 2001A&A...372L..13S.

Straus, T., Deubner, F.L., Fleck, B.: 1992, Is Mesogranulation a Distinct Regime of Convection? *Astron. Astrophys.* **256**, 652 – 659, 1992A&A...256..652S.

Strous, L.H.: 1995, Feature Tracking: Deriving Horizontal Motion and More. In: *Helioseismology, ESA Special Publication* **376**, 213 – 217, 1995ESASP.376b.213S.

Strous, L.H., Scharmer, G., Tarbell, T.D., Title, A.M., Zwaan, C.: 1996, Phenomena in an Emerging Active Region. I. Horizontal Dynamics. *Astron. Astrophys.* **306**, 947 – 959, 1996A&A...306..947S.

Stuart, F.E., Rush, J.H.: 1954, Correlation Analyses of Turbulent Velocities and Brightness of the Photospheric Granulation. *Astrophys. J.* **120**, 245 – 250, 1954ApJ...120..245S.

Sudol, J.J., Harvey, J.W.: 2005, Longitudinal Magnetic Field Changes Accompanying Solar Flares. *Astrophys. J.* **635**, 647 – 658, 2005ApJ...635..647S.

Tan, C., Chen, P.F., Abramenko, V., Wang, H.: 2009, Evolution of Optical Penumbral and Shear Flows Associated with the X3.4 Flare of 2006 December 13. *Astrophys. J.* **690**, 1820 – 1828, 2009ApJ...690.1820T.

Thomas, J.H.: 1988, Siphon Flows in Isolated Magnetic Flux Tubes. *Astrophys. J.* **333**, 407 – 419, 1988ApJ...333..407T.

Title, A.M., Tarbell, T.D., Topka, K.P., Ferguson, S.H., Shine, R.A., SOUP Team: 1989, Statistical Properties of Solar Granulation Derived from the SOUP Instrument on Spacelab 2. *Astrophys. J.* **336**, 475 – 494, 1989ApJ...336..475T.

Tokmakian, R., Strub, P.T., McClean-Padman, J.: 1990, Evaluation of the Maximum Correlation Method of Estimating Sea Surface Velocities from Sequential Satellite Images. *J. Atmos. Oceanogr. Tech.* **7**, 852 – 865, 1990JAtOT...7..852T.

Tritschler, A., Schmidt, W.: 1997, Some Properties of Sunspot Umbral Dots. *Astron. Astrophys.* **321**, 643 – 651, 1997A&A...321..643T.

Tritschler, A., Schlichenmaier, R., Bellot Rubio, L.R., Berkefeld, T., Schelenz, T.: 2004, Two-Dimensional Spectroscopy of a Sunspot. I. Properties of the Penumbral Fine Structure. *Astron. Astrophys.* **415**, 717 – 729, 2004A&A...415..717T.

Tsuneta, S., Ichimoto, K., Katsukawa, Y., Nagata, S., Otsubo, M., Shimizu, T., Suematsu, Y., Nakagiri, M., Noguchi, M., Tarbell, T., Title, A., Shine, R., Rosenberg, W., Hoffmann, C., Jurcevich, B., Kushner, G., Levay, M., Lites, B., Elmore, D., Matsushita, T., Kawaguchi, N., Saito, H., Mikami, I., Hill, L.D., Owens, J.K.: 2008, The Solar Optical Telescope for the Hinode Mission: An Overview. *Solar Phys.* **249**, 167 – 196, 2008SoPh..249..167T.

Unsöld, A.: 1930, Konvektion in der Sonnenatmosphäre (nebst einer Bemerkung zur Deutung der Novae). *Z. Astrophys.* **1**, 138 – 148, 1930ZA.....1..138U.

Ustyugov, S.D.: 2009, Realistic Magnetohydrodynamical Simulations of Local Solar Supergranulation. In: Dikpati, M., Arentoft, T., González Hernández, I., Lindsey, C., Hill, F. (eds.) *Solar-Stellar Dynamos as Revealed by Helio- and Asteroseismology: GONG 2008/SOHO 21*, *ASP Conf. Ser.* **416**, 427 – 432, 2009ASPC..416..427U.

van Driel-Gesztelyi, L., Hofmann, A., Demoulin, P., Schmieder, B., Csepura, G.: 1994, Relationship between Electric Currents, Photospheric Motions, Chromospheric Activity, and Magnetic Field Topology. *Solar Phys.* **149**, 309 – 330, 1994SoPh..149..309V.

Vargas Domínguez, S., Rouppe van der Voort, L., Bonet, J.A., Martínez Pillet, V., Van Noort, M., Katsukawa, Y.: 2008, Moat Flow in the Vicinity of Sunspots for Various Penumbral Configurations. *Astrophys. J.* **679**, 900 – 909, 2008ApJ...679..900V.

Vargas Domínguez, S., de Vicente, A., Bonet, J.A., Martínez Pillet, V.: 2010, Characterization of Horizontal Flows around Solar Pores from High-Resolution Time Series of Images. *Astron. Astrophys.* **516**, A91, 2010A&A...516A..91V.

Verma, M., Denker, C.: 2011, Horizontal Flow Fields Observed in Hinode G-Band Images. I. Methods. *Astron. Astrophys.* **529**, A153, 2011A&A...529A.153V.

Verma, M., Balthasar, H., Deng, N., Liu, C., Shimizu, T., Wang, H., Denker, C.: 2012, Horizontal Flow Fields Observed in Hinode G-Band Images. II. Flow Fields in the Final Stages of Sunspot Decay. *Astron. Astrophys.* **538**, A109, 2012A&A...538A.109V.

Vögler, A., Shelyag, S., Schüssler, M., Cattaneo, F., Emonet, T., Linde, T.: 2005, Simulations of Magneto-Convection in the Solar Photosphere. Equations, Methods, and Results of the MURaM Code. *Astron. Astrophys.* **429**, 335 – 351, 2005A&A...429..335V.

von der Lühe, O., Volkmer, R., Kentischer, T.J., Geißler, R.: 2012, The GREGOR Broad-Band Imager. *Astron. Nachr.* **333**, 894 – 900, 2012AN....333..894V.

Wang, H., Zirin, H.: 1992, Flows around Sunspots and Pores. *Solar Phys.* **140**, 41 – 54, 1992SoPh..140...41W.

Wang, H., Deng, N., Liu, C.: 2012, Rapid Transition of Uncombed Penumbrae to Faculae during Large Flares. *Astrophys. J.* **748**, 76 2012ApJ...748...76W.

Wang, H., Ji, H., Schmahl, E.J., Qiu, J., Liu, C., Deng, N.: 2002, Sudden Disappearance of a Small Sunspot Associated with the 2002 February 20 M2.4 Flare. *Astrophys. J.* **580**, L177 – L180, 2002ApJ...580L.177W.

Wang, H., Liu, C., Qiu, J., Deng, N., Goode, P.R., Denker, C.: 2004, Rapid Penumbral Decay Following Three X-Class Solar Flares. *Astrophys. J. Lett.* **601**, 195 – 198, 2004ApJ...601L.195W.

Warmuth, A., Vršnak, B., Magdalenić, J., Hanslmeier, A., Otruba, W.: 2004a, A Multiwavelength Study of Solar Flare Waves. I. Observations and Basic Properties. *Astron. Astrophys.* **418**, 1101 – 1115, 2004A&A...418.1101W.

Warmuth, A., Vršnak, B., Magdalenić, J., Hanslmeier, A., Otruba, W.: 2004b, A Multiwavelength Study of Solar Flare Waves. II. Perturbation Characteristics and Physical Interpretation. *Astron. Astrophys.* **418**, 1117 – 1129, 2004A&A...418.1117W.

Wedemeyer-Böhm, S., Rouppe van der Voort, L.: 2009, On the Continuum Intensity Distribution of the Solar Photosphere. *Astron. Astrophys.* **503**, 225 – 239, 2009A&A...503..225W.

Welsch, B.T., Fisher, G.H., Abbett, W.P., Regnier, S.: 2004, ILCT: Recovering Photospheric Velocities from Magnetograms by Combining the Induction Equation with Local Correlation Tracking. *Astrophys. J.* **610**, 1148 – 1156, 2004ApJ...610.1148W.

Welsch, B.T., Abbett, W.P., De Rosa, M.L., Fisher, G.H., Georgoulis, M.K., Kusano, K., Longcope, D.W., Ravindra, B., Schuck, P.W.: 2007, Tests and Comparisons of Velocity-Inversion Techniques. *Astrophys. J.* **670**, 1434 – 1452, 2007ApJ...670.1434W.

Welsch, B.T., Kusano, K., Yamamoto, T.T., Muglach, K.: 2012, Decorrelation Times of Photospheric Fields and Flows. *Astrophys. J.* **747**, 130, 2012ApJ...747..130W.

Westendorp Plaza, C., del Toro Iniesta, J.C., Ruiz Cobo, B., Martinez Pillet, V., Lites, B.W., Skumanich, A.: 1997, Evidence for a Downward Mass Flux in the Penumbral Region of a Sunspot. *Nature* **389**, 47, 1997Natur.389...47W.

Wöger, F., von der Lühe, O., Reardon, K.: 2008, Speckle Interferometry with Adaptive Optics Corrected Solar Data. *Astron. Astrophys.* **488**, 375 – 381, 2008A&A...488..375W.

Worden, S.P., Simon, G.W.: 1976, A Study of Supergranulation Using a Diode Array Magnetograph. *Solar Phys.* **46**, 73 – 91, 1976SoPh...46...73W.

Yang, G., Xu, Y., Wang, H., Denker, C.: 2003, High Spatial Resolution Observations of Pores and the Formation of a Rudimentary Penumbra. *Astrophys. J.* **597**, 1190 – 1199, 2003ApJ...597.1190Y.

Yang, G., Xu, Y., Cao, W., Wang, H., Denker, C., Rimmele, T.R.: 2004, Photospheric Shear Flows along the Magnetic Neutral Line of Active Region 10486 prior to an X10 Flare. *Astrophys. J. Lett.* **617**, 151 – 154, 2004ApJ...617L.151Y.

Yurchyshyn, V.B., Wang, H., Goode, P.R.: 2001, On the Correlation between the Orientation of Moving Magnetic Features and the Large-Scale Twist of Sunspots. *Astrophys. J.* **550**, 470 – 474, 2001ApJ...550..470Y.

Zhang, H., Ai, G., Wang, H., Zirin, H., Patterson, A.: 1992, Evolution of Magnetic Fields and Mass Flow in a Decaying Active Region. *Solar Phys.* **140**, 307 – 316, 1992SoPh..140..307Z.

Zhao, J., Kosovichev, A.G., Duvall, T.L. Jr.: 2001, Investigation of Mass Flows beneath a Sunspot by Time-Distance Helioseismology. *Astrophys. J.* **557**, 384 – 388, 2001ApJ...557..384Z.

Zirin, H.: 1988, *Astrophysics of the Sun*, Cambridge University Press, New York, 1998assu.book.....Z.

Zuccarello, F., Romano, P., Guglielmino, S.L., Centrone, M., Criscuoli, S., Ermolli, I., Berrilli, F., Del Moro, D.: 2009, Observation of Bipolar Moving Magnetic Features Streaming out from a Naked Spot. *Astron. Astrophys.* **500**, L5 – L8, 2009A&A...500L...5Z.

Acknowledgments

I owe my deepest gratitude to my supervisor Prof. Dr. Carsten Denker and attribute the level of this work to his encouragement and effort. Without his support this thesis would not have been written and completed. One simply could not wish for a better and friendlier supervisor. I hope to carry on the enthusiasm for research and ideal work-ethics introduced to me by him. Furthermore, it is an honor for me to thank the co-advisor of the work, Prof. Dr. Klaus G. Strassmeier.

I am grateful to all the members of Optical Solar Physics group at AIP. Their company and assistance has made my PhD journey more enjoyable. In particular I would like to thank Dr. Horst Balthasar for proof-reading the thesis and for his valuable suggestions to improve it. I thank Drs. Na Deng, Klaus G. Puschmann, Alexandra Tritschler, Haimin Wang, Toshi Shimizu, and Rohan E. Louis for carefully reading the manuscripts of my papers and for providing comments significantly enhancing their contents. I am also heartly grateful to the Dr. Alexandra Tritschler for her support and help as the supervisor during my stay supported by the NSO as part of the Summer Research Associate program. All the help from Drs. Jürgen Rendtel, Christian Beck and Manuel Collados during the observing campaign at VTT is sincerely appreciated.

I would like to express my sincere gratitude to my previous supervisor Prof. Dr. Jagdev Singh for sharing his experiences and insights. I am also indebted to my teachers at Punjabi University Patiala, Prof. Dr. Darshan Singh, Dr. Balwant S. Salaria, and Dr. Paramjit S. Goraya, who introduced me to the whole new world of astronomy and motivated me to learn more about it. My special thanks goes to German Academic Exchange Service (DAAD) for granting me a Doctoral Scholarship (PKJ: A/08/74404) and providing me with the financial assistance for my stay and studies in Germany.

It is a pleasure to thank my friend Manu, who is solely responsible for introducing the idea of pursuing my Doctorate degree in Germany. He has made available his support in a number of ways, whenever I needed. With pleasure and gratitude I would like to appreciate the wonderful company of my friends Anne, Cindy, Karthick, Mica, Rossitsa, and Shilly, which is like sunshine on dark cold winter days.

Finally, I want to thank my wonderful family. A special thought is devoted to my parents: Poonam and Sushil Kumar Verma for their never-ending support and encouragement to pursue my interests. Whatever I am doing or achieving has only become possible because of their hardship and struggle. I would like to thank Anu, Geetika, and Apoorv for being such a supportive siblings. Furthermore, I would like to acknowledge the love and support of my parents in-law Lila and Dr. Ranajit Kumar Pal and sister in-law Saveri. Above all, I would like to express special thanks to my husband, Parth, for his great patience and trust. Without his unconditional love and encouragement, this work would have been a distant dream.

I would like to sincerely thank the efforts of all the people involved in maintaining and providing solar observational data. Below is the acknowlegment of the observatories and instruments used to obtain data for this thesis.

The Vacuum Tower Telescope is operated by the Kiepenheuer-Institut für Sonnenphysik, Freiburg, at the Spanish Observatorio del Teide of the Instituto de Astrofísica de Canarias. The National Solar Observatory is operated by the Association of Universities for Research in Astronomy, Inc. (AURA), under cooperative agreement with the National Science Foundation. IBIS was constructed by INAF/OAA with contributions from the University of Florence, the University of Rome, MIUR, and MAE, and is operated with support of the National Solar Observatory. HMI data are courtesy of NASA/SDO and the HMI science team. They are provided by the Joint Science Operations Center-Science Data Processing at Stanford University. The GOES X-ray flux measurements were made available by the National Geophysical Data Center. Hinode is a Japanese mission developed and launched by ISAS/JAXA, collaborating with NAOJ as a domestic partner, NASA and STFC (UK) as international partners. Scientific operation of the Hinode mission is conducted by the Hinode science team organized at ISAS/JAXA. This team mainly consists of scientists from institutes in the partner countries. Support for the post-launch operation is provided by JAXA and NAOJ (Japan), STFC (U.K.), NASA, ESA, and NSC (Norway). This research has made use of NASA's Astrophysics Data System. SolarSoftware is a public-domain software package for analysis of solar data written in the Interactive Data Language by Exelis Visual Informations Solutions.

Appendix A – Abstracts

Articles

Properties of a Decaying Sunspot

Balthasar, H., Beck, C., Gömöry, P., Muglach, K., Puschmann, K.G., Shimizu, T., Verma, M.: 2013, Cent. Eur. Astrophys. Bull., in press, 2013arXiv1301.1562B

A small decaying sunspot was observed with the Vacuum Tower Telescope (VTT) on Tenerife and the Japanese Hinode satellite. We obtained full Stokes scans in several wavelengths covering different heights in the solar atmosphere. Imaging time series from Hinode and the Solar Dynamics Observatory (SDO) complete our data sets. The spot is surrounded by a moat flow, which persists also on that side of the spot where the penumbra already had disappeared. Close to the spot, we find a chromospheric location with downflows of more than 10 km s^{-1} without photospheric counterpart. The height dependence of the vertical component of the magnetic field strength is determined in two different ways that yielded different results in previous investigations. Such a difference still exists in our present data, but it is not as pronounced as in the past.

Posters

Statistical Characteristics of Horizontal Proper Motions in the Vicinity of Pores

Verma, M., Denker, C.: 2012, Solar and Astrophysical Dynamos and Magnetic Activity, A.G. Kosovichev, E.M. de Gouveia Dal Pino & Y.Yan (eds.), Proc. IAU Symp. **294**, in press, 2012arXiv1210.5145V.

Movement and coalescence of magnetic elements could explain the evolution and growth of pores. There have been numerous studies focusing on flow fields in and around individual pores. We have undertaken a systematic study of the statistical properties of such flows. Data of the Hinode Solar Optical Telescope offer an opportunity for this type of research, because of the uniform data quality and absence of seeing so that pores can directly be compared in different environments and at various stages of their evolution. We analyzed about 220 time-series of G-band images using local correlation tracking. The thus computed flow maps make up a database, which covers various scenes on the solar surface. We use an isolated pore to illustrate the statistical parameters collected for further statistical analysis, which include information about morphology, horizontal flows, evolutionary stage (young, mature, or decaying), complexity of the surrounding magnetic field, and proximity to sunspots or cluster of G-band bright points.

Flow Fields in the Vicinity of Decaying Sunspots and Pores

Verma, M., Denker, C.: 2012, Hinode-6 meeting on *Out with the Old (Cycle) . . . and in with the New*, University of St. Andrews, Scotland, 14–17 August 2012.

Generation and dissipation of magnetic fields is a fundamental physical process on the Sun. Coalescence and movement of magnetic elements could explain growth and decay of Sunspots. There have been numerous studies focusing on flux emergence and the initial stages of sunspot formation. However, the demise of sunspots still lacks a comprehensive description. We are interested in changes of flows and magnetic fields, which are related to the decay of sunspots. We developed a Local Correlation Tracking (LCT) algorithm for Hinode G-band images to follow horizontal proper motions in and around sunspots. In the time period from 2006–2009, we found more than 200 days of G-band images with a suitable cadence, so that more than 500 individual flow maps could be computed. The thus computed flow maps make up a database, which covers various scenes on solar surface. We present two case studies focusing on the decay of sunspots: (1) Flux submergence and slow penumbral decay within a satellite sunspot of active region NOAA 10930 led to a significant restructuring of the magnetic field topology and a subsequent M2.0 flare. (2) Comparing two pores with different histories and backgrounds - an isolated pore in the active chromospheric network and a residual pore, i.e., the end product of a decaying sunspot - we found noticeable differences in various physical quantities related to the flow fields.

Horizontal Flow Fields Observed in *Hinode*/SOT G-Band Images

Verma, M., Denker, C.: 2010, Hinode-4 meeting on *Unsolved Problems and Recent Insights*, Palermo, Italy, 11–15 October 2010.

The data volume of Hinode has become so large that it is practically impossible for a single researcher to inspect each individual image. We analyzed about one Terabyte of G-band images to study horizontal proper motions using Local Correlation Tracking (LCT) techniques. A package of IDL programs was developed for this task, which performs all the steps from preprocessing, over computing the horizontal flow fields, to publishing the results on web pages. Only a minimum of user interaction is needed, and only if unforeseen data problems arise. These LCT data are a complete sample of G-band time-series with a cadence shorter than 100 s and a duration of at least one hour. All derived data products will be made available as a small data project within the scope of the German Astrophysical Virtual Observatory (GAVO). We describe the data products, which will be accessible in the VO. In addition, we present a case study focusing on the flow field of an isolated pore and its immediate surroundings.

Observations of On-Disk Type I and II Spicules

Deng, N., Denker, C., Verma, M., Shimizu, T., Liu, C., Wang, H.: 2011, 42 SPD meeting in 2011 June 12–16, 2011SPD....42.1737D.

A coordinated observing campaign was carried out during 2010 November 16-30 using German Vacuum Tower Telescope (VTT) and Hinode to investigate properties of small-scale spicules on the solar disk. The high-spectral resolution Echelle spectrograph at the VTT on Tenerife acquired spectra of the chromospheric Hα (656.28 nm) and photospheric Fe I (656.92 nm) lines in a region centered on a small pore. Hinode mission provides high-cadence vector magnetograms, G-band and Ca II H images, EUV Imaging Spectrometer (EIS) and X-Ray Telescope (XRT) observations of the same region. We present statistical properties of spicules (type I and II), such as spectral characteristics, velocities, spatial distribution and temporal evolution, paying particular attention to type II spicules or chromospheric jets. We investigate the photospheric magnetic structure, flow field and their evolution attempting to find the origin of chromospheric jets. The vertical extent of identified chromospheric jets in the transition region and corona will be studied using EIS and XRT observations in conjunction with SDO observations.

Appendix B – List of Acronyms

3D	Three-Dimensional
AIP	Leibniz-Institut für Astrophysik Potsdam
AMV	Astmospheric Motion Vector
ASD	Atmospheric Science Division
ATST	Advanced Technology Solar Telescope
AVHRR	Advance Very High Resolution Radiometer
AVI	Audio Video Interleave
BBI	Broad-Band Imager
BFI	Broad-Band Filter Imager
CCD	Charge-Coupled Device
CLV	Center-to-Limb-Variation
CME	Coronal Mass Ejection
CMV	Cloud Motion Winds
CZCS	Coastal Zone Color Scanner
DAAD	Deutscher Akademischer Austausch Dienst
DAVE	Differential Affine Velocity Estimator
EIS	EUV Imaging Spectrometer
EST	European Solar Telescope
EUV	Extrem Ultra-Violet
FFT	Fast Fourier Transform
FITS	Flexible Image Transport System
FOV	Field-of-View
FPP	Focal Plane Package
FT	Feature Tracking
FWHM	Full-Width-at-Half-Maximum
GAVO	German Astrophysical Virtual Observatory
GOES	Geostationary Operational Environmental Satellites
HMI	Helioseismic and Magnetic Imager
HOP	Hinode Observing Plan
HTML	Hyper Text Markup Language
IA	Interrogation Area
IDL	Interactive Data Language
IIA	Indian Institute of Astrophysics
IR	Infrared
ISAS	Institute of Space and Astronautical Science
ISRO	Indian Space Research Organization
JAXA	Japanese Aerospace Exploration Agency
KSC	Kennedy Space Center
LCT	Local Correlation Tracking
LOS	Line-of-Sight

MCC Maximum Cross-Correlation
MDI Michelson Doppler Imager
MHD Magnetohydrodynamics
MMF Moving Magnetic Feature
MOG Meterology and Oceanography Group

NAOJ National Astronomical Observatory of Japan
NASA National Aeronautics and Space Administration
NAVE Non-Linear Affine Velocity Estimator
NFI Narrow-Band Filter Imager
NGDC National Geophysical Data Center
NLST National Large Solar Telescope
NOAA National Oceanic and Atmospheric Administration
NSC Norwegian Space Centre
NST New Solar Telescope
NWP Numerical Weather Prediction
OTA Optical Telescope Assembly

PIV Particle Image Velocimetry
PMU Polarization Modulation Unit
PNG Portable Network Graphics

ROI Region-of-Interest

SAC Space Application Center
SDO Solar Dynamics Observatory
SIR Stokes Inversion based on Response function
SoHO Solar and Heliospheric Observatory
SO Solar Orbiter
SOT Solar Optical Telescope
SOUP Solar Optical Universal Polarimeter
SP SpectroPolarimeter
SSW SolarSoft
STFC Science and Technology Facilities Council
SVST Swedish Vacuum Solar Telescope

UBF Universal Birefringent Filter
UK United Kingdom
URL Uniform Resource Locater
US United States

VTT Vacuum Tower Telescope

WV Water Vapor
WWW World Wide Web

XRT X-Ray Telescope